

Project Report
ASAP-9
Volume 2

**Proceedings of the Adaptive Sensor Array
Processing (ASAP) Workshop**
13-14 March 2001

J.E. Daneu
Editor

20 July 2001

Lincoln Laboratory
MASSACHUSETTS INSTITUTE OF TECHNOLOGY
LEXINGTON, MASSACHUSETTS



Prepared for the Defense Advanced Research Projects Agency and the Department of the Navy
under Air Force Contract F19628-00-C-0002.

Approved for public release; distribution is unlimited.

20010809 041

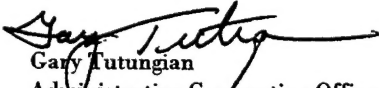
This report is based on studies performed at Lincoln Laboratory, a center for research operated by Massachusetts Institute of Technology. The work was sponsored in part by the Defense Advanced Research Projects Agency and in part by the Department of the Navy under Air Force Contract F19628-00-C-0002.

This report may be reproduced to satisfy needs of U.S. Government agencies.

The ESC Public Affairs Office has reviewed this report, and it is releasable to the National Technical Information Service, where it will be available to the general public, including foreign nationals.

This technical report has been reviewed and is approved for publication.

FOR THE COMMANDER


Gary Tutungian
Administrative Contracting Officer
Plans and Programs Directorate
Contracted Support Management

Non-Lincoln Recipients

PLEASE DO NOT RETURN

Permission is given to destroy this document
when it is no longer needed.

Massachusetts Institute of Technology
Lincoln Laboratory

**Proceedings of the Adaptive Sensor Array
Processing (ASAP) Workshop
13–14 March 2001**

J.E. Daneu
Editor
Division 10

Project Report ASAP-9, Volume 2

20 July 2001

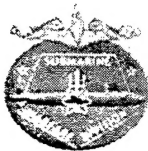
Approved for public release; distribution is unlimited.

ASAP 2001 Workshop Theme

This year marks the ninth annual Adaptive Sensor Array Processing Workshop, which is sponsored jointly by the DARPA Advanced Technology and Tactical Technology Offices, the Navy AEGIS and E2C Program Offices, the Office of Naval Research, and the NAVSEA Advanced Systems Technology Office.

As the ASAP Workshop has evolved over its nine-year history, a common theme has been to highlight the similarity of adaptive sensor array processing techniques for various disciplines. The ASAP forum has provided researchers from academia, government, and industry the opportunity to discuss common problems, developing ideas, and solutions related to how these diverse technologies can be applied to national defense interests. This year will continue to stress the strong coupling between government, industry and academia. A key theme will be the cross-fertilization of ideas to provide new areas of exploration and accelerate technological advances.

We welcome your participation in the ninth annual ASAP Workshop.



RADM Malcolm Fages
US Navy / Submarine
Warfare Division (N77)



Dr. John Tague
ONR



Mr. Fred Lee
US Navy/PMA-231



Dr. Joseph Guerci
DARPA/SPO



Mr. James Thompson
NAVSEA 93 ASTO



CAPT John Geary
US Navy PMS-400



Workshop Chairman, Dr. Edward Baranoski
Technical Program Coordinator, Dr. Steve Behrends
Workshop Administrator, Jane Daneu

Technical Committee

Prof. Kristine Bell / George Mason University
Dr. Henry Cox / ORINCON
Prof. Daniel Fuhrmann / Washington University
Dr. Peter Mikhalevsky / SAIC
Dr. Tom Miller / Raytheon
Prof. Arye Nehorai / University of Illinois

Prof. Louis Scharf / University of Colorado
Prof. Lee Swindlehurst / Brigham Young University
Prof. Donald Tufts / University of Rhode Island
Dr. James Ward / MIT Lincoln Laboratory
Dr. Michael Zatman / MIT Lincoln Laboratory

ADAPTIVE SENSOR ARRAY PROCESSING WORKSHOP

13-14 March 2001

**Sponsored jointly by
the DARPA Advanced Technology and Tactical
Technology Offices, the Navy AEGIS and E2C Program Offices,
the Office of Naval Research, and the NAVSEA Advanced Systems Technology
Office.**

**Massachusetts Institute of Technology
Lincoln Laboratory
Lexington, MA 02420-9108**

Table of Contents

	Page
Adaptive Beamforming for Submarine-Satellite Communications with the (MBCA) Multielement Buoyant Cable Array Antenna <i>B. Carlson</i>	1
RFI and Mainlobe Jamming Mitigation for Multi-channel Imaging Radars <i>P. Bidigare</i>	7
Further Evaluations of STAP Tests in Compound-Gaussian Radar Clutter <i>J. Michels, M. Rangaswamy, and B. Himed</i>	13
Impulsive Noise Mitigation in Spatial and Temporal Domains for Surface-Wave Over-the-Horizon Radar <i>Y. Abramovich and P. Turcaj</i>	19
Subband Energy Detection Methods in Passive Array Processing <i>M. Bono, B. Shapo, P. McCarty, and R. Bethel</i>	25
Case of Short Data Record for Both Training and Signal Detection <i>B. Freburger and D. Tufts</i>	31
Optimal Target Identification via Adaptive Radar Transmission <i>D. Garren, M. Osborn, A. Odom, and J. Goldstein</i>	37
Constrained Maximum-Likelihood Covariance Estimation for Time-Varying Sensor Arrays <i>D. Rieken and D. Fuhrmann</i>	43
Resolution of Mainlobe and Sidelobe Detections Using Model Order Determination <i>A. Jaffer, J. Chen, and T. Miller</i>	49
Space-Time Adaptive FIR Filtering with Staggered PRI <i>R. Klemm</i>	55

Parametric Filters for Non-Stationary Interference Mitigation in Airborne Radars <i>P. Parker and A. Swindlehurst</i>	61
Interference Estimation and Mitigation for STAP Using the Two-Dimensional Wold Decomposition Parametric Model <i>J. Francos, W. Fu, and A. Nehorai</i>	67
The Relationship between Detection Algorithms for Hyperspectral and Radar Applications <i>N. Keshava, S. Kogon, and D. Manolakis</i>	73
Linear Feature Detection in SAR Images <i>P. Courmontagne</i>	79
Space-Time Adaptive Matched-Field Processing (STAMP) <i>Y. Lee</i>	85
Moving Target Depth Estimation for Passive Sonar, Using Sequential Resampling Techniques <i>S. Kraut and J. Krolik</i>	91
Covariance Matrix Filtering for Adaptive Beamforming with Moving Interference <i>B. Newhall</i>	97
Beamspace Adaptive Beamforming for Hydrodynamic Towed Array Self-Noise Cancellation <i>V. Premus, S. Kogon, and J. Ward</i>	103

ADAPTIVE BEAMFORMING FOR SUBMARINE-SATELLITE COMMUNICATIONS WITH THE (MBCA) MULTIELEMENT BUOYANT CABLE ARRAY ANTENNA

Blair D. Carlson

MIT Lincoln Laboratory
244 Wood Street
Lexington, MA 02420, USA

bcarlson@ll.mit.edu

ABSTRACT

In order to provide the capability for submarines to communicate through a satellite while remaining submerged and traveling at operational speeds a towed buoyant cable array antenna is being developed. The array is adaptive from the point of view that the direction of the satellite need not be known, the position and orientation of the array need not be known, and the shape of the flexible array need not be known. A blind equalization procedure is used to estimate the signal space from the downlink signal and create a spatial matched filter for receive. While the frequency division satellite system is intended to allow only one signal per frequency slot, the system can also operate in the presence of jamming by separating multiple sources spatially.

Once the downlink receive antenna weights have been obtained, the more difficult task of obtaining uplink weights at a separated frequency must be performed. Since no data is available for blind equalization at the transmit frequency a frequency extrapolation method is used to extend the downlink receive weights to frequencies beyond where the equalization data was collected. This extrapolation is complicated by 2- π ambiguities of the measured phases as well as amplification of measurement errors in the extrapolation process. An algorithm has been developed that performs well.

1. INTRODUCTION

An adaptive array antenna is being developed to provide the capability for submarines to communicate through a satellite while remaining submerged and traveling at operational speeds[1]. The antenna consists of 12 elements in a linear floating hose that is attached at the end of a long tow cable. The flexible antenna rides the waves so the instantaneous shape and orientation of the array are unknown. The multiple elements provide margin to the communication link budget through the increased gain compared to a single element system, but the principle advantage of the multiple elements is the element diversity which provides resistance to element wash-over effects[2]. When one or several elements are washed over and incapable of receiving or transmitting the remainder of the array will carry the load with only a small fade rather than the deep dropout that would be experienced by a single element antenna.

In order to provide the antenna gain and stability from the multiple elements, the downlink, i.e., receive, signals are combined in an RF beamformer after being phase shifted with digitally controlled analog phase shifter. The only amplitude control is 1-bit, i.e. the channel can be turned on or off. This on/off switch allows an element to be turned off when its adaptive weight is very small and the use of the element at full gain would add more noise than signal. This results in only a modest loss relative to implementation of the actual optimum amplitude weight. The beamforming is done in the analog domain so that the whole adaptive array system can be used as a drop-in antenna for existing communication systems without impacting other aspects of the communications hardware or methods of operation. The weight determination for receive beamforming is based on sampling the downlink signal on the multiple elements to determine their phases and is covered in section 2.

When a signal is to be sent up to the satellite a different frequency is used, differing from the downlink frequency by about 15%. Since there is no signal from the satellite at the uplink frequency to sample, an alternative method of determining the transmit weights must be used. The method of transmit phase determination is based on calculating receive weight phases on two different downlink frequencies that are separated. The phase on each of the elements is then extrapolated linearly to the frequency where the transmit weights are to be used. Since the satellite is constantly transmitting on all downlink frequencies there is no problem finding two sets of separated adaptive weights for the extrapolation process. Transmit beamforming with frequency extrapolation is covered in section 3.

2. RECEIVE BEAMFORMING

2.1 Algorithm and Estimation Accuracy

The main goal of making the system adaptive is to phase shift the element signals so that their phasors are aligned tip-to-tail to create the largest possible resultant and therefore high gain. This is accomplished by receiving and sampling the downlink signal from the satellite on each of the elements and creating a sample covariance matrix. The satellite system that this antenna system works with is frequency channelized so there should be only one signal, i.e., the signal of interest, passed through the receivers

and into the sampled covariance matrix. There should only be a single large eigenvalue of the matrix corresponding to the signal of interest and the eigenvector associated with the largest eigenvalue corresponds to the spatial mode of excitation of that signal on the array. The conjugate of this primary eigenvector then represents the spatial matched filter to best receive the downlink signal. At this point any element whose adaptive weight is down from the nominal level by more than 6 dB is turned off. The actual level where a reduced-signal element does more harm than good in the beamforming is a function of the number of elements in the system, but converges to -6 dB for large numbers of elements in the array. This adaptive process is repeated at a rate that is faster than any changes in the ocean-antenna environment and is on the order of 10-100 Hz.

The accuracy of the adaptive phase determination is not as critical in this type of beamforming compared to nulling systems since a small misalignment of phasers all in a line will still have a large resultant. An analysis of Gaussian distributed phase errors on the element channels leads to an expected loss (or relative gain) in the beamformer of

$$G = e^{-\sigma^2},$$

where σ is the RMS phase error level in radians. This beamforming loss is independent of the number of elements. The spread about the expected value, however, does depend on the number of elements in the system. This loss equation is plotted in Fig. 1 as the solid line along with simulation results for a 10-element system, where 10 runs were made at each 0.1 radian phase error level. The spread about the expected value is larger for large phase errors and for small numbers of elements.

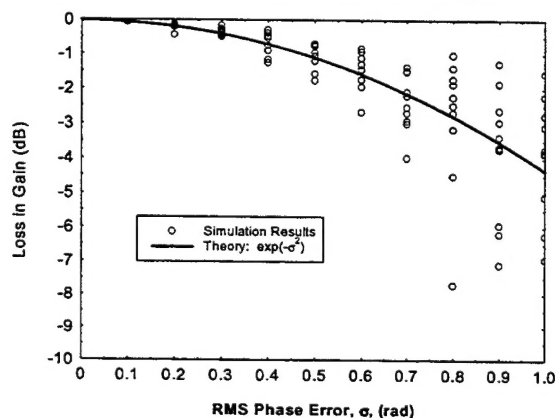


Figure 1. RMS phase errors effect the relative gain of the beamformer. The theoretical loss is shown along with simulation results for a 10-element system as a function of the level of the Gaussian distributed errors.

The number of samples, k , used in forming the sample covariance matrix and the signal-to-noise ratio, SNR , on the elements effect both the phase error level and the amplitude error level. These effects can be incorporated into the relative gain expression resulting in a simple approximate expression for loss as a function of k and SNR :

$$G = e^{-\frac{1}{k \cdot SNR}}.$$

A plot of this equation is shown in Fig. 2 as the solid line for a $k=10$ sample case. A series of simulations were run, one at each integer dB level of SNR , and Fig. 2 shows the inner product of the signal vector with each of the eigenvectors as circles in the plot. It can be seen that the primary eigenvector is a very good estimate of the signal vector, especially at higher SNR levels.

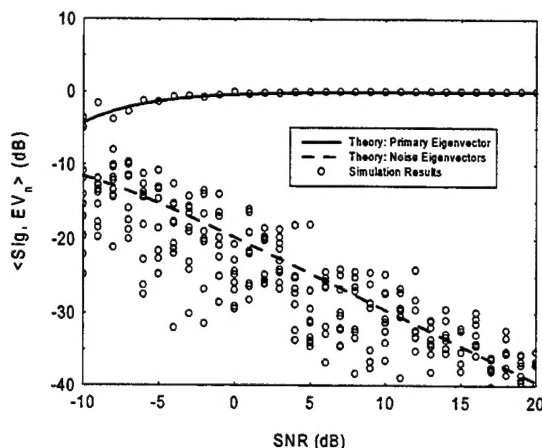


Figure 2. Lines show theory and circles show simulations of inner product of signal and eigenvectors. The simulation was run at each integer dB level.

The other noise eigenvectors will be orthogonal to the primary eigenvector and approximately orthogonal to the signal vector. One measure of the quality of the signal estimate that is more readily seen in the plot of Fig. 2 is the level of the inner product of the signal with the noise eigenvectors. High SNR leads to a high degree of orthogonality. A theoretical expression for these noise inner products levels, NIL s, can be given by

$$NIL = \frac{1 - e^{-\frac{1}{k \cdot SNR}}}{N - 1},$$

where N is the number of elements in the system. The equation points out that NIL is not nil, although it is close. These approximate expressions show that SNR and k can be traded off against one another as needed in the system design, however the accuracies of the expressions are worse at very low SNR values and care should be used in the tradeoff.

2.2 Experimental Results

A seven element experimental array was built to prove the beamforming concept. A strong CW signal transmitted from a helicopter passing the 170 foot towed array was used as a substitute for the satellite downlink signal. The power received from each of the seven elements is plotted in Fig. 3 and the dropouts of individual channels from ocean washover is evident.

The overall change in power levels over the 40 second run is caused by the changing range of the source on the helicopter as it flew past from stern to bow. The output of the RF beamformer was also received and sampled and is shown as the top curve of Fig. 3. It is clear that the seven elements provided both gain and signal stability. Dropouts on individual channels show up in the beamformed signal as small dips on a signal that has much higher SNR due to the array gain.

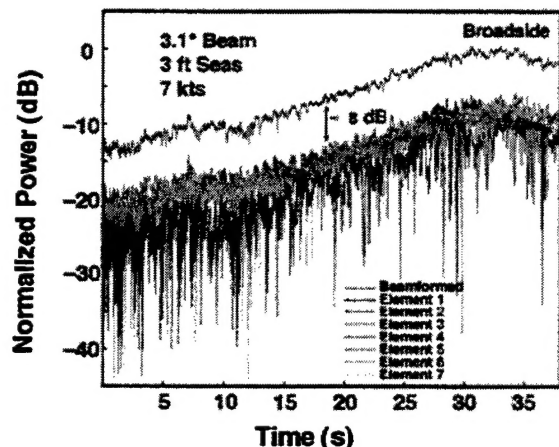


Figure 3. The element power vs. time is plotted for a helicopter fly-by experiment. The beamformer output is the top curve.

The individual elements are spaced far enough apart so that the waves impact them in an independent fashion. If the elements are too close, a washout on one element would be highly correlated with washouts on the neighboring elements and many more elements would be needed in the array to reach the performance achieved with the widely separated element. Since there is a desire to make the array as short as possible with few elements for simplicity, an interesting tradeoff arises for the array design of the spacing and number of elements required to meet the performance goals [3][4].

2.3 Weight Smoothing

In addition to providing gain and signal level stability, it is also necessary to be sure that the phase at the output of the beamformer is stable so that the signal modulation is not corrupted. While this is not a beamforming task in itself, it is necessary for any modulation system that depends on the signal phase. The beamformer output phase is arbitrarily set at every weight update cycle by the adaptive weights which are only determined within a random phase factor. Both the old weights and the new will provide good beamforming at the transition time, but there will be a phase jump at the beamformer output unless corrective action is taken. In this adaptive system a correction phase is determined for the new weights by applying both sets of weights digitally to the new block of data and calculating the average phase shift between the output of the old weights relative to the new weights. This measured phase offset

is then used as an adjustment on the new weights before they are applied to the RF beamformer.

2.4 Interference

While it is intended that the system operate with only one signal present during the estimation of the covariance matrix, it is possible that a jammer from a direction other than the direction of the satellite would try to confuse the adaptive process. If a large jammer signal is present along with the smaller desired signal, the covariance matrix will have two large eigenvalues rather than one. The two eigenvectors associated with the two large eigenvalues span the signal space of the two signal vectors. To a large extent a one-to-one association can be made between each eigenvector and one of the signals if the power of the two signals is different, although strictly speaking each eigenvector will have a portion of each signal if the signals are not spatially orthogonal. With a larger jammer, the signal vector can be estimated by the second eigenvalue and eigenvector. If the conjugated of this second eigenvector is used as the array weight vector then the desired signal will be well received and the jammer will be well rejected since the eigenvectors are orthogonal to each other.

The degree of separation of the signals into separate eigenvectors can be seen by looking at the inner product of the second eigenvector with each of the two signal vectors. The difference between the two represents the null depth that is achievable. The degree of separation, i.e., the null depth, for spatially separated signals can be represented by:

$$ND = \frac{\left(\frac{P_1}{P_2} \right)^2}{N},$$

where P_n is the signal power and N is the number of element in the system. This is illustrated in Fig. 4 for a 10-element system where simulation results are plotted at each integer dB level of signal power separations. For most levels of signal power separations nulling and signal reception can be achieved.

This has been confirmed in seatrials with digital beamforming on the seven element system where a jammer signal was placed on the tow boat while the weaker desired signal was transmitted from a helicopter. The jammer to signal level was 16 dB on the elements so 40 dB null depth was predicted. By using the second eigenvector, the array signal-to-interference-ratio was improved by 45 dB relative to the single element signal-to-interference-ratio.

Jamming and interference are not expected in the current application, but if they are expected, these results show that enough signal separation can be achieved to improve the beamformer output. If nulling is desired it is expected that digital beamforming and amplitude control would be required for better accuracy unlike in the current application.

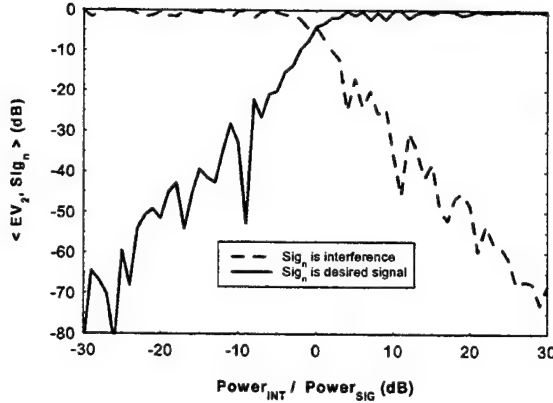


Figure 4. Simulation results show the degree of alignment between the second eigenvector and the desired signal and the jammer interference.

3. TRANSMIT BEAMFORMING WITH FREQUENCY EXTRAPOLATION

3.1 Algorithm

Beamforming on transmit for the uplink to the satellite is a much more difficult task than receive beamforming on the downlink because the uplink frequency is separated from the downlink frequency by about 15%. There is no data at the uplink frequency to use for the weight estimation. There are, however, many downlink frequencies that are constantly in use, so receive weights can be estimated at multiple separated receive frequencies. The approach taken in this design is to estimate receive weights at two separated frequencies and linearly extrapolate the phase of each element to the transmit frequency, using the first two terms of a Taylor series expansion of the element phase.

3.2 Weight Bandwidth

Before investigating the extrapolation, it is useful to look at the effective bandwidth of array weights. If array weights are used at a frequency that is different from the frequency where they were calculated, they will still work with a small degradation as long as the frequency change is not too big. The loss due to the use of array weights with a frequency change of Δf can be approximated by

$$L = \frac{\sin^2\left(\frac{\pi}{c} \Delta f L \sin \theta\right)}{\left(\frac{\pi}{c} \Delta f \sin \theta\right)^2},$$

where c is the speed of propagation, L is the length of the array, and θ is the angle of arrival measured from broadside to the array. This leads to a weight bandwidth, BW , of approximately

$$BW = \frac{c}{L \sin \theta}$$

The 15% change in frequency in this application is well beyond one half of the effective weight bandwidth calculated for moderate arrival directions of 60 degrees off broadside and an array length of 100 feet. This means that new transmit weights will have to be estimated.

3.3 Frequency Extrapolation

Two potential problems arise with frequency extrapolation of the element weights. The actual phase on receive is only known modulo 2π since that is what comes out of the receivers. The extrapolation will yield erroneous results if unknown additions of 2π are left out. The other complication arises from the amplification of measurement errors that can occur with large levels of extrapolation. The 2π ambiguity problem will be considered first.

The truncated Taylor series of the eigenvector phases can be expressed as

$$\phi_3 = \phi_1 + \left(\frac{\phi_2 - \phi_1}{f_2 - f_1} \right) (f_3 - f_1) = \phi_1 + \Delta\phi_{2-1} \left(\frac{\Delta f_{3-1}}{\Delta f_{2-1}} \right)$$

where ϕ s are the phases, the subscripts refer to the frequencies (1 and 2 are the lower and upper receive frequencies and 3 is the higher transmit frequency), and Δ s refer to frequency or phase differences. The factor in parentheses on the right will be referred to as M or the extrapolation ratio, i.e.,

$$M = \left(\frac{\Delta f_{3-1}}{\Delta f_{2-1}} \right)$$

The actual receive phases or Δ phases on the channels can be expressed as

$$\phi_{actual} = 2\pi n + \phi_{measured} \quad n = 0, \pm 1, \pm 2, \dots$$

If the extrapolation ratio, M , is restricted to be an integer then the value of $M\phi_{actual} \pmod{2\pi}$ is the same as $M\phi_{measured} \pmod{2\pi}$ so it does not matter that we do not know the value of n . The 2π ambiguity problem is eliminated by using integer extrapolation ratios.

In the current application there are many downlink receive frequency channels that can be used as an auxiliary receive weight estimation frequency for the extrapolation. An auxiliary channel can be found such that the extrapolation ratio is close to an integer ratio. The previous analysis of the effective bandwidth of the weights shows that integer extrapolation to a frequency that is close to the uplink frequency is good enough.

The problem of measurement noise amplification in the extrapolation process can be thought of as arising from the derivative in the Taylor series, since it is well known that differentiating noise will amplify errors. If an assumption is made that the RMS measurement phase noise is the same at each of the two downlink receive frequencies an expression for the phase error amplification factor can be given by

$$A = \sqrt{1 - 2M + 2M^2}.$$

This says that if the RMS phase error at the two downlink receive frequencies is σ , then the RMS phase error after using an extrapolation ratio of M is $A\sigma$ at the uplink transmit frequency. The amplification factor, A , is always greater than 1.0 and is approximately linear for M s ranging from one to five. A plot of the amplification factor is shown in Fig. 5. It can be seen that if a certain phase error level is required on transmit in order to minimize the beamforming loss then the phase error requirement on the receive weights is five times tighter for an extrapolation ratio of 4.0.

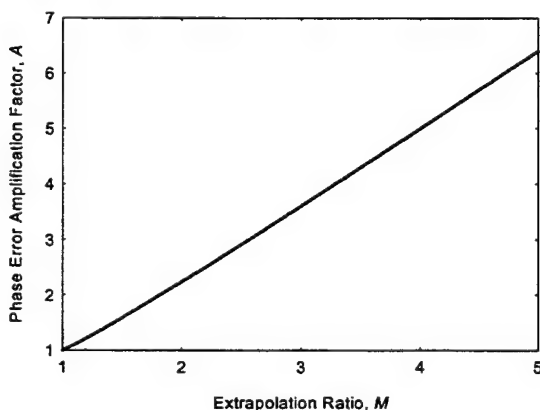


Figure 5. The phase error amplification factor, A , is approximately a linear function of extrapolation ratio, M , for values of M ranging from one to five.

It can be calculated and it is shown in Fig. 1 that if the transmit beamformer loss is to be limited to about 1.0 dB, then the RMS transmit phase error must be limited to about 0.5 radians (28 deg.). The plot in Fig. 6 shows the limit of RMS receive phase errors that must be obtained in order to achieve the required 0.5 radians at the transmit frequency after extrapolating. It can be seen that transmit beamforming becomes quite difficult for large extrapolation ratios.

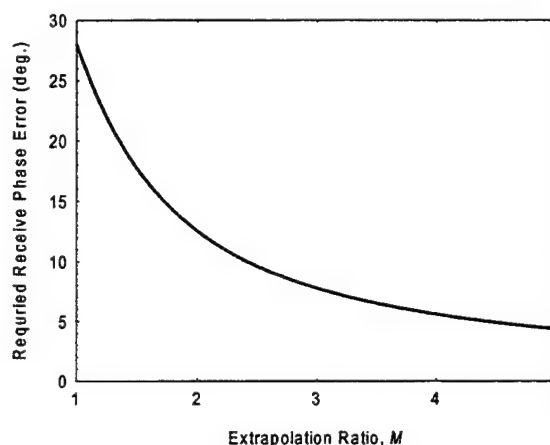


Figure 6. The RMS receive phase error that is required in order to achieve 1 dB of transmit beamforming loss is plotted as a function of the extrapolation ratio, M .

3.4 Experimental Results

A field experiment has been conducted to prove the concept of transmit extrapolation beamforming using the receive-only test array described earlier in Sec. 2. Modifications were made to the system to accommodate the transmit demonstration through a receive-only test system by using reciprocity. Four elements were used. Signals were transmitted from the helicopter at three frequencies, representing the two downlink frequencies and the one uplink frequency. Adaptive weights were calculated using the receive algorithm at all three frequencies. The two sets of weights at the downlink frequencies were then extrapolated to estimate weights for the transmit frequency. These extrapolated "transmit" weights were then compared to the receive adaptive weights that were calculated directly at the transmit frequency by performing digital beamforming with the two sets of "transmit" weights. The results are plotted in Fig. 7 along with the powers of each of the four individual channels for a case with an extrapolation ratio of 2.0. It is clear that both sets of transmit weights perform well with only a small loss using the extrapolated weights relative to the directly calculated (non-extrapolated) weights.

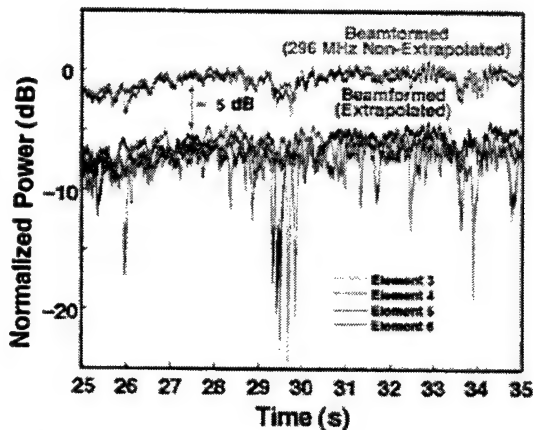


Figure 7. "Transmit" extrapolation beamforming results for an experiment using receive data and reciprocity for an extrapolation ratio, M , of 2.0.

4. SUMMARY

An adaptive beamforming system has been designed and built that will enable submarines to communicate through satellites while remaining at operational speeds and depths. The downlink receive beamforming is based on weights derived from the primary eigenvector of the sample covariance matrix. Only moderate phase accuracy is required to provide both gain and element diversity to overcome the dropouts in the ocean environment. Interference signals can be spatially separated from the desired signal from the satellite with this type of algorithm, although no interference is anticipated in this application.

The transmit uplink beamformer cannot use the same weights as are used on the receive downlink because the uplink and the downlink frequencies are separated by about 15%. A frequency extrapolation method is used where the phases and derivatives of phases with respect to frequency are estimated and used to project the element phases to the uplink frequency by the use of a truncated Taylor series. In order to avoid 2π ambiguity problems in the extrapolation, it is necessary that the frequency gap to the uplink frequency be an integer multiple of the frequency gap between the two downlink frequencies. An exact integer ratio is not required since the weights have a reasonably sized bandwidth, based on the array length and the signal angle of arrival. Much greater accuracy is required in the receive weight estimation in order to have reasonable accuracy at the transmit frequency after extrapolation since phase errors are amplified in the extrapolation process.

Both the receive and transmit algorithms and beamforming have been tested at sea with good results.

5. REFERENCES

- [1] Somers G. A., Carlson B. D., and Thompson G. R., "Buoyant Cable Array Antenna (BCAA) Technologies for Enhanced Submarine Connectivity at Speed and Depth," Submarine Technology Symposium 1999, Applied Physics Laboratory, Johns Hopkins University, 11 May 1999.
- [2] Simon M. K. and Alouini M-S., "Digital Communication over Fading Channels," John Wiley and Sons Inc., 2000.
- [3] Carlson B. D. and Goodman L. M., "Adaptive Antenna System Design for Multielement Combining with Transient Interrupted Channels," submitted to the IEEE Transactions on Vehicular Technology.
- [4] Carlson B. D. and Goodman L. M., "MBCA (Multielement Buoyant Cable Array: Submarine-Satellite Communications Array Design Study," 2001 Joint Undersea Warfare Spring Conference, San Diego, CA, 20-22 March 2001.

RFI and Mainlobe Jamming Mitigation for Multi-channel Imaging Radars

Patrick Bidigare

Veridian Systems
3300 Plymouth Rd.
Ann Arbor, MI 48130
bidigare@erim-int.com

ABSTRACT

A common approach to suppressing jamming or RFI is (adaptive) beamforming, where an antenna pattern null is formed by appropriately combining multiple receive channels. A sidelobe canceller is a common such implementation.

Beamforming is undesirable when the interference source is in the mainlobe of the radar, because the antenna pattern null created by the beamformer produces a region where ground imaging cannot be performed.

This paper presents two conceptual alternatives to spatial beamforming. The first approach produces a SAR image by combining the pulse returns from multiple channels in a non-separable way. This "space time beamforming" is shown to produce a null which is significantly narrower and shallower than that produced by conventional spatial beamforming. Further, we demonstrate that the space time beamforming null becomes narrower as the length of the synthetic aperture (i.e. the doppler resolution) increases.

A second alternative to spatial beamforming is presented which is useful when the interference source is non-white or when it is desirable to estimate the (spatially localized) interfering signal. This signal separation approach allows generic localized sources such as moving target signatures, vibrating target paired echoes, etc. to be separated from the clutter data.

1. INTRODUCTION

A typical approach to radio frequency interference (RFI) and jamming suppression for multi-channel radars is (spatial) beamforming [1]. Here, a linear combination of receive channels is used to produce an antenna pattern null on receive in the direction(s) of the interference. A sidelobe canceller is a common such implementation.

Spatial beamforming works well when the RFI source is in the sidelobes of the radar, however in the mainbeam, spatial beamforming produces a deep, wide notch. For imaging radars, this notch produces a region where clutter reflectivity cannot be estimated.

In this paper we present two alternative approaches to spatial beamforming. The first uses non-separable space time beamforming to produce a much narrower, shallower null. The second approach provides a method for separating the clutter and localized interference signals when both of these are of interest. We compare the performance of spatial beamforming vs. space time beamforming in terms of the width and depth of the clutter notch produced.

Consider SAR image formation as a problem of estimating the radar cross section of each range/Doppler cell in the presence of thermal noise and localized RFI. We consider the width of the region of range/Doppler cells whose Cramer-Rao variance bounds exceed a given threshold. We show that the non-separable spatial (multiple channels) and temporal (multiple pulses) processing, produces a much narrower null width (as defined above) than conventional separable beamforming.

The example results shown in this utilize video phase history data collected by Veridian System's DCS radar with synthetic RFI introduced prior to image formation.

The author would like to thank Mike Beauvais for his help with producing the examples shown in the paper and Mark Stuff for several interesting discussions.

2. TECHNICAL DISCUSSION

2.1 Spatial Beamforming

A typical approach to RFI suppression is adaptive beamforming. Here, a particular coherent combination of the receive channels from a multi-channel antenna is chosen so as to maximize the signal to interference plus noise (SINR) ratio in a particular steering direction. This is illustrated in Figure 1 and Figure 2.

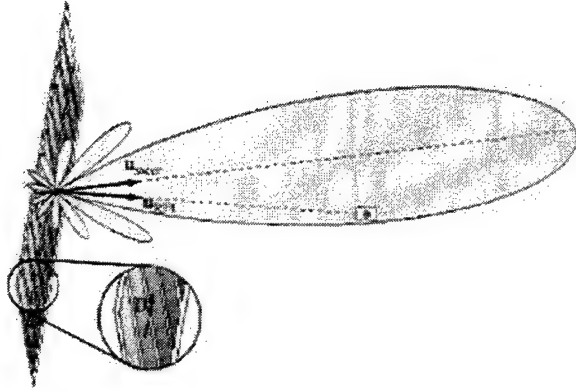


Figure 1: Multi-channel antenna

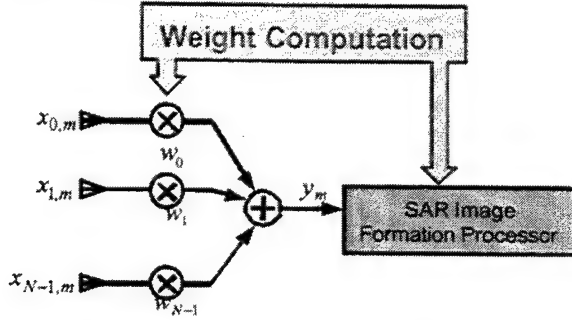


Figure 2: Beamforming applied to SAR imaging.

The Gauss-Markov theorem provides a closed-form for the weight vector \mathbf{w} which maximizes this SINR when the covariance of the interference and noise are known.

We model our interference covariance as the sum of a spatially white thermal noise term with variance σ_n^2 and a (rank 1) spatially localized RFI term which is the outer product of the steering vector $\mathbf{z}_{\text{RFI}} = (z_{\text{RFI}}^0, \dots, z_{\text{RFI}}^{N-1})$ to the RFI source with itself.

$$\mathbf{R}^u = \mathbf{R}^n + \mathbf{R}^i = \sigma_n^2 \begin{bmatrix} 1 & 0 & \dots & 0 \\ 0 & 1 & & 0 \\ \vdots & & \ddots & \\ 0 & & & 1 \end{bmatrix} + \sigma_i^2 \begin{bmatrix} 0 & 1 & \dots & z_{\text{RFI}}^{N-1} \\ z_{\text{RFI}}^0 & 0 & & z_{\text{RFI}}^{N-2} \\ \vdots & z_{\text{RFI}}^1 & \ddots & z_{\text{RFI}}^1 \\ \vdots & \vdots & \ddots & 0 \end{bmatrix}$$

Here $z_{\text{RFI}} = \exp \left\{ 2\pi i \frac{\mathbf{D} \cdot \mathbf{u}_{\text{RFI}}}{\lambda} \right\}$ is the complex root of unity corresponding to the channel-to-channel phase change due to the position of the RFI source in the scene (see Figure 1).

The weight vector is given by

$$\mathbf{w} = \mathbf{R}^{-1}(\mathbf{z}_{\text{steer}} \cdot \mathbf{t}),$$

where \mathbf{t} is a tapering vector and \cdot denotes the Hadamard (pointwise) product. The weight vector is optimal when $\mathbf{t} = (1, 1, \dots, 1)$, however for purposes of sidelobe reduction, a weighted taper is generally used.

A typical implementation of beamforming is a sidelobe canceller. Here the main subarrays of the antenna are used for beamsteering and a small number of auxiliary channels are then adaptive combined with the main channel for RFI cancellation in the sidelobes.

Beamforming can be applied to SAR image formation by first forming a coherent (spatial) combination of the receive channels and then passing this into a SAR image formation processor which then forms the temporal combination of received pulses appropriate to scene reconstruction. This approach is shown in Figure 2.

This separable spatial-then-temporal processing works well when the RFI source occurs in the sidelobes, but has undesirable effects as the RFI source enters the mainlobe. The -40dB Taylor tapered adapted antenna patterns for various RFI source locations are shown in Figure 3.

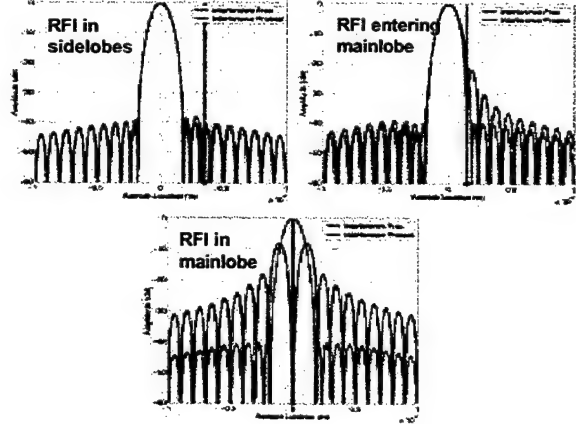


Figure 3: Beamformer antenna patterns.

As can be seen, an RFI source in the sidelobes has very little effect on the sidelobe levels or on the mainlobe shape. However as soon as the source enters the mainlobe, the sidelobe levels rise and the mainlobe distorts. The worst degradation occurs when the RFI source coincides with the beamsteering direction. In this case a wide, deep notch appears in the mainbeam and the sidelobes are elevated by 20dB.

2.2 Space Time Beamforming

The problem inherent with separable spatial-then-temporal beamforming for SAR imaging is that the optimal weights maximize the SINR only in the steering direction. Simultaneous maximization of SINR in all directions inherently requires a non-separable approach. To develop

such an approach, we consider the very simple DPCA data model shown in Figure 4.

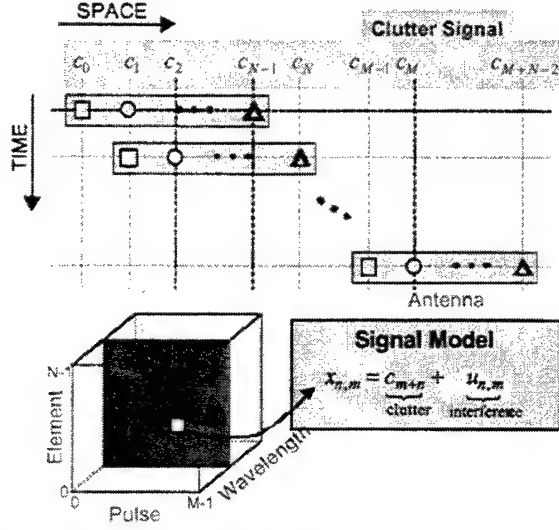


Figure 4: Space time signal model.

Here a received data sample shown in the radar data cube is indexed by channel (element), pulse and wavelength and consists of a deterministic clutter coefficient and a random noise + RFI component. We model the clutter as stationary and thus dependent only on the spatial location of the receiving antenna phase center. For illustration, we consider the simple DPCA situation where the antenna moves one phase center spacing between pulses. In this case, the clutter coefficient c_{m+n} in $x_{n,m}$ depends on the sum $m+n$.

Written as a matrix equation in the case of $M = 4$ pulses and $N = 3$ channels we have

$$\begin{bmatrix} x_{0,0} \\ x_{0,1} \\ x_{0,2} \\ x_{0,3} \\ x_{1,0} \\ x_{1,1} \\ x_{1,2} \\ x_{1,3} \\ x_{2,0} \\ x_{2,1} \\ x_{2,2} \\ x_{2,3} \end{bmatrix} = \begin{bmatrix} 1 & 0 & 0 & 0 & 0 & 0 \\ 0 & 1 & 0 & 0 & 0 & 0 \\ 0 & 0 & 1 & 0 & 0 & 0 \\ 0 & 0 & 0 & 1 & 0 & 0 \\ 0 & 1 & 0 & 0 & 0 & 0 \\ 0 & 0 & 1 & 0 & 0 & 0 \\ 0 & 0 & 0 & 1 & 0 & 0 \\ 0 & 0 & 0 & 0 & 1 & 0 \\ 0 & 0 & 1 & 0 & 0 & 0 \\ 0 & 0 & 0 & 1 & 0 & 0 \\ 0 & 0 & 0 & 0 & 1 & 0 \\ 0 & 0 & 0 & 0 & 0 & 1 \end{bmatrix} \begin{bmatrix} c_0 \\ c_1 \\ c_2 \\ c_3 \\ c_4 \\ c_5 \end{bmatrix} + \begin{bmatrix} u_{0,0} \\ u_{0,1} \\ u_{0,2} \\ u_{0,3} \\ u_{1,0} \\ u_{1,1} \\ u_{1,2} \\ u_{1,3} \\ u_{2,0} \\ u_{2,1} \\ u_{2,2} \\ u_{2,3} \end{bmatrix}$$

We model the interference as consisting of a spatially and temporally white noise component and a spatially localized and temporally white RFI source.

$$\mathbf{R}_u = \underbrace{\begin{bmatrix} 1 & 0 & 0 \\ 0 & 1 & 0 \\ 0 & 0 & 1 \end{bmatrix}}_{\text{spatialcovariance}} + \underbrace{\delta_j^2 \begin{bmatrix} z_j^0 & z_j^1 & z_j^2 \\ z_j^{-1} & z_j^0 & z_j^1 \\ z_j^{-2} & z_j^{-1} & z_j^0 \end{bmatrix}}_{\text{temporalcovariance}} \otimes \begin{bmatrix} 1 & 0 & 0 & 0 \\ 0 & 1 & 0 & 0 \\ 0 & 0 & 1 & 0 \\ 0 & 0 & 0 & 1 \end{bmatrix}$$

Here $z_j = \exp \left\{ 2\delta j \frac{\mathbf{D} \cdot \hat{\mathbf{u}}_j}{\bar{c}} \right\}$ is complex root of unity

corresponding to the position of the RFI source as shown in Figure 5.

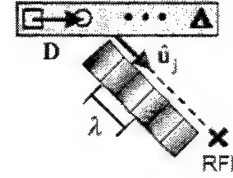


Figure 5: RFI source geometry.

The Gauss-Markov theorem can be used to construct the best linear unbiased estimator for the clutter coefficients in this colored interference environment. The clutter estimator is given by

$$\mathbf{c} = (\mathbf{Z}^H \mathbf{R}_u^{-1} \mathbf{Z})^{-1} \mathbf{Z}^H \mathbf{R}_u^{-1} \mathbf{x}$$

The purpose of this paper is to present and compare conceptual approaches to RFI suppression without introducing actual algorithms, however it's worth noting that the BLUE for clutter coefficient estimation has a matrix structure (Figure 6) which makes it particularly amenable to solution using linear solvers. Evaluation of the matrix-vector product $\mathbf{Z}^H \mathbf{R}_u^{-1} \mathbf{x}$ amounts to evaluating the Z transform of \mathbf{x} at various locations and thus can be efficiently evaluated using the chirp-Z transform. Further, it's straightforward to show that the matrix $\mathbf{Z}^H \mathbf{R}_u^{-1} \mathbf{Z}$ has a banded matrix structure with upper and lower bandwidths $N-1$, thus efficient sparse matrix solvers can be applied.

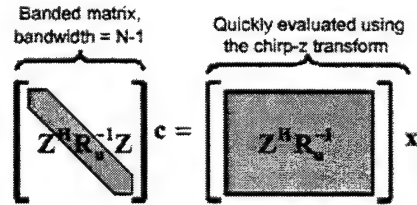


Figure 6: Space time beamforming matrix structure.

Figure 7 shows the results of the separable spatial beamforming and non-separable space-time beamforming approaches applied to real SAR video phase history with synthetic RFI.

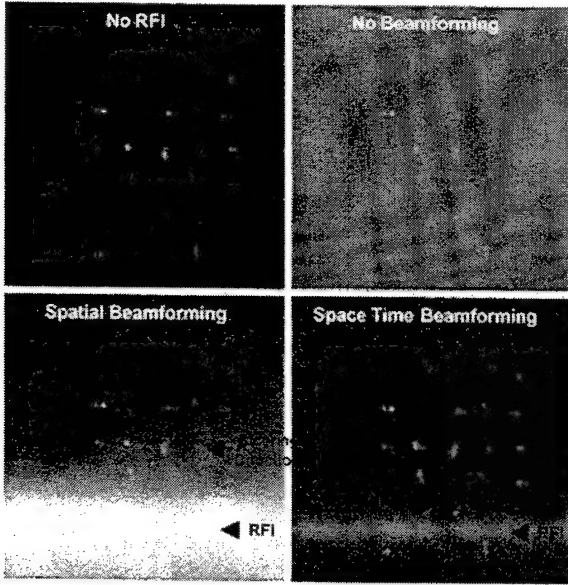


Figure 7: Spatial vs. space time beamforming.

This example corresponds to a radar with a standoff range of 100km, having a 3m antenna. The simulation uses a CNR of 26dB and a JNR of 38dB with $N = 6$ channels and $M = 2750$ pulses.

The separable spatial beamforming null is seen to be deeper and wider than its space-time counterpart. In fact, the SINR in the direction of the RFI is actually worse than had no beamforming been performed. This is because the separable beamforming is only optimal in the steering direction. The space time beamformer is never any worse than the case of no beamforming and recovers most of the image everywhere but very near the RFI source.

2.3 Beamforming Comparison

The spatial and space time beamforming approaches to RFI suppression can be compared somewhat more rigorously by considering the clutter to noise ratios produced by these methods as a function of the azimuth position of a clutter patch and the azimuth position of the RFI source. These clutter to noise ratios are given by

$$CNR_{\text{spatial}} = M \frac{((\mathbf{v}_{\text{steer}} \cdot \mathbf{t})^H \mathbf{R}_u^{-1} \mathbf{v}_{\text{clut}})^2}{(\mathbf{v}_{\text{steer}} \cdot \mathbf{t})^H \mathbf{R}_u^{-1} (\mathbf{v}_{\text{steer}} \cdot \mathbf{t})}$$

and

$$CNR_{\text{space-time}} = \frac{(t_0 + t_1 + \dots + t_{M+N-2})^2}{(\mathbf{v}_{\text{clut}} \cdot \mathbf{t})^H (\mathbf{Z}^H \mathbf{R}_u^{-1} \mathbf{Z})^{-1} (\mathbf{v}_{\text{clut}} \cdot \mathbf{t})}$$

These clutter to noise ratios for the spatial and space time beamforming are shown in Figure 8.

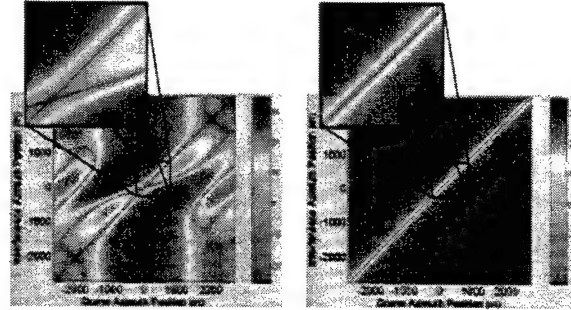


Figure 8: CNR for spatial (left) vs. space time (right) beamforming.

The x-axis corresponds to the azimuth position of the clutter patch and the y axis is the azimuth position of the RFI over a 5km scene. The effects of the RFI position (mainlobe vs. sidelobe) on the spatial beamforming are evident here. No antenna pattern can be seen for the space time beamforming because the individual subarrays patterns were not modeled.

The width of the "notch" produced by beamforming can be defined in terms of a minimally acceptable CNR level. Figure 9 compares the two approaches as the number of pulses used increases (and the doppler resolution gets finer). As can be seen, the spatial beamformer produces a null whose depth is relatively independent of the number of pulses used and whose width improves only slowly with increasing doppler resolution. By contrast, the depth of the space time beamformer notch rises as the number of pulses increases and the width improves dramatically with increasing doppler resolution.

This observation suggests that the width of the null is proportional to the doppler resolution for space time beamforming, although the author has not proven or disproved this as yet.

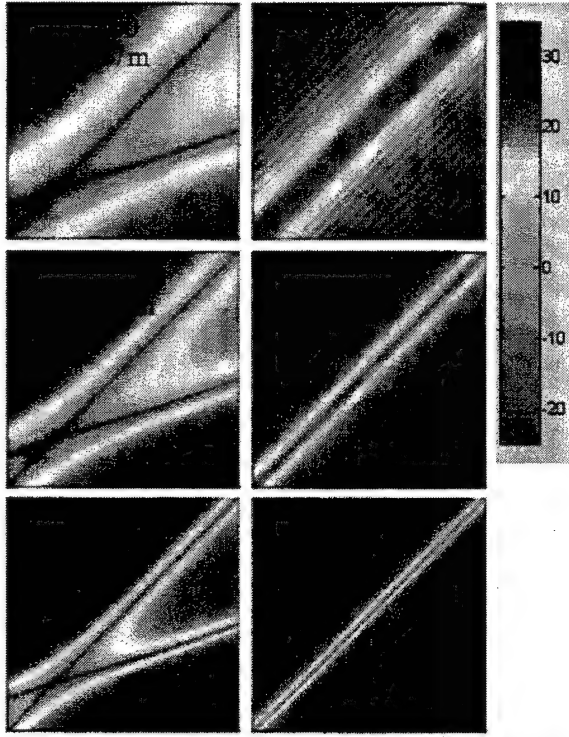


Figure 9: CNR comparison of spatial (left) vs. space time (right) beamforming at various doppler resolutions.

2.4 Signal Separation

Space time beamforming is a potentially useful technique for suppressing RFI in the mainlobe, however in some situations, the interference may be temporally colored or even highly structured. Further, for many applications, the "RFI" may correspond to a spatially localized signal of interest. Such signals can include covert RF tag communication signals, paired echoes from rotating or vibrating objects [3] or even returns from moving targets [2,4,5] where an objective might be to image the moving targets.

In such situations, we would like a method for extracting the clutter signal from the localized source. Figure 10 illustrates the distribution of clutter and localized source energy in the radar data cube. The relation between the azimuth location of a stationary patch of clutter and the doppler frequency it manifests causes the clutter energy to concentrate onto a 2D "clutter ridge". The localized source energy also concentrates onto a plane at the azimuth location of the source. It's reasonable to expect, then, that these signals can be separated except where they intersect in the data cube.

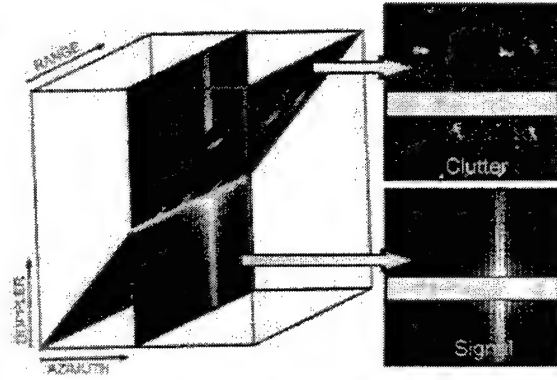


Figure 10: Signal separation cartoon.

We introduce another data model in which both the clutter and the localized source are deterministic quantities. The interference in this case is simply white thermal noise. As before, we model the clutter signal as depending only on the spatial location of the receiving phase center (Figure 11).

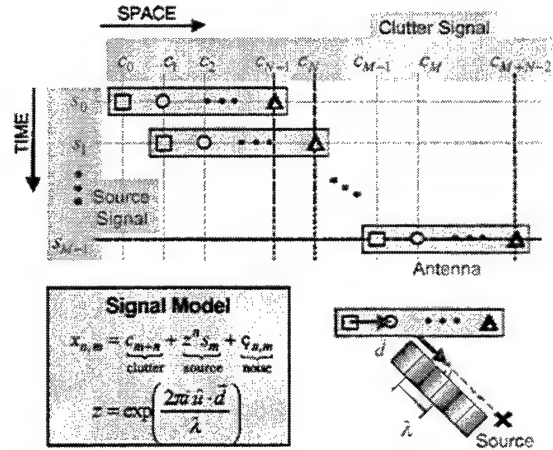


Figure 11: Signal separation data model.

The localized source, on the other hand, is modeled as the product of a temporal term s_m depending only on the pulse number, and spatial term z^n depending on the phase center n and azimuth position z of the source. In matrix notation, we have

$$\begin{bmatrix} x_{0,0} \\ x_{0,1} \\ x_{0,2} \\ x_{0,3} \\ x_{1,0} \\ x_{1,1} \\ x_{1,2} \\ x_{1,3} \\ x_{2,0} \\ x_{2,1} \\ x_{2,2} \\ x_{2,3} \end{bmatrix} = \begin{bmatrix} 1 & 0 & 0 & 0 & 0 & 0 \\ 0 & 1 & 0 & 0 & 0 & 0 \\ 0 & 0 & 1 & 0 & 0 & 0 \\ 0 & 0 & 0 & 1 & 0 & 0 \\ 0 & 1 & 0 & 0 & 0 & 0 \\ 0 & 0 & 1 & 0 & 0 & 0 \\ 0 & 0 & 0 & 1 & 0 & 0 \\ 0 & 0 & 0 & 0 & 1 & 0 \\ 0 & 0 & 1 & 0 & 0 & 0 \\ 0 & 0 & 0 & 1 & 0 & 0 \\ 0 & 0 & 0 & 0 & 1 & 0 \\ 0 & 0 & 0 & 0 & 0 & 1 \end{bmatrix} \begin{bmatrix} z^0 & 0 & 0 & 0 \\ 0 & z^1 & 0 & 0 \\ 0 & 0 & z^2 & 0 \\ 0 & 0 & 0 & z^3 \\ z^0 & 0 & 0 & 0 \\ 0 & z^1 & 0 & 0 \\ 0 & 0 & z^2 & 0 \\ 0 & 0 & 0 & z^3 \\ z^0 & 0 & 0 & 0 \\ 0 & z^1 & 0 & 0 \\ 0 & 0 & z^2 & 0 \\ 0 & 0 & 0 & z^3 \end{bmatrix} \begin{bmatrix} c_0 \\ c_1 \\ c_2 \\ c_3 \\ c_4 \\ c_5 \\ c_6 \\ c_7 \\ c_8 \\ c_9 \\ c_{10} \\ c_{11} \end{bmatrix} + \begin{bmatrix} u_{0,0} \\ u_{0,1} \\ u_{0,2} \\ u_{0,3} \\ u_{1,0} \\ u_{1,1} \\ u_{1,2} \\ u_{1,3} \\ u_{2,0} \\ u_{2,1} \\ u_{2,2} \\ u_{2,3} \end{bmatrix}$$

$\mathbf{x} \qquad \qquad \qquad \mathbf{Z} \qquad \qquad \qquad \mathbf{u}$

Since our interference is spatially and temporally white, the best estimator of the clutter and signal coefficients is the least squares solution

$$\mathbf{CS} = (\mathbf{Z}^H \mathbf{Z})^{-1} \mathbf{Z}^H \mathbf{X}$$

As might be expected, the matrix \mathbf{Z} is not full rank. This rank deficiency corresponds to the intersection region (Figure 10) between the clutter ridge and localized source. This problem can be corrected by introducing an extra row in \mathbf{Z} which effectively allows us to specify whether the inseparable energy in the intersection should be included with the clutter signal or the localized source signal.

Figure 12 shows the result of applying this signal separation technique to 3 channel SAR video phase history with synthetic RFI and then processing the separated signals into SAR images using a conventional image formation processor.

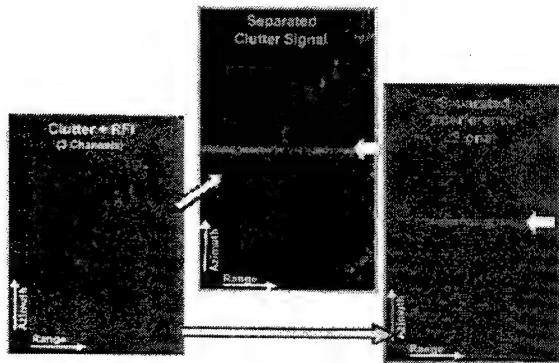


Figure 12: Signal separation example.

Here we used 1024 pulses and set up the simulation to have a CNR of 30dB and a JNR of 40dB. We included the overlap region with the clutter signal.

Our initial results suggest that the width of the intersection region wherein the clutter cannot be discerned from the source is proportional to the doppler resolution of the radar, and thus can be made more narrow by collecting more pulses.

3. CONCLUSIONS + FURTHER WORK

The purpose of this paper was to suggest three conceptual approaches to the problem of RFI mitigation and more generally the problem of separating the clutter signal from a localized source. It was shown that non-separable space time beamforming is necessary to effectively combat mainbeam RFI.

Any practical implementation of these techniques would have to solve three problems not addressed by the paper. The first problem is determining the azimuth position of the RFI or localized source. The second is the estimation of the interference environment (or at very least, the noise σ_n^2 and RFI σ_j^2 variances). Lastly, the problem of channel balancing must be addressed. Innovative adaptive signal processing approaches will be required to solve these problems.

4. REFERENCES

- [1] J.R. Guerci, J.S. Goldstein, I.S. Reed, "Optimal and Adaptive Reduced-Rank STAP," *IEEE Transactions on Aerospace and Electronic Systems*, vol. 36, no. 2, 2000, pp. 647-663.
- [2] J.H.G. Ender, "Space-time processing for multichannel synthetic aperture radar," *Electronics and Communication Engineering Journal*, vol. 1, no. 1, 1999, pp. 29-38.
- [3] N.S. Subotic, B.J. Thelen, D.A. Carrara, "Cyclostationary signal models for the detection and characterization of vibrating objects in SAR data," *Proceedings of the 1998 32nd Asilomar Conference on Signals, Systems and Computers*, Part 2 (of 2) Pacific Grove, CA, USA 1998 1101-1998 1104 IEEE
- [4] S.A. Werness, M.A. Stuff, J.R. Fienup, "Two-dimensional imaging of moving targets in SAR data," *1990 (24th) Asilomar Conference on Signals, Systems and Computers*, Part 1 (of 2).
- [5] M.A. Stuff, "Three-dimensional analysis of moving target radar signals: Methods and implications for ATR and feature aided tracking", *Proceedings of the SPIE*, v 3721 1999, pp. 485-496

Further Evaluations of STAP Tests in Compound-Gaussian Radar Clutter

¹J.H. Michels, ²M. Rangaswamy, and ¹B. Himed

¹AFRL/SNRT, 26 Electronic Parkway Rome, NY 13441

²ARCON Corporation, Waltham, MA 02451-1080

Abstract—The performance of a parametric space-time adaptive processing (STAP) method is presented here. Specifically, we consider signal detection in additive disturbance containing compound-Gaussian clutter plus additive Gaussian thermal white noise. Performance is compared to the normalized adaptive matched filter and the Kelly GLRT receiver using simulated and measured data. We focus on the issues of detection and false alarm probabilities, constant false alarm rate (CFAR), robustness with respect to clutter texture power variations, and reduced training data support.

I. INTRODUCTION

This paper undertakes a performance comparison of several candidate space-time adaptive processing (STAP) algorithms in compound-Gaussian clutter for airborne radar applications. The STAP problem is equivalent to hypothesis testing on a complex (base-band) measurement (test data) vector $\mathbf{x} \in C^{JN}$ with J channels and N time pulses. Typically, \mathbf{x} contains an unwanted additive disturbance \mathbf{d} with unknown covariance matrix \mathbf{R}_d and may contain a desired signal \mathbf{a} with unknown complex amplitude, a , and known signal steering vector \mathbf{e} . The binary detection problem is to select between hypothesis $H_0 : a = 0$ and $H_1 : a \neq 0$ given a single realization of \mathbf{x} .

Current research [1–10] is addressing the detection problem wherein \mathbf{d} contains partially correlated clutter described by a product model [11]. Here, the clutter is modeled as a Gaussian process with random power variations (scale changes) over range. This model is the basis of the spherically invariant random process (SIRP) (or compound-Gaussian) clutter model, which includes the Weibull and K-distributions as special cases.

In [6, 12, 13] the optimal processor for detecting a rank one signal in SIRP clutter was shown to be equivalent to a matched filter compared to a data dependent threshold. With a simple normalization, this test can be cast in the form of the normalized matched filter (NMF) test compared to a data dependent threshold, the calculation of which requires knowledge of the underlying clutter probability density function (PDF). Determination of the clutter PDF imposes onerous training data requirements. Consequently, ad hoc methods have been popular in recent studies [7–10]. A popular

ad-hoc method is the NMF test compared to a data independent threshold, which was independently derived in [7, 8].

The work of [14] (and references therein) considered an invariance framework for hypothesis testing in Gaussian noise having a covariance matrix with known structure but unknown level. Interestingly, the test statistic reported in [14] is identical to the NMF of [7, 8]. The work of [14] also extended the NMF test to allow for an unknown noise covariance matrix and unknown scaling, η^2 , denoting the ratio of the test and training data variances. We refer to this test as the normalized adaptive matched filter (NAMF). The invariance principle of [14] (and references therein), and perforce constant false alarm rate (CFAR), applies only when all the training data vectors are scaled identically [10].

In SIRP clutter, however, each training data vector realization is scaled by a different random parameter. Although the NAMF has no known optimality properties for SIRP clutter, it has the important feature of minimizing dependence upon texture power. Some performance results of the NAMF in SIRP clutter are presented in [7, 8].

Multichannel model-based (i.e., parametric) methods for target detection and estimation in clutter are described in [2–4, 9, 10, 15–17]. In particular, a model-based STAP method called the non-Gaussian parametric adaptive matched filter (NG-PAMF), requiring knowledge of the underlying clutter statistics was first proposed in [3].

In this paper, the performance of the normalized parametric adaptive matched filter (N-PAMF) [10, 18] is evaluated and compared with that of several candidate STAP algorithms. Its form is the model-based approximation of the NAMF. Statistical equivalence of the N-PAMF test to the NG-PAMF test was shown in [10]. However, unlike the NG-PAMF, the N-PAMF test requires no ‘a priori’ knowledge of the disturbance statistics [10]. This feature is important in real-time applications where such information is lacking. Robustness of P_d over a broad range of K-distribution shape parameters (α) ranging from Gaussian ($\alpha = \infty$) to high-tailed PDF ($\alpha = 0.1$) is presented here. These considerations enable assessments of CFAR performance with respect to the amplitude probability density function (APDF)

associated with clutter texture variations. Finally, we examine performance versus data support size used for disturbance estimation. This issue is of considerable importance in applications where training data support is limited.

II. THE CLUTTER MODEL

Clutter observed in a single channel admits a representation of the form

$$c_k(n) = v_k(n)g_k(n) \quad (1)$$

where a complex-Gaussian process $g_k(n)$ (speckle component) corresponding to time n and range cell k is modulated by a statistically independent non-negative process $v_k(n)$ (texture component). Frequently, $v_k(n)$ is approximated as a random variable V over k , but constant over time if it has long temporal coherence. Thus, (1) reduces to the representation theorem [11] for an SIRP and is given by

$$c_k(n) = v_k g_k(n). \quad (2)$$

For the multichannel problem, the clutter in each of the J channels is given by (2). The PDF of V , $f_V(v)$, is defined to be the characteristic PDF of the SIRP. The amplitude of $c_k(n)$ is K-distributed for Generalized-Chi distributed $f_V(v)$ and includes the Gaussian model ($\alpha = \infty$) as a special case. The disturbance \mathbf{d} contains partially correlated clutter \mathbf{c} modeled by a K-distributed amplitude, with PDF

$$f_R(r) = \frac{\beta^{\alpha+1} r^\alpha}{2^{\alpha-1} \Gamma(\alpha)} K_{\alpha-1}(\beta r) \quad r \geq 0, \beta, \alpha > 0 \quad (3)$$

where β and α are the distribution scale and shape parameters, respectively, $K_\nu(\cdot)$ is the modified Bessel function of the second kind of order ν , and $\Gamma(\cdot)$ is the Euler-Gamma function. Small values of α result in heavy-tails for the PDF of (3). From (2), the clutter covariance matrix is $\mathbf{R}_c = \mathbf{R}_g E(V^2)$ where $\mathbf{R}_g \in \mathbb{C}^{JN \times JN}$ is the covariance of the Gaussian (speckle) component and $E(V^2)$ relates to the texture power.

In practice, \mathbf{R}_d is unknown, and must be estimated from a signal-free $JN \times K$ secondary data matrix, \mathbf{Z} , whose columns are assumed to be statistically independent and identically distributed (iid) as the test data. For Gaussian disturbance, the maximum likelihood (ML) estimator is the sample matrix $\hat{\mathbf{R}}_d = \mathbf{Z}\mathbf{Z}^H/K$. However, $\hat{\mathbf{R}}_d$ is not the ML estimate for compound-Gaussian clutter.

III. TEST STATISTIC DESCRIPTIONS

We now consider several non-adaptive and adaptive detection test statistics in this section.

A. Non-Adaptive Test Statistics

For known \mathbf{R}_d , the optimal test for detecting a rank one signal in Gaussian interference is given by

$$\Lambda_{MF} = \frac{|\mathbf{e}^H \mathbf{R}_d^{-1} \mathbf{x}|^2}{\mathbf{e}^H \mathbf{R}_d^{-1} \mathbf{e}} \underset{H_0}{\overset{H_1}{>}} \lambda_{MF}. \quad (4)$$

In some instances, the test data vector can have a covariance matrix $\eta^2 \mathbf{R}_d$, where η^2 is an unknown level. The phase invariant matched filter (PI-MF) test for these problems is expressed as [14]

$$\Lambda_{PIMF} = \frac{|\mathbf{e}^H \mathbf{R}_d^{-1} \mathbf{x}|^2}{\eta^2 \mathbf{e}^H \mathbf{R}_d^{-1} \mathbf{e}} \underset{H_0}{\overset{H_1}{>}} \lambda_{PIMF} \quad (5)$$

where \mathbf{e} and \mathbf{x} are the concatenated $JN \times 1$ signal 'search' steering and data vectors, respectively. The inner product of whitened vectors $\mathbf{b} = \mathbf{R}_d^{-\frac{1}{2}} \mathbf{x}$ and $\mathbf{f} = \mathbf{R}_d^{-\frac{1}{2}} \mathbf{e}$ is the matched filtering operation. Although (5) does not require knowledge of signal phase, it does require knowledge of the level η^2 to be CFAR. The optimal test for this problem is the NMF test [14] given by

$$\Lambda_{NMF} = \frac{|\mathbf{e}^H \mathbf{R}_d^{-1} \mathbf{x}|^2}{[\mathbf{e}^H \mathbf{R}_d^{-1} \mathbf{e}][\mathbf{x}^H \mathbf{R}_d^{-1} \mathbf{x}]} \underset{H_0}{\overset{H_1}{>}} \lambda_{NMF}. \quad (6)$$

The test statistic of (6) is simply the squared magnitude of the inner product of the vectors \mathbf{f} and \mathbf{b} normalized by their squared norms, so that $0 \leq \Lambda_{NMF} \leq 1$.

B. Adaptive Test Statistics

For the adaptive problem, $\hat{\mathbf{R}}_d$ replaces \mathbf{R}_d . Consequently, the adaptive version of the test of (4) denoted as the AMF is given by

$$\Lambda_{AMF} = \frac{|\mathbf{e}^H \hat{\mathbf{R}}_d^{-1} \mathbf{x}|^2}{\mathbf{e}^H \hat{\mathbf{R}}_d^{-1} \mathbf{e}} \underset{H_0}{\overset{H_1}{>}} \lambda_{AMF}. \quad (7)$$

Observe that Λ_{AMF} is simply the adaptive version of Λ_{MF} . For the special case of $\eta = 1$, this test was developed independently in [19,20] where its CFAR behavior was noted. This property is lost when $\eta \neq 1$.

The adaptive version of the test of (6) is given by

$$\Lambda_{NAMF} = \frac{|\mathbf{e}^H \hat{\mathbf{R}}_d^{-1} \mathbf{x}|^2}{[\mathbf{e}^H \hat{\mathbf{R}}_d^{-1} \mathbf{e}][\mathbf{x}^H \hat{\mathbf{R}}_d^{-1} \mathbf{x}]} \underset{H_0}{\overset{H_1}{>}} \lambda_{NAMF}. \quad (8)$$

Another adaptive detection test known as the Kelly GLRT [21] is expressed as

$$\Lambda_{GLRT} = \frac{|\mathbf{e}^H \hat{\mathbf{R}}_d^{-1} \mathbf{x}|^2}{[\mathbf{e}^H \hat{\mathbf{R}}_d^{-1} \mathbf{e}][1 + \frac{\mathbf{x}^H \hat{\mathbf{R}}_d^{-1} \mathbf{x}}{K}]} \underset{H_0}{\overset{H_1}{>}} K \lambda_{GLRT} \quad (9)$$

where $0 \leq \lambda_{GLRT} \leq 1$. For $K \rightarrow \infty$, the tests of (7) and (9) converge to the test of (4), whereas the test of (8) converges to that of (6).

In this paper, we consider the performance of the tests of (7)-(9) in compound-Gaussian clutter. No optimality or CFAR claims of these tests can be made for the case of SIRP disturbance.

C. Model-Based STAP Tests

For multichannel model-based methods [15], the whitening operation is performed using prediction error filters (PEF) involving time series or state space architectures. We define $\mathbf{y}_p(n)$ as the $J \times 1$ vector error residual output of a P^{th} -order multichannel linear filter. For a multi-channel (vector) autoregressive model, a tapped delay line architecture is used where the P^{th} order filter coefficients, $\hat{\mathbf{A}}(k)$, are estimated from \mathbf{Z} using a multichannel parameter estimation algorithm. These $J \times J$ matrix coefficients provide a succinct description of the spatio-temporal disturbance correlation. Specifically,

$$\begin{aligned} \mathbf{y}_p(n) &= \hat{\mathbf{D}}_0^{-\frac{1}{2}} \hat{\mathbf{L}}_0^{-1} \mathbf{u}_p(n) \\ &= \hat{\mathbf{D}}_0^{-\frac{1}{2}} \hat{\mathbf{L}}_0^{-1} [\mathbf{x}(n|H_1) + \sum_{k=1}^P \hat{\mathbf{A}}(k) \mathbf{x}(n-k+P|H_1)] \\ n &= 0, 1, \dots, N-P-1 \end{aligned} \quad (10)$$

where (10) implicitly defines the temporally whitened $J \times 1$ error residual $\mathbf{u}_p(n)$, with covariance Σ_u . In practice, Σ_u is unknown and the estimation algorithms produce its estimate $\hat{\Sigma}_u$. However, this paper employs $\hat{\Sigma}_u$ obtained by averaging the outer products of $\mathbf{u}_p(n)$, where $\mathbf{u}_p(n)$ results from a transformation of the secondary data by the prediction error filter with fixed $\hat{\mathbf{A}}(k)$. The \mathbf{LDL}^H decomposition of $\hat{\Sigma}_u$ yields $(\hat{\mathbf{L}}_0, \hat{\mathbf{D}}_0)$ which are used to spatially whiten $\mathbf{u}_p(n)$ [15]. Finally, $\mathbf{y}_p(n)$ is obtained by a transformation of $\mathbf{x}(n)$ by the multichannel prediction error filter with coefficients $(\hat{\mathbf{L}}_0, \hat{\mathbf{D}}_0)$ and $\hat{\mathbf{A}}(k)$ as denoted in (10). Similarly, the transformed steering vector $\mathbf{s}(n)$ is obtained by sequencing the sequential form of the 'search' steering vector $\mathbf{e}(n)$ through the PEF [3, 16]. The normalized parametric adaptive matched filter (N-PAMF) [10, 18] is now defined as

$$\Lambda_{N-PAMF} = \frac{\left| \sum_{n=0}^{N-P-1} \mathbf{s}^H(n) \mathbf{y}_p(n) \right|^2}{\left[\sum_{n=0}^{N-P-1} \mathbf{s}^H(n) \mathbf{s}(n) \right] \left[\sum_{n=0}^{N-P-1} \mathbf{y}_p^H(n) \mathbf{y}_p(n) \right]} \quad (11)$$

A related parametric adaptive matched filter (PAMF) test was first derived in [3] for Gaussian disturbance.

The PAMF test is identical to (11) but excludes the second bracketed denominator term. In [16], several estimation algorithms are considered in the PAMF implementation for Gaussian disturbance. In this paper the multichannel least squares method is used for filter parameter estimation.

IV. ANALYTICAL RESULTS

The probability of false alarm and probability of detection for NMF operating in compound-Gaussian clutter (without background white noise) are given by [9]

$$P_{fa-NMF} = P(\Lambda_{NMF} > \lambda_{NMF} | H_0) = (1 - \lambda_{NMF})^{JN-1} \quad (12)$$

$$P_{d-NMF} = 1 - (1 - \lambda_{NMF})^{JN-1} \times \sum_{k=1}^{JN-1} b_k \left(\frac{\lambda_{NMF}}{1 - \lambda_{NMF}} \right)^k g_k[A^2(1 - \lambda_{NMF})] \quad (13)$$

where $g(\cdot)$ is defined in [9] and $b_k = \frac{\Gamma(JN)}{\Gamma(k+1)\Gamma(JN-k)}$.

The expressions for P_{fa} and P_d for the NAMF operating in Gaussian clutter are given by [9]

$$P_{fa-NAMF} = \int_0^1 \frac{f_\Gamma(\gamma)}{[1 + (1 - \gamma)\lambda_{NAMF}]^L} d\gamma \quad (14)$$

$$\begin{aligned} P_{d-NAMF} &= 1 - \int_0^1 \frac{1}{[1 + (1 - \gamma)\lambda_{NAMF}]^L} \\ &\times \sum_{m=1}^L \binom{L}{m} \eta^m (1 - \gamma)^m \\ &\times [1 - \text{gammainc}\left(\frac{A(1 - \gamma)}{1 + (1 - \gamma)\lambda_{NAMF}}, m\right)] f_\Gamma(\gamma) d\gamma \end{aligned} \quad (15)$$

where Γ , $\text{gammainc}(\cdot)$ and $f_\Gamma(\gamma)$ are defined in [9].

Corresponding P_{fa} and P_d expressions for the NAMF operating in SIRP clutter are difficult to derive. This is due to the fact that the ML estimate of the SIRP covariance matrix is not available in closed form [22]. Hence, the NAMF PDF cannot be determined analytically.

The P_{fa} and P_d expressions for the N-PAMF and PAMF operating in both Gaussian and non-Gaussian clutter scenarios are lacking since the analysis becomes mathematically intractable. Consequently, performance evaluation of these methods is carried out by Monte-Carlo techniques.

V. PERFORMANCE RESULTS

Performance is now presented for the detectors described above. Probability of detection (P_d) is computed for a P_{fa} of 0.01 via 100,000 Monte-Carlo trials using a physical model of an airborne radar scenario [4]. The target signal is located at a normalized Doppler frequency $f_{dt} = 0.15$ (unless otherwise

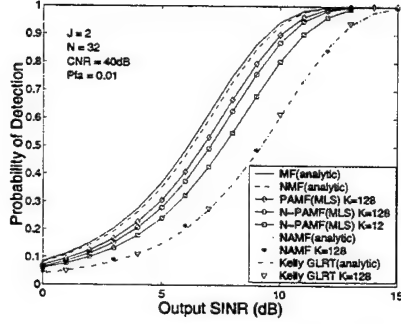


Fig. 1. P_d versus output SINR in Gaussian disturbance

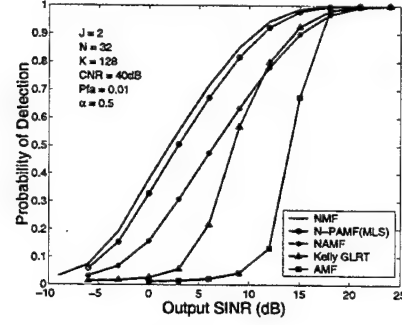


Fig. 2. P_d versus SINR in K-distributed Clutter $\alpha = 0.5$

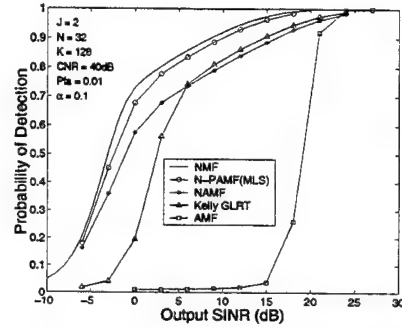


Fig. 3. P_d versus output SINR in K-distributed Clutter $\alpha = 0.1$

stated) and azimuth $\phi = 0$. The clutter ridge is located along the normalized angle-Doppler plane diagonal with a 40 dB (per pulse, per channel) clutter-to-noise ratio(CNR). The one-lag clutter temporal correlation parameter [15] is 0.999. Disturbance correlation estimates are obtained using K secondary data cells. The output signal-to-interference plus noise ratio (SINR) is defined as $SINR = |a|^2 e^H \mathbf{R}_d^{-1} e$. All performance results are obtained with compound-Gaussian clutter plus additive thermal white noise.

Figure 1 shows P_d versus output SINR for Gaussian disturbance with $\eta^2 = 1$. Shown here are analytical P_d plots for the MF and NMF with known \mathbf{R}_d . The analytical NMF P_d curve is also shown for $K=128$. Monte-Carlo generated P_d results for the PAMF(MLS), N-PAMF(MLS), NAMF, and Kelly GLRT are depicted. Performance of the Kelly GLRT and the NAMF are indistinguishable for this example. Note that the N-PAMF method with $P = 3$, nearly achieves the NMF performance for low sample support size $K=12$. Singularity of $\hat{\mathbf{R}}_d$ for $K=12$ precludes implementation of the AMF, NAMF, and Kelly GLRT. Figures 2 and 3 display P_d versus output SINR for the NMF, NAMF, N-PAMF(MLS), Kelly GLRT and AMF receivers for clutter processes with shape parameters $\alpha = 0.5$ and $\alpha = 0.1$, respectively. Observe the robust behavior of the N-PAMF, NAMF, Kelly GLRT in compound-Gaussian clutter. The Kelly GLRT outperforms the NAMF at high SINRs, whereas this condition reverses at low SINRs. Figure 4 plots P_d versus the clutter shape parameter α at output SINR=6dB with α ranging from 0.1 to 1,000. For the K-distribution, $\alpha > 4$ approximates the Gaussian case. The results reveal the robustness of the N-PAMF and NAMF tests over a wide range of shape parameters. However, the N-PAMF(MLS) shows superior performance approaching that of the NMF. Performance of the PAMF and AMF degrade in heavy-tailed compound-Gaussian clutter.

However, for $\alpha > 100$ (Gaussian region), they incur no performance degradation. Figure 5 shows P_{fa} versus shape parameter α with each test statistic threshold held fixed to obtain $P_{fa} = 0.01$ for Gaussian disturbance ($\alpha = \infty$). A significant increase in P_{fa} for the NAMF and Kelly GLRT confirms their lack of CFAR with respect to texture variations. Figures 6, 7, and 8 depict plots of P_{fa} versus threshold for the Kelly GLRT, NAMF, and N-PAMF, respectively, for several K-distribution shape parameter values. The curves for the N-PAMF exhibit much lower variability compared to the Kelly GLRT and NAMF, reflecting a robust CFAR performance with respect to the texture PDF. Figures 9 and 10 plot the test statistic vs range cell using data from the Air Force Research Laboratory (AFRL) Multichannel Airborne Radar Measurement (MCARM) program with an inserted target signal at range bin index 310. Specifically, data corresponding to acquisition '220' from flight '5' cycle 'e' is used in the examples presented here. For these results, we use $J=8$ and $N=32$. We define the performance measure Ψ_1 as the ratio of the test statistic at the test cell to the mean of the test statistics formed from adjacent cells, and Ψ_2 as the ratio of the test statistic at the test cell

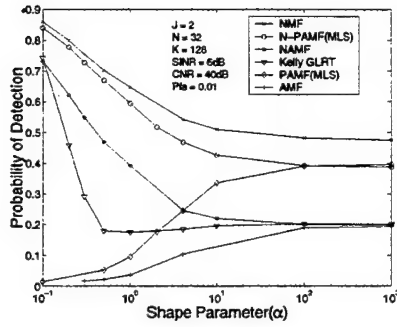


Fig. 4. P_d versus shape parameter (α)

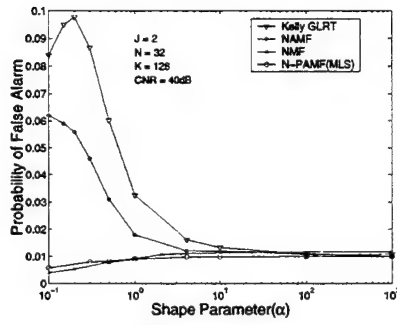


Fig. 5. P_{fa} versus clutter shape parameter(α):fixed threshold

to the highest test statistic formed from adjacent cells. Figure 9 plots the test statistics for the NAMF with $K=512$ and N-PAMF(MLS) ($P=2$) with $K=16$. Figure 10 plots the test statistics for the Kelly GLRT with $K=512$ and the N-PAMF (MLS)($P=2$) with $K=16$. Table 1 shows Ψ_1 and Ψ_2 for several values of K and P using the N-PAMF. Note that the N-PAMF with $P=2$ and $K=16$ provides the best performance for this scenario. In this instance, large sample support does not result in improved performance due to training data nonhomogeneity.

	P	Ψ_1 (dB)	Ψ_2 (dB)
NAMF ($K=512$)		16.2	7.45
Kelly GLRT ($K=512$)		16.71	8.03
N-PAMF ($K=512$)	4	19.3	12.3
N-PAMF ($K=32$)	3	22.1	14.7
N-PAMF ($K=16$)	3	21.6	15.2
N-PAMF ($K=32$)	2	21.8	11.3
N-PAMF ($K=16$)	2	22.4	14.7

Table 1: Values of Ψ_1 and Ψ_2 for the N-PAMF(MLS), NAMF, and Kelly GLRT

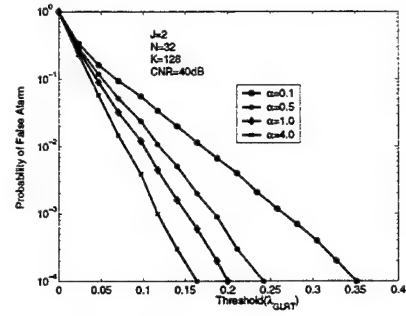


Fig. 6. P_{fa} versus threshold (λ_{GLRT}) for the Kelly GLRT

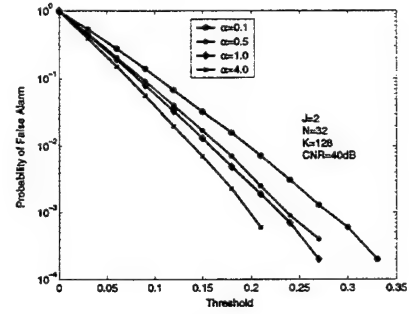


Fig. 7. P_{fa} versus threshold for the NAMF

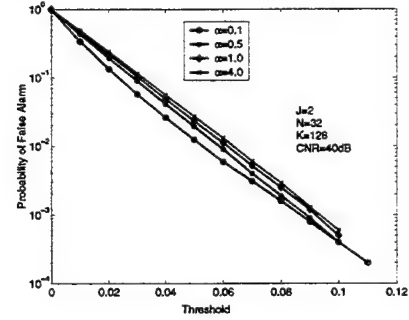


Fig. 8. P_{fa} versus threshold for the N-PAMF

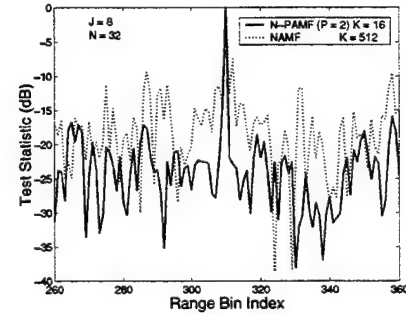


Fig. 9. Test Statistic versus Range

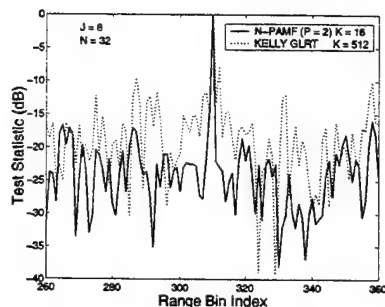


Fig. 10. Test Statistic versus Range

VI. SUMMARY AND FUTURE RESEARCH

In this paper, we have evaluated the performance of the N-PAMF, NAMF, and Kelly GLRT in compound-Gaussian clutter disturbance. The robust detection performance of these methods was shown over a wide range of clutter texture power variations (shape parameters) for K-distributed clutter processes. Performance of the N-PAMF was found to be close to the NMF. Next, the CFAR behavior was considered by observing the detection threshold variations with respect to shape parameter. Additionally, we demonstrate the robustness of the N-PAMF method with respect to small sample support size K (secondary data cells) used to estimate the disturbance correlation. This property is significant in operational scenarios involving range varying nonstationary clutter which severely limits the availability of representative training data. Examples with real data illustrate the potential for considerable performance improvement of the N-PAMF over the NAMF and Kelly GLRT.

VII. ACKNOWLEDGMENTS

This work was supported by the Air Force Office of Scientific Research (AFOSR) and in-house research efforts at AFRL/SNRT.

REFERENCES

- [1] M. Rangaswamy, D. Weiner, and J. Michels, "On the multichannel innovations based detection algorithm for correlated non-Gaussian random processes," in *Proceedings of twenty-seventh Asilomar Conference on Signals, Systems and Computers*, (Pacific Grove, CA), 1993.
- [2] M. Rangaswamy, J. Michels, and D. Weiner, "Multichannel detection for correlated non-Gaussian random processes based on innovations," *IEEE Trans. on Signal Processing*, vol. SP-43, pp. 1915-1922, 1995.
- [3] M. Rangaswamy and J. Michels, "A Parametric Multichannel Detection Algorithm For Correlated Non-Gaussian Random Processes," in *Proceedings of the IEEE National Radar Conference*, (Syracuse, NY), 1997.
- [4] J. Michels, T. Tsao, B. Himed, and M. Rangaswamy, "Space-Time Adaptive Processing (STAP) in Airborne Radar Applications," in *Proceedings of the IASTED Conference on Signal Processing and Communications*, (Canary Islands, Spain), 1998.
- [5] K. Gerlach, "Spatially distributed target detection in non-Gaussian clutter," *IEEE Trans. on Aerospace and Electronic Systems*, vol. 35, no.3, pp. 1058-1069, 1999.
- [6] M. Rangaswamy and J. H. Michels, "Performance Analysis of Space-Time Adaptive Processing Methods in Non-Gaussian Radar Clutter Backgrounds," in *Proceedings of the International Conference on Radar Systems*, (Brest, France), 1999.
- [7] E. Conte, M. Lops, and G. Ricci, "Asymptotically optimum radar detection in compound-Gaussian clutter," *IEEE Trans. on Aerospace and Electronic Systems*, vol. AES-31, pp. 617-625, 1995.
- [8] F. Gini, "Sub-optimum coherent radar detection in a mixture of K-distributed and Gaussian clutter," *IEE Proc.F, Radar, Sonar and Navigation*, vol. 144 (1), pp. 39-48, 1997.
- [9] J. Michels, M. Rangaswamy, and B. Himed, "Performance of STAP tests in compound Gaussian clutter," in *Proceedings of the First IEEE Workshop on Sensor Array and Multichannel Processing (SAM-2000)*, (Cambridge, MA), 2000.
- [10] J. Michels, B. Himed, and M. Rangaswamy, "Performance of STAP tests in Gaussian and Compound-Gaussian Clutter," *Digital Signal Processing*, vol. 10, no.4, pp. 309-324, 2000.
- [11] K. Yao, "A representation theorem and its applications to spherically invariant random processes," *IEEE Trans. on Information Theory*, vol. IT-19, pp. 600-608, 1973.
- [12] F. Gini, M. Greco, and A. Farina, "Clairvoyant and adaptive signal detection in non-Gaussian clutter: A data-dependent threshold interpretation," *IEEE Trans. on Signal Processing*, vol. 47, no.6, pp. 1522-1531, 1999.
- [13] K. Sangston, F. Gini, M. Greco, and A. Farina, "Structures for radar detection in compound Gaussian clutter," *IEEE Trans. on Aerospace and Electronic Systems*, vol. 35, no.2, pp. 445-458, 1999.
- [14] S. Kraut, L. L. Scharf, and L. McWhorter, "Adaptive subspace detectors," *IEEE Trans. on Signal Processing*, vol. 49, pp. 1-16, 2001.
- [15] J. Michels, *Multichannel Detection Using the Discrete-Time Model-Based Innovations Approach*. PhD thesis, Syracuse University, 1991.
- [16] J. Roman, M. Rangaswamy, D. Davis, Q. Zhang, B. Himed, and J. Michels, "Parametric adaptive matched filter for airborne radar applications," *IEEE Trans. on Aerospace and Electronic Systems*, vol. 36, no.2, pp. 677-692, 2000.
- [17] A. Swindlehurst and P. Stoica, "Maximum Likelihood Methods in Radar Array Signal Processing," *Proceedings of the IEEE*, vol. 86, No. 2, pp. 421-441, 1998.
- [18] J. Michels, "Space-time adaptive processing (STAP) in Gaussian and non-Gaussian airborne radar clutter," in *Adaptive Radar Clutter Suppression Workshop*, <http://siwg.eris.dera.gov.uk/signal/asp/>, (DERA, Malvern, U.K.), July 14 1999.
- [19] L. Cai and H. Wang, "On adaptive filtering with the CFAR feature and its performance sensitivity to non-Gaussian interference," in *Proceedings of the 24th Annual conference on Information Sciences and Systems*, (Princeton, NJ), pp. 558-563, 1990.
- [20] F. Robey, D. Fuhrmann, E. Kelly, and R. Nitzberg, "A CFAR adaptive matched filter detector," *IEEE Trans. on Aerospace and Electronic Systems*, vol. AES-28, pp. 208-216, 1992.
- [21] E. Kelly, "An adaptive detection algorithm," *IEEE Trans. on Aerospace and Electronic Systems*, vol. AES-22, pp. 115-127, 1986.
- [22] M. Rangaswamy and J. H. Michels, "Adaptive Processing in Non-Gaussian Noise Backgrounds," in *Proceedings of the Ninth IEEE Workshop on Statistical Signal and Array Processing*, (Portland, OR), 1998.

IMPULSIVE NOISE MITIGATION IN SPATIAL AND TEMPORAL DOMAINS FOR SURFACE-WAVE OVER-THE-HORIZON RADAR

Yuri I. Abramovich, Pavel Turcuj

CSSIP
SPRI Building
Technology Park Adelaide
Mawson Lakes
SA 5095, Australia
yuri@cssip.edu.au, pavel@cssip.edu.au

ABSTRACT

Surface-wave over-the-horizon radars, especially ones located in tropical areas, such as Northern Australia, are usually strongly affected by external impulsive noise. Apart from thunderstorm activity, man-made (industrial) noise over typically quite long coherent integration time often is of impulsive nature as well.

In this paper we analyse the efficiency of temporal and spatial adaptive techniques for impulsive noise mitigation. We demonstrate that for heavily contaminated dwells, new spatio-temporal adaptive processing is most effective. Initial impulsive noise mitigation, produced by adaptive spatial processing is used for range and azimuth dependent sea-clutter spectrum estimation. Estimated sea-clutter spectrum is then used to "restore" the "missing" data, originally contaminated by impulsive noise.

1. DESCRIPTION AND ANALYSIS OF MITIGATION TECHNIQUES

The High Frequency Over-the-Horizon Radar (HF OTHR) probably constitutes the most prominent example of radars subjected to severe impulsive noise interference. Tropical thunderstorms which are extremely active in equatorial regions such as Northern Australia, typically generate a significant number of lightning strikes within the operational range of HF OTHR due to relatively long coherent processing intervals. In [2] based on experimental data collected in Northern Australia, we introduced point process models for atmospheric noise adequate to spatial and temporal adaptive impulsive noise mitigation. It has been suggested that optimal mitigation technique should incorporate both spatial and temporal domains based on the properties of particular lightning strike.

Our recent experimental trial conducted from May to September 2000 in Northern Australia revealed that accidental human-made noise that quite often interferes with a HF radar, is in most cases also highly nonstationary. The atmospheric strike typically occupies a single repetition period or at most a few consecutive repetition periods (for high air-mode waveform repetition frequencies WRF=40 - 60 Hz), man-made impulsive interference typically occupies significantly longer intervals, measured in dozens of repetition periods (sweeps). Typical examples of atmospheric and man-made impulsive noise are presented in Fig. 1, 2. The amplitude of the range processed data at the output of one particular beam are shown for different ranges (y-axis) as a function of repetition period (x-axis). One can see significant difference in number of sweeps contaminated by atmospheric and man-made impulsive noise. Another important feature demonstrated by these figures is the availability of "sea clutter-free ranges". These ranges allow for straight-forward identification of sweeps affected by impulsive noise.

Obviously, analysis of impulsive noise mitigation efficiency should be expanded to man-made interference. Indeed, since only up to 30% of entire dwell is typically corrupted, there is a reason to compare spatial techniques with temporal ones[1].

In this paper we introduce comparative analysis of different temporal and spatial adaptive techniques, suitable for impulsive noise mitigation.

Since the actual interval corrupted by impulsive noise is easily identified, temporal techniques are focused on a proper estimation of the missing sea-clutter data. For surface-wave radars with typically very high sub-clutter visibility that can range far above 60 dB, an accurate estimation can become a problem.

To address this problem two major approaches could be adopted. The first one is based on classical Weiner prediction filter. Complicated nature and range/azimuth variability of sea-clutter Doppler spectrum impose limitations on the actual accuracy of this approach.

The second technique is based on direct optimization of replacement data to minimize the total power within the specified range of Doppler frequencies which are expected to be free of sea clutter. This technique has a different limitations, especially when the number of missing data is quite large and consecutive. However, in attempt to minimize the overall power, strong targets could be suppressed and some important features of the sea-clutter spectrum could be significantly damaged. Spatial techniques are effective when strong impulsive interference impinges on a beam pattern sidelobes. Meantime, when the entire coverage is important, there would always exist directions corrupted by impulsive noise propagated via the main beam.

Comparative analysis of the above mentioned techniques was done firstly on uncorrupted SW OTHR data with subclutter visibility close to the limit. One selected example is shown in Fig. 3. A certain number of sweeps has been nominated as being "corrupted" and two abovementioned temporal techniques have been used to restore the "missing" data.

In order to apply the classic prediction (interpolation) approach, we first estimated the sea-clutter temporal covariance matrix. With

$N = 1000$ repetition periods typically used in ship mode, we selected $M < N/2$, $M = 400$ as a dimension of prediction/interpolation filter in expectation that whatever the actual number of missing repetition periods is, there still should be a sufficient number of uncorrupted repetition periods (sweeps) within corresponding M-variate "sliding window" of our prediction filter. The M-variate (range-dependent) sea-clutter covariance matrix is estimated here by forward-backward averaging:

$$\hat{R}_d = \sum_{j=1}^{N-M+1} (X_j^d (X_j^d)^H + J \bar{X}_j^d X_j^{dT} J) \quad (1)$$

where

$$X_j^d = (x_j^d, x_{j+1}^d, \dots, x_{j+M}^d) \quad (2)$$

$$J = \begin{bmatrix} 0 & \dots & 1 \\ \vdots & \ddots & \vdots \\ 1 & \dots & 0 \end{bmatrix}, \quad (3)$$

and x_j^d is the complex number that corresponds to j -th repetition period and d -th range cell. Particular beam number is not essential for this temporal processing.

Let us introduce an $M \times (M - m)$ variate incidence matrix H_m that is constructed as standard identity matrix with m deleted rows at positions that correspond to the "missing" sweeps. Then the adaptive prediction filter that generates an estimate of the k -th missing data is defined as

$$W_k^d = [H_m^T \hat{R}_d H_m]^{-1} H_m r_k^d, \quad k = 1, \dots, m \quad (4)$$

where r_k^d is k -th column of the M-variate matrix \hat{R}_d .

Correspondingly, the estimate \hat{x}_k^d , $k = 1, \dots, m$ of the k -th missing sweep is defined as

$$\hat{x}_k^d = W_k^{dH} H_m^T X^d, \quad k = 1, \dots, m \quad (5)$$

Our second approach is based on direct search for the m -variate vector \hat{X}_m for "missing" data that with respect to the remaining $(N - m)$ "valid" data results in the minimal total power within some designated range of Doppler frequencies.

Specifically let us present the overall N-variate vector X^d as

$$X^d = X_0^d + A_m \hat{x}_m \quad (6)$$

here X_0^d is a N-variate vector with zeroes the positions of "missing" data, A_m is $N \times m$ -variate incidence matrix, where rows of the m -variate matrix are "spread" over N rows, corresponding to the positions of the missing data.

Weighted Discrete Fourier Transform (DFT) over the vector X^d could be presented as

$$FD(X_0^d + A_m \hat{x}_m) \quad (7)$$

and with $(N - n) \times N$ selection matrix S , the $(N - m)$ -variate vector of selected Doppler bins within the d -th range Doppler spectrum could be presented as

$$SFD(X_0^d + A_m \hat{x}_m) \quad (8)$$

where F is the N-variate DFT matrix, D is a diagonal weighting matrix (e.g. Blackman window).

Finally, the overall power within this Doppler window could be presented as

$$X_0^{dH} D F^H S S^T F D X_0^d + \hat{x}_m^H A_m^H D F^H S S^T D A_m \hat{x}_m + \quad (9)$$

$$cr \hat{x}_m^H A_m^H D F^H S S^T F D X_0^d + X_0^{dH} D F^H S S^T F D A_m \hat{x}_m. \quad (10)$$

Correspondingly the optimum solution is

$$\hat{x}_m = -[A_m^H D F^H S S^T F D A_m]^{-1} A_m^H D F^H S S^T D X_0^d. \quad (11)$$

(For rank deficient matrix $[A_m^H D F^H S S^T F D A_m]$ this solution is modified to operate on signal subspace of this matrix.) Now these techniques could be compared. Fig 4 presents the Doppler spectra for $m = 100$ of "missing" data for one range cut. Both random (atmospheric like) and continuous (man-made like) distributions of "missing" data within the 400 sweeps long window have been analysed. Different number of missing sweeps have been analysed, $m = 1, 40, 60, 100$, however only $m = 100$ continuous case processed with optimization filter is shown (the only one which shows any difference from the original).

The results demonstrate that for randomly distributed "missing" data both techniques provide equally good restoration. The prediction errors are equally small and sub-clutter visibility is restored to the original level in this case. However in the case of continuous "missing" data both methods work equally well only for a small number of "missing" sweeps. For increased number of consecutive missing data the difference between these two techniques becomes more significant. While classical prediction is still efficiently restoring missing data (up to 100 of missing data for 400-variate prediction filter), optimization (11) generates estimates \hat{x}_m significantly different from the true missing ones. These estimates lead to reduction in overall noise power within the specified Doppler area, but the overall structure of the Doppler spectrum changes significantly. For most practical applications these changes could not be tolerated. Moreover, with significant number of "degrees of freedom", total power minimization could considerably reduce the target signal as well. Thus, for a randomly distributed missing data or small number of consecutive missing data (up to 20 consecutive sweeps) the optimization technique (11) could be recommended as a preferred option since it does not involve (adaptive) sea-clutter spectrum estimation. For typical man-made impulsive interferences, this approach is not appropriate and attention should be attracted to a practical implementation of adaptive prediction technique (4)-(5). Main problem here is to get an accurate enough estimate for the sea clutter covariance matrix \hat{R}_d . Since the dimension of this matrix (prediction filter) should be significantly greater than the number of missing sweeps - real (corrupted) data should not be used directly for sample matrix estimation (1) in the way it has been done in our previous study with uncorrupted data. Since all ranges are usually equally corrupted by impulsive noise, spatial diversity could be explored to assist sea-clutter covariance matrix estimation. Indeed, in most cases truly dominant impulsive noise sources are well localized and even with conventional beamformer it is usually possible to find the least contaminated direction (beam). While Fig 2 displays the range map for the most occupied beam, the top line in Fig 6 demonstrates distribution of this impulsive noise power-to-noise ratio across the beams. It is quite obvious, that in the "minimal" beam ($N=7$) the power of this noise is significantly smaller and range processed data of this beam could be used for covariance matrix estimation. Obviously, adaptive spatial processing is even more effective in terms of reduction of antenna pattern sidelobes

affected by impulsive noise. The bottom line in Fig 6 presents the similar impulsive noise to white noise ratio as a function of beam direction for spatial adaptive processing (SAP). Here sea clutter-free ranges are used to estimate sample spatial covariance matrix \hat{R}_{sp} :

$$\hat{R}_{sp} = \sum_{d,j \in \theta} X_{d,j}^{sp} X_{d,j}^{spH} \quad (12)$$

where

$$X_{d,j}^{sp} = (x_{d,j}^{(1)}, \dots, x_{d,j}^{(32)})^T \quad (13)$$

θ is the sea-clutter free ranges area and SAP beamformer is defined as usual by

$$\hat{W}_{SAP}(l) = \frac{\hat{R}_{SP}^{-1} S_l}{S_l^H \hat{R}_{SP}^{-1} S_l} \quad (14)$$

with S_l as a 32-variate steering vector.

The most important issue that needs to be addressed to justify this approach is sensitivity of this technique with respect to sea-clutter azimuthal variability. Indeed, we are prepared to use the sea clutter training data collected at the output of one particular (adaptive) beam, but apply it to quite a different (conventional) beamformer output. In order to investigate the efficiency of such technique, we analysed our "clean" data with nominated "missing" data. For Wiener prediction filter there is no visible difference for one range-doppler cut between the original data and restored ones even for quite large number of missing data ($m=100$), regardless of the fact if the data are random or consecutive. For the optimization filter the same can be said for random distribution of the replaced sweeps. However the same cannot be said for consecutive sweeps as the inverted matrix becomes ill conditioned. The Fig 4 demonstrates, there is some degradation of the signal in the "sea clutter" area.

Finally we illustrate the practical efficiency of our approach by processing the real contaminated data shown in Fig 1,2.

For the data shown in Fig 1 optimization technique (11) should be appropriate since only one dominant "strike" is recorded here.

The results of this technique applied to one beam Fig 5 demonstrate quite impressive improvement in sub-clutter visibility. Particular range profile shown in Fig 7 demonstrates 35 dB improvement in sub-clutter visibility, while the standard SAP has delivered only mere 8-10 dB.

Our second example deals with the man-made impulsive noise, as per Fig 2. While SAP is practically not effective for the data collected at the direction of impulsive noise arrival (beam 4) it provides quite reasonable improvement for beam 7 data that thus could be used as training one. The above described approach with adaptive prediction filter "trained" on beam 7 data and applied to beam four data is illustrated by Fig 8. The particular range profile demonstrates improvement in sub-clutter visibility up to 20 dB. Note that quite significant part of coherent processing interval (CPI) has been contaminated here. Interestingly enough, when the same prediction filter is applied to the training data of the beam 7 (Fig 9), still considerable additional improvement with respect to the SAP processing has been obtained. The reason behind becomes clear when sea clutter free ranges processed by SAP are analysed: impulsive noise residues are still some 10 dB above the ambient noise floor. Therefore the replacement of these corrupted repetition intervals by predicted ones results in additional improvement in sub-clutter visibility.

2. CONCLUSION

Analysis of selected temporal and spatial adaptive techniques for atmospheric and man-made impulsive noise mitigation for SW OTHR has been performed. It has been demonstrated that temporal or spatial only processing could be effective only in special cases. For contaminated repetition periods which are randomly distributed over CPI, direct optimization method is shown to be very effective. For some beam directions affected by impulsive noise via antenna pattern sidelobes, standard spatial adaptive processing could be also quite effective on its own. In more general case, when the number of contaminated sweeps is quite significant and consecutive (man-made impulsive noise), and impulsive noise must be rejected in all directions, proposed spatio-temporal adaptive processing is shown to be most effective. Here spatial (adaptive) processing is used for initial impulsive noise mitigation, and the beam where this reduction is maximal is used as a training one for sea-clutter (temporal) covariance matrix estimation. Adaptive Wiener filter trained by the spatially processed data is then applied to contaminated (conventionally) beamformed data with similar energetic content of Doppler spectra.

3. REFERENCES

- [1] Y.I. Abramovich, J.F. Böhme, A.Y. Gorokhov, and D. Maiwald. GEM-algorithm for sea echo Doppler analysis with data corrupted by sparkling interference. In *Proc. of the SPIE*, pages 194–203, San Diego, 1993.
- [2] Y.I. Abramovich, N.K. Spencer, and S.J. Anderson. Experimental trials on non-Gaussian environmental noise mitigation for surface-wave over-the-horizon radar by adaptive antenna array processing. In *Proc. HOS-99*, pages 340–344, Ceasarea, 1999.

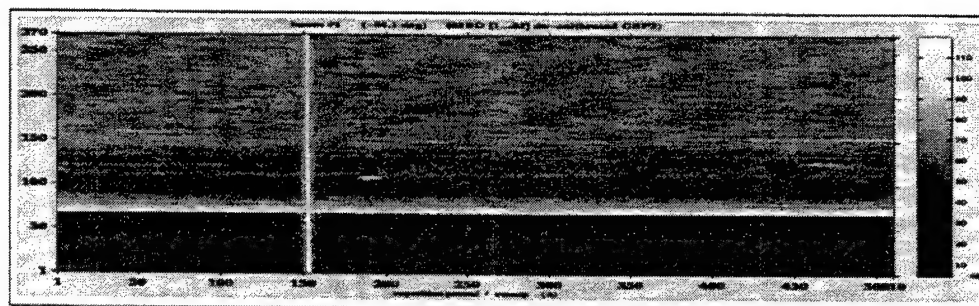


Figure 1: Atmospheric impulsive noise, beam 1.

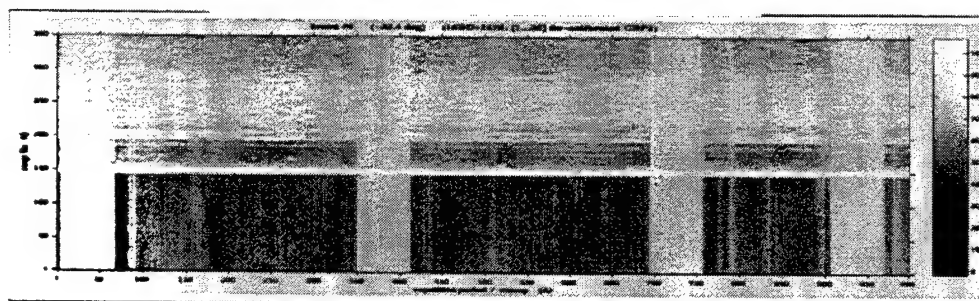


Figure 2: Man-made impulsive noise, beam 4.

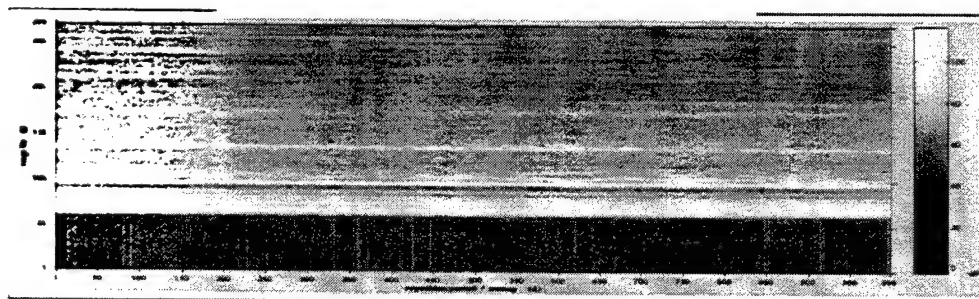


Figure 3: "Clean" data used for comparison.

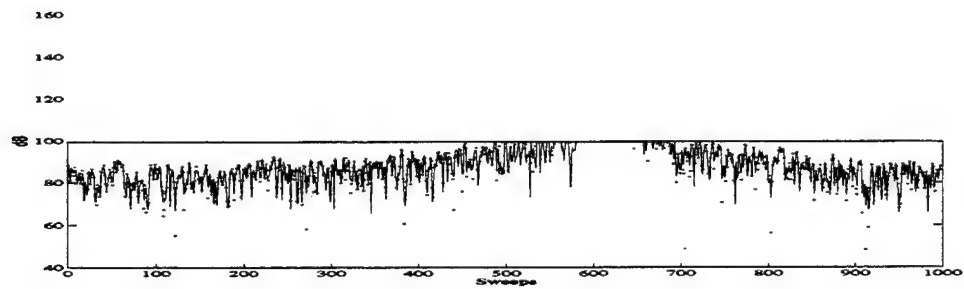


Figure 4: Comparison of original data and optimization filter with 100 consecutive sweeps replaced.

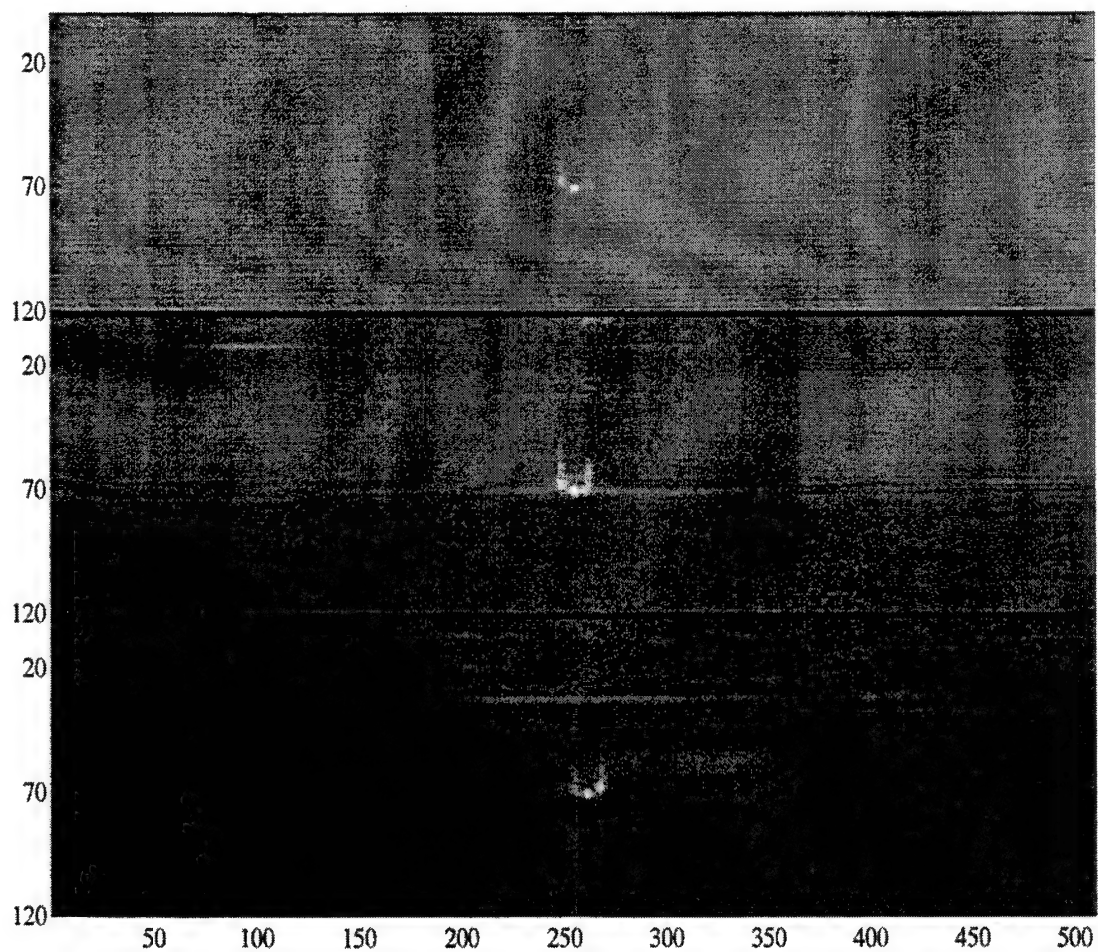


Figure 5: Comparison of conventional, SAP and optimization beamformer.

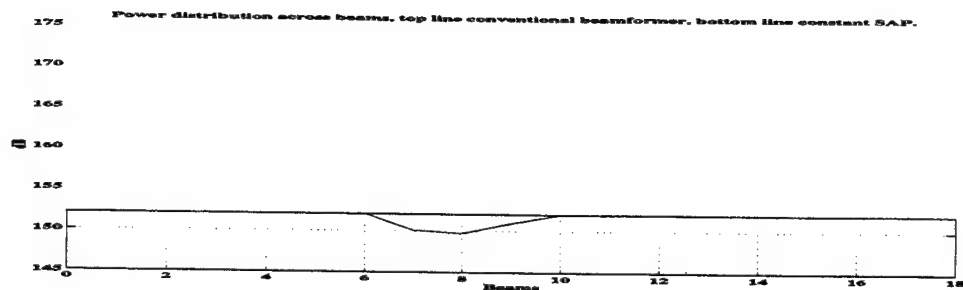


Figure 6: Power distribution across beams, top conventional beamformer, bottom SAP.

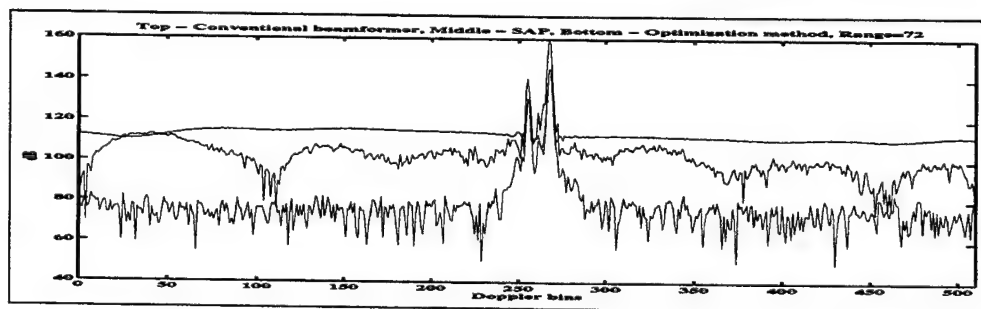


Figure 7: One range cross section, top-original, middle-SAP, bottom-optimization

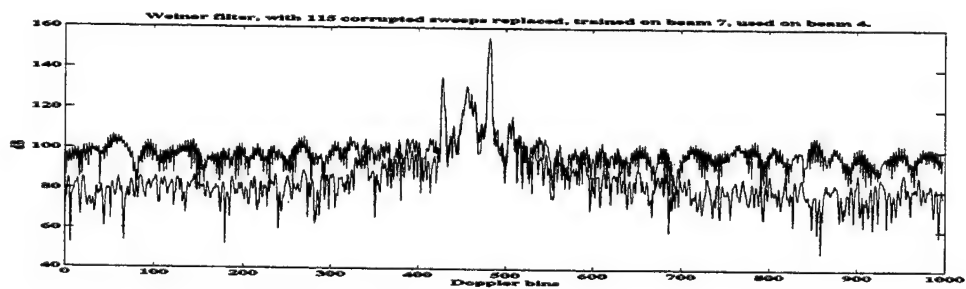


Figure 8: Weiner prediction filter trained on beam 7, used on beam 4.

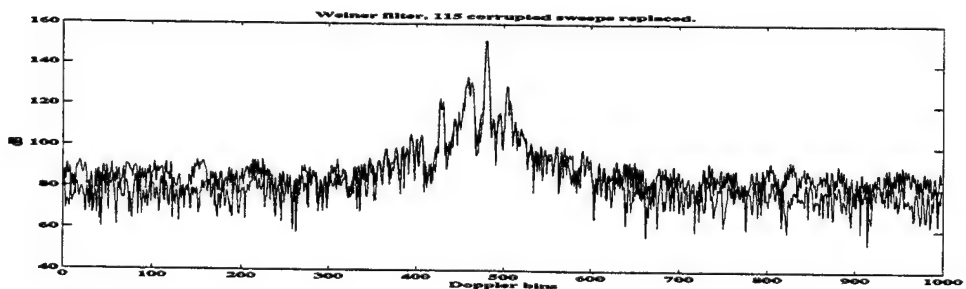


Figure 9: Weiner prediction filter trained on beam 7, used on beam 7 top line - SAP bottom line - Weiner prediction filter.

SUBBAND ENERGY DETECTION IN PASSIVE ARRAY PROCESSING

Michael Bono, Ben Shapo, Pete McCarty, Roy Bethel***

Applied Research Laboratories
University of Texas at Austin
P.O. Box 8029
Austin, TX 78713-8029
mbono@arlut.utexas.edu,
mccartyp@arlut.utexas.edu

*Digital System Resources
12450 Fair Lakes Circle
Suite #500
Fairfax, VA 22003
bshapo@dsrnet.com

**MITRE Corporation
11493 Sunset Hills Road
Reston, VA 20190-5214
rbethel@mitre.org

ABSTRACT

Broadband processing is an important part of the Navy's current and future SONAR systems. This paper provides an introduction to a new class of passive broadband processing algorithms, Subband Energy Detection (SED), which includes both Subband Peak Energy Detection (SPED) and Subband Extrema Energy Detection (SEED). It will be shown that SED has several performance advantages over Conventional Energy Detection (CED), also known as Linear Rectify (LR).

SED exploits the spatial coherence of the signal's local maxima ("peaks") and minima ("valleys") compared to the randomness of noise to increase the quality of the broadband processing display. Instead of summing the energy in each single beam over the frequency band, SED sums the energy of the peaks and valleys in the azimuth spectrum for each frequency bin.

The objective of this paper is to examine the theory, advantages, and limitations of Subband Energy Detection. In doing so, we will first give an overview of broadband processing and discuss energy detection theory. We will then describe the theory of both CED and SED. Processed data from both sets of algorithms will then be analyzed to uncover the relative advantages and disadvantages of each method.

1. INTRODUCTION

For a single time scan, the output of the beamformer is a 2dimensional matrix in frequency and azimuth known as a FRAZ (FRequency AZimuth). A 2-dimensional FRAZ cell contains a measurement of the energy for each azimuthal and frequency bin. A typical

example FRAZ is shown in Fig. 1a. Broadband processing methods collapse the FRAZ over frequency to a single dimension, azimuth. The result is a bearing-time record (BTR) display, Fig. 1b, which allows the operators to detect contacts and provides a high level of situational awareness.

In the past, broadband detection methods such as CED and cross-correlation (CC) have provided this critical function while attempting to maximize the operator's detection ability. Recently, a new class of broadband detection methods, Subband Energy Detection (SED), has been developed and has emerged as an accepted alternative [1].

2. ENERGY DETECTION

The goal of energy detection methods is to create an estimate of the probability of detection of an acoustic source at a given time and location. This requires the reduction of the beamformer output, which is a function of time, azimuth, and frequency into the time-azimuth plane. As a result, both CED and SED collapse the beamformer output over frequency but each takes a different approach.

2.1 Acoustic Environment

The ocean acoustic environment consists of acoustic energy from both contact signals and random noise. This noise field is the result of a large number of factors such as wave action, seismic events, marine life, and distant shipping activity.

Since this noise field is a collection of sources, it also has a certain level of directionality associated with it. The attenuation factor for acoustic waves is also larger for higher frequencies. The result is a noise field dominated in power by low frequency spectral content and significantly less high frequency content.

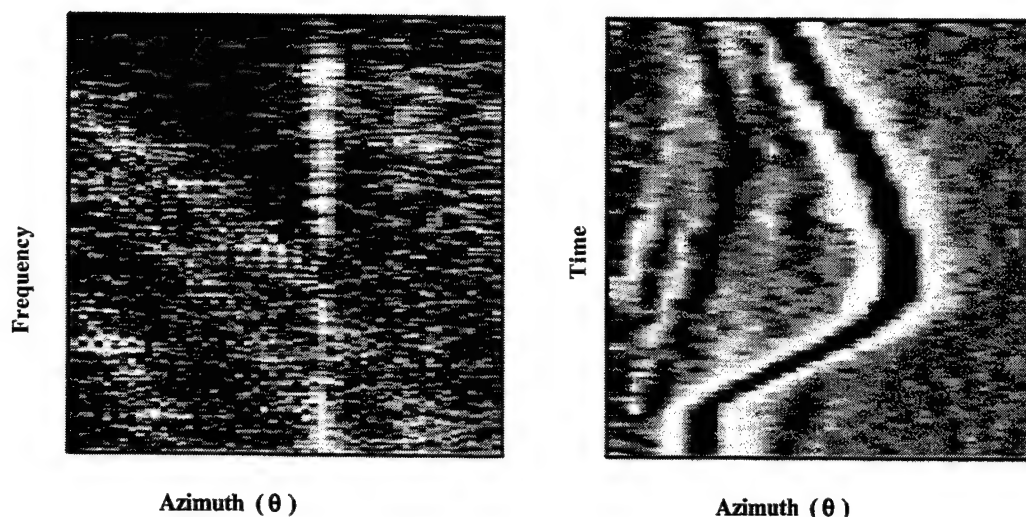


Figure 1: Broadband Processing Methodology (A) FRAZ- FRequency Azimuth plot for a single time scan, (B) BTR- Bearing Time Record Display that is the final broadband display.

2.2 Normalization

Due to the nature of the noise field, energy detection methods typically utilize a noise floor estimate. This is done since signal to noise ratio (SNR) is used as the energy value. It has been shown that the use of SNR versus raw signal typically increases the performance of the algorithm. Simply summing the raw energy in each frequency bin ignores the fact that low frequencies dominate the energy distribution. Doing so may prevent the detection of primarily high frequency contacts.

Energy detection methods with noise floor estimation have demonstrated good detection capability including the detection of low SNR contacts (i.e. signals quieter than the average noise floor) [2]. In part, this detection capability benefits from two primary concepts: spatial coherence and sidelobe rejection.

2.3 Energy Detection Concepts

Spatial coherence is defined as the alignment of distinct frequency components of a contact signal. Since the frequency components spatially align, they strengthen the energy estimate and increase the detectability of contact signals over random noise.

Energy detection methods also provide inherent sidelobe rejection. The reason for this is related to the beamforming process. Beamforming spatially filters the elemental array timeseries. Ideally, there is a unity gain in the look direction and a zero gain in all others. Realistically, the array gain pattern, or beam pattern includes a mainlobe of a certain width and several sidelobes which allow noise and interferer energy to leak into the beam measurement.

At high frequencies, the beam pattern has a narrow mainlobe and many narrow sidelobes. As the frequency is reduced, the lobe width increases and the location of the sidelobe peaks shift in azimuth. The result is that for a single beam measurement, the mainlobe peaks line up in the same azimuth bin for all frequencies while sidelobe peaks spatially shift and will not line up over the frequency range. This mitigates the effect of sidelobe energy leakage.

3. CONVENTIONAL ED

Conventional Energy Detection (CED), also known as Linear Rectify (LR), is a traditional energy detection method. CED will be utilized as a baseline for evaluating Subband Energy Detection (SED) performance.

3.1 CED Principles of Operation

CED starts with a FRAZ for a single time scan and processes each azimuth bin, Fig 2a. A single azimuth bin contains a frequency spectrum of signal plus noise, as seen in Fig. 2b. As mentioned above, the next step is to perform a noise estimate. The method used by CED for estimating the noise floor applies a median filter in frequency and azimuth.

CED then calculates the signal to noise ratio (SNR) by dividing the beamformer output (signal plus noise), Fig. 2b, by the noise floor estimate, Fig 2c. Finally, it calculates an energy estimate by summing the SNR values in all desired frequency bins for the single azimuth bin. This process is repeated for each azimuth bin and

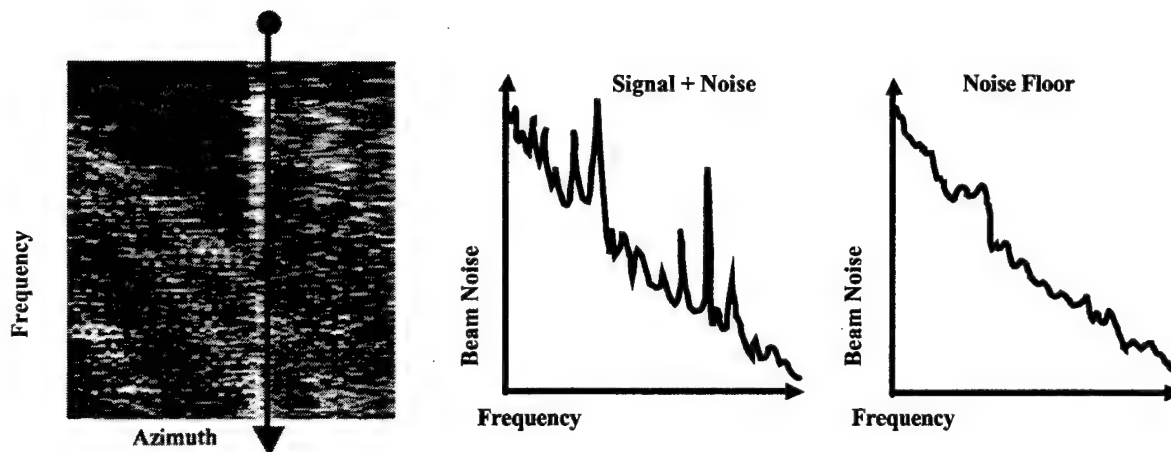


Figure 2: Conventional Energy Detection (A) FRAZ display with arrow showing a single azimuth bin, (B) Frequency spectrum of the measured signal plus noise for a single azimuth bin, (C) Frequency spectrum of the normalized noise estimate.

every time scan to produce a BTR display which is used to detect acoustic contacts.

3.2 CED Performance

CED has been shown to provide optimal single signal detection in uncorrelated noise fields. The theoretical minimum detectable level (MDL) of CED for this case is better than that of the SED algorithms presented next. As such, CED provides raw optimum detection ability for isolated signals.

There is, however, one major limitation of CED. CED produces wider contact traces due to the limited bearing resolution. As a result, CED is not optimal for real world acoustic environments with multiple signals. This produces BTR displays with wide, blurry traces for loud contacts.

The detection ability of the system for cluttered, real world acoustic noise environments is impaired since the wide, blurry traces may suppress nearby, quieter contacts. So, despite the theoretical MDL advantage of CED for isolated signals, SED has an overall detection advantage in clutter due to the increased bearing resolution and narrower contact traces. This can be seen in the results in Fig. 5 and will be discussed further later.

4. SUBBAND ED

Subband Energy Detection (SED) is a new class of energy detection methods. These algorithms have gained acceptance and are currently used in real world SONAR systems.

4.1 SED Principles of Operation

SED starts with the same FRAZ information as CED. However, instead of looking at the frequency spectrum in a single beam, SED looks at the azimuth spectrum for a single frequency bin, Fig 3a. SED finds the locations of all "peaks" and "valleys" in the azimuth spectrum for each frequency bin. An example azimuth spectrum is seen in Fig. 3b. A peak is simply a local maximum in azimuth and a valley is a local minimum in azimuth. These peaks and valleys are then used to generate an energy estimate using one of several algorithms. Fig. 4 shows BTRs for a real acoustic data set processed by each of the four primary SED algorithms.

4.2 SPED and SEED

There are two fundamental classes of Subband ED algorithms: Subband Peak Energy Detection (SPED) and Subband Extrema Energy Detection (SEED). In addition, each class has at least one version from two modes: Clutter Suppress (CS) and Energy Detection (ED).

SPED utilizes only the peak information to estimate the detection probability. It examines the azimuth spectrum for every frequency bin and locates the peaks. For each azimuth bin containing a peak, a value, or "reward", will be added to the energy estimate for that azimuth bin. The actual value of the reward will depend on the mode of the algorithm (i.e. CS or ED). This is repeated for each frequency bin.

Unlike with CED processing, if the bin does not contain a peak then SPED will not add to the energy estimate for that azimuth. In other words, SPED sums only the energy at the peaks.

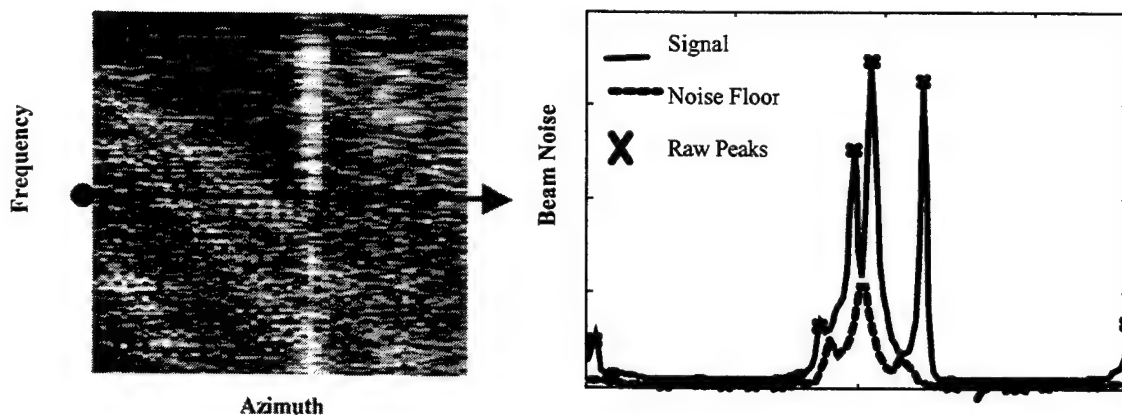


Figure 3: Subband Energy Detection (A) FRAZ display with arrow showing a single frequency bin, (B) Azimuth spectrum of a single frequency bin showing the signal peaks and the noise floor.

Subband Extrema Energy Detection utilizes both peak and valley information to estimate the detection probability. Like SPED, it will add a reward for peaks. In addition, it will also subtract a value, or assess a "penalty" for any valley that is located in an azimuth bin.

4.3 CS and ED Modes

The clutter suppress mode (CS) assigns a reward and penalty of unity for each peak and valley. This mode can be thought of as a histogram and basically counts the number of peaks (and, in the case of SEED, subtracts the number of valleys). It does not attempt to account for the magnitudes of these peaks and valleys. As a result, the CS mode does not require noise floor estimation. This method works well with broadband contacts but poorly with contacts containing only a few loud frequency components.

The energy detect mode assigns a reward and penalty based on signal to noise ratio. This requires the calculation of a noise estimate. The reward is simply the measured beam noise (signal plus noise) divided by the noise estimate. The penalty calculation is less straightforward and is an area of current research [3,4,5].

The noise estimate typically used is a complex algorithm that averages over time, clips tonals, applies a smoothing filter, and then takes the quiet value in an azimuth sector as the noise floor.

4.4 SED Theory

Peaks and valleys occur due to both contact signals and random noise. Even when the average noise floor is greater than the contact, the fluctuations of the

noise may cause it to drop below the contact signal. When this happens, there is a peak due to the contact signal.

In one frequency bin of the beam noise versus azimuth spectrum, there may be several peaks due to the signal but still many more due to noise. Although noise peaks outnumber signal peaks, low SNR contacts may still be detected because peaks due to contact signals will have spatial coherence (i.e. occur in the same azimuth bin for each frequency) while noise peaks will not. As a result, these signal peaks add "constructively" when summed over the entire range of frequency bins.

SED is often referred to as a "peak-picking" method. Instead of summing the energy in every frequency bin, SED sums only the energy values for the bins that contain extrema. In effect, this detects only the peak of the mainlobe, reduces the width of the contact traces, and provides increased spatial resolution of the BTR display. This serves to provide SED with a detection advantage over CED in cluttered environments since quiet contacts are no longer hidden by nearby louder ones.

5. RESULTS

Fig. 5 shows four acoustic data sets processed by both CED and SEED CS. The first example (on the left) shows comparable detection ability. Despite the better theoretical MDL of CED for isolated targets, this and most other real data sets show no appreciable difference in detection ability.

The peak-picking provides SEED CS with sharper, more clearly defined contact traces as can be seen

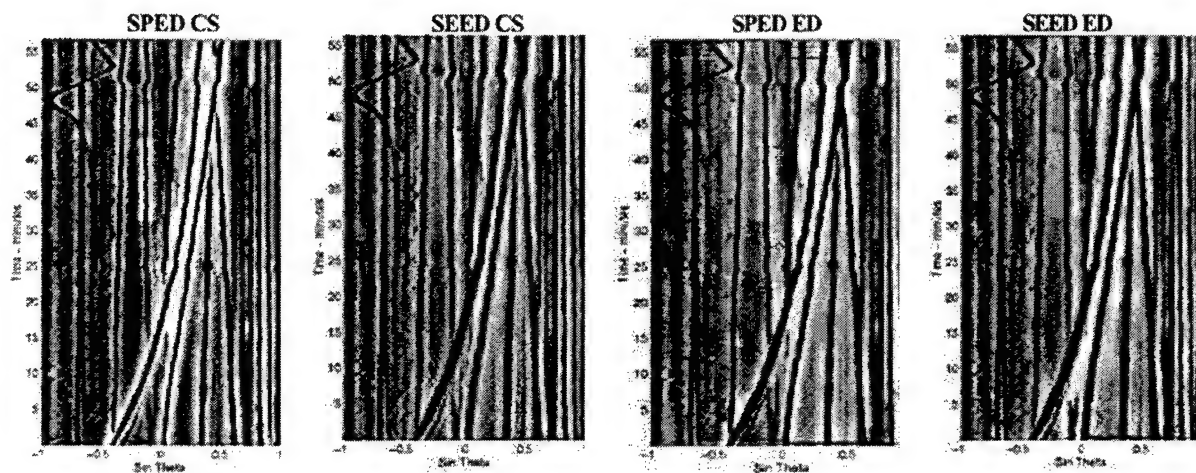


Figure 4: BTR displays for a real acoustic data set processed by several Subband ED algorithms (A) SPED CS, (B) SEED CS, (C) SPED ED, (D) SEED ED

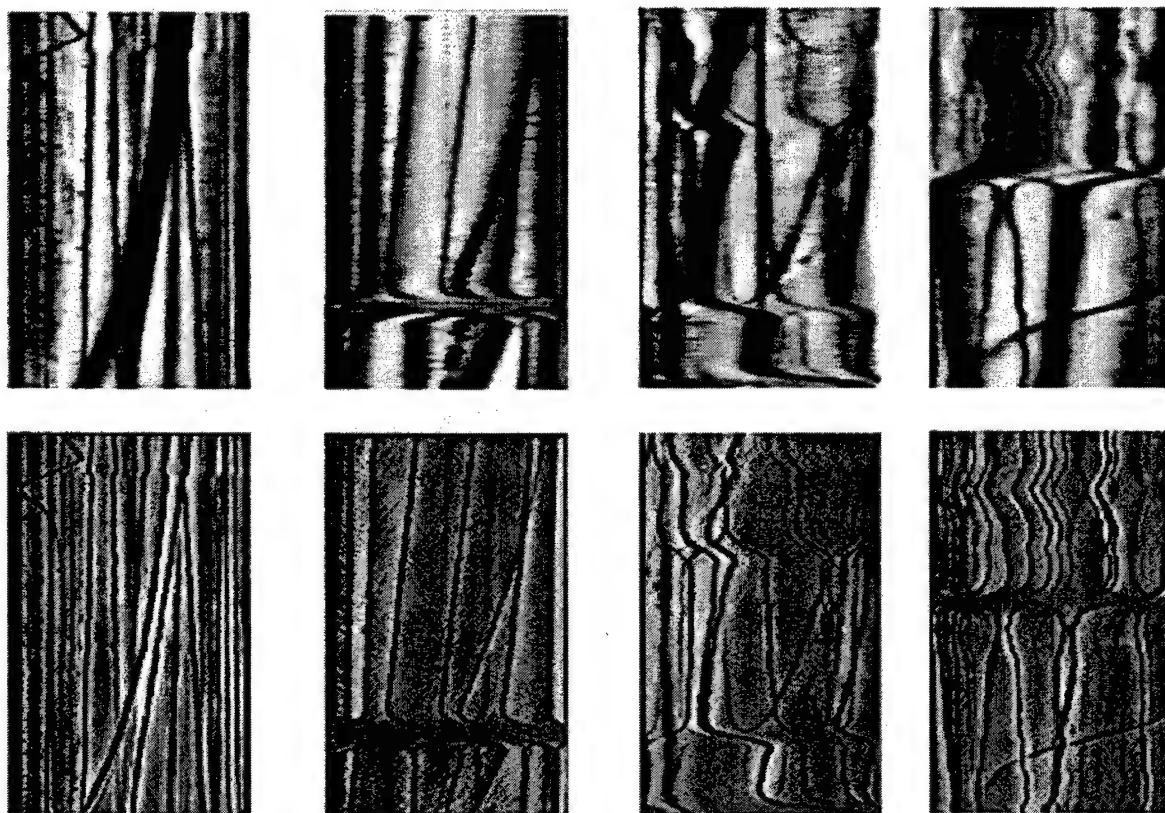


Figure 5: BTR displays for Conventional ED (top row) and Subband Extrema Energy Detection- Clutter Suppress Mode, SEED CS, (bottom row) for four real acoustic data sets.

in the second example from the left. This reduces the 'blacked out' areas resulting from loud contacts. In this example, the increased spatial resolution does not improve performance substantially since both grams contain all traces.

In the third example from the left, which shows a cluttered environment, the increased spatial resolution does provide a significant detection advantage. Traces that are blurred together in the CED gram can clearly be seen in the SEED CS gram.

The final example again shows the detection advantage of SED in cluttered noise environments. It also shows comparable detection performance for the contact of interest, the high bearing rate trace at the bottom.

6. SUMMARY

This paper has compared the theory and results of both Conventional Energy Detection and Subband Energy Detection. The results have shown that SED provides narrower contact traces and increased bearing resolution since only the energy of the peaks and valleys are summed. There is also reduced smearing of acoustic energy over large azimuths and an improved ability to detect nearby contacts. Additionally, despite a lower theoretical MDL for isolated signals, SED displays a significant detection advantage in real world (cluttered) acoustic environments. The overall conclusion is that Subband Energy Detection is an important broadband processing method that provides increased performance to Navy SONAR systems.

7. REFERENCES

- [1] B. Zarnich, "A Fresh Look at Broadband Passive Sonar Processing," *Seventh Annual ASAP '99 Workshop*, March 10, 1999.
- [2] R. Gramann, P. McCarty, C. Penrod, "Detection Performance of Cross Correlation and Energy Detection with Towed Arrays" *Submarine Superiority Conference at the Naval War College*, April 1998.
- [3] R. Bethel, B. Shapo, "Improved Broadband Processing: Subband Extrema Energy Detection," *Signal Processing Working Group*, January 18, 2000.
- [4] R. Bethel, B. Shapo, "Improved Broadband Processing: Subband Extrema Energy Detection II," *Signal Processing Working Group*, March 01, 2000.
- [5] M. Bono, "SEED ED vs. SPED ED Evaluation," *Signal Processing Working Group*, November 2, 2000, Applied Research Laboratories: The University of Texas at Austin, ARL-TL-EV-00-61.

CASE OF SHORT DATA RECORD FOR BOTH TRAINING AND SIGNAL DETECTION

Brian E Freburger

Naval Air Warfare Center, Aircraft Division
Patuxent River, MD
freburgerbe@navair.navy.mil

Donald W Tufts

Dept. of Electrical and Computer Engineering
University of Rhode Island
Kingston, RI

1. INTRODUCTION

Detection of a signal embedded in interference is a common problem encountered in radar, sonar and communication systems. In cases where it is known that the interference is low rank (or approximately so) the amount of data required for adaptation can be reduced by using reduced rank estimation methods. Three proposed methods for making the selection of basis vectors are the Cross Spectral Metric (CSM) [1] method, the Principal Components Inverse (PCI) [2] method and Multistage Wiener Filter (MWF) [3]. The examination here is for detection of a signal that may or may not be present within a given set of data. That is, training and signal detection must be performed using the same data set. The case of independent training and test data has been treated in [4, 5].

2. ADAPTIVE CSM, MWF AND PCI

The methods of CSM, PCI and the MWF offer differing ways of providing an adaptive processor in the signal based coordinates,

$$|S^H X - W_{GSLC}^H (B^H X)| \quad (1)$$

where S is orthogonal to the columns of B . Referring to Figure 1, given a set of K data vector samples, form a $1 \times K$ vector $\mathbf{d} = [d_1 \ d_2 \ \dots \ d_K]$ and a $N-1 \times K$ matrix $\mathbf{Z} = [Z_1 \ Z_2 \ \dots \ Z_K] = \hat{\mathbf{U}} \hat{\Sigma} \hat{\mathbf{V}}^H$ from the data in the signal and orthogonal space respectively. Subsequently, we will use the $\hat{\cdot}$ symbol to denote estimation from data. For example, \mathbf{R}_Z is the the covariance matrix of the vector Z_k and $\hat{\mathbf{R}}_Z$ is an estimate of \mathbf{R}_Z using a finite number of vector samples.

Adaptive versions of CSM, PCI and the MWF can be constructed by using covariance and cross-covariance estimates.

$$\hat{\mathbf{R}}_Z = \frac{1}{K} \mathbf{Z} \mathbf{Z}^H \quad \hat{\mathbf{r}}_{dZ} = \frac{1}{K} \mathbf{Z} \mathbf{d}^H \quad (2)$$

For CSM and PCI the weight vector is formed as

$$\hat{W}_{GSLC} = \hat{\mathbf{U}}_p \hat{\Sigma}_p^{-2} \hat{\mathbf{U}}_p^H \hat{\mathbf{r}}_{dZ} \quad (3)$$

using the p singular vectors and values selected by the given method. Adaptive CSM uses the estimated cross spectral metric; whereas, PCI uses only the estimated singular values to determine which singular vectors are kept. The MWF uses the estimated quantities in place of the known quantities in the construction of the multistage decomposition. It should be noted that the philosophy in the development of these methods have differences. CSM and MWF were formulated as a rank reduction for a prescribed rank and general covariance; whereas, PCI was developed with the assumption that the covariance is from a low rank process and the rank is estimated from data over the adaptation interval [6].

3. TRAIN AND TEST ON SAME DATA

Often the scenario is such that the calculation and application of the weight vector is to be performed on the same data set. In this case, with no signal present, CSM has been shown to be the optimal method with respect to mean square error for the selection of singular vectors, and an upper bound to the performance of PCI. Consider, the assumption that the interference has a correct rank such that CSM and PCI should nominally choose the same singular vectors. Suppose the realization of data has a swap [4] in the singular vectors chosen by CSM. Then CSM will choose a set of singular vectors which may not be best for the entire set of all possible realizations, but that doesn't matter since the weight vector will only be used on this realization. PCI on the other hand, chooses singular vectors which should work best on all possible realizations and thus does not perform as well as CSM on this particular realization. That is, the reasoning that allows PCI to outperform CSM in the independent data case is the reason that it is poorer in the same data case with respect to mean square error.

3.1. Toy Example

Let us construct a simple concrete example which can be used to highlight the characteristics of each method. Assume a five element array with four sample snapshots and

two jammers. Without loss of generality assume that the beams of the orthogonal space are chosen to be the eigencoordinates. Choose an equal power of 1000 for the jammers and let the signal channel be given as $\mathbf{d}_k = 0.01\mathbf{Z}_{1,k} + 0.1\mathbf{Z}_{2,k} + 0\mathbf{Z}_{3,k} + 0\mathbf{Z}_{4,k}$. Suppose the data with only jamming (no signal or background noise) is

$$\mathbf{d} = \begin{bmatrix} -90 & 90 & 110 & -110 \end{bmatrix} \quad (4)$$

$$\mathbf{Z} = \begin{bmatrix} 1000 & -1000 & 1000 & -1000 \\ -1000 & 1000 & 1000 & -1000 \\ 0 & 0 & 0 & 0 \\ 0 & 0 & 0 & 0 \end{bmatrix} \quad (5)$$

The cross covariance of this data is

$$\mathbf{r}_{dZ} = \begin{bmatrix} 10000 & 100000 & 0 & 0 \end{bmatrix}^T \quad (6)$$

and the cross correlation is given by

$$\rho_{dZ} = \begin{bmatrix} 0.0995 & 0.9950 & 0 & 0 \end{bmatrix}^T \quad (7)$$

Clearly all three methods will choose identical subspaces and thus have identical performance. Let us now include the effects of background noise, \mathbf{N} , in the orthogonal beams such that $\mathbf{Z} + \mathbf{N}$ is now given as

$$\mathbf{Z} + \mathbf{N} = \begin{bmatrix} 1000.3 & -999.2 & 1001 & -1002 \\ -998 & 1001 & 1002 & -1000.2 \\ -1 & -0.5 & 0.5 & 1 \\ 0.5 & 0.2 & 0.1 & -0.5 \end{bmatrix} \quad (8)$$

The cross covariance for this situation has now become

$$\mathbf{r}_{dZ} = \begin{bmatrix} 10094 & 100038 & -2.5 & 0.75 \end{bmatrix}^T \quad (9)$$

and the cross correlation has changed to

$$\rho_{dZ} = \begin{bmatrix} 0.1004 & 0.9951 & -0.0315 & 0.0201 \end{bmatrix}^T \quad (10)$$

The addition of the background noise has caused some perturbation but not sufficient to cause PCI and CSM to disagree on the singular vector selection. The first MWF basis vector will also have a negligible change since $10094 \gg 2.5$. Let us now introduce a signal level of 100 in the first snapshot such that the signal channel data is given by

$$\mathbf{d} = \begin{bmatrix} 10 & 90 & 110 & -110 \end{bmatrix} \quad (11)$$

The cross covariance has now changed to

$$\mathbf{r}_{dZ} = \begin{bmatrix} 35101 & 75088 & -27.5 & 13.25 \end{bmatrix}^T \quad (12)$$

and the cross correlation has changed to

$$\rho_{dZ} = \begin{bmatrix} 0.3898 & 0.8341 & -0.3865 & 0.3970 \end{bmatrix}^T \quad (13)$$

Recall that the PCI choice of subspace is only determined by the power of each eigenchannel and so is unaffected by

the presence of signal. Although the values of the cross covariance have changed quite a bit, the first two channels are still the dominant values and the two dimensional subspace chosen by the MWF will only slightly be affected. CSM on the other hand has undergone a change in its choice of subspace due to perturbations in the correlation as a result of the signal presence. CSM will now choose channels 2 and 4 as opposed to 1 and 2. Thus one would now expect decreased jammer suppression as well as increased signal cancellation. The fact that the MWF uses the cross covariance, which is a combination of power and correlation makes it less susceptible to perturbation by introduction of signal in a jamming environment.

Consider now the cases when the estimation of the rank is greater than the true rank. The PCI method will choose basis vectors which contain residual power due to errors in the estimation of the true interference subspace but will be unaffected by the presence of signal. The CSM method will continue to choose singular vectors based on the signal perturbed values of the cross correlation. Once the interference is essentially canceled, CSM is choosing the singular vector for which the noise can best be used to cancel signal and thus will suffer a loss of performance. For the MWF, the subspace selection for ranks at or below the interference rank provides good subspace estimation although some perturbation due to signal presence does exist. However, the strength of the interference in the well estimated subspace will dominate the calculation of the weight for that stage. Once the interference has been suppressed, the MWF will then construct the next basis vector from the residual noise in an attempt to cancel out the signal channel. Unlike CSM which can only choose between singular vectors based upon correlation, the MWF utilizes correlation in the construction of the basis vector. The MWF will therefore suffer significant signal cancellation once the rank is overestimated.

3.2. Single Jammer Simulation

Simulations for the same training and test data were run using a signal plus noise to average noise criteria. The signal used was a single snapshot, random phase signal at broadside to the array. Placing the signal only in a single snapshot is done without loss of generality since it does not statistically change the SVD or cross covariance and cross correlation estimates.

A set of 16 signal free snapshots was created and filtered using the PCI, CSM and MWF methods followed by matched filtering in time with a squaring of the output. The signal was then added to this set of snapshots and the filtering process was repeated on the signal plus noise data. The ratio $\frac{(S+N)_{OUT}}{MEAN(N_{OUT})}$ was computed for each method. The first set of simulations is performed with only one jamming signal present near a null at 22 degrees and 20dB JNR as

shown in Figure 2.

The results for PCI and CSM are plotted as scatter plots for varying levels of input SNR in Figure 7. Each dot represents an X-Y plot of the results of two methods to an identical input. The upper left Figure is for the case of no signal. The dots are scattered nearly symmetrically about the diagonal with the two methods rarely producing the same result. There does appear a slight bias of the scattering towards PCI which one would expect since CSM provides the minimum mean squared error. Since the jammer level is 20dB, the PCI choice of basis vector should be nearly constant. Therefore, the disagreement of the methods is a result of the varying CSM choice [4]. Again, from the perspective of mean squared error, the choices are optimum. In the plot at the top right, a signal at 0dB is included in the data. An increase in the shift of the data to the PCI side of the diagonal is evident. Increasing the signal level to 12dB in the lower left, the vast majority of the disagreements between PCI and CSM result in a higher output $\frac{(S+N)_{out}}{MEAN(N_{out})}$ for the PCI method. When the signal level is raised to 24dB, as shown in the lower right plot, essentially all the disagreements of the two methods favors the PCI method.

Scatter plots for PCI and the MWF are plotted in Figure 12. For the cases of no signal and 0dB signal (top left and top right respectively) the two methods produce similar results spread around the diagonal. Recall that since PCI and the MWF construct the basis vectors differently, the agreement along the diagonal would not be exact as in the case of PCI and CSM. When the signal level is increased to 12dB and 24dB (bottom left and bottom right respectively) a slight advantage for the PCI method is created.

In Figure 13 the mean $\left(\frac{S+N}{MEAN(N)}\right)$ is plotted as a function of the signal strength for each method. The three methods are nearly identical at the -6dB signal level but the CSM method begins to show a drop in performance relative to PCI and MWF for signals beginning at 0dB. The difference in the methods holds nearly constant as the signal level is increased past 6dB. The MWF method is slightly below the PCI for larger signal levels although it is difficult to see on the plot.

Let us now examine the performance as a function of rank in Figures 14 and 15. As described earlier, the performance of the MWF drops significantly once the rank is over-estimated. The CSM method shows the performance loss for the correct rank and drops faster than the PCI method when the rank used is above the true rank.

3.3. Multiple Jammers

Now consider a five jammer scenario. The pictograph of the scenario is plotted in Figure 16.

The scatter plots for PCI versus CSM are shown in Figure 21. The plots resemble those of the single jammer case

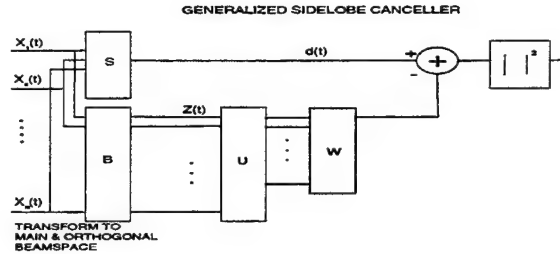


Figure 1: Generalized Sidelobe Canceller Structure

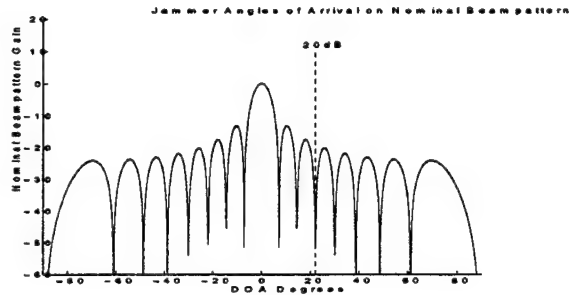


Figure 2: Single Jammer in Null at 20dB JNR

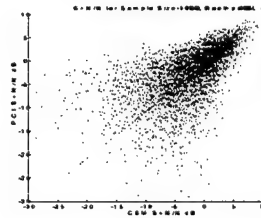


Figure 3: No Signal

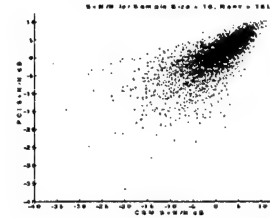


Figure 4: 0dB Signal

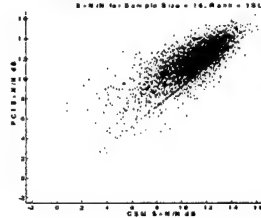


Figure 5: 12dB Signal

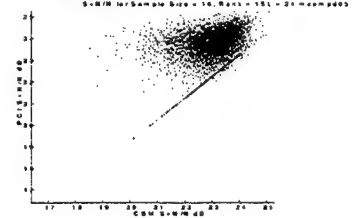


Figure 6: 24dB Signal

Figure 7: PCI Vs CSM $\frac{(S+N)_{out}}{MEAN(N_{out})}$

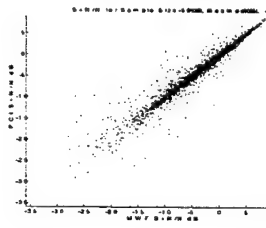


Figure 8: No Signal

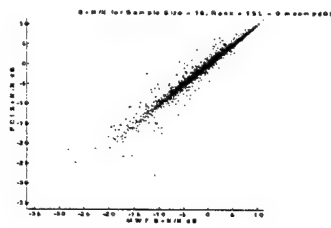


Figure 9: 0dB Signal

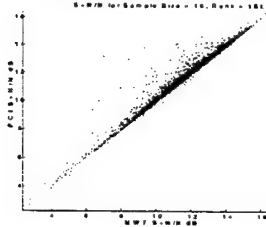


Figure 10: 12dB Signal

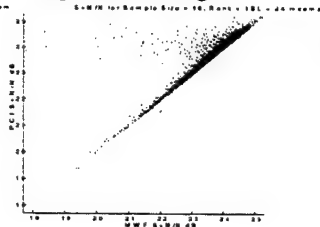


Figure 11: 24dB Signal

Figure 12: PCI Vs MWF $\frac{(S+N)_{out}}{MEAN(N_{out})}$

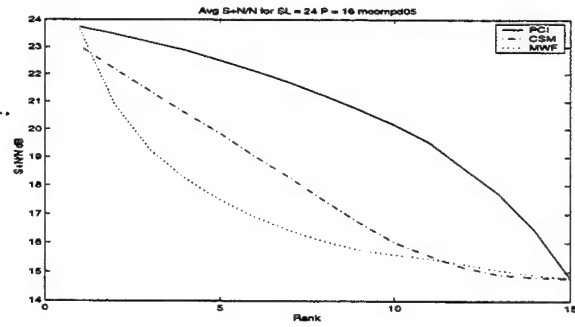


Figure 15: Performance as s Function of Rank for 24dB Signal with Single Jammer

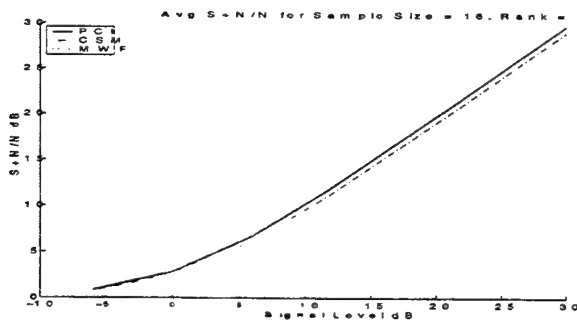


Figure 13: Performance as a Function of Signal Level

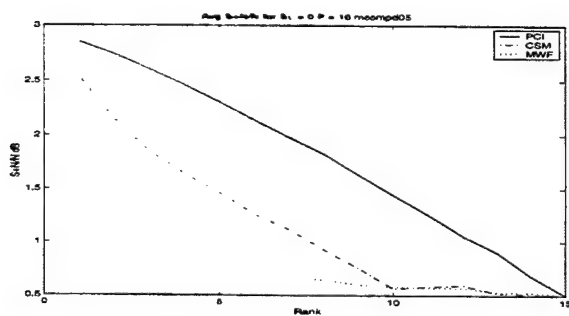


Figure 14: Performance as s Function of Rank for 0dB Signal with Single Jammer

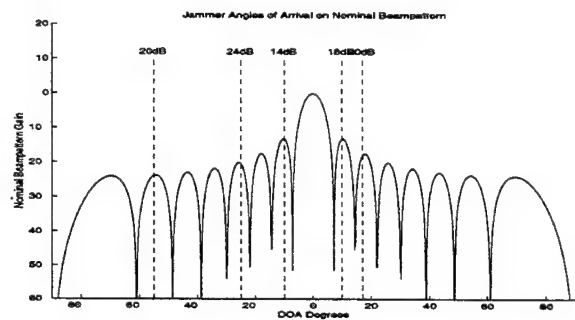


Figure 16: Five Jammer Scenario

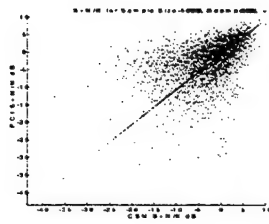


Figure 17: No Signal

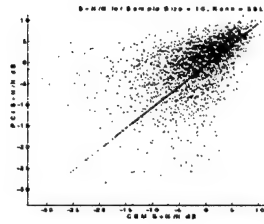


Figure 18: 0dB Signal

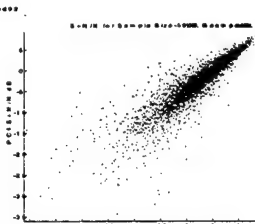


Figure 22: No Signal

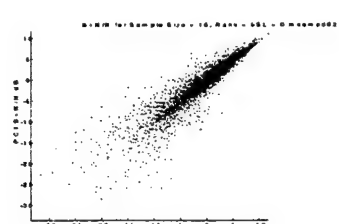


Figure 23: 0dB Signal

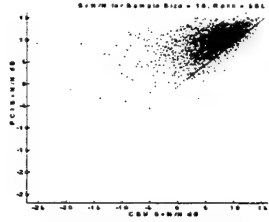


Figure 19: 12dB Signal

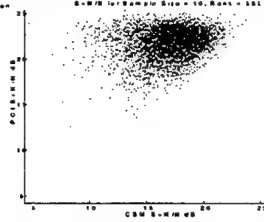


Figure 20: 24dB Signal

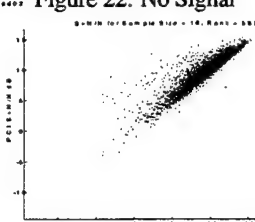


Figure 24: 12dB Signal

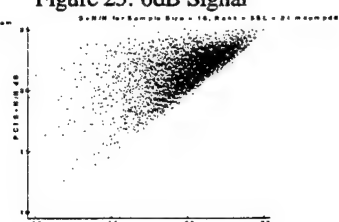


Figure 25: 24dB Signal

Figure 21: PCI Vs CSM $\frac{(S+N)_{out}}{MEAN(N_{out})}$

Figure 26: PCI Vs MWF $\frac{(S+N)_{out}}{MEAN(N_{out})}$

although the performance difference of the two methods has increased. In Figure 26, the scatter plots are shown for PCI verses the MWF. The performance difference between the two methods is now more noticeable for the higher signal level cases than was apparent with the single jammer. This results from the fact that the power levels in the last two or three basis vectors chosen by the MWF are not nearly as strong as the first two or three.

The view of the performance of the five jammer scenario verses signal level is plotted in Figure 27. As before, the CSM method shows a performance loss even for low signal levels. As the signal level is increased, the performance difference also increases as multiple errors in the choice of basis vectors occur. The MWF method agrees well with the PCI method up to a signal level of 6dB at which point the performance of the MWF begins to lag that of PCI. The performance degradation of the MWF grows as the signal level increased.

Turning to the performance verses rank for a 0 dB signal in Figure 28, one first notices that the performance of CSM and the MWF peaks at a rank of 4 as opposed to 5. Estimation of the 5th basis vector is corrupted by signal and better performance results from only using 4 basis vectors. As expected, performance for ranks below the number of jammers is significantly better for the MWF and CSM than the PCI method. However, once the rank is overestimated the performance of the MWF and CSM decrease rapidly for reasons discussed previously. The signal level is increased in Figure 29 to 24dB. Most notable in this plot is the relatively poor performance of the CSM method for all ranks.

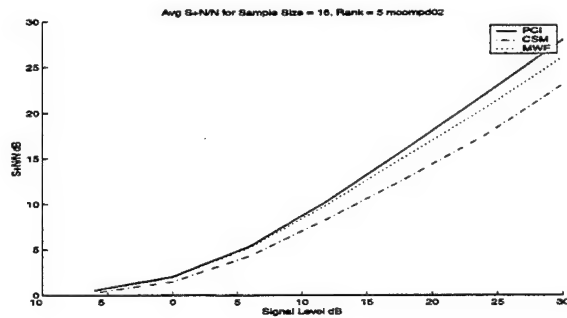


Figure 27: Performance as a Function of Signal Level with 5 Jammers

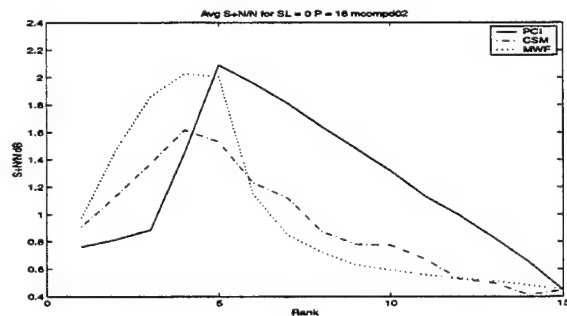


Figure 28: Performance as a Function of Rank for 0dB Signal with 5 Jammers

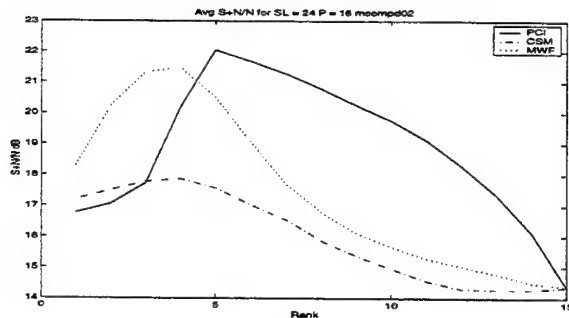


Figure 29: Performance as a function of Rank for 24dB Signal with 5 Jammers

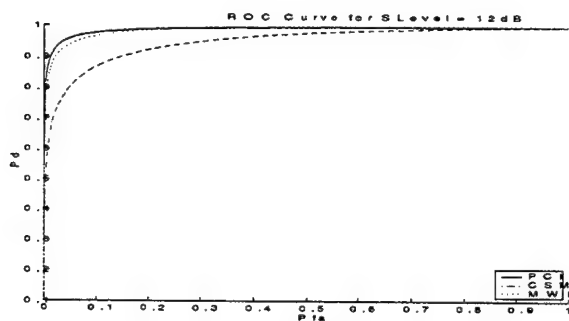


Figure 30: Receiver Operating Characteristic for 12dB Signal

As a final way of looking at the performance of the methods, the Receiver Operating Characteristic (ROC) curves for a 12dB signal level are plotted in Figure 30. The curve was generated using 2^{15} samples. The performance loss of both MWF and CSM is evident.

Overall, the experiments validate the insights that were gained by examining our toy example.

4. CONCLUSIONS

The Cross Spectral Metric (CSM) and the Multistage Wiener Filter (MWF) are two recently introduced alternatives to the Principal Components Inverse (PCI) method of rank reduction for adaptive detection. By gaining insight into the parameters that each method utilizes and the estimation characteristics of those parameters, one can predict how each method will perform under differing scenarios. PCI selects basis vectors by use of an SVD and selects a subspace based upon singular values. The subspace of the SVD is stable under conditions of strong power. CSM selects basis vectors by use of an SVD but then selects a subset based upon correlation with the desired channel. Thus the basis vectors are chosen with respect to power but then a subset is selected by

use of the cross spectral metric. Since singular vectors are not necessarily stable, even though a subspace is, CSM has difficulty since the metric depends upon the singular vectors rather than the entire subspace. The MWF forms and chooses basis vectors based upon the cross covariance with the desired channel which is a combination of power and correlation. By creating scenarios where the estimates of these parameters are similar to those obtained by the background white noise, errors in the selection of the basis vectors can be made to occur. These errors are responsible for decreases in the detection performance of the methods.

5. REFERENCES

- [1] J.S. Goldstein and I.S. Reed, "Theory of partially adaptive radar," *IEEE Transactions on Aerospace and Electronic Systems*, vol. 33, no. 4, pp. 1309-1325, October 1997.
- [2] I.P. Kirsteins and D.W. Tufts, "Rapidly adaptive nulling of interference," in *High Resolution Methods in Underwater Acoustics*, M. Bouvet and G. Bienvenu, Eds. Springer-Verlag, New York, N.Y., 1991.
- [3] Jay Scott Goldstein, *Optimal Reduced-Rank Statistical Signal Processing, Detection and Estimation Theory*, Ph.D. thesis, University of Southern California, 1997.
- [4] B. E. Freburger and D. W. Tufts, "Adaptive detection performance of principal components inverse, cross spectral metric and the partially adaptive multistage wiener filter," in *Proceedings 32nd Asilomar Conference on Signals, Systems and Computers*, Pacific Grove, CA, November 1998.
- [5] Brian E Freburger, *Principal Components Inverse: Comparisons and Applications for Rapidly Adaptive Detection*, Ph.D. thesis, University of Rhode Island, 2000.
- [6] Abhijit A. Shah and Donald W. Tufts, "Determination of the dimension of a signal subspace from short data records," *IEEE Transactions on Signal Processing*, vol. 42, no. 9, pp. 2531-2535, September 1994.

Optimal Target Identification via Adaptive Radar Transmission

David A. Garren, Michael K. Osborn, Anne C. Odom, J. Scott Goldstein
Science Applications International Corporation
4001 Fairfax Drive, Suite 675
Arlington, VA 22203-1303, USA
david.a.garren@saic.com

S. Unnikrishna Pillai
Polytechnic University
Six Metrotech Center
Brooklyn, NY 11201, USA
pillai@hora.poly.edu

Joseph R. Guerci
Defense Advanced Research Projects Agency
Special Projects Office
Arlington, VA 22203, USA
jguerci@darpa.mil

Abstract – This paper investigates the optimization of both single and full polarization radar transmission waveforms to maximize target identification discrimination. This theory is applied to the discrimination of the T-72 and M1 battle tanks based upon simulated target frequency response data. Significant performance improvement in identification is obtained using an optimized transmission waveform over that of a standard chirped pulse.

1 INTRODUCTION

A number of researchers [1, 2, 3, 4, 5, 6, 7] have considered the use of sophisticated pulse shaping techniques in order to maximize the radar energy reflected off of a non-point target. In particular, Grieve, Guerci, Pillai, Oh, and Youla, [1, 2, 3] have developed a general theory of optimized pulse shaping that maximizes the target SINR, including the effects of both generic colored noise and colored signal-dependent clutter. In addition, Guerci and Pillai [8, 9] developed the theory of optimized pulse shaping for single-channel target identification discrimination via the use of techniques that are similar to that used for detection. This paper extends this target discrimination analyses in permitting multiple-channels, colored noise, and non-zero colored clutter.

The present analysis applies the theory of optimized pulse shaping for target identification discrimination using two simulated surface targets: the T-72 and M1 main battle tanks. SAIC-Champaign [10] generated the full-polarization VHF-band radar signatures for a single elevation angle of 15° and the full spectrum 0° – 360° of aspect angles relative to the sensor. These VHF-band data were

generated using the Fast Illinois Solver Code (FISC) that applies a method-of-moments technique to provide high fidelity at relatively low radar frequencies. The specific VHF-band data generated by SAIC-Champaign cover frequencies between 225-375 MHz at an aspect interval of 2°.

2 OPTIMIZED SINGLE-POLARIZATION TARGET IDENTIFICATION

The derivation begins with the result that the maximization of the probability of correct classification between two target classes α and β is equivalent [12, 13] to the maximization of the square of the Mahalanobis distance

$$\eta^2 \equiv (\mathbf{y}_\alpha - \mathbf{y}_\beta)^H \mathbf{R}^{-1} (\mathbf{y}_\alpha - \mathbf{y}_\beta) \quad (1)$$

between the two target echoes. Here, $\mathbf{y}_\alpha = \mathbf{q}_\alpha \mathbf{f}$ and $\mathbf{y}_\beta = \mathbf{q}_\beta \mathbf{f}$ are real-valued vectors of length $2N - 1$ giving the temporal samples of the echoes from targets α and β , respectively. The real-valued vector $\mathbf{f} \equiv [f_0, f_1, \dots, f_{N-1}]^T$ gives the temporal samples of the transmission pulse. The real-valued matrices \mathbf{q}_α and \mathbf{q}_β are the convolution impulse responses for targets α and β , respectively, having the form

$$\mathbf{q} = \begin{pmatrix} q_0 & 0 & \dots & 0 \\ q_1 & q_0 & \dots & 0 \\ \vdots & \vdots & \ddots & \vdots \\ q_{N-1} & q_{N-2} & \dots & q_0 \\ 0 & q_{N-1} & \dots & q_1 \\ \vdots & \vdots & \ddots & \vdots \\ 0 & 0 & \dots & q_{N-1} \end{pmatrix} \quad (2)$$

The $(2N - 1) \times (2N - 1)$ Hermitian-Toeplitz matrix

$$\mathbf{R} = \begin{pmatrix} r_0 & r_1 & \cdots & r_{2N-2} \\ r_1^* & r_0 & \cdots & r_{2N-3} \\ \vdots & \vdots & \ddots & \vdots \\ r_{2N-2}^* & r_{2N-3}^* & \cdots & r_0 \end{pmatrix} \quad (3)$$

is the temporal autocorrelation of the noise plus clutter, with matrix coefficients

$$r_\ell \equiv \frac{1}{2\pi} \int_{-\pi}^{\pi} \{G_n(\omega) + G_c(\omega)|F(\omega)|^2\} e^{j\ell\omega} d\omega. \quad (4)$$

Thus, η^2 can be expressed in the form

$$\eta^2 = \mathbf{f}^H \Omega \mathbf{f}, \quad (5)$$

with the matrix Ω defined by

$$\Omega \equiv (\mathbf{q}_\alpha - \mathbf{q}_\beta)^H \mathbf{R}^{-1} (\mathbf{q}_\alpha - \mathbf{q}_\beta). \quad (6)$$

For the case of zero clutter $G_c(\omega) = 0$, the minimax theorem implies that the maximization of η^2 is obtained when the transmission pulse vector \mathbf{f} is equal to the eigenvector of Ω corresponding to the largest eigenvalue.

For the case of non-zero clutter $G_c(\omega) \neq 0$, the autocorrelation matrix \mathbf{R} depends upon the power spectrum $|F(\omega)|^2$ of the transmission pulse vector \mathbf{f} via Eqs. (3) and (4), so that an iterative procedure similar to that used for optimized target detection [2] must be applied, as described below:

- 1) For the initialization $k = 0$, begin with any real causal temporal vector \mathbf{f}_0 of duration t_0 and energy E_0 .
- 2) Let $\mathbf{f}_k \leftrightarrow F_k(\omega)$ and find the corresponding temporal autocorrelation matrix \mathbf{R}_k using Eqs. (3) and (4).
- 3) Compute the Ω_k matrix using Eq. (6) in terms of the autocorrelation matrix \mathbf{R}_k and the target impulse response matrix \mathbf{q} .
- 4) Find the largest eigenvalue $\lambda_1^{(k)}$ and corresponding normalized eigenvector $\mathbf{v}_1^{(k)}$ of the Ω_k matrix.
- 5) Define the error at stage k by

$$\epsilon_k = \sqrt{2\sqrt{E_0}(\sqrt{E_0} - \mathbf{f}_k^H \mathbf{v}_1^{(k)})}, \quad (7)$$

and invoke the same update rule that is applied in Pillai and Guerci [2]

$$\mathbf{f}_{k+1} = \frac{\mathbf{f}_k + \epsilon_k \mathbf{v}_1^{(k)}}{\sqrt{\left(1 + \frac{\epsilon_k}{\sqrt{E_0}}\right)^2 - \left(\frac{\epsilon_k}{\sqrt{E_0}}\right)^3}}. \quad (8)$$

- 6) Let $\mathbf{f}_{k+1} \leftrightarrow F_{k+1}(\omega)$ and go back to Step 2 with k replaced by $k + 1$, and repeat until ϵ_k is sufficiently small. Then the optimized transmission vector is

$$\mathbf{f} = \lim_{k \rightarrow \infty} \mathbf{f}_k. \quad (9)$$

Figure 1 gives the improvement in the square of the Mahalanobis distance squared between the T-72 and the M1 at VHF-band resulting from the use of the optimized transmission pulse over that of a standard chirped pulse. This figure shows two values of the CNR: 0 and 10. The improvement in the square of the Mahalanobis distance degrades as the CNR level is increased, as occurs with the SINR improvement in the detection problem [2].

For the case of aspect uncertainty, it is necessary to compute the expected value of the square of the Mahalanobis distance, i.e.,

$$\overline{\eta^2} = \int d\theta \xi(\theta) \eta^2(\theta) = \int d\theta \xi(\theta) \mathbf{f}^H \Omega(\theta) \mathbf{f}, \quad (10)$$

with the density function $\xi(\theta)$ characterizing the *a priori* likelihood of the target aspect θ . The matrix $\Omega(\theta)$ now includes aspect dependence, i.e.,

$$\Omega(\theta) = (\mathbf{w}_\alpha(\theta) - \mathbf{w}_\beta(\theta))^H \mathbf{R}^{-1} (\mathbf{w}_\alpha(\theta) - \mathbf{w}_\beta(\theta)). \quad (11)$$

Inserting Eq. (11) into Eq. (10) implies that

$$\overline{\eta^2} = \mathbf{f}^H \overline{\Omega} \mathbf{f}. \quad (12)$$

can be expressed in terms of

$$\overline{\Omega} = \int d\theta \xi(\theta) \Omega(\theta). \quad (13)$$

Thus, optimization of the transmission waveform to maximize identification performance under conditions of aspect uncertainty involves the computation of the weighted average of $\Omega(\theta)$ matrices with respect to aspect. Furthermore, the iterative procedure described above for the case of non-zero clutter is modified only by the replacement of the Ω matrix by its weighted average $\overline{\Omega}$.

3 OPTIMIZED FULL-POLARIZATION TARGET IDENTIFICATION

This section describes the theory of optimal waveform transmission and reception in order to maximize the Mahalanobis distance between two target echoes for the case of a single full-polarization waveform, i.e., one containing both horizontal and vertical components. Consider the $2N$ -length real-valued transmission signal vector and corresponding frequency response vector

$$\mathbf{f} \equiv \begin{pmatrix} \mathbf{f}_h \\ \mathbf{f}_v \end{pmatrix} \leftrightarrow \mathbf{F} \equiv \begin{pmatrix} \mathbf{F}_h \\ \mathbf{F}_v \end{pmatrix}, \quad (14)$$

with \mathbf{f}_h , \mathbf{f}_v , \mathbf{F}_h and \mathbf{F}_v each containing N temporal samples. The subscripts h and v denote the horizontal and vertical channels, respectively. This transmit vector is further constrained to have finite energy E_0 . This energy constraint corresponds to the case in which the sum of the transmission energies in both the horizontal and vertical channels are fixed, so that a single power supply supports both transmission channels. The $2N \times 2N$ target impulse response matrix and corresponding frequency response matrix have the form

$$\mathbf{q} = \begin{pmatrix} \mathbf{q}_{hh} & \mathbf{q}_{hv} \\ \mathbf{q}_{vh} & \mathbf{q}_{vv} \end{pmatrix} \leftrightarrow \mathbf{Q} \equiv \begin{pmatrix} \mathbf{Q}_{hh} & \mathbf{Q}_{hv} \\ \mathbf{Q}_{vh} & \mathbf{Q}_{vv} \end{pmatrix}. \quad (15)$$

The target echo vector has the form

$$\mathbf{s} \equiv \begin{pmatrix} s_h \\ s_v \end{pmatrix} = \mathbf{q}\mathbf{f}. \quad (16)$$

The full-polarization matrix

$$\mathbf{R} = \begin{pmatrix} \mathbf{r}_0 & \mathbf{r}_1 & \cdots & \mathbf{r}_{N-1} \\ \mathbf{r}_1^* & \mathbf{r}_0 & \cdots & \mathbf{r}_{N-2} \\ \vdots & \vdots & \ddots & \vdots \\ \mathbf{r}_{N-1}^* & \mathbf{r}_{N-2}^* & \cdots & \mathbf{r}_0 \end{pmatrix} \quad (17)$$

is the temporal autocorrelation of the noise plus clutter, with the 2×2 sub-matrix coefficients

$$\mathbf{r}_\ell \equiv \frac{1}{2\pi} \int_{-\pi}^{\pi} \{ \mathbf{G}_n(\omega) + \mathbf{G}_F(\omega) \} e^{j\ell\omega} d\omega. \quad (18)$$

The matrices $\mathbf{G}_n(\omega)$ and $\mathbf{G}_F(\omega)$ are the full-polarization spectral densities corresponding to the noise and the clutter, respectively. The total clutter power spectral density has the form

$$\mathbf{G}_F(\omega) \equiv \mathbf{G}_{hh}(\omega)|F_h(\omega)|^2 + \mathbf{G}_{hv}(\omega)F_h(\omega)F_v^*(\omega) \quad (19)$$

$$+ \mathbf{G}_{vh}(\omega)F_v(\omega)F_h^*(\omega) + \mathbf{G}_{vv}(\omega)|F_v(\omega)|^2 > 0 \quad (20)$$

The optimization of the transmission vector \mathbf{f} in order to maximize the square of the full-polarization Mahalanobis distance gives

$$\eta^2 = \max_{\mathbf{f}} \mathbf{f}^H \Omega \mathbf{f}. \quad (21)$$

with the matrix Ω defined by

$$\Omega \equiv \{ \mathbf{q}_\alpha - \mathbf{q}_\beta \}^H \mathbf{R}^{-1} \{ \mathbf{q}_\alpha - \mathbf{q}_\beta \}. \quad (22)$$

For the case of zero clutter $\mathbf{G}_c(\omega) = 0$, the minimax theorem implies that the maximization of η^2 is obtained when the transmission pulse vector \mathbf{f} is equal to the eigenvector of Ω corresponding to the largest eigenvalue. For the case of non-zero clutter $\mathbf{G}_c(\omega) \neq 0$, the autocorrelation matrix \mathbf{R} depends upon the full-polarization power spectrum of the transmission pulse vector \mathbf{f} via Eq. (20), so that the iterative

procedure described for single-polarization above must be applied.

Figure 2 gives the full-polarization waveforms optimized to maximize the Mahalanobis distance between the T-72 and the M1, as a function of the relative aspect angle for the case of white noise and zero clutter. The optimized waveform typically focuses the majority of its energy into a narrow frequency band corresponding to the maximum target response at that aspect angle. Figure 3 demonstrates that the optimized full-polarization waveform gives an improvement of 1.5 dB in the Mahalanobis distance over that obtained from the transmission of a full-polarization chirped waveform.

The analysis described above for the case of aspect certainty can be extended to the case of aspect uncertainty in a manner similar to that performed for the single-polarization case. The resulting theory requires a weighted-average with respect to relative aspect angle be performed on the autocorrelation kernel matrix Ω . This averaging of the full-polarization kernel matrices yields a smoothing of the Mahalanobis curves, as was obtained in the single-polarization case.

4 CONCLUSION

This study investigates the optimization of a single transmission pulse shape and the receiver impulse response in order to maximize the probability of correct identification between two target classes. The optimization of the transmission pulse shaping in order to maximize target identification performance that was developed by Guerri and Pillai [9] is extended to include multiple channels, colored noise, and non-zero colored clutter. These extensions [11] for the identification problem are developed via a maximization of the Mahalanobis distance, and thus the probability of correct classification, between the echoes of two target classes.

This study applies this theory [9] and extensions of optimized transmission pulse shaping in order to investigate the maximization of the probability of correct identification. Algorithmic implementation for the simulated T-72 and M1 frequency response data at both single and multiple polarizations of the VHF frequency band reveals significant improvements in the Mahalanobis distance of using a single optimized waveform over that of a standard chirped pulse.

5 ACKNOWLEDGMENTS

The authors gratefully acknowledge the assistance of Dennis J. Andersh and John T. Moore of SAIC-Champaign in providing the VHF-band and X-band frequency response data of the T-72 and M1 main battle tanks. In addition, the authors would like to thank Iram Weinstein, Jeffrey Wilcox,

Steven Huang, Matthew Weippert, and Chee-Yee Chong for useful suggestions.

References

- [1] P. G. Grieve and J. R. Guerci, "Optimum Matched Illumination-Reception Radar," U.S. Patent S517552, Filed: 18 June 1991, Issued: 29 December 1992.
- [2] S. U. Pillai, H. S. Oh, D. C. Youla, and J. R. Guerci, "Optimum Transmit-Receiver Design in the Presence of Signal-Dependent Interference and Channel Noise," *IEEE Transactions on Information Theory*, Vol. 46, No. 2, March 2000.
- [3] S. U. Pillai, H. S. Oh, and J. R. Guerci, "Multichannel Matched Transmit-Receiver Design in Presence of Signal-Dependent Interference and Noise," *Proceedings of the First IEEE Sensor Array and Multichannel Signal Processing Workshop*, 16-17 March 2000, Cambridge, MA.
- [4] D. T. Gjessing, "Target Adaptive Matched Illumination Radar Principles and Applications," IEE Electromagnetic Waves Series (22), Peter Peregrinus Ltd., 1986.
- [5] A. Farina and F. A. Studer, "Detection with High Resolution Radar: Great Promise, Big Challenge," *Microwave Journal*, pp. 263-273, May 1991.
- [6] I. J. LaHaie, R. O. Harger, S. R. Robinson, J. K. Miller, "An Evaluation of Nonsinusoidal Radar Techniques," Final Report, AD-A171-484, ERIM, Ann Arbor, MI, June 1985.
- [7] H. H. Schrieber and M. G. O'Conner, "Adaptive Waveform Radar," U.S. Patent 4,901,082, February 1990.
- [8] J. R. Guerci, "Optimum Matched Illumination-Reception Radar for Target Classification," U.S. Patent S5381154, Filed: 3 September 1993, Issued: 10 January 1995.
- [9] J. R. Guerci, and S. Pillai, Unnikrishna, "Theory and Application of Optimum Transmit-Receive Radar," *Proceedings of the IEEE International Radar Conference*, 07-12 May 2000, Alexandria, VA, p. 705.
- [10] D. Andersh, J. Moore, S. Kosanovich, D. Kapp, R. Bhalla, R. Kipp, T. Courtney, A. Nolan, F. German, J. Cook, and J. Hughes, "XPatch4: The Next Generation in High Frequency Electromagnetic Modeling and Simulation Software," *IEEE 2000 International Radar Conference*, 07-12 May 2000, Alexandria, VA, pp. 844-9.
- [11] D. A. Garren, M. K. Osborn, A. C. Odom, J. S. Goldstein, S. U. Pillai, and J. R. Guerci, "Optimization of Single Transmit Pulse Shape to Maximize Detection and Identification of Ground Mobile Targets," to appear in *Proceedings of 34th Asilomar Conference on Signals, Systems, and Computers*, Pacific Grove, CA, 29 October - 01 November, 2000.
- [12] H. L. Van Trees, *Detection, Estimation, and Modulation Theory: Part I*, New York: Wiley, 1968.
- [13] C.-Y. Chong, private communication.

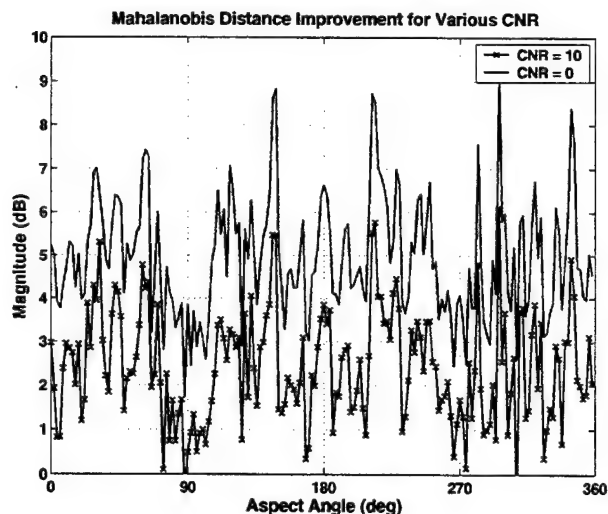


Figure 1. This plot presents the Mahalanobis distance improvement at VHF-band with respect to a chirped transmission waveform resulting from use of a transmission pulse shape optimized for T-72 versus M1 identification discrimination. The two curves corresponding to $\text{CNR} = 1$ and $\text{CNR} = 10$ are plotted as a function of aspect for $0^\circ - 360^\circ$.

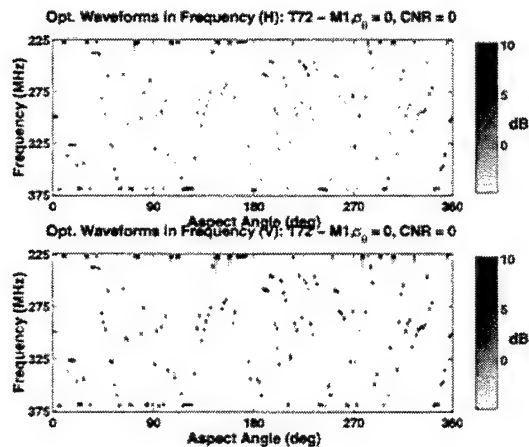


Figure 2. This figure gives the full-polarization waveforms optimized to maximize the Mahalanobis distance between the T-72 and the M1, as a function of the relative aspect angle for the case of white noise and zero clutter. The optimized waveform typically focuses the majority of its energy into a narrow frequency band corresponding to the maximum target response at that aspect angle.

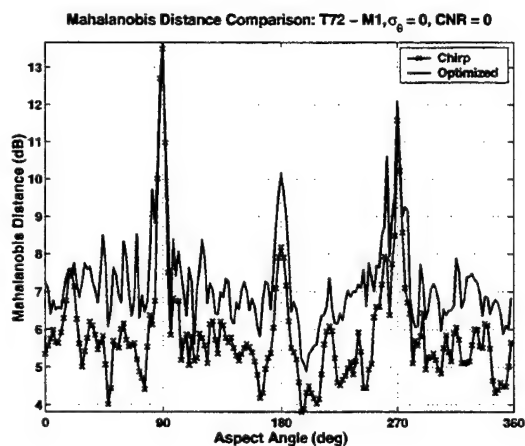


Figure 3. This figure demonstrates that the optimized full-polarization waveform gives an improvement of 1-5 dB in the Mahalanobis distance over that obtained from the transmission of a full-polarization chirped waveform.

CONSTRAINED MAXIMUM-LIKELIHOOD COVARIANCE ESTIMATION FOR TIME-VARYING SENSOR ARRAYS

David W. Rieken and Daniel R. Fuhrmann

Electronic Systems and Signals Research Laboratory
Department of Electrical Engineering
Washington University in St. Louis
St. Louis, MO 63130
riecken@essrl.wustl.edu, danf@essrl.wustl.edu

ABSTRACT

We examine the problem of maximum likelihood covariance estimation using a sensor array in which the relative positions of individual sensors change over the observation interval. The problem is cast as one of estimating a structured covariance matrix sequence. A vector space structure is imposed on such sequences, and within that vector space we define a constraint space given by the intersection of a hyperplane W_1 and the space of sequences of nonnegative definite matrices W_2 . Knowledge of the changing array geometry is used to reduce the dimension of the search space. An extension of the inverse iteration algorithm of Burg et al. is proposed for finding the maximum likelihood solution.

1. INTRODUCTION

In many array signal processing applications knowledge of the observation covariance matrix is essential. Examples of such applications include MVDR beamforming and direction of arrival estimation using MUSIC. Many algorithms for estimating the covariance matrix are available. Perhaps the simplest and at the same time most common is given by

$$\hat{\mathbf{R}} = \frac{1}{M} \sum_{m=1}^M \mathbf{x}_m \mathbf{x}_m^H \quad (1)$$

which is the maximum-likelihood estimate given identical, independent, zero-mean random vectors \mathbf{x}_m with covariance \mathbf{R} . Other estimators incorporate information about the array geometry. These are commonly called structured covariance estimators and were introduced in [1].

When the array changes shape significantly over an observation interval the statistics of the data vectors change, however. This invalidates the identical distribution assumption used to obtain (1) and the assumptions of most structured covariance estimation algorithms. The phenomenon

This research was funded by a grant from MIT Lincoln Laboratory.

of time-varying arrays of sensors exists in nearly all array applications. (No array is truly time-invariant, although they may be close enough to achieve the desired performance.) The effect is exaggerated, though, in towed sonar arrays which are subject to underwater currents and the maneuvering of their parent platform. An array of sensors in which each sensor is mounted on a different platform with its own propulsion also constitutes a time-varying array.

Direction-of-arrival and spectrum estimation for time-varying arrays has been addressed by a number of authors. Direction-of-arrival estimation was addressed in [2] and [3]. Fast algorithms for doing the same which are based on the eigenstructure of the matrix are presented in [4]. In [5] the EM algorithm is used to estimate the power of far-field sources using a time-varying array.

In this paper we address the problem of maximum likelihood (ML) covariance estimation for time-varying arrays. We proceed by defining a mathematical infrastructure and applying commonly used linear algebra techniques. We then propose several search algorithms to find the covariance that maximizes the likelihood under several constraints imposed by the array motion. What results may be considered a time-varying structured covariance estimation algorithm.

2. DEFINITIONS

Let N be the number of elements in the array and $\mathbf{p}_n(t) \in \mathbb{R}^3$ be the position of the n th element at time t . Let M denote the number of data vectors sampled by the array at times $\{t_1, t_2, \dots, t_M\}$ with sampling frequency F_s . The m th data vector we represent by \mathbf{x}_m which is a normally distributed complex random variable with mean $\mathbf{0}$ and covariance $\mathbf{R}(t_m) = \mathbf{R}_m$. The time-varying nature of the array implies that \mathbf{R}_m need not equal \mathbf{R}_{m+1} . The problem is therefore to estimate \mathbf{R}_m for $m = 1, \dots, M$.

We make two assumptions regarding the available infor-

mation. First, the $N \times 1$ steering vector $\mathbf{a}(\Theta, t)$ is known for all t_m and for all $\Theta \in S^2$. The n th element of the steering vector is given by

$$\mathbf{a}_n(\Theta, t) = \exp \left[-\frac{\mathbf{k}^T(\Theta) \mathbf{p}_n(t)}{\lambda} \right] \quad (2)$$

where $\mathbf{k}(\Theta)$ is the unit vector associated with the direction Θ . Secondly, the signal originating at any direction is uncorrelated with signals originating at other directions. Also, the sampling rate is such that the sampled signals are independent random variables. The time-varying covariance matrix is then given by

$$\mathbf{R}_m = \int_{S^2} \sigma^2(\Theta) \mathbf{a}(\Theta, t_m) \mathbf{a}^H(\Theta, t_m) d\Theta \quad (3)$$

where $\sigma^2(\Theta) d\Theta$ is the time-invariant power of the differential emitter at location Θ .

Since we are interested in a sequence of Hermitian matrices let us introduce the following notation:

Definition 1 For positive integers N and M , let $V_{N,M}$ be a space such that $\bar{\mathbf{X}} \in V_{N,M}$ implies that $\bar{\mathbf{X}} \equiv [\mathbf{X}_1, \dots, \mathbf{X}_M]$ where $\mathbf{X}_m \in C^{N \times N}$ and $\mathbf{X}_m^H = \mathbf{X}_m$.

Observe that we denote elements of this space by capital, bold-faced letters with an overbar and the m th element of the sequence by the same letter with a subscript. For some $\alpha \in R$ and $\bar{\mathbf{X}} \in V_{N,M}$ we define scalar multiplication as

$$\alpha \bar{\mathbf{X}} \equiv [\alpha \mathbf{X}_1, \dots, \alpha \mathbf{X}_M]. \quad (4)$$

Similarly, addition is defined element-wise, that is for $\bar{\mathbf{X}}, \bar{\mathbf{Y}} \in V_{N,M}$

$$\bar{\mathbf{X}} + \bar{\mathbf{Y}} \equiv [\mathbf{X}_1 + \mathbf{Y}_1, \dots, \mathbf{X}_M + \mathbf{Y}_M]. \quad (5)$$

It is easy to see that under these operations $V_{N,M}$ is a vector space over R . For notational convenience we also define the following operations on vectors:

$$\bar{\mathbf{X}} \bar{\mathbf{Y}} \equiv [\mathbf{X}_1 \mathbf{Y}_1, \dots, \mathbf{X}_M \mathbf{Y}_M] \quad (6)$$

$$\bar{\mathbf{X}}^{-1} \equiv [\mathbf{X}_1^{-1}, \dots, \mathbf{X}_M^{-1}]. \quad (7)$$

Notice that under vector addition as defined in (5) and using (6) as vector multiplication, $V_{N,M}$ forms a non-commutative ring. The multiplicative identity is then the length- M sequence of $N \times N$ identity matrices and (7) is the multiplicative inverse of $\bar{\mathbf{X}}$. With this in mind, it would be appropriate to refer to (6) and (7) as multiplication and inversion respectively.

Definition 2 $\forall \bar{\mathbf{X}}, \bar{\mathbf{Y}} \in V_{N,M}$ let

$$\langle \bar{\mathbf{X}}, \bar{\mathbf{Y}} \rangle \equiv \sum_{m=1}^M \text{tr}(\mathbf{X}_m^H \mathbf{Y}_m).$$

We claim that this is an inner product on $V_{N,M}$. This is a result of the following facts which are easily proved for all $\alpha \in R$ and $\bar{\mathbf{X}}, \bar{\mathbf{Y}}, \bar{\mathbf{Z}} \in V_{N,M}$:

$$\langle \bar{\mathbf{X}}, \bar{\mathbf{Y}} \rangle \in R$$

$$\langle \bar{\mathbf{X}} + \bar{\mathbf{Y}}, \bar{\mathbf{Z}} \rangle = \langle \bar{\mathbf{X}}, \bar{\mathbf{Z}} \rangle + \langle \bar{\mathbf{Y}}, \bar{\mathbf{Z}} \rangle$$

$$\langle \alpha \bar{\mathbf{X}}, \bar{\mathbf{Y}} \rangle = \alpha \langle \bar{\mathbf{X}}, \bar{\mathbf{Y}} \rangle$$

$$\langle \bar{\mathbf{X}}, \bar{\mathbf{Y}} \rangle = \langle \bar{\mathbf{Y}}, \bar{\mathbf{X}} \rangle$$

$$\langle \bar{\mathbf{X}}, \bar{\mathbf{X}} \rangle \geq 0 \text{ with equality iff } \bar{\mathbf{X}} = [\mathbf{0}, \dots, \mathbf{0}]$$

Therefore $(V_{N,M}, \langle \cdot, \cdot \rangle)$ is an inner product space.

The covariance matrix sequence is an element, $\bar{\mathbf{R}}$, of $V_{N,M}$. With this in mind we can rewrite (3) as

$$\bar{\mathbf{R}} = \int_{S^2} \sigma^2(\Theta) \bar{\Psi}(\Theta) d\Theta \quad (8)$$

where

$$\bar{\Psi}(\Theta) = \{\mathbf{a}(\Theta, t_1) \mathbf{a}^H(\Theta, t_1), \dots, \mathbf{a}(\Theta, t_M) \mathbf{a}^H(\Theta, t_M)\}.$$

The span of $\bar{\Psi}(\Theta)$ over all $\Theta \in S^2$ is a vector subspace of $V_{N,M}$. We will call this subspace W_1 . It is clear from (8) that $\bar{\mathbf{R}} \in W_1$. Being a vector space, W_1 is convex and therefore path-connected. Furthermore, there exists an orthonormal basis for W_1 . We will let $W_2 \in V_{N,M}$ be the space of all length- M sequences of non-negative definite Hermitian matrices. Since any covariance matrix is non-negative definite, $\bar{\mathbf{R}} \in W_2$. It can be shown that W_2 is also convex. Since the desired sequence lies within both subspaces the constraint space is their intersection $W \equiv W_1 \cap W_2$. As the intersection of two convex sets, W is also convex.

We remark that the set of matrix sequences W may not coincide exactly with the space of matrix sequences given by the model in (3), although as has been shown the latter is a subset of W . Our constraint space may contain elements outside of the cone described by (3). The discrepancy between the two spaces, and the consequences thereof, remain open questions.

We will now derive the log-likelihood function of the covariance matrix sequence for the given data set. The pdf of the data vectors is defined only for the interior of W_2 :

$$f(\mathbf{x}_1, \dots, \mathbf{x}_M) = \pi^{-NM} \left(\prod_{m=1}^M |\mathbf{R}_m|^{-1} \right) \times \exp \left(- \sum_{m=1}^M \mathbf{x}_m^H \mathbf{R}_m^{-1} \mathbf{x}_m \right). \quad (9)$$

The log-likelihood is then

$$\begin{aligned} l(\bar{\mathbf{R}}) &= - \sum_{m=1}^M \ln |\mathbf{R}_m| - \sum_{m=1}^M \text{tr}(\mathbf{x}_m^H \mathbf{R}_m^{-1} \mathbf{x}_m) \\ &= - \sum_{m=1}^M \ln |\mathbf{R}_m| - \sum_{m=1}^M \text{tr}(\mathbf{R}_m^{-1} \mathbf{S}_m) \end{aligned} \quad (10)$$

where we shall call

$$\mathbf{S}_m = \mathbf{x}_m \mathbf{x}_m^H \quad (11)$$

the sample covariance matrix at time t_m . Observe that $\mathbf{S}_m = \mathbf{S}_m^H$ and therefore the length- M sequence of all such matrices, $\bar{\mathbf{S}}$, is an element of $V_{N,M}$. We can use the notation of definition 2 to simplify (10):

$$l(\bar{\mathbf{R}}; \bar{\mathbf{S}}) = - \sum_{m=1}^M \ln |\mathbf{R}_m| - \langle \bar{\mathbf{R}}^{-1}, \bar{\mathbf{S}} \rangle. \quad (12)$$

To find the gradient of the log-likelihood function we will make use of several differentiation theorems found in [1].

Theorem 1 For $\mathbf{R}, \Phi \in C^{N \times N}$,

$$\frac{d}{dx} \ln |\mathbf{R} + x\Phi| = \text{tr}(\mathbf{R}^{-1} \Phi).$$

Theorem 2 For $\mathbf{R}, \mathbf{S}, \Phi \in C^{N \times N}$,

$$\frac{d}{dx} \text{tr}((\mathbf{R} + x\Phi)^{-1} \mathbf{S}) = -\text{tr}(\mathbf{R}^{-1} \Phi \mathbf{R}^{-1} \mathbf{S}).$$

The directional derivative of the log-likelihood along the vector $\bar{\Phi}$ is

$$\begin{aligned} \frac{d}{dx} l(\bar{\mathbf{R}} + x\bar{\Phi}; \bar{\mathbf{S}}) &= - \frac{d}{dx} \sum_{m=1}^M \ln |\mathbf{R}_m + x\Phi_m| \\ &\quad + \text{tr}((\mathbf{R}_m + x\Phi_m)^{-1} \mathbf{S}_m) \\ &= - \sum_{m=1}^M \text{tr}(\mathbf{R}_m^{-1} \Phi_m) - \text{tr}(\mathbf{R}_m^{-1} \Phi_m \mathbf{R}_m^{-1} \mathbf{S}_m) \\ &= - \sum_{m=1}^M \text{tr}(\mathbf{R}_m^{-1} \Phi_m - \mathbf{R}_m^{-1} \mathbf{S}_m \mathbf{R}_m^{-1} \Phi_m) \\ &= - \sum_{m=1}^M \text{tr}((\mathbf{R}_m^{-1} - \mathbf{R}_m^{-1} \mathbf{S}_m \mathbf{R}_m^{-1}) \Phi_m) \\ &= \langle \bar{\mathbf{R}}^{-1} \bar{\mathbf{S}} \bar{\mathbf{R}}^{-1} - \bar{\mathbf{R}}^{-1}, \bar{\Phi} \rangle. \end{aligned} \quad (13)$$

Therefore the gradient of the log-likelihood function is given by

$$\nabla l(\bar{\mathbf{R}}, \bar{\mathbf{S}}) = \bar{\mathbf{R}}^{-1} \bar{\mathbf{S}} \bar{\mathbf{R}}^{-1} - \bar{\mathbf{R}}^{-1}. \quad (14)$$

Note the similarity of this expression to the analogous expression for the gradient of the log-likelihood in Burg *et al.* [1]. Here the matrices have been replaced with matrix sequences.

3. ESTIMATION ALGORITHMS

One possible estimator is the projection of the sample covariance matrix sequence, $\bar{\mathbf{S}}$, onto the constraint space W . This is equivalent to selecting the point in W that is the closest to $\bar{\mathbf{S}}$ by the standard distance metric for inner product spaces:

$$d(\bar{\mathbf{X}}, \bar{\mathbf{Y}}) = \langle \bar{\mathbf{X}} - \bar{\mathbf{Y}}, \bar{\mathbf{X}} - \bar{\mathbf{Y}} \rangle^{\frac{1}{2}}. \quad (15)$$

Because of the similarity between this estimator and classic filtering where a signal is projected onto the subspace of all signals which satisfy a certain constraint, we will refer to this estimator as the sample sequence filter. Since W is the intersection of two convex spaces we employ the method of projection onto convex sets (POCS) in which the estimate is first projected onto W_1 and then onto W_2 . This iterative procedure continues until the improvement in likelihood gained with each iteration is negligible. Since W_1 is a vector subspace the projection of a vector $\bar{\mathbf{X}}$ onto W_1 is given by

$$\bar{\mathbf{X}}' = \sum_{l=1}^L \langle \bar{\mathbf{X}}, \bar{\Phi}_l \rangle \bar{\Phi}_l \quad (16)$$

where $\bar{\Phi}_l$ are the members of an orthonormal basis of W_1 and L is the dimension.

Projection onto W_2 for the given inner product is found in [6]. First, the eigendecomposition is determined:

$$\mathbf{X}_m = \Gamma_m \Lambda_m \Gamma_m^{-1} \quad (17)$$

Then the projection onto the set of non-negative definite matrices is given by setting the negative eigenvalues to 0:

$$\mathbf{X}'_m = \Gamma_m \max(\Lambda_m, 0) \Gamma_m^{-1}. \quad (18)$$

The projection of the sequence $\bar{\mathbf{X}}$ onto W_2 is the element-wise projection of each \mathbf{X}_m as described by this equation.

The sample sequence filter, by its definition, finds the sequence which is in the constraint space and the closest to the sample sequence by the distance metric given in (15). Experience has shown, however, that the best estimate is rarely the closest to the sample sequence. We therefore propose searching the constraint space for the maximum likelihood estimate using the filtered sample sequence as a starting point.

Each of the search algorithms which we will consider proceed by calculating a search direction, $\bar{\mathbf{D}} \in W_1$, along

which the likelihood function must be maximized. That is, in each iteration we determine a $\bar{\mathbf{D}}$ and then find λ_0 such that

$$\lambda_0 = \arg \max l(\hat{\mathbf{R}}^{(i)} + \lambda \bar{\mathbf{D}}).$$

The updated estimate is

$$\hat{\mathbf{R}}^{(i+1)} = \hat{\mathbf{R}}^{(i)} + \lambda_0 \bar{\mathbf{D}}.$$

This iterative process should be allowed to continue until the gradient is sufficiently close to being orthogonal to W_1 , that is until

$$\frac{\sum_{i=1}^L \langle \nabla l(\hat{\mathbf{R}}; \bar{\mathbf{S}}), \bar{\Phi}_i \rangle^2}{\langle \nabla l(\hat{\mathbf{R}}; \bar{\mathbf{S}}), \nabla l(\hat{\mathbf{R}}; \bar{\mathbf{S}}) \rangle} < \epsilon. \quad (19)$$

Observe that since l is defined only on the interior of W_2 and $\bar{\mathbf{D}} \in W_1$, the estimate will be within the constraint space at each iteration.

Perhaps the most obvious approach to calculating $\bar{\mathbf{D}}$ is to use the gradient in (14). $\bar{\mathbf{D}}$ can be the projection of the gradient onto W_1 . Alternatively, a conjugate gradient direction can be calculated by incorporating memory of previous search directions. We suggest, however, a modification of the inverse iteration algorithm proposed by Burg, *et al.* in [1]. Burg's algorithm was designed for estimation of a single matrix rather than a sequence of matrices but is easily generalized for sequences. For some estimate $\hat{\mathbf{R}}^{(i)}$ select a search direction, $\bar{\mathbf{D}}$, such that $\nabla l(\hat{\mathbf{R}}^{(i)}; \bar{\mathbf{S}} - \bar{\mathbf{D}})$ is orthogonal to W_1 . Clearly, if $\bar{\mathbf{D}} = 0$ then $\hat{\mathbf{R}}^{(i)}$ is the maximum likelihood estimate since the likelihood gradient is orthogonal to the constraint space at that point.

Before the modified inverse iteration algorithm may be seriously considered, though, one must ask whether a stable point of the algorithm maximizes the likelihood function within the constraint space. That is, does each iteration of the algorithm lead to an improvement in likelihood for a nonzero search direction? The answer is yes, as shown by the following theorem:

Theorem 3 Suppose there exists $\bar{\mathbf{D}} \neq 0 \in W_1$ such that $\nabla l(\bar{\mathbf{R}}; \bar{\mathbf{S}} - \bar{\mathbf{D}})$ is orthogonal to W_1 . Then there exists $\lambda \in \mathbb{R}$, $\lambda \neq 0$, such that $l(\bar{\mathbf{R}} + \lambda \bar{\mathbf{D}}; \bar{\mathbf{S}}) > l(\bar{\mathbf{R}}; \bar{\mathbf{S}})$.

Proof: By way of contradiction, suppose that

$$\arg \max l(\bar{\mathbf{R}} + \lambda \bar{\mathbf{D}}; \bar{\mathbf{S}}) = 0.$$

This implies that $\nabla l(\bar{\mathbf{R}}; \bar{\mathbf{S}})$ is orthogonal to $\bar{\mathbf{D}}$. That is,

$$\langle \nabla l(\bar{\mathbf{R}}; \bar{\mathbf{S}}), \bar{\mathbf{D}} \rangle = 0.$$

Therefore,

$$\begin{aligned} \langle \nabla l(\bar{\mathbf{R}}; \bar{\mathbf{S}} - \bar{\mathbf{D}}), \bar{\mathbf{D}} \rangle &= \langle \bar{\mathbf{R}}^{-1}(\bar{\mathbf{S}} - \bar{\mathbf{D}})\bar{\mathbf{R}}^{-1} - \bar{\mathbf{R}}^{-1}, \bar{\mathbf{D}} \rangle \\ &= \langle \nabla l(\bar{\mathbf{R}}; \bar{\mathbf{S}}) - \bar{\mathbf{R}}^{-1}\bar{\mathbf{D}}\bar{\mathbf{R}}^{-1}, \bar{\mathbf{D}} \rangle \\ &= -\langle \bar{\mathbf{R}}^{-1}\bar{\mathbf{D}}\bar{\mathbf{R}}^{-1}, \bar{\mathbf{D}} \rangle \end{aligned}$$

Since $\bar{\mathbf{D}} \in W_1$ we know that $\langle \nabla l(\bar{\mathbf{R}}; \bar{\mathbf{S}} - \bar{\mathbf{D}}), \bar{\mathbf{D}} \rangle = 0$. Therefore

$$\langle \bar{\mathbf{R}}^{-1}\bar{\mathbf{D}}\bar{\mathbf{R}}^{-1}, \bar{\mathbf{D}} \rangle = 0.$$

It can be shown that this implies that $\bar{\mathbf{R}}_m^{-1}\bar{\mathbf{D}}_m = 0$ for all m . Therefore $\bar{\mathbf{D}}_m = 0$ for all m which is a contradiction. ■

We now concentrate on finding the direction which satisfies the necessary condition on the gradient. This is equivalent to finding $\bar{\mathbf{D}}$ which satisfies

$$\langle \bar{\mathbf{R}}^{-1}(\bar{\mathbf{S}} - \bar{\mathbf{D}})\bar{\mathbf{R}}^{-1} - \bar{\mathbf{R}}^{-1}, \bar{\Phi}_i \rangle = 0 \quad (20)$$

for all i . We note that this is a system of equations which are linear in $\bar{\mathbf{D}}$ and that therefore a closed-form solution exists. Since $\bar{\mathbf{D}} \in W_1$ there exist real α_j such that

$$\bar{\mathbf{D}} = \sum_j \alpha_j \bar{\Phi}_j. \quad (21)$$

Substituting (21) into (20) and rearranging we get

$$\begin{aligned} &\langle \bar{\mathbf{R}}^{-1}(\bar{\mathbf{S}} - \bar{\mathbf{D}})\bar{\mathbf{R}}^{-1} - \bar{\mathbf{R}}^{-1}, \bar{\Phi}_i \rangle \\ &= \langle \bar{\mathbf{R}}^{-1}(\bar{\mathbf{S}} - \sum_j \alpha_j \bar{\Phi}_j)\bar{\mathbf{R}}^{-1} - \bar{\mathbf{R}}^{-1}, \bar{\Phi}_i \rangle \\ &= \langle \nabla l(\bar{\mathbf{R}}; \bar{\mathbf{S}}), \bar{\Phi}_i \rangle - \sum_j \alpha_j \langle \bar{\mathbf{R}}^{-1}\bar{\Phi}_j\bar{\mathbf{R}}^{-1}, \bar{\Phi}_i \rangle. \end{aligned} \quad (22)$$

Therefore we need only find $\alpha \in \mathbb{R}^L$ such that

$$\mathbf{A}\alpha = \mathbf{B} \quad (23)$$

where

$$\mathbf{A}_{ij} = \langle \bar{\mathbf{R}}^{-1}\bar{\Phi}_j\bar{\mathbf{R}}^{-1}, \bar{\Phi}_i \rangle \quad (24)$$

$$\mathbf{B}_i = \langle \nabla l(\bar{\mathbf{R}}; \bar{\mathbf{S}}), \bar{\Phi}_i \rangle. \quad (25)$$

4. COMPUTER SIMULATION

We have simulated a uniform linear array (ULA) consisting of $N = 5$ isotropic sensors which is rotating with rotational velocity ω about the center element. The axis of rotation is orthogonal to the axis of the ULA. There are 3 source fields impinging upon the array which originate at (azimuth, elevation) = $(45^\circ, 0^\circ)$, $(85^\circ, 20^\circ)$, and $(110^\circ, 0^\circ)$. Here azimuth is the angle made with the axis of the array at $t = 0$ and within the plane of rotation. Elevation

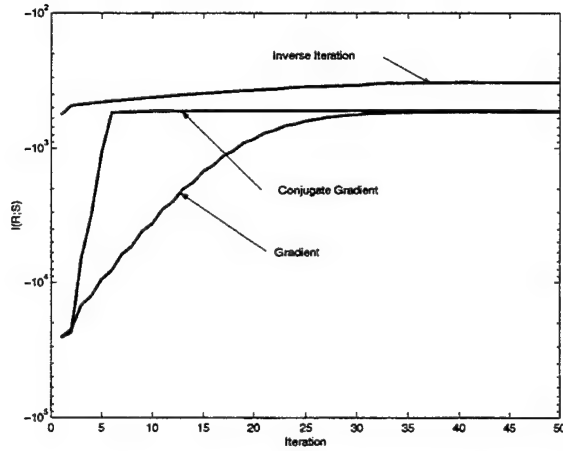


Figure 1: Algorithm convergence rate comparison.

is the angle made with the plane of rotation. For example, $(90^\circ, 10^\circ)$ would describe a direction orthogonal to the initial array axis and 10° above the plane of rotation. Each of the sources are assumed to be narrowband with wavelength λ and the separation between elements in the ULA is $\frac{\lambda}{2}$. The power of each source at the array is 30dB, 15dB, and 20dB respectively. Receiver noise is 0dB. The rotational velocity of the array is $\omega = 2\pi$ rad/sec, the sampling rate is $F_s = 32s^{-1}$, and the number of samples collected is $M = 16$. Therefore, the array gathers 16 data vectors while completing a half rotation. Since the statistics of the data vector change dramatically over this observation interval one expects the covariance estimator in (1) to perform badly. It is unclear even what steering vector to use with this covariance estimate in, for example, an MVDR or MUSIC estimator. That makes this scenario a good candidate for covariance matrix *sequence* estimation.

Each of the algorithms considered begins by calculating the sample covariance matrix sequence and filtering it by the method of POCS using the projections in (16) and (18). The $\bar{\Phi}_l$ are obtained by Gram-Schmidt orthonormalization of the set of vectors $\bar{\Psi}(\Theta)$ where Θ is a discretization of the 2-sphere. For this example, the dimension of W_1 is $L = 76$. Note that the dimension of $V_{N,M}$ is $N^2M = 400$ and we have managed to eliminate 324 parameters of the matrix sequence by applying information about the motion of the array.

The ML search routine follows the filtering. We applied a gradient and conjugate gradient search algorithm in addition to the modified inverse iteration algorithm. The likelihood of the estimate at each iteration is plotted in Figure 1 for each of the algorithms.

Observe that the gradient and conjugate gradient algorithms converge to points with the same likelihood. The

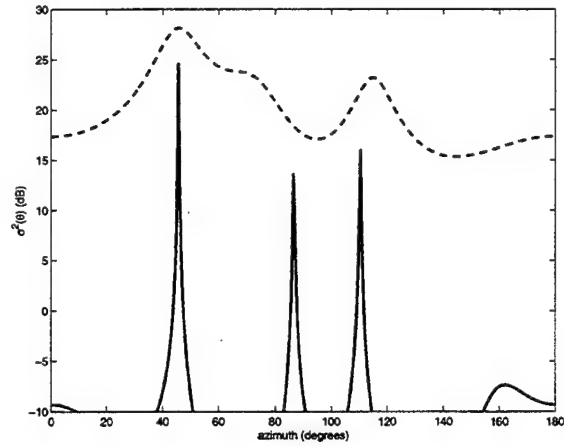


Figure 2: MVDR spectrum estimated from the first matrix in the sequence. The dashed line is that obtained from the sample sequence filtering procedure. The solid line was calculated from the ML sequence.

conjugate gradient reaches this point in fewer iterations, which is to be expected. However, the convergence point of the inverse iteration algorithms exceeds the likelihood of the estimate obtained from either gradient algorithm after only a few iterations. Inspection of the likelihood gradient at what appears to be the convergence point of the gradient algorithms reveals that it is not orthogonal to W_1 and that while successive iterations yield only slight improvement in likelihood, they have failed to reach a local maxima. One possibility is that they have stumbled upon a "ridge" in the likelihood function. It is clear that, in this example at least, the inverse iteration algorithm reaches a solution in fewer iterations than even the conjugate gradient algorithm. It should be noted, however, that finding the solution to (23) requires more computation than calculating the likelihood gradient and projecting it onto W_1 .

To demonstrate the validity of the ML estimate, the MVDR spectrum corresponding to the first matrix in the sequence has been calculated and plotted in Figure 2. The spectrum is calculated using

$$\hat{\sigma}^2(\theta) = \frac{1}{\mathbf{a}^H(\theta, t_1) \hat{\mathbf{R}}_1^{-1} \mathbf{a}(\theta, t_1)}. \quad (26)$$

$\hat{\mathbf{R}}_1$ is the first matrix in the sequence obtained by the inverse iteration algorithm since the other two algorithms failed to produce a maximum likelihood estimate. The position of each of the sources is easily ascertained from the plot as is a feeling for their intensities. Also plotted is the spectrum obtained from just the sample sequence filter. While peaks which correspond to two of the sources can be seen, the third is lost and the background noise is quite high. This

demonstrates the necessity of the ML search algorithms.

5. CONCLUSIONS

We have developed an algorithm for estimating the sequence of matrices which are the covariances of the data vectors of a time-varying sensor array. Since each matrix in the sequence is structured to satisfy (3) this may be classified as a structured covariance estimation algorithm in which the sequence of matrices itself is structured. This method will have good performance for time-varying arrays in which the array motion is periodic, as with the rotating ULA, since the constraint space basis need not be continuously recalculated, which relieves the processor of some of the computational burden. It has been demonstrated that the modified inverse iterations algorithm can converge faster and more reliably than a simple gradient search algorithm, although with increased computational complexity per iteration.

6. REFERENCES

- [1] J. P. Burg, D. G. Luenberger, and D. L. Wenger, "Estimation of structured covariance matrices," *Proc. IEEE*, vol. 70, pp. 963–974, Sept. 1982.
- [2] A. Zeira and B. Friedlander, "Direction finding with time-varying arrays," *IEEE Trans. on Signal Processing*, vol. 43, pp. 927–937, April 1995.
- [3] J. Sheinvald, M. Wax, and A. J. Weiss, "Localization of multiple sources with moving arrays," in *Proc. ICASSP '97*, pp. 3521–3524, 1997.
- [4] B. Friedlander and A. Zeira, "Eigenstructure-based algorithms for direction finding with time-varying arrays," *IEEE Trans. on Aerospace and Electronic Systems*, vol. 32, pp. 689–701, April 1996.
- [5] D. W. Rieken, A. D. Lanterman, and D. R. Fuhrmann, "Spatial spectrum estimation for time-varying arrays using the EM algorithm," in *Proc. of the 38th Ann. Allerton Conf. on Communication, Control, and Computing*, October 2000.
- [6] N. J. Higham, "Computing a nearest symmetric positive semidefinite matrix," *Linear Algebra and Its Applications*, vol. 103, pp. 103–188, May 1988.

RESOLUTION OF MAINLOBE AND SIDELOBE DETECTIONS USING MODEL ORDER DETERMINATION

Amin G. Jaffer, Joe C. Chen, and Thomas W. Miller

Raytheon Electronic Systems
2200 E. Imperial Highway
Los Angeles, California 90009-2426
e-mail: ajaffer@west.raytheon.com

ABSTRACT

This paper presents the development and performance evaluation of a methodology for distinguishing between mainlobe and sidelobe detections that arise in adaptive radar systems operating in adverse environments. Various adaptive detection test statistics such as the adaptive matched filter (AMF), the generalized likelihood ratio test (GLRT) and adaptive coherence estimate (ACE), and combinations of these, have been previously analyzed with respect to their sidelobe rejection capabilities. In contrast to these methods which are based on detecting a single target with known direction and Doppler, the present method uses model order determination techniques applied to the AMF or GLRT data observed over the range of unknown angle and Doppler parameters. The determination of model order, i.e., the number of signals present in the data, is made by using least-squares model fit error residuals and applying the Akaike Information Criterion. Comprehensive computer simulation results are presented which demonstrate substantial improvement in sidelobe rejection performance and detections of multiple sources compared to previous methods.

1. INTRODUCTION

A variety of constant false-alarm rate (CFAR) adaptive detection statistics have been developed and analyzed for radar target detection in adverse environments [1]-[8]. Adaptive beamforming, adaptive filtering and, generally, joint space-time adaptive processing (STAP) methods are being increasingly considered for airborne radar detection of low-Doppler targets immersed in ground clutter and subject to directional noise jamming. An important issue that needs to be considered is the sidelobe performance of these adaptive detection algorithms. "False" sidelobe detections can arise due to undermulated interferences, intrinsically high sidelobes generated by the adaptive beamforming space-time algorithms used with limited data snapshots, and other reasons. This can result in an unacceptably high false alarm rate. Previous works have focused on determining the sidelobe rejection performance of the adaptive matched filter (AMF) test [3],[6], the generalized likelihood ratio test (GLRT) of Kelly [1], the adaptive coherence estimator (ACE) test and a cascade of AMF/ACE test [4] or AMF/GLRT test [8]. It is to be noted that all of these previous methods are based on applying adaptive detection criteria developed for detecting a single target signal with known direction and Doppler in correlated noise. In contrast to this, the present work uses multiple maximum-likelihood model order fits to the AMF or GLRT data

observed over the range of the unknown angle and Doppler parameters. The resulting fit error residuals are used in the Akaike Information Criterion (AIC) to deduce the correct model order and thereby reject "false" sidelobe detections, and improve detection and resolution of multiple sources.

2. MAXIMUM-LIKELIHOOD MODEL ORDER DETERMINATION USING AMF OR GLRT

We begin by considering two well-known adaptive detection methods, AMF and GLRT, as a starting point for our new method described below and also for performance comparison purposes. We consider an N -element array and seek to determine the presence of one or more signals in an observation vector (or snapshot) \mathbf{x} called the test cell. The methodology developed here applies to the general STAP problem where the data vector \mathbf{x} can be a concatenated space-time vector of array element data and coherent pulse samples; however, the computer simulation results presented in section 5 use only simulated spatial array data so our development here will be mainly presented in that context.

Consider then that the AMF [3] and GLRT [1] metrics have been computed as a function of angle (azimuth) and result in the following test:

$$J_{\text{AMF}}(\theta) = \frac{|\mathbf{d}(\theta)^H \hat{\mathbf{R}}^{-1} \mathbf{x}|^2}{\mathbf{d}(\theta)^H \hat{\mathbf{R}}^{-1} \mathbf{d}(\theta)} = \left| \mathbf{w}(\theta)^H \mathbf{x} \right|^2 \underset{H_0}{\overset{H_1}{\geq}} K_{\alpha_{\text{AMF}}}, \quad (1)$$

where $\mathbf{d}(\theta)$ is the signal steering vector for angle θ , i.e., the array response vector, $\hat{\mathbf{R}}$ is the sample covariance matrix of the interference plus noise (whose true covariance matrix is \mathbf{R}), based on an auxiliary set of K data vectors \mathbf{x}_i , $i = 1, \dots, K$ which share the same interference plus noise only covariance matrix with the test data \mathbf{x}

$$\hat{\mathbf{R}} = \frac{1}{K} \sum_{i=1}^K \mathbf{x}_i \mathbf{x}_i^H, \quad (2)$$

and $K_{\alpha_{\text{AMF}}}$ is the threshold which can be determined numerically for a given false alarm P_{FA} . The hypothesis H_1 denotes signal plus noise and the null hypothesis H_0 denotes noise only. An alternate form is shown on the right side of (1) where an array weight vector $\mathbf{w}(\theta)$ can be defined as $\mathbf{w}(\theta) = \hat{\mathbf{R}}^{-1} \mathbf{d}(\theta) / \sqrt{\mathbf{d}(\theta)^H \hat{\mathbf{R}}^{-1} \mathbf{d}(\theta)}$.

Equation (1) represents the adapted array output for the test vector \mathbf{x} normalized by the output interference plus noise power.

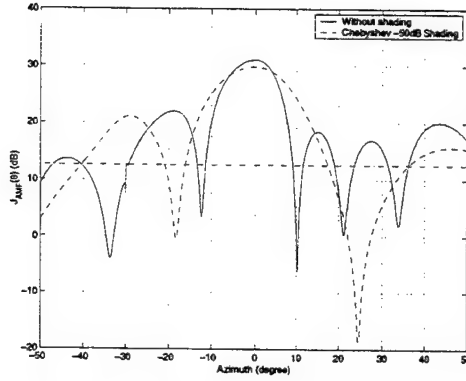


Fig. 1. $J_{AMF}(\theta)$ function for a 20dB signal at broadside, $N = 10$, $K = 100$, $PFA = 10^{-6}$.

In order to control the sidelobe response of the adaptive array, the weight vector $\mathbf{w}(\theta)$ is often computed as $\mathbf{w}(\theta) = \hat{\mathbf{R}}^{-1} \mathbf{d}_{sh}(\theta) / \sqrt{\mathbf{d}_{sh}(\theta)^H \hat{\mathbf{R}}^{-1} \mathbf{d}_{sh}(\theta)}$, where $\mathbf{d}_{sh}(\theta) = \mathbf{d}(\theta) \odot \mathbf{w}_T$ and \mathbf{w}_T is an appropriate taper or shading function, and \odot denotes the element-by-element Schur product.

The GLRT test is

$$J_{GLRT}(\theta) = \frac{J_{AMF}(\theta)}{1 + \frac{1}{K} \mathbf{x}^H \hat{\mathbf{R}}^{-1} \mathbf{x}} \stackrel{H_1}{\geq} K\gamma, \quad (3)$$

where $K\gamma$ is the threshold which can be determined for a given false alarm P_{FA} . The $J_{AMF}(\theta)$ or $J_{GLRT}(\theta)$ are evaluated at some discrete set of points in the angle θ which covers the range of expected target angles. Note that as far as variation with θ is concerned, $J_{GLRT}(\theta)$ is merely proportional to $J_{AMF}(\theta)$ since the denominator in (3) does not depend explicitly on the search variable θ . An example of the $J_{AMF}(\theta)$ function for a single target is shown in Figure 1. Note that if all peaks above the threshold, which has been set for a probability of false alarm P_{FA} of 10^{-6} , were to be considered detections the figure shows that there should be six detections of which five of them would be false alarms (solid line). Even if a Chebyshev taper with -50dB sidelobe level is used, there are still two false detections (dashed line). The shading is only partly effective in the presence of interferences, in this case one jammer at -30 degrees.

Now assume that the test data vector contains m target signals, $m = 0, 1, \dots, M$ where the maximum number M may be known from system considerations. Then,

$$\mathbf{x} = \mathbf{D}_s \mathbf{a} + \mathbf{n}, \quad (4)$$

where $\mathbf{D}_s = [\mathbf{d}(\theta_{s1}), \dots, \mathbf{d}(\theta_{sm})]$ is a $N \times m$ matrix of target steering vectors and \mathbf{a} is an $m \times 1$ vector of complex amplitudes of the m signals. The complex value of the $J_{AMF}(\theta)$ function represents the application of the weight vector $\mathbf{w}(\theta)$ to the vector \mathbf{x} resulting in the expression

$$y(\theta) = \mathbf{w}(\theta)^H \mathbf{x} = \mathbf{w}(\theta)^H \mathbf{D}_s \mathbf{a} + v(\theta), \quad (5)$$

where $v(\theta) = \mathbf{w}(\theta)^H \mathbf{n}$. We assume that $y(\theta)$ has been evaluated at K_P distinct points $\theta_1, \dots, \theta_{K_P}$, where $K_P \geq m$. These points

would include the peaks of the $J_{AMF}(\theta)$ function. We have

$$\begin{bmatrix} y_1 \\ \vdots \\ y_{K_P} \end{bmatrix} = \begin{bmatrix} \mathbf{w}(\theta_1)^H \mathbf{D}_s \mathbf{a} \\ \vdots \\ \mathbf{w}(\theta_{K_P})^H \mathbf{D}_s \mathbf{a} \end{bmatrix} + \begin{bmatrix} v(\theta_1) \\ \vdots \\ v(\theta_{K_P}) \end{bmatrix}, \quad (6)$$

or, compactly,

$$\mathbf{Y} = \mathbf{H} \mathbf{a} + \mathbf{v}, \quad (7)$$

where $\mathbf{H} = \mathbf{W}^H \mathbf{D}_s$, and $\mathbf{W} = [\mathbf{w}(\theta_1), \dots, \mathbf{w}(\theta_{K_P})]$, and $\mathbf{v} = [v(\theta_1), \dots, v(\theta_{K_P})]^T$. The covariance matrix of \mathbf{v} is

$$\mathbf{R}_v = E[\mathbf{v} \mathbf{v}^H] = \mathbf{W}^H \mathbf{R} \mathbf{W}. \quad (8)$$

Since the order of the square matrix \mathbf{R}_v is K_P and the transformation in (8) necessarily yields $\text{rank}(\mathbf{R}_v) \leq N$, it follows that we must have $K_P \leq N$ for \mathbf{R}_v to be nonsingular. Hence we require that $m \leq K_P \leq N$. Denote the sample covariance matrix of \mathbf{v} as $\hat{\mathbf{R}}_v$. Under the assumption of Gaussian statistics for the interference plus noise vector \mathbf{n} , the maximum-likelihood estimates of the amplitude vector \mathbf{a} and the angles $\Theta_s = [\theta_{s1}, \dots, \theta_{sm}]$ are obtained by minimizing the nonlinear weighted least-squares criterion

$$J_{ML}(\mathbf{a}, \Theta_s) = [\mathbf{Y} - \mathbf{H} \mathbf{a}]^H \hat{\mathbf{R}}_v^{-1} [\mathbf{Y} - \mathbf{H} \mathbf{a}] = \|\hat{\mathbf{R}}_v^{-1/2} [\mathbf{Y} - \mathbf{H} \mathbf{a}]\|^2, \quad (9)$$

where $\hat{\mathbf{R}}_v^{-1/2}$ is the square-root of the Hermitian positive-definite matrix $\hat{\mathbf{R}}_v^{-1}$ and $\|\cdot\|$ denotes the Euclidean norm of a vector. Let $\mathbf{Z} = \hat{\mathbf{R}}_v^{-1/2} \mathbf{Y}$, the "whitened" data vector and $\mathbf{H}_w = \hat{\mathbf{R}}_v^{-1/2} \mathbf{H}$. Then,

$$J_{ML}(\mathbf{a}, \Theta_s) = \|\mathbf{Z} - \mathbf{H}_w(\Theta_s) \mathbf{a}\|^2. \quad (10)$$

For a given Θ_s , as is well known, J_{ML} is minimized with respect to \mathbf{a} when

$$\hat{\mathbf{a}} = [\mathbf{H}_w^H(\Theta_s) \mathbf{H}_w(\Theta_s)]^{-1} \mathbf{H}_w^H(\Theta_s) \mathbf{Z}. \quad (11)$$

Substitution of $\hat{\mathbf{a}}$ as given by (11) into (10) yields the weighted least-squares residual J_{ML} as

$$J_{ML}(\hat{\mathbf{a}}, \Theta_s) = \|(\mathbf{I} - \mathbf{P}(\Theta_s)) \mathbf{Z}\|^2, \quad (12)$$

where $\mathbf{P}(\Theta_s) \equiv \mathbf{H}_w(\Theta_s) [\mathbf{H}_w^H(\Theta_s) \mathbf{H}_w(\Theta_s)]^{-1} \mathbf{H}_w^H(\Theta_s)$ is the orthogonal projection operator and \mathbf{I} is the identity matrix. Equation (12) can be further minimized with respect to Θ_s yielding the maximum-likelihood estimate $\hat{\Theta}_s$. However, it is noted that this is a nonlinear optimization problem which may be computationally expensive to solve for $m \geq 2$. For most of the sidelobe detection problems considered here involving comparable strength targets that are likely to be separated from each other by more than a beamwidth, the locations of the peaks of the $J_{AMF}(\theta)$ function (which can be readily computed) provide a reasonably accurate estimate of Θ_s and are used to evaluate (12). However, for some problems, e.g., the detection and resolution of a weak source in presence of a strong source, the location of the global peak of $J_{AMF}(\theta)$ may be taken as the angle estimate $\hat{\theta}_1$ corresponding to one source while $\hat{\theta}_2$ is varied so as to minimize (12), keeping $\hat{\theta}_1$ fixed.

It is noted that the preceding development has been given in "beam-space" since this reduces computations and is most appropriate for resolving sidelobe detections obtained with using the $J_{AMF}(\theta)$ function (a normalized beam-space function). It can be seen that the element-space solution can be obtained either directly or from the preceding development by choosing $K_p = N$ and \mathbf{W} to be the $N \times N$ identity matrix. A simulation example using the element-space solution is given in section 5.

The number of target signals is determined by applying the procedure described above for model orders $m = 1, 2, \dots, M$ and choosing that m for which the Akaike Information Criterion [9],[10] given below is a minimum:

$$\begin{aligned} AIC(m) &= -\log(\text{Likelihood function}|\hat{\mathbf{a}}, \hat{\Theta}_s, m) \\ &\quad + (\text{number of independently} \\ &\quad \text{adjusted parameters in model}) \\ &= J_{ML}(\hat{\mathbf{a}}, \hat{\Theta}_s) + 3m, \end{aligned} \quad (13)$$

where $J_{ML}(\hat{\mathbf{a}}, \hat{\Theta}_s)$ is given by (12) and the approximate estimate $\hat{\Theta}_s$ discussed above is used. The method derived here is referred to as the Multi-Target AMF (MT-AMF) method.

3. DIAGONAL LOADING

Diagonal loading is a simple and commonly used procedure for sidelobe reduction. It is often used when the number of snapshots K is small, e.g., less than twice the number of elements. The diagonal loading operation simply adds a diagonal matrix to the sample covariance matrix to overweight its diagonal elements, i.e.,

$$\hat{\mathbf{R}}_{DL} = \hat{\mathbf{R}} + \sigma \mathbf{I}, \quad (14)$$

where σ is the diagonal loading factor. In the case of uncorrelated interference and noise, diagonal loading modifies the sample covariance matrix at the cost of noise enhancement. In the case of correlated interference, a large amount of diagonal loading also degrades the adaptive interference cancellation. However, it has been shown that a reasonable amount of σ can dramatically improve the performance for small K .

When diagonal loading is applied, the AMF function is given by

$$J_{AMF}(\theta) = \frac{|\mathbf{d}(\theta)^H \hat{\mathbf{R}}_{DL}^{-1} \mathbf{x}|^2}{\mathbf{d}(\theta)^H \hat{\mathbf{R}}_{DL}^{-1} \hat{\mathbf{R}} \hat{\mathbf{R}}_{DL}^{-1} \mathbf{d}(\theta)}. \quad (15)$$

Additional tapered weight can be applied by replacing $\mathbf{d}(\theta)$ by $\mathbf{d}_{sh}(\theta)$. In the matched filter (MF) case, i.e., $K = \infty$, the detection statistic does not change when diagonal loading is applied. However, in the case of limited snapshots, the determination of the threshold for a given P_{FA} seems to be analytically intractable [11]. Thus, a Monte Carlo computation is required. For an uncorrelated interference and noise case, the authors in [12] have shown improvement of signal detection for small K using diagonal loading. In this paper, we show similar improvement of P_D in the case of correlated interference. In addition, we apply the MT-AMF to the diagonally loaded AMF function to further reduce false sidelobe detections.

4. MULTI-TARGET GLRT

Although this paper has emphasized the multi-target AMF in the development and performance evaluation, it is noted here that the authors have derived [13] a generalization of Kelly's GLRT adaptive detection statistic [1] to multiple targets. It is shown in [13] that the multi-target version of Kelly's GLRT for M targets located at angles $\Theta_s = [\theta_{s1}, \dots, \theta_{sM}]$ is given by

$$J_{MT-GLRT}(\Theta_s) = \frac{\|\tilde{\mathbf{P}}(\Theta_s) \mathbf{y}\|^2}{1 + \frac{1}{K} \|\mathbf{y}\|^2}, \quad (16)$$

where $\tilde{\mathbf{P}}(\Theta_s) = \mathbf{D}_w(\Theta_s) [\mathbf{D}_w^H(\Theta_s) \mathbf{D}_w(\Theta_s)]^{-1} \mathbf{D}_w^H(\Theta_s)$ and $\mathbf{D}_w(\Theta_s) = \hat{\mathbf{R}}^{-1/2} \mathbf{D}_s(\Theta_s)$. $\hat{\mathbf{R}}^{-1/2}$ is the square-root of the Hermitian positive-definite matrix $\hat{\mathbf{R}}^{-1}$. $\mathbf{y} = \hat{\mathbf{R}}^{-1/2} \mathbf{x}$ is the "whitened" data vector and $\tilde{\mathbf{P}}(\Theta_s)$ is the orthogonal projection operator that projects any vector onto the subspace spanned by the columns of $\mathbf{D}_s(\Theta_s)$ (i.e., the subspace spanned by the steering vectors of the M targets).

5. PERFORMANCE EVALUATION

The P_{FA} of the GLRT test is given by [3]

$$P_{FA, GLRT} = \frac{1}{(1 + \alpha)^L}, \quad (17)$$

where $L \equiv K + 1 - N$, $\alpha = \gamma / (1 + \gamma)$, and γ is the threshold term of (3). The threshold for the AMF is determined by evaluating the following integral using numerical integration and bisection iterations as in [3]:

$$P_{FA, AMF} = \int_0^1 \frac{f_\beta(\rho; L+1, N-1)}{(1 + \rho \alpha_{AMF})^L} d\rho, \quad (18)$$

where

$$f_\beta(x; n, m) = \frac{(n+m-1)!}{(n-1)!(m-1)!} x^{n-1} (1-x)^{m-1} \quad (19)$$

is the central Beta density function, and ρ is the loss factor which considers the SNR loss due to finite number of snapshots in the sample covariance matrix. The analytic form of the probability of detection for a single source is also given in [3] which we excluded for brevity. Our Monte Carlo simulation results have been confirmed to match these analytical curves.

We consider a linear equally spaced array of 10 elements with half-wavelength spacing (nominal beamwidth = 12 degrees) for most of the simulations provided in this section. A noise jammer signal of strength 40dB relative to thermal noise is placed at -30 degrees and the P_{FA} is set to be 10^{-6} . The scanning angles are from -50 to 50 degrees in azimuth. A single source of varying SNR is placed at broadside and the performance of the algorithms in single source detection and false sidelobe rejections are compared. The AMF detection only relies on the peaks above the given threshold, but the MT-AMF test takes the peaks (for all simulation examples except the last one) and tests for model order $m = 1$ and 2. If $m = 1$ is decided, the overall peak is retained as an indicator of a single signal and the other peaks are rejected. The probability of detecting the mainlobe signal is plotted in Figure 2, regardless of the number of peaks or model decisions, after 5000 Monte Carlo

runs. We observe no loss in the detection for the MT-AMF method. Then, the probability of false sidelobe detections is plotted for the two algorithms in Figure 3. The AMF gives rise to high false sidelobe detections at high SNR, but the MT-AMF greatly reduces the false sidelobe detections and its probability also saturates as SNR increases. The false sidelobe detections of the proposed method go down rapidly for increasing K and the lower bound is for $K = \infty$, which is the multi-target matched filter. For tapered weight vector $w(\theta)$, we also compare the sidelobe rejections performance, as depicted in Figure 4. Note that the use of a taper with the conventional AMF method only reduces sidelobe detections slightly at the cost of a slight decrease in mainlobe detection probability (not shown). However, the use of model order determination using AIC with tapered AMF data shows almost the same dramatic improvement in reducing false sidelobe detections as before with the same mainlobe detection probability as the conventional tapered AMF.

The same single source scenario except for a P_{FA} of 10^{-3} and $K = 20$ using diagonal loading and tapered weights is further studied. Monte Carlo simulations are performed to determine the thresholds which yield the equivalent P_{FA} for various levels of diagonal loading. Note in this case the P_{FA} accounts for not only the noise but also the jammer that is not effectively cancelled due to the use of diagonal loading. The probability of detecting the mainlobe signal is plotted in Figure 5. Note the improved P_D performance using various levels of diagonal loading. The MT-AMF with diagonal loading and tapering also yields identical P_D performance. The probability of false sidelobe detections is plotted for the two methods in Figure 6. As the diagonal loading level increases, the probability of false sidelobe detections using AMF lowers most of the time (except for the high SNR region). On the other hand, the MT-AMF shows significant improvement in reducing false sidelobe detections comparing to the AMF with the same diagonal loading level.

Then, two sources of equal strength are placed at broadside and 45 degrees. The probability of detecting both sources within a ± 10 degrees angle constraint is plotted for the AMF and MT-AMF algorithms, as depicted in Figure 7. We observe the same detections between the conventional method and the proposed algorithm. The two sources detections using the GLRT is plotted in Figure 8. However, for $K = 20$, the GLRT yields extremely poor performance in detecting both sources due to the normalization factor in the denominator of (3). The derivation of the GLRT is under the assumption of a single source; therefore, despite its advantage in single source detections, as depicted in Figure 9, and sidelobe rejections for lower K , as depicted in Figure 10, it is not an appropriate model for two sources.

Another two sources detection scenario is analyzed for a linear equally spaced array of 32 elements. One mainlobe source is placed at broadside with an array SNR of 25dB, and a second sidelobe source is placed at 45 degrees with varying SNR levels. A noise jammer signal of strength 40dB relative to thermal noise is again placed at -30 degrees and the P_{FA} is set to be 10^{-6} . The MT-AMF and MT element space methods are applied to source detections with a varying angle search of the weaker source and fixing the angle of the stronger source at the global peak of the AMF function. The number of data points K_p used in the MT-AMF is nominally $N/2$ and are taken from the peaks of the AMF function without the threshold constraint. We count detections of both sources when the model order decision yields $m = 2$ and the angle estimates are within ± 3.2 degrees (nominal beamwidth)

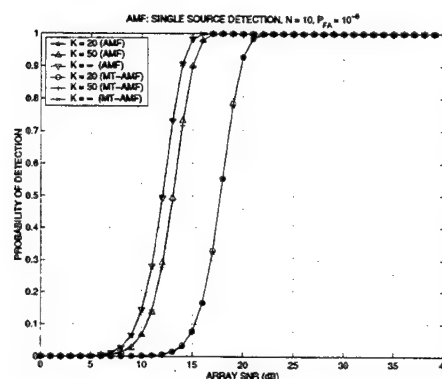


Fig. 2. Probability of detecting single mainlobe target signal using AMF and MT-AMF. Note equal performances of the two methods.

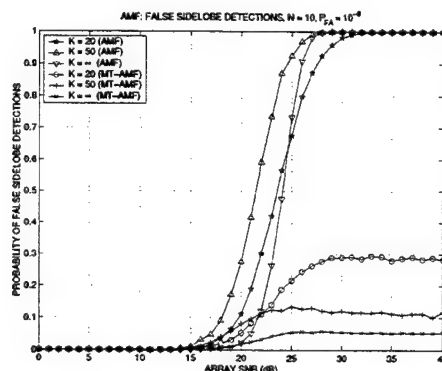


Fig. 3. Probability of false sidelobe detections using AMF and MT-AMF. Note the substantial improvement of the MT-AMF method in false sidelobe rejections at high SNR.

of the true angle of arrivals. As depicted in Figure 11, the MT-AMF method improves the detections of both sources significantly from the AMF method, where the detections are based on the top two peaks above the threshold. When the strength of the sidelobe source dominates, strong interactions of its sidelobe response would perturb the weaker mainlobe source and reduce the probability of detections. Nevertheless, we can resolve such problem by using the MT-AMF method. The MT element space method is applied to the element data x and further improves the two sources detections; nonetheless, the beam-space MT-AMF method has significant computational advantages when the number of elements is large. The ML element space method, which searches for the absolute minimum residual on the two-dimensional angle parameter space (high computational complexity), is also shown as the upper bound of the two sources detections.

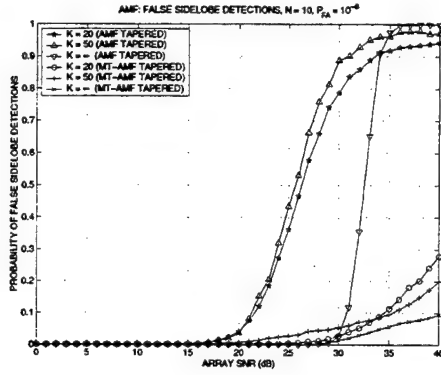


Fig. 4. Probability of false sidelobe detections using tapered AMF weights (-50dB Chebyshev). Note significant improvement even when taper is used.

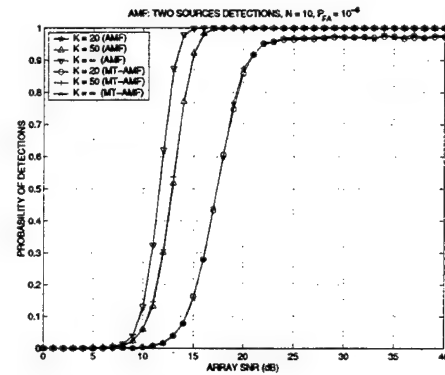


Fig. 7. Probability of detecting both sources within ± 10 degrees using AMF and MT-AMF. Note equal performances of the two methods.

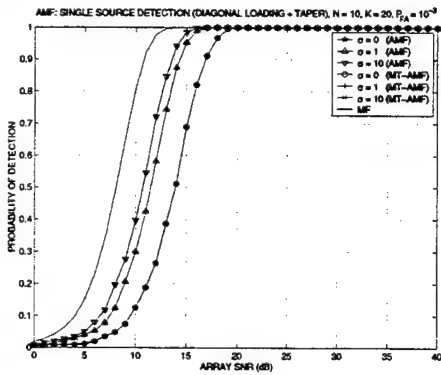


Fig. 5. Probability of detecting single mainlobe target signal using the diagonal loaded and tapered (-50dB Chebyshev) AMF and MT-AMF. Note equal performances of the two methods.

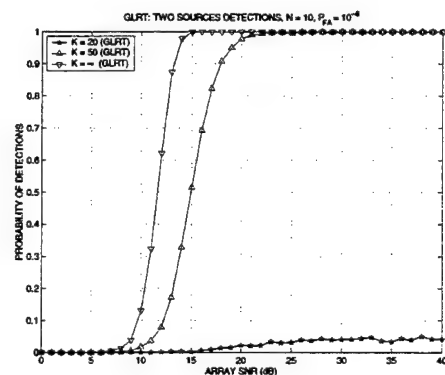


Fig. 8. Probability of detecting both sources within ± 10 degrees using GLRT. Note the degraded performance, especially for smaller K .

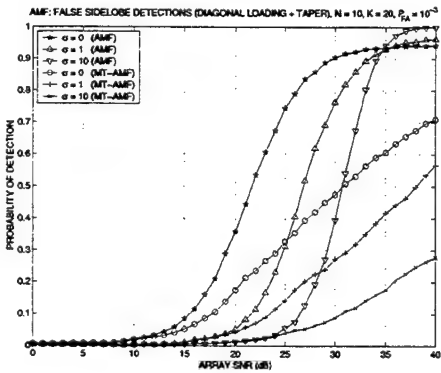


Fig. 6. Probability of false sidelobe detections using diagonally loaded and tapered AMF weights. Note significant improvement even when diagonal loading and taper are used.

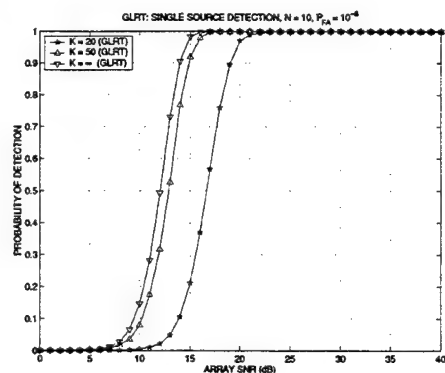


Fig. 9. Probability of detecting single mainlobe target signal using GLRT. Note superior performance over AMF and MT-AMF for small K .

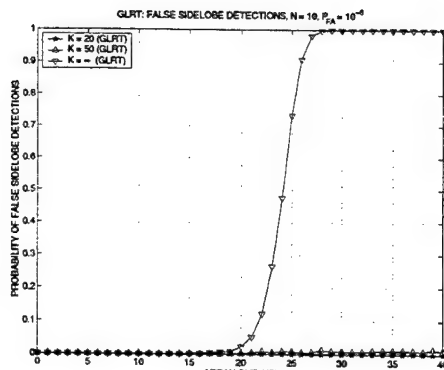


Fig. 10. Probability of false sidelobe detections using GLRT. Note good sidelobe rejection capability for smaller K at the expense of reduced detections of two sources (Fig. 8).

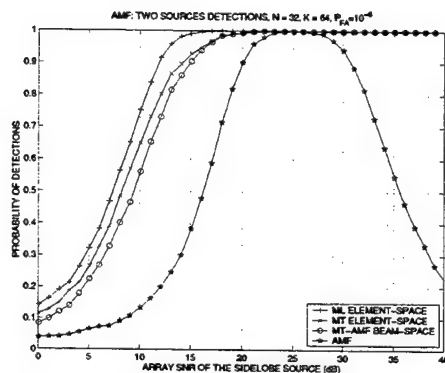


Fig. 11. Probability of detecting both sources within ± 3.2 degrees using AMF, MT-AMF, and MT element space methods. Note superior performances of the two MT methods.

6. CONCLUSIONS

In this paper, we have shown substantial false sidelobe rejection improvement and two sources detections using the proposed model order determination method. The algorithm is efficient in computations and can be easily implemented in existing adaptive radar systems.

7. REFERENCES

- [1] E.J. Kelly, "An Adaptive Detection Algorithm," *IEEE Trans. on Aerospace and Electronics Systems*, vol. AES-22, no. 1, pp. 115-127, Mar. 1986.
- [2] E.J. Kelly, "Performance of an Adaptive Detection Algorithm: Rejection of Unwanted Signals," *IEEE Trans. on Aerospace and Electronics Systems*, vol. AES-25, no. 2, pp. 122-133, Mar. 1989.
- [3] F.C. Robey, D.R. Fuhrmann, E.J. Kelly, and R. Nitzberg, "A CFAR Adaptive Matched Filter Detector," *IEEE Trans. on Aerospace and Electronics Systems*, vol. 28, no. 1, pp. 208-216, Mar. 1992.
- [4] D. E. Kreithen, C.F. Pearson, and C.D. Richmond, "Adaptive Sidelobe Blanker: A Novel Method of Performance Evaluation and Threshold Setting in the Presence of Inhomogeneous Clutter," in *Proc. 32nd Asilomar Conf. Signals Syst. & Comp.*, vol. 2, pp.528-32, Pacific Grove, CA, Nov. 1998.
- [5] C.D. Richmond, "Performance of the Adaptive Sidelobe Blanker Detection Algorithm in Homogeneous Environments," *IEEE Trans. on Signal Processing*, vol. 48, no. 5, pp. 1235-47, May 2000.
- [6] C.D. Richmond, "Performance of a Class of Adaptive Detection Algorithms in Nonhomogeneous Environments," *IEEE Trans. on Signal Processing*, vol. 48, no. 5, pp. 1248-62, May 2000.
- [7] R.A. Monzingo and T.W. Miller, *Introduction to Adaptive Arrays*, John Wiley, New York, 1980.
- [8] N.B. Pulsone and M.A. Zatman, "A Computational Efficient Two-Step Implementation of the GLRT," *IEEE Trans. on Signal Processing*, vol. 48, no. 3, pp 609-616, Mar. 2000.
- [9] H. Akaike, "A New Look at the Statistical Model Identification," *IEEE Trans. on Automatic Control*, vol. AC-19, pp. 716-723, Dec. 1974.
- [10] A.G. Jaffer, "Maximum-Likelihood Angular Resolution of Multiple Sources," in *Proc. 19th Asilomar Conf. Signals Syst. & Comp.*, pp.68-72, Pacific Grove, CA, Nov. 1985.
- [11] S.Z. Kalson, "Adaptive Array CFAR Detection," *IEEE Trans. on Aerospace and Electronics Systems*, vol. 31, no. 2, pp. 534-42, Apr. 1995.
- [12] T.F. Ayoub and A.M. Haimovich, "Modified GLRT Signal Detection Algorithm," *IEEE Trans. on Aerospace and Electronics Systems*, vol. 36, no. 3, pp. 810-8, Jul. 2000.
- [13] A.G. Jaffer, J.C. Chen, and T.W. Miller, "Generalization of GLRT Adaptive Detection to Multiple Targets," to be submitted to *IEEE Trans. on Aerospace and Electronics Systems*.

SPACE-TIME ADAPTIVE FIR FILTERING WITH STAGGERED PRI

R. Klemm

FGAN-FHR, 53343 Wachtberg, Germany

Tel: ++49 228 9435 377, Fax: ++49 228 9435 618, E-mail: r.klemm@fgan.de

ABSTRACT

Space-time least squares FIR filters have proven excellent clutter rejection performance at extremely low computational load so that ground moving target indication (GMTI) kann be carried out in real-time. Staggering the pulse repetition interval (PRI) is an appropriate way of avoiding Doppler ambiguities and blind velocities. Fully adaptive space-time processors can cope well with staggered echo data. FIR filtering techniques are based on constant PRI and, therefore, will suffer some degradation if the radar pulses are staggered. In this contribution the concept of re-adaptation of the FIR filter coefficients at each PRI is put forward. It is shown by simulations that the total loss caused by staggering the PRI is of the order of magnitude of a few dB. However, applying a constant FIR filter to staggered data results in dramatic losses in signal-to-clutter+noise ratio.

1. INTRODUCTION

1.1. Preliminaries

The motion of an air- or spaceborne radar causes clutter returns from the ground to be Doppler shifted. The Doppler shift of an arrival from a single scatterer is proportional to the cosine of the angle of arrival of the backscattered echo. The total of all clutter arrivals results in a Doppler broadband signal where the Doppler bandwidth is determined by the platform velocity. The clutter bandwidth degrades the detectability of slow moving targets. Space-time adaptive processing (STAP) has been shown to compensate for the platform motion effect so that basically no losses in slow moving target detection will occur.

The basis of STAP techniques is the likelihood ratio (LR) test which states that the space-time echoes received by a coherent array antenna have to be multiplied with the inverse of the space-time clutter covariance matrix, followed by coherent signal integration using a beamformer and Doppler filters. If the number of array elements N and the number of processed echoes M is large the matrix inverse may not be available by various reasons:

- Adaptation means estimation of the clutter covariance

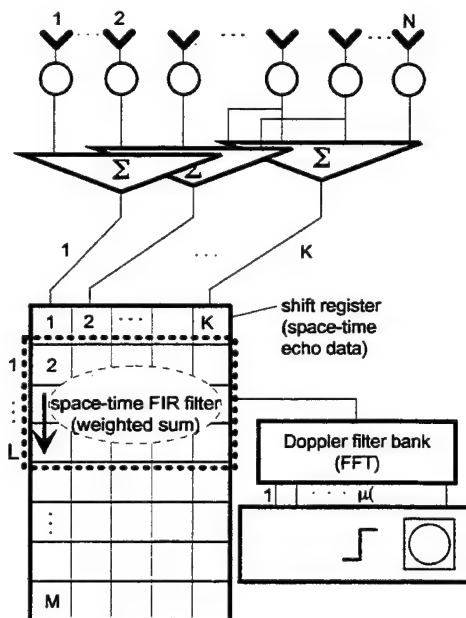


Figure 1: Overlapping subarray processor with space-time FIR filter

matrix. The number of operations required may be prohibitive if N and M are large.

- There may be a lack of representative clutter data to estimate the covariance matrix.
- The computation of the matrix inverse may be impossible because of extensive computational load.
- The computation of the matrix inverse may be impossible due to limited numerical accuracy.
- Implementation of the LR processor requires that all elements of the array antenna are cascaded with digitized channels. This is currently unrealistic by reasons of cost.

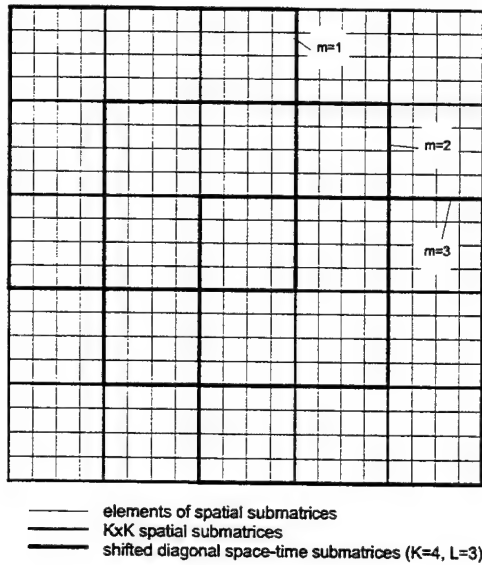


Figure 2: Matrix scheme for space-time FIR filtering, $K=4$, $M=5$

1.2. Subspace Techniques

A lot of publications deal with suboptimum approximations (frequently referred to as subspace techniques) of the space-time LR processor (e.g. WARD [11], KLEMM [2] GOLDSTEIN & REED [4]).

There are rank reducing techniques which conduct clutter suppression in the clutter subspace of the space-time covariance matrix while maintaining the order of the order of the filter matrix. The eigencanceler type of architectures (HAIMOVICH & BAR-NESS [3]) belong to this class. Saving of operations is achieved during the adaptation and filter calculation phase, however not during filtering the echo data at range sample speed.

Order reduction STAP techniques lead to reduced size architectures which promise a reduction of the computational load for adaptation, filter calculation and filterings as well. This class of processors has specific aptitude to real-time processing.

A large class of order reduction architectures are based on certain linear transforms. There are space-time transforms, spatial transforms and temporal transforms ([2, Chapter 5-7]). For large M post-Doppler techniques which operate in the Doppler domain may lead to very efficient receiver schemes.

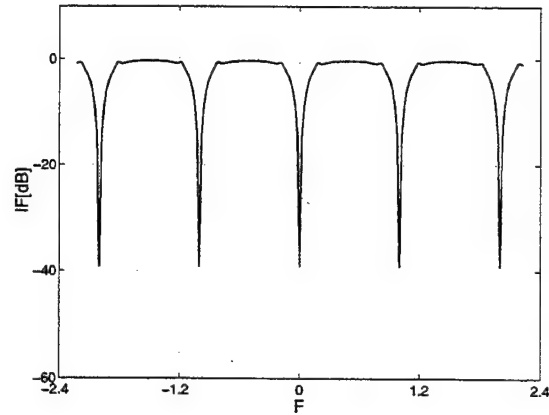


Figure 3: Fully adaptive processing, constant PRI

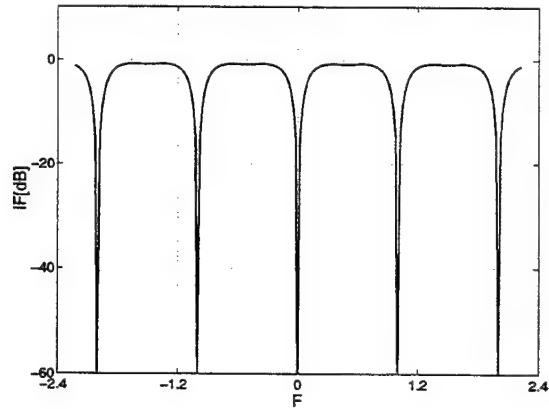


Figure 4: FIR filter, based on data from first 5 echoes, constant PRI

1.3. The Space-Time FIR Filter

1.3.1. The principle

Space-time FIR filters exploit the stationarity of echo sequences. KLEMM & ENDER [8] analysed a least squares space-time filter for GMTI processing in real-time. Related approaches have been described by BARANOSKI [10], ROMAN et al. [9] and SWINDLEHURST & PARKER [7]. In the concept of GOLDSTEIN & REED [5] several 1-delay subfilters are cascaded.

The space-time least squares FIR filter introduced by The use of *space-time* least squares FIR filters for airborne applications introduced in [8] and described in detail in [2, Chapter 7] has proven to be a highly efficient way of adaptive ground clutter suppression for moving radar. The filter is closely related to the Maximum Entropy Method (BURG [1]). A block

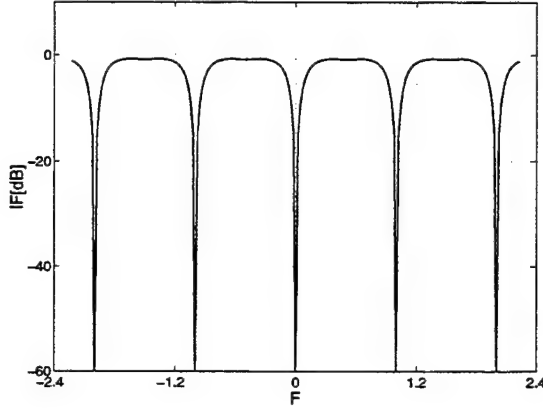


Figure 5: FIR filter, sliding calculation of coefficients, constant PRI

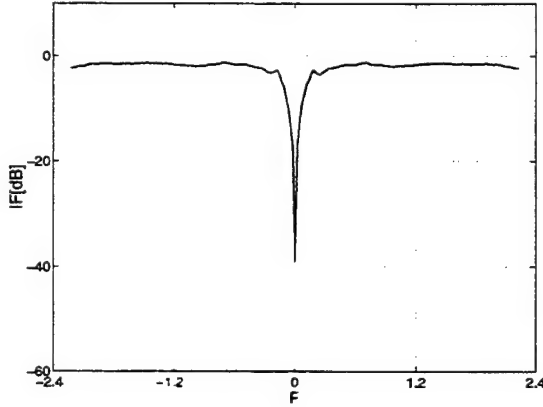


Figure 6: Fully adaptive processing, randomly staggered PRI

diagram of a FIR filter based GMTI processor is shown in Figure 1. Notice that the spatial dimension has been reduced by subdividing the array antenna into K subarrays. If $K \ll N$ the number of operations for clutter suppression is strongly reduced. Further reduction can be obtained by choosing a space-time FIR filter with $L \ll M$ delays. The FIR filter is calculated as follows:

- Choose a segment of L echoes with $L \ll M$.
- Calculate the associated space-time clutter covariance matrix. It will be one of the submatrices along the diagonal of the matrix scheme shown in Figure 2. These submatrices are denoted as $m = 1, 2, 3$.
- Calculate the inverse of the submatrix.
- Select the first $K \times KL$ block row of the inverse to

become $\tilde{\mathbf{K}}$.

- Multiplying a $N \times 1$ beamformer vector \mathbf{b} with $\tilde{\mathbf{K}}$ results in a $1 \times KL$ vector of space-time filter coefficients $\tilde{\mathbf{K}}\mathbf{b}$.

It has been demonstrated that the temporal filter length can be chosen independently of the coherent processing interval M (CPI). This is a desirable property, particularly when the filter is used in a multi-mode radar where the CPI varies with different operational modes. Even with very low filter dimensions (e.g., $K = L = 3$, total number of coefficients: 9) excellent approximation of the performance of the optimum processor can be achieved.

1.3.2. Mathematical description

The first column of the inverse of a Toeplitz matrix is called a *prediction error filter*. It has the property of minimizing the output power of a stationary process determined by the Toeplitz covariance matrix. The inverse of the space-time covariance matrix \mathbf{Q} has the same form as \mathbf{Q} :

$$\mathbf{K} = \mathbf{Q}^{-1} = \begin{pmatrix} \mathbf{K}_{11} & \mathbf{K}_{12} & \dots & \mathbf{K}_{1L} \\ \mathbf{K}_{21} & \mathbf{K}_{22} & \dots & \mathbf{K}_{2M} \\ \vdots & \vdots & \ddots & \vdots \\ \mathbf{K}_{M1} & \mathbf{K}_{M2} & \dots & \mathbf{K}_{MM} \end{pmatrix} \quad (1)$$

Let us consider now a small segment of L echoes out of M where by L we denote the temporal filter length. We assume that $L \ll M$. Recall that the submatrices \mathbf{K}_{ik} are spatial, that means, they are related either the antenna array ($N \times N$) or the subspace given by the antenna channels ($K \times K$).

Then the order reduced space-time covariance matrix becomes

$$\mathbf{K} = \mathbf{Q}^{-1} = \begin{pmatrix} \mathbf{K}_{11} & \mathbf{K}_{12} & \dots & \mathbf{K}_{1L} \\ \mathbf{K}_{21} & \mathbf{K}_{22} & \dots & \mathbf{K}_{2L} \\ \vdots & \vdots & \ddots & \vdots \\ \mathbf{K}_{L1} & \mathbf{K}_{L2} & \dots & \mathbf{K}_{LL} \end{pmatrix} \quad (2)$$

where L is the temporal dimension of the space-time FIR filter. Assuming for instance $K = 3$ and $L = 3$ this matrix has the dimensions 9×9 . The space-time prediction error filter is the first block column of \mathbf{K}

$$\tilde{\mathbf{K}} = \begin{pmatrix} \mathbf{K}_{11} \\ \mathbf{K}_{21} \\ \vdots \\ \mathbf{K}_{L1} \end{pmatrix} \quad (3)$$

The FIR filter operation can be formulated as follows

$$\mathbf{y} = \tilde{\mathbf{H}}^* \begin{pmatrix} \mathbf{x}_1 \\ \mathbf{x}_2 \\ \vdots \\ \mathbf{x}_M \end{pmatrix} \quad (4)$$

where

$$\tilde{\mathbf{H}}^* = \begin{pmatrix} \mathbf{K}_{11}^* & \dots & \mathbf{K}_{L1}^* & \mathbf{0}^* & \dots \\ \mathbf{0}^* & \mathbf{K}_{11}^* & \dots & \mathbf{K}_{L1}^* & \mathbf{0}^* & \dots \\ \vdots & \vdots & \vdots & \vdots & \vdots & \vdots \end{pmatrix} \quad (5)$$

is a shift operator, $\mathbf{0}$ is a $K \times K$ zero matrix. The spatial dimension of the FIR filter can be removed by pre-beamforming

$$\mathbf{h} = \tilde{\mathbf{K}}\mathbf{b} \quad (6)$$

so that the filtering operation can be written as

$$\mathbf{z}^* = \mathbf{H}^* \mathbf{x} = \mathbf{H}^* \begin{pmatrix} \mathbf{x}_1 \\ \mathbf{x}_2 \\ \vdots \\ \mathbf{x}_M \end{pmatrix} \quad (7)$$

where

$$\mathbf{H}^* = \begin{pmatrix} \mathbf{h}_1^* & \dots & \mathbf{h}_L^* & \mathbf{o}^* & \dots \\ \mathbf{o}^* & \mathbf{h}_1^* & \dots & \mathbf{h}_L^* & \mathbf{o}^* & \dots \\ \vdots & \vdots & \vdots & \vdots & \vdots & \vdots \end{pmatrix} \quad (8)$$

with \mathbf{o} being a K -dimensional zero vector and \mathbf{x}_m is the signal vector at the array outputs at time m . Notice that \mathbf{z} is temporal only with the dimension $M - L + 1$ while the dimension of the space-time vector \mathbf{y} was $(M - L + 1) \times K$. The processor is completed with a Doppler filter bank with Doppler filters of length $M - L + 1$ whose output signals are obtained as

$$\mathbf{d} = \mathbf{F}\mathbf{z} \quad (9)$$

where the matrix \mathbf{F} describes the Doppler filter bank, for instance, the DFT. The elements of \mathbf{d} are fed into a detection device.

The improvement factor in SCNR becomes

$$IF(\omega_d) = \frac{\mathbf{s}^*(\omega_d)\mathbf{H}\mathbf{H}^*\mathbf{s}(\omega_d)\mathbf{s}^*(\omega_d)\mathbf{H}\mathbf{H}^*\mathbf{s}(\omega_d) \cdot \text{tr}(\mathbf{Q})}{\mathbf{s}^*(\omega_d)\mathbf{H}\mathbf{H}^*\mathbf{Q}\mathbf{H}\mathbf{H}^*\mathbf{s}(\omega_d) \cdot \mathbf{s}^*(\omega_d)\mathbf{s}(\omega_d)} \quad (10)$$

where we made the usual assumption that the processor is perfectly matched to the target signal vector and ω_d means

Doppler frequency. In the discussion below we use the $IF(\omega_d)$ to judge the efficiency of processing and the effect of parameters. Instead of $IF(\omega_d)$ we show $IF(F)$ where $F = \omega_d/(2\pi PRF)$ is the normalized Doppler frequency.

2. STAGGERED PRI RADAR

2.1. General Aspects

The PRF is commonly chosen constant which, however, has a couple of drawbacks

- The target Doppler cannot be estimated unambiguously.
- The clutter filter produces ambiguous notches at the blind velocities.
- The PRF can be estimated by hostile ESM (electronic support measure) and countered with spot jamming.

Alternatively one may either stagger the PRF or the PRI. PRF staggering has the disadvantage that several pulse bursts have to be transmitted which means a waste of radar energy. This problem is circumvented by PRI staggering (it has the little drawback that the FFT algorithm cannot be used as Doppler filter bank).

The effect of PRI staggering for use with STAP has been discussed in [6]. It was demonstrated that the optimum (LR) processor can cope well with staggered PRI, provided that the Doppler filters are matched to the staggered pulse sequence.

2.2. FIR Filtering with Staggered PRI

Now the question arises how an extremely efficient clutter filter technique such as the adaptive space-time FIR filter can operate with staggered PRI. Staggering the transmit pulses means that the received echo sequence is no longer stationary. Recall that the efficiency of the adaptive FIR relies on stationary data sequences.

Stationarity of the echo sequence means that the space-time submatrices ($m = 1, 2, 3$) in Figure 2 are equal. If the pulse sequence is staggered these matrices are different. A straight forward approach to cope with this non-stationarity is to readapt the filter at each PRI. That means, at each PRI the space-time submatrix is estimated anew. Then we obtain a space-time FIR filter with time-varying coefficients.

The adaptation of the FIR filter with each PRI causes additional expense in terms of computations. This is, however, tolerable, because the FIR filter is based on a small number of coefficients. Therefore, the associated time-depending subcovariance matrix is very small and needs only very few clutter echo samples for estimation. These can easily be taken at each PRI from the received range samples.

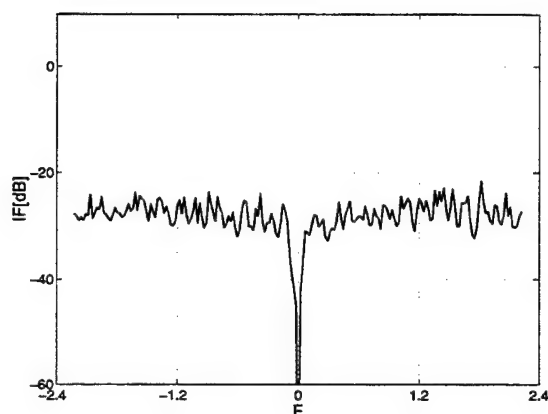


Figure 7: FIR filter, constant coefficients, randomly staggered PRI

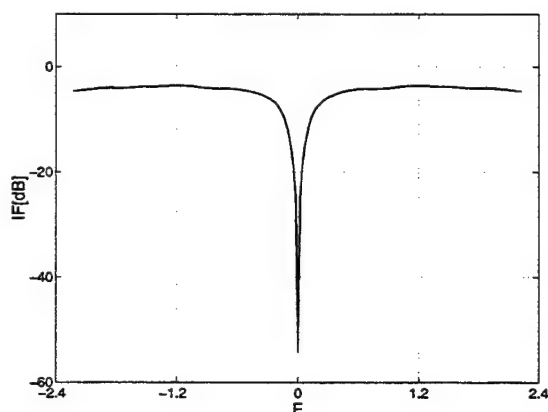


Figure 8: FIR filter, sliding calculation of coefficients, randomly staggered PRI

3. NUMERICAL EXAMPLES

The principle of clutter FIR filtering with time-varying coefficients is illustrated in Figures 3-8. As example, a sidelooking radar with linear array antenna was assumed. The look direction is perpendicular to the flight path, i.e., broadside.

Figure 3 shows the improvement factor in signal-to-clutter+noise ratio versus the normalized target Doppler frequency. The PRF is constant and has been chosen so that ambiguous clutter notches show up in the clutter band ($\text{PRF} = 4 \times \text{Nyquist}$ of the clutter band). The primary clutter notch is at $F = 0$. The other notches are repetitions due to Doppler ambiguity.

The same kind of IF plot has been calculated for the space-time FIR filter as given by Figure 4. The curve is quite

similar to the one in Figure 3, however, with slightly broadened and deeper clutter notches. In Figure 5 we applied the principle of re-adaptation on echo data with constant PRF. Then the filter coefficients are calculated from the different submatrices ($m = 1 \dots 3$). As can be noticed Figure 5 is identical to Figure 4. The reason is obvious: For constant PRF the echo sequence is stationary, and the submatrices are identical.

Let us now introduce a pseudorandom stagger code. Figure 6 shows again the behaviour of the optimum LR processor. As can be seen there is only one clutter notch left. The ambiguities do not show up anymore.

Applying a space-time FIR filter with constant coefficients leads to an IF curve as shown in Figure 7. There is only one clutter notch, however, due to the mismatch of the constant filter to the stagger pattern we obtain heavy losses in the passband of the filter. A FIR filter with sliding computation of the filter coefficients yields an IF curve as shown in Figure 8. We notice that except for a loss of a few dB a good filter characteristics is obtained.

4. CONCLUSIONS

Space-time least squares FIR filters are a highly efficient way of clutter rejection in air- or spaceborne radar. Radar operation with staggered PRI may be an attractive feature of airborne pulse-Doppler radars, with the potential of unambiguous Doppler estimation and avoidance of blind velocities. The optimum STAP processor as suggested by the likelihood ratio test can cope well with instationarities of the received echo sequence caused by PRI staggering. FIR filters with constant coefficients are by nature based on stationary echo sequences. Such filters, however, can be applied to staggered echo sequences if the filter is re-adapted with every PRI. It is shown by numerical examples that the time-varying space-time FIR filter can operate well on staggered echo data. The penalty for staggering is a loss in signal-to-clutter ratio of a few dB.

5. REFERENCES

- [1] Burg, J. P., "Maximum Entropy Spectral Analysis", in: *Proc. NATO Advanced Study Institute*, Enschede, Netherlands, 1968
- [2] Klemm, R., *Space-Time Adaptive Processing - Principles and Applications* (IEE, London, UK, 1998)
- [3] Haimovich, A. L., Bar-Ness, Y., "An Eigenanalysis Interference Canceler", *IEEE Trans. Signal Processing*, Vol. 39, No. 1, January 1991, pp. 76-84
- [4] Goldstein, J. S., Reed, I. S., "Theory of Partially Adaptive Radar", *IEEE Trans. AES*, Vol. 33, No. 4, October 1997, pp. 1309-1325
- [5] Goldstein, J. S., Reed, I. S., Scharf, L., "A multistage representation of the Wiener filter based on orthogonal

- projections", *IEEE Trans. IT*, Vol. 44, No. 7, November 1998, pp. 2943-2959
- [6] Klemm, R., "STAP with staggered PRF", *RADAR'99*, 17-21 May 1999, Brest, France
 - [7] Swindlehurst, A. L., Parker, P., "Parametric clutter rejection for space-time adaptive processing", *ASAP 2000 Workshop*, MIT LL, Lexington, USA, 13-14 March 2000, pp. 7-12
 - [8] Klemm, R., Ender, J., "New Aspects of Airborne MTI", *Proc. IEEE Radar 90*, Arlington, USA, 1990, pp. 335-340
 - [9] Roman, J. R., Rangaswamy, M., Davis, D. W., Zhang, Q., Himed, B., Michels, J. H., "Reduced rank STAP performance analysis", *IEEE Transactions AES*, Vol. 36, No. 2, April 2000, pp. 677-692
 - [10] Baranoski, E. J., "Improved Pre-Doppler STAP Algorithm for Adaptive Nulling in Airborne Radars", *IEEE Proc. 29th ASILOMAR Conference on Signals, Systems and Computers*, Pacific Grove, USA, 30 Oct.-2 Nov. 1995, pp. 1173-1177
 - [11] Ward, J., "Space-Time Adaptive Processing for Airborne Radar", *Technical Report No. 1015*, Lincoln Laboratory, MIT, December 1994

PARAMETRIC FILTERS FOR NON-STATIONARY INTERFERENCE MITIGATION IN AIRBORNE RADARS

Peter Parker and A. Lee Swindlehurst

Dept. of Electrical & Computer Engineering
Brigham Young University
Provo, UT 84602
{parkerp, swindle}@ee.byu.edu

ABSTRACT

Multichannel parametric filters are currently being studied as a means of reducing the dimension of STAP algorithms for interference rejection in airborne pulsed-Doppler radar systems. These filters are attractive to use due to the low computational cost associated with their implementation as well as their near optimal performance with a small amount of training data for a stationary environment. However, these filters do not perform well in certain types of non-stationary environments. This paper presents two modifications to the Space-Time AutoRegressive (STAR) filter that we previously proposed. The first modification is based on the Extended Sample Matrix Inversion (ESMI) technique and is used in the presence of range varying clutter which arises from the use of non-linear antenna arrays or bistatic radar systems. The second modification to the STAR filter is for use in the presence of hot clutter and is a three-dimensional STAP algorithm. Using a realistic simulated data set for circular array STAP, we show that the modifications to the STAR filter improve the performance when in the presence of the non-stationary interference.

1. INTRODUCTION

The use of space-time adaptive processing (STAP) for airborne radar interference mitigation is usually limited by the lack of stationary secondary data used for training the filter. This problem is made worse when the radar platform is operating under circumstances that lead to additional non-stationary components to the interference. Such circumstances include the use of a non-linear or non-side-looking array which leads to a range variation of the clutter statistics or the presence of an airborne jamming source which leads to hot clutter or terrain scattered interference.

Partially adaptive STAP filters alleviate this problem to a degree by taking advantage of the low-rank nature of the clutter. The partially adaptive STAP filters use fewer degrees of freedom and therefore need fewer training samples than the fully adaptive STAP filter. One such partially adaptive STAP filter that is discussed in this paper is the Space-Time AutoRegressive (STAR) filter [1]. The partially adaptive STAP filters offer an improvement over the fully adaptive STAP filter but are still derived based upon the assumption that the interference is stationary. When the non-stationary component of the interference follows a specified

model, this model may be taken into account to derive a filter to cancel the non-stationary interference. A few partially adaptive STAP algorithms have been derived to account for range-varying interference [2] and hot clutter [3].

Parametric filters (such as the STAR filter) have been shown to achieve near optimal performance with a small amount of training data when the interference is stationary [4]. However, the performance when the interference is non-stationary leaves much room for improvement. In this paper, two extensions of the STAR filter to account for both range-varying interference and hot clutter are presented. The improvements that the range-varying Extended STAR (ESTAR) filter offers over the standard STAR filter is illustrated with a synthetic data set generated by MIT Lincoln Laboratory that simulates the output of a 20 element antenna array whose elements lie along a circular arc of 120° [2]. This ESTAR filter is also shown to have better performance than a range-varying extended post-Doppler algorithm.

The three-dimensional STAR filter used to mitigate hot clutter is tested using the same data set as above augmented with synthetic hot clutter. The 3D-STAR filter achieves a significant improvement in signal-to-interference plus noise ratio (SINR) over the standard STAR approach. In comparing the 3D-STAR filter to a three-dimensional optimized pre-Doppler algorithm, it is shown that the performance of the two filters are nearly the same but that the 3D-STAR filter has a narrower clutter notch. This narrow clutter notch allows for improved detection of slowly moving targets.

In the next section, we briefly present the standard data model used for STAP problems and introduce the notation used throughout the paper. The STAR filtering technique is described in Section 3 as a background for the extensions presented herein. Section 4 presents the range-varying extended STAR filter that is used when the clutter statistics are range-varying. Section 5 derives a 3D-STAR filter used for the mitigation of hot clutter and Section 6 shows the results of several numerical simulations of the filters.

2. DATA MODEL

A target present in a particular range bin during some coherent processing interval (CPI) may be modeled as producing the following baseband vector signal (after pulse compression and demodulation) [5]:

$$\mathbf{x}_\ell(t) = b\mathbf{a}(\theta)e^{j\omega t} + \mathbf{n}_\ell(t) \in \mathbb{C}^m, \quad t = 1, \dots, N, \quad (1)$$

where ℓ is the range bin in which the target is located, b is the complex amplitude of the signal, ω is the Doppler shift due to the

This work was supported by the Office of Naval Research under contract N00014-00-1-0338.

relative motion between the array platform and the target, $\mathbf{a}(\theta)$ is the response of the array to a unit amplitude plane wave arriving from direction θ (azimuth and elevation angles), and $\mathbf{n}_\ell(t)$ contains contributions from clutter, jamming, and thermal noise. In (1), we are assuming an array of m elements and a total of N transmitted pulses covering R range bins.

If we stack the N array outputs into a single $mN \times 1$ space-time snapshot, we may re-write (1) as

$$\chi_\ell = \begin{bmatrix} \mathbf{x}(1) \\ \vdots \\ \mathbf{x}(N) \end{bmatrix} = \mathbf{b}s(\theta, \omega) + \eta \quad (2)$$

where

$$\begin{aligned} \mathbf{s}(\theta, \omega) &= \mathbf{v}(\omega) \otimes \mathbf{a}(\theta) \\ \mathbf{v}(\omega) &= [1 \ e^{j\omega} \ \dots \ e^{j(N-1)\omega}]^T \\ \eta &= [\mathbf{n}(1)^T \ \dots \ \mathbf{n}(N)^T]^T \end{aligned}$$

and \otimes represents the Kronecker product. The vector η_ℓ contains the stacked vector samples of the clutter and interference for range bin ℓ , and has an unknown covariance matrix denoted by

$$\mathcal{E}\{\eta_\ell \eta_\ell^H\} = \mathbf{R}.$$

The clutter is neither temporally nor spatially white; in fact, the rank of \mathbf{R} is typically much less than mN . The rank (ρ) of \mathbf{R} is important because it determines how many secondary data samples are required to accurately estimate \mathbf{R} . According to [6], the number of required samples is on the order of 2ρ to 5ρ . The fully adaptive approach to whitening this type of data is to multiply the data by the inverse square-root of an estimate of the matrix \mathbf{R} . Because the size of this matrix can become quite large, its low rank nature is exploited to derive reduced-dimension whitening algorithms. The next section summarizes the work in [1] as a background for extending the STAR filter.

3. SPACE-TIME AUTOREGRESSIVE FILTERING

Following the derivation in [1], the STAR approach assumes that a set of L matrices $\mathbf{H}_0, \mathbf{H}_1, \dots, \mathbf{H}_{L-1}$ of dimension $m' \times m$ exist that satisfy

$$\sum_{i=0}^{L-1} \mathbf{H}_i \mathbf{n}(t+i) = 0, \quad t = 1, \dots, N-L+1, \quad (3)$$

for the interference and clutter in the primary range bin. We may also write (3) in the following two different ways:

$$\underbrace{[\mathbf{H}_0 \ \dots \ \mathbf{H}_{L-1}]}_{\mathbf{H}^*} \underbrace{\begin{bmatrix} \mathbf{n}(1) & \dots & \mathbf{n}(N-L+1) \\ \vdots & \dots & \vdots \\ \mathbf{n}(L) & \dots & \mathbf{n}(N) \end{bmatrix}}_{\mathbf{N}} = 0 \quad (4)$$

or

$$\mathcal{H}^* \eta = 0, \quad (5)$$

where

$$\mathcal{H}^* = \begin{bmatrix} \mathbf{H}_0 & \dots & \mathbf{H}_{L-1} & & \\ & \mathbf{H}_0 & \dots & \mathbf{H}_{L-1} & \\ & & \ddots & \ddots & \\ & & & \mathbf{H}_0 & \dots & \mathbf{H}_{L-1} \end{bmatrix}. \quad (6)$$

In cases where the clutter is stationary, we assume that equations (4) and (5) also hold for the secondary data as well:

$$\mathbf{H}^* \mathbf{N}_k = 0 \quad (7)$$

$$\mathcal{H}^* \eta_k = 0, \quad (8)$$

for $k = 1, \dots, N_s$, where N_s is the number of secondary data snapshots used to train the filter.

The matrix \mathcal{H} is $mN \times m'(N-L+1)$. If (3) holds and m' and L are chosen so that $m'(N-L+1)$ is large enough, the columns of \mathcal{H} form a basis for the space orthogonal to the clutter and interference subspace. Although this relationship does not hold in practice due to the presence of thermal noise, a least squares solution is applied to approximate the subspace. This suggests the following space-time filter (similar to the matched subspace detectors in [7]) be used for interference rejection:

$$\mathbf{w}_{AR}(\theta, \omega) = \mathbf{P}_{\mathcal{H}} \mathbf{s}(\theta, \omega), \quad (9)$$

where $\mathbf{P}_{\mathcal{H}}$ is the projection onto the columns of \mathcal{H} :

$$\mathbf{P}_{\mathcal{H}} = \mathcal{H}(\mathcal{H}^* \mathcal{H})^{-1} \mathcal{H}^*. \quad (10)$$

We refer to the implementation of STAP with the weight vector of (9) as Space-Time AutoRegressive (STAR) filtering. The STAR filter weights are "adaptive" in the sense that \mathcal{H} must be estimated from the secondary data prior to computation of \mathbf{w}_{AR} .

4. RANGE-VARYING EXTENDED STAR FILTER

The STAR filter of the previous section is not designed to handle non-stationary interference of any kind. This section derives a STAR-based filter that assumes the clutter statistics vary linearly with range. This assumption is reasonable if the training region is kept short. The idea of using time-varying weights in a STAP algorithm was introduced in [8] as an extended sample matrix inversion algorithm and this idea was used for range-varying STAP weights in [2]. This technique increases the dimension of the problem by a factor of two but does improve the performance when there is a rapidly changing clutter locus.

The idea behind range-varying weights is that the weight vector is a function of range (r) to account for the non-stationary clutter locus. Expanding the weight vector into a power series yields

$$\mathbf{w}(r) = \mathbf{w}_o + r\tilde{\mathbf{w}}_o + \frac{r^2\tilde{\tilde{\mathbf{w}}}_o}{2} + \dots \quad (11)$$

The assumption is made that the clutter locus is changing slowly enough that for a given collection of ranges the weight vector is linear in r . Ignoring the higher order terms in the Taylor series, the weight vector as a function of the k^{th} range bin becomes

$$\mathbf{w}_k = \mathbf{w}_o + \alpha k \Delta \mathbf{w}_o, \quad (12)$$

where α is a normalization constant. Defining

$$\tilde{\mathbf{w}} = \begin{bmatrix} \mathbf{w}_o \\ \Delta \mathbf{w} \end{bmatrix} \quad (13)$$

the output of the filter may be written as

$$\mathbf{z} = \tilde{\mathbf{w}}^* \begin{bmatrix} \chi_k \\ \alpha k \chi_k \end{bmatrix} = \tilde{\mathbf{w}}^* \tilde{\chi}_k, \quad (14)$$

where $\tilde{\mathbf{x}}_k$ is the extended data vector.

Using this same idea for the STAR filter (*i.e.*, assuming that the STAR filter coefficients that null the clutter vary linearly with range) we can rewrite (3) using an extended data vector:

$$\sum_{i=0}^{L-1} [\mathbf{H}_i \quad \Delta\mathbf{H}_i] \begin{bmatrix} \mathbf{n}_k(t-i) \\ \alpha k \mathbf{n}_k(t-i) \end{bmatrix} = \mathbf{0}, \quad t = L+1, \dots, N. \quad (15)$$

Letting $\Delta\mathbf{H}$ and $\Delta\mathcal{H}$ be defined similar to \mathbf{H} in (4) and \mathcal{H} in (6) we may rewrite (7) and (8) as

$$\begin{bmatrix} \mathbf{H}^* & \Delta\mathbf{H}^* \end{bmatrix} \begin{bmatrix} \mathbf{N}_k \\ \alpha k \mathbf{N}_k \end{bmatrix} = \mathbf{0} \quad (16)$$

$$\begin{bmatrix} \mathcal{H}^* & \Delta\mathcal{H}^* \end{bmatrix} \begin{bmatrix} \eta_k \\ \alpha k \eta_k \end{bmatrix} = \mathbf{0}. \quad (17)$$

The filter parameters \mathbf{H} and $\Delta\mathbf{H}$ may then be estimated using the left null space of the matrix

$$\tilde{\mathbf{N}} = \begin{bmatrix} \mathbf{N}_{-Q} & \dots & \mathbf{N}_Q \\ -\alpha Q \mathbf{N}_{-Q} & \dots & \alpha Q \mathbf{N}_Q \end{bmatrix}, \quad (18)$$

where $Q = \frac{N_s}{2}$. Following what was done in [2], the constant α is chosen as

$$\alpha = \sqrt{\frac{12}{(N_s + 2)(N_s + 1)}} \quad (19)$$

to yield a "flat" noise subspace.

To define what the weight vector is, let

$$\tilde{\mathbf{H}} = \begin{bmatrix} \mathcal{H} \\ \Delta\mathcal{H} \end{bmatrix} \quad (20)$$

so that

$$\mathbf{w}_E(\theta, \omega) = \mathbf{P}_{\tilde{\mathbf{H}}} \begin{bmatrix} s(\theta, \omega) \\ \mathbf{0} \end{bmatrix}. \quad (21)$$

Filtering the extended data vector with (21) is referred to as the Extended STAR (ESTAR) filter. When estimating a range varying weight vector using data that also varies with range, a higher number of training vectors may be used before performance starts to degrade.

5. STAR FILTERING FOR HOT CLUTTER

When the radar platform is operating in an environment where there is an airborne jamming source present, two main considerations must be made. First, the hot clutter covariance changes from pulse to pulse and second, the hot clutter has non-zero correlations across range bins [3]. This section derives a STAR based filter that is effective in canceling hot clutter. The baseline STAR filter is first modified to handle any type of interference that changes from pulse to pulse (as with intrinsic clutter motion) and then an additional dimension is added to the vector autoregressive filter to account for the correlations across range bins.

The model for the clutter in (3) is no longer valid since the spatial covariance changes from pulse to pulse. If the standard STAR model is used in a non-stationary environment like hot clutter, it tries to account for the time variations in the data by increasing the number of filter taps required to achieve clutter cancellation.

A better model for this is to let the coefficients of the space-time prediction error filter change with time:

$$\mathcal{H}_{TV}^* = \begin{bmatrix} \mathbf{H}_0(1) & \dots & \mathbf{H}_{L-1}(1) & & \\ & \ddots & & \ddots & \\ & & \mathbf{H}_0(n) & \dots & \mathbf{H}_{L-1}(n) \end{bmatrix}, \quad (22)$$

where $n = N - L + 1$ and where each block row is a set of new coefficients based on dropping the data from the oldest pulse and adding the data from the most recent pulse. For this time-varying STAR filter, a greater number of filter parameters must be estimated (n times the degrees of freedom required for the standard STAR algorithm) and therefore, more sample support is required to train the filter.

To complete the derivation of the 3D-STAR filter, a few definitions need to be made. To clarify the notation, sampling across pulses is called slow-time sampling and sampling across range bins is called fast-time sampling. Let P be the number of fast-time samples over which the hot clutter is correlated.

In order to utilize the fast-time correlation of the data, an extra dimension is added to the STAR filter. We assume for a moment that the interference is stationary across the pulses (slow-time). This filter will model the fast-time and slow-time correlations with a two-dimensional VAR filter. For a set of LJ matrices of size $M' \times M$, assume that the clutter obeys the model

$$\sum_{j=0}^{J-1} \sum_{i=0}^{L-1} \mathbf{H}_{i,j} \mathbf{n}_{k+j}(t+i) = \mathbf{0}, \quad t = 1, \dots, N - L + 1$$

$$k = 1, \dots, P - J + 1, \quad (23)$$

where $k = 0$ is the range bin of interest and $\mathbf{n}_k(t)$ is the spatial snapshot for the t^{th} pulse and the k^{th} range bin. This may also be expressed as

$$\sum_{j=0}^{J-1} \mathcal{H}_j^* \mathbf{e}_{k+j} = \mathbf{0} \quad k = 1, \dots, P - J + 1, \quad (24)$$

where \mathcal{H}_j is the matrix defined in (6) with a subscript j to indicate which fast-time sample it is associated with. From this point we again take into account the slow-time variations caused by the hot clutter by replacing \mathcal{H}_j with the slow-time varying filter $\mathcal{H}_{TV,j}$.

Rewriting this sum with the time-varying filter we get

$$\mathbf{H}^* \eta_{3d}(k) = \mathbf{0}, \quad (25)$$

where

$$\eta_{3d}(k) = \begin{bmatrix} \eta_k \\ \vdots \\ \eta_{k+P-1} \end{bmatrix}$$

$$\mathbf{H}^* = \begin{bmatrix} \mathcal{H}_{TV,0}^* & \dots & \mathcal{H}_{TV,J-1}^* & & \\ & \ddots & & \ddots & \\ & & \mathcal{H}_{TV,0}^* & \dots & \mathcal{H}_{TV,J-1}^* \end{bmatrix}.$$

Assuming that there is target energy in the $k = 0$ range bin, then there will also be target energy in the vectors $\eta_{3d}(0)$, $\eta_{3d}(-1)$, \dots , $\eta_{3d}(-P+1)$ which may not be used for training the filter. In

order to define the algorithm to find the filter coefficients let

$$\tilde{\mathbf{H}}(t)^* = [\mathbf{H}_{0,0}(t) \cdots \mathbf{H}_{L-1,J-1}(t)] \quad (26)$$

$$\mathbf{g}_k(t) = \begin{bmatrix} \mathbf{n}_k(t) \\ \vdots \\ \mathbf{n}_k(t+L-1) \end{bmatrix} \quad (27)$$

$$\mathbf{G}_k(t) = \begin{bmatrix} \mathbf{g}_k(t) & \cdots & \mathbf{g}_{k+P-J}(t) \\ \vdots & & \vdots \\ \mathbf{g}_{k+J-1}(t) & \cdots & \mathbf{g}_{k+P-1}(t) \end{bmatrix} \quad (28)$$

$$\mathbf{G}(t) = [\mathbf{G}_1(t) \cdots \mathbf{G}_{N_s}(t)]. \quad (29)$$

The filter coefficients can then be found by the following least squares criterion:

$$\hat{\mathbf{H}}(t) = \arg \min_{\mathbf{H}(t)} \| \tilde{\mathbf{H}}(t)^* \mathbf{G}(t) \|_F^2 \quad t = 1, \dots, N-L+1 \quad (30)$$

subject to the constraint that $\mathbf{H}(t)^* \mathbf{H}(t) = \mathbf{I}$. From this point the m' left singular vectors corresponding to the smallest singular values of each $\mathbf{G}(t)$ matrix will be used to compute the $N-L+1$ sets of filter coefficients which define $\tilde{\mathbf{H}}$. With a defined subspace, a weight vector for mitigation of hot clutter is

$$\mathbf{w}_{3D}(\theta, \omega) = \mathbf{P}_{\tilde{\mathbf{H}}} \mathbf{s}_{3D}(\theta, \omega), \quad (31)$$

where

$$\mathbf{s}_{3D}(\theta, \omega) = \begin{bmatrix} 1 \\ 0 \\ \vdots \\ 0 \end{bmatrix} \otimes \mathbf{s}(\theta, \omega). \quad (32)$$

This 3D-STAR filter will require more training data than the STAR filter (on the order of $N-L+1$ times more) due to the non-stationary prediction error filter that is used in the implementation. This additional sample support requirement is less of an issue than with other 3D implementations because the STAR approach typically requires much less secondary data for good performance. The 3D-STAR filter also assumes that the data is stationary for P fast-time samples.

6. NUMERICAL RESULTS

The algorithms presented herein are tested using a data set created by MIT Lincoln Laboratory that simulates the output of a 20 element array. These elements lie along a circular arc of 120° with radius 2.96m and are assumed to have a cosine-shaped response with a -30 dB backlobe for both azimuth and elevation dimensions. The airborne platform is moving with a velocity of 100 m/s above a 4/3 earth model at an altitude of 9000m. The operating frequency of the radar is taken to be 435 MHz, the radar bandwidth and sampling frequency are 3.75 MHz, the pulse-repetition frequency is 300 Hz, and $N = 18$ pulses are assumed to be transmitted during one CPI. Data are generated for 9325 range gates between 20 and 400 km with a clutter-to-white-noise power ratio of 40 dB at a range of 100km.

Hot clutter is included in the data by adding a term of the form

$$\mathbf{j}_k = b_j \begin{bmatrix} \mathbf{c}_k(1) \\ \vdots \\ \mathbf{c}_k(N) \end{bmatrix},$$

where b_j is the amplitude of the jammer,

$$\mathbf{c}_k(t) = \mathbf{a}(\theta_j) z_k + \sum_{i=1}^{\ell} \mathbf{b}_i(t) z_{k-i}$$

is the contribution of the hot clutter for a single pulse at range k , ℓ is the longest multipath delay, θ_j is the direction of arrival of the jammer signal, z_k is the jammer waveform (white in both slow and fast-time), and \mathbf{b}_i is a random vector that approximates the sum of the spatial steering vectors for each of the multipath signals. When present, the jammer-to-clutter power ratio is assumed to be 10 dB. When secondary data are used to estimate the clutter covariance or STAR filter parameters, equal amounts of data from range bins on either side of the target range bin are used.

The true clutter covariance matrix used to generate the data is known for 20 of the 9325 range bins, and thus the maximum achievable SINR can be calculated at these ranges. To illustrate the performance of the algorithms we use either the SINR loss as a function of Doppler for an azimuth of 0° or the "average" SINR loss as compared with the optimal (known covariance) solution. This average SINR loss is defined as the area between the algorithm's SINR curve and that achievable assuming \mathbf{R} is known. This is depicted in Figure 1. The ESTAR filter will be compared to the range-varying extended post-Doppler PRI staggered STAP algorithm [2] and the 3D-STAR algorithms will be compared with the optimized 3D pre-Doppler STAP algorithm [3]. For the STAR based filters, $M' = 20$ is used for all the examples and for the partially adaptive STAP algorithm, three pulses at a time are processed and a diagonal loading of about five times the noise level is used for sample matrix inversion.

A performance evaluation of the ESTAR filter at a range of 20km is shown in Figures 2 and 3. Figure 2 compares the performance of the ESTAR filter and the basic STAR filter as a function of L for $N_s = 50$ (2km training window). This figure shows that the ESTAR filter does perform better than the STAR filter at close ranges. We also see that the ESTAR filter requires fewer filter taps than the STAR filter thus offsetting some of the additional computational cost associated with the extended implementation. Figure 3 compares the performance of the STAR filters with the range-varying extended PRI staggered and fully adaptive STAP algorithms as a function of training length. Note that the performance of the STAR algorithm degrades quickly as more training data is used. The extended PRI STAP and ESTAR filters both have nearly flat performance as N_s is increased due to the range-varying weights. The ESTAR filter also has much better performance than the extended PRI STAP algorithm because it requires much less training data to converge to its best performance.

Another aspect of performance is the computational load required to implement the algorithms. For the STAR algorithms the implementation is broken up into two steps. The first step involves taking the SVD of the $2ML \times (N-L+1)N_s$ data matrix $\tilde{\mathbf{N}}$ and the second is forming the projection operator. The bulk of the computation involved in this second step is finding the inverse of $\tilde{\mathbf{H}}^* \tilde{\mathbf{H}}$ which is usually a sparse banded matrix. Taking this into account the computational load for the ESTAR algorithm is

$$O(4(ML)^2(N-L+1)N_s) + O((ML)^2(N-L+1)M').$$

For the parameters of the circular array data with $L = 4$ and $M' = 20$, the computational cost is

$$\text{ESTAR} = O(3.84 \times 10^5 N_s) + O(1.92 \times 10^6).$$

Comparing this with the cost of the STAR filter (at $L = 5$):

$$\begin{aligned}\text{STAR} &= O((ML)^2(N-L+1)N_s) \\ &\quad + O((ML)^2(N-L+1)M') \\ &= O(1.4 \times 10^5 N_s) + O(2.8 \times 10^6)\end{aligned}$$

the ESTAR algorithm has only a small increase in computational load. The extended PRI STAP algorithm has a computational cost of

$$\begin{aligned}\text{EPRI-STAP} &= O(4(MK)^2(N-K+1)N_s) \\ &\quad + O(4(MK)^2(N-K+1)\rho) \\ &= O(2.3 \times 10^5 N_s) + O(2.0 \times 10^7)\end{aligned}$$

where $K = 3$ pulses that are processed at a time and $\rho = 90$ is the approximate rank of each sub-CPI. From this we see that if N_s is not too big ($N_s < 100$), then the ESTAR algorithm requires much fewer computations than the PRI-staggered STAP algorithm.

Figures 4-6 illustrate the performance of the 3D-STAR filter when there is hot clutter present and when the direct path jamming signal is in the mainbeam of the radar system. Figure 4 compares the performance of the 3D-STAR filter to the basic STAR filter as a function of L . The 3D-STAR filter outperforms the STAR filter with a small number of filter taps by utilizing the slow-time-varying taps as well as the additional fast time tap. Figure 5 compares the STAR filters to the 3D optimized pre-Doppler and fully adaptive STAP algorithms as a function of training data. In this case the pre-Doppler and 3D-STAR algorithms have a very similar performance with the pre-Doppler algorithm slightly outperforming the 3D-STAR filter. However, Figure 6, which shows the SINR at $N_s = 80$ or 3.2 km, illustrates that the 3D-STAR filter has a narrower clutter notch which results in a lower detectable velocity. If the small loss in performance away from the clutter notch is tolerable, the 3D-STAR filter is more desirable due to its greater percentage of usable Doppler space.

The computational cost of the STAR ($L = 7$), 3D-STAR ($L = 2$, $J = 2$), and 3D-pre Doppler ($K = 3$ pulses) algorithms for the system parameters described above are as follows:

$$\begin{aligned}\text{STAR} &= O(2.35 \times 10^5 N_s) + O(4.7 \times 10^6) \\ \text{3D-STAR} &= O((MLJ)^2(N-L+1)(P-J+1)N_s) \\ &\quad + O((MLJ)^2(N-L+1)(P-J+1)M') \\ &= O(2.18 \times 10^5 N_s) + O(4.35 \times 10^6) \\ \text{pre-Dopp} &= O((MKP)^2(N-K+1)N_s) \\ &\quad + O((MKP)^2(N-K+1)\rho) \\ &= O(5.18 \times 10^5 N_s) + O(7.0 \times 10^7)\end{aligned}$$

where $\rho = 135$ is the approximate rank of the sub-CPI covariance matrix. Again we see that the STAR and 3D-STAR algorithms have nearly the same computational cost when the filter orders are chosen close to the best value. It is also seen that the pre-Doppler algorithm requires a large number of computations when compared with the 3D-STAR algorithm.

7. CONCLUSIONS

This paper has presented modifications to the space-time autoregressive (STAR) filter for two types of non-stationary interference.

The first modified filter (ESTAR) is used when the clutter statistics are varying with range as is the case for non-linear antenna arrays or bistatic radar systems. The second modification (3D-STAR) is used in the presence of hot clutter which arises when an airborne jamming source is present. These two modifications provide an increase in performance over the standard STAR filter when used in non-stationary environments without a major increase in computational burden. We have shown in numerical experiments and computational analysis that the ESTAR filter is superior to the extended PRI-staggered post-Doppler STAP algorithm when there is a rapidly changing clutter locus. We have also shown that the 3D-STAR filter has a little more usable Doppler space than the 3D optimized pre-Doppler STAP algorithm and the 3D-STAR algorithm achieves this performance with much less computation.

8. REFERENCES

- [1] A. L. Swindlehurst and P. Parker, "Parametric clutter rejection for space-time adaptive processing," in *Proc. of the ASAP-2000 Workshop*, (MIT Lincoln Laboratory, Lexington, MA), 2000.
- [2] M. Zatman, "Circular array STAP," *IEEE Trans. on Aerospace and Electronic Systems*, vol. 36, pp. 510-517, April 2000.
- [3] D. J. Rabideau, "Clutter and jammer multipath cancellation in airborne adaptive radar," *IEEE Trans. on Aerospace and Electronic Systems*, vol. 36, pp. 565-583, April 2000.
- [4] J. Román, D. Davis, and J. Michels, "Multichannel parametric models for airborne phased array clutter," in *Proc. IEEE Radar Conf.*, vol. 1, (Syracuse, NY), pp. 72-77, 1997.
- [5] J. Ward, "Space-time adaptive processing for airborne radar," Tech. Rep. TR-1015, MIT Lincoln Labs, Dec 1994.
- [6] I. S. Reed, J. D. Mallett, and L. E. Brennan, "Rapid convergence rate in adaptive arrays," *IEEE Trans. on Aerospace and Electronic Systems*, vol. AES-10, pp. 853-863, Nov 1974.
- [7] L. Scharf and B. Friedlander, "Matched subspace detectors," *IEEE Trans. on Sig. Proc.*, vol. 42, pp. 2146-2157, August 1994.
- [8] S. D. Hayward, "Adaptive beamforming for rapidly moving arrays," in *Int. Conf. on Radar*, (Beijing), pp. 480-483, CIE, Oct. 1996.

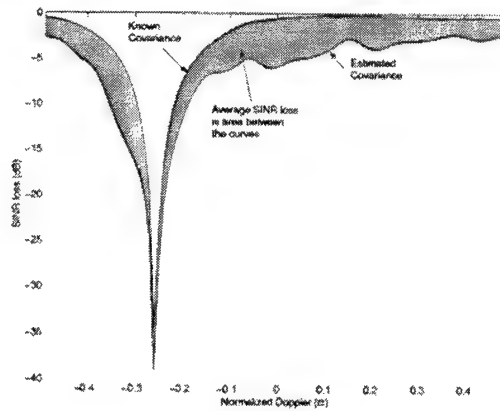


Figure 1: Definition of average SINR loss for a particular algorithm.

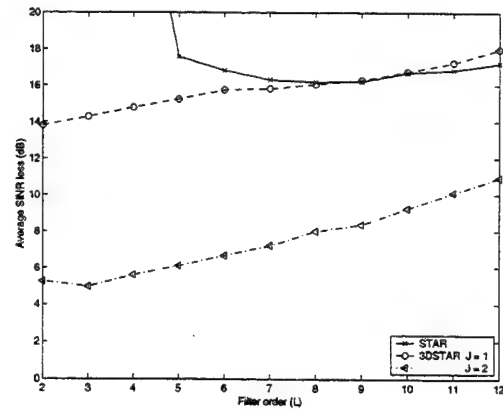


Figure 4: Performance of STAR filters as a function of filter order with hot clutter present.

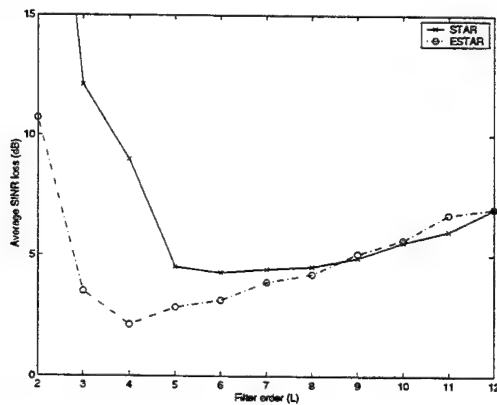


Figure 2: Performance of ESTAR and STAR at 20 km as a function of filter order.

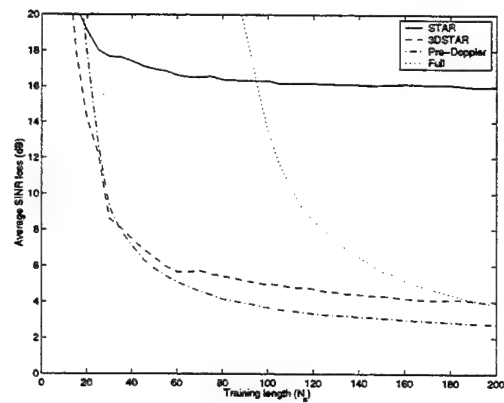


Figure 5: Convergence of STAR, 3D-STAR, pre-Doppler, and fully adaptive algorithms with hot clutter present.

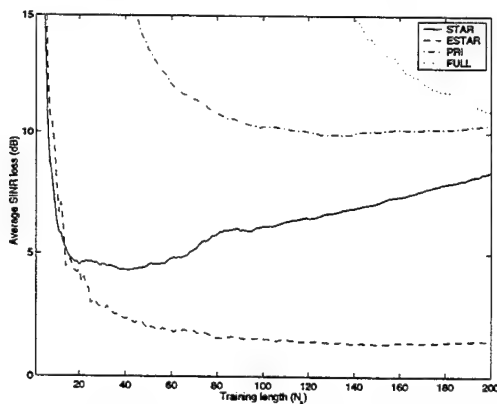


Figure 3: Comparison with PRI-Staggered and fully adaptive STAP at 20 km as a function of training length

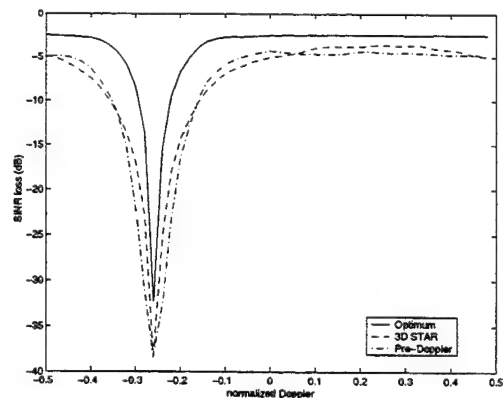


Figure 6: SINR of 3D-STAR and pre-Doppler algorithms with $N_s = 80$ and hot clutter present.

INTERFERENCE ESTIMATION AND MITIGATION FOR STAP USING THE TWO-DIMENSIONAL WOLD DECOMPOSITION PARAMETRIC MODEL

Joseph M. Francos

Elec. & Comp. Eng. Dept.
Ben-Gurion University
Beer Sheva 84105, Israel

Wenyin Fu and Arye Nehorai

Elec. Eng. & Comp. Sci. Dept.
University of Illinois at Chicago
Chicago, IL 60607-7053, U.S.A.

ABSTRACT

We develop parametric modeling and estimation methods for STAP data based on the results of the 2-D Wold-like decomposition. We show that the same parametric model that results from the 2-D Wold-like orthogonal decomposition naturally arises as the physical model in the problem of space-time processing of airborne radar data. We exploit this correspondence to derive computationally efficient parametric fully adaptive and partially adaptive detection algorithms. Having estimated the parametric models of the noise and interference components of the field, the estimated parameters are substituted into the parametric expression of the covariance matrix to obtain an estimate of the interference-plus-noise covariance matrix. Hence the fully-adaptive weight vector is obtained. Moreover, it is proved that it is sufficient to estimate only the spectral support parameters of each interference component in order to obtain a projection matrix onto the subspace orthogonal to the interference subspace. The proposed partially adaptive parametric processing algorithm employs this property. The proposed parametric interference mitigation procedures can be applied even when only the information in a single range gate is available, thus achieving high performance gain when the data in the different range gates cannot be assumed stationary.

1. INTRODUCTION

We propose a new approach for parametric modeling and estimation of space-time airborne radar data, based on the 2-D Wold-like decomposition of random fields. The goal of space-time adaptive processing is to manipulate the available data to achieve high gain at the target angle and Doppler and maximal mitigation along both the jamming and clutter lines. Because the interference covariance matrix is unknown a priori, it is typically estimated using sample covariances obtained from averaging over a few range gates. Next, a weight vector is computed from the inverse of the sample covariance matrix, [1]-[5]. In [8], an approach

that bypasses the need to estimate the covariance matrix was presented: The data collected in a single range gate was employed to obtain a least squares estimate of the signal power at each hypothesized DOA, through evaluation of a weight vector constrained to null the unknown interference and noise. In [9] a simple ad-hoc model of the clutter signal and covariance matrix is proposed. The model represents the spectral density of the clutter as a sum of Gaussian-shaped humps along the support of the clutter ridge. In [10] this model is employed to estimate the clutter covariance matrix from the data observed in a single range gate.

In this paper, we suggest to adopt the 2-D Wold-like decomposition of random fields, [6], as the parametric model of the observed data. Employing this model, we derive computationally efficient algorithms useful for parametrically estimating both the jamming and clutter fields. The estimation procedure we propose is capable of producing estimates of the interference signals parametric models even from the information in a single range gate. Hence, no averaging over a few range gates is required, achieving high performance gain in the practical case when the data in the different range gates is non-stationary. Having estimated the interference terms parametric models, their covariance matrix can be evaluated based on the estimated parameters. Moreover, the problem of evaluating the rank of the low-rank covariance matrix of the interference is solved as a by-product of obtaining the parametric estimates of the interference components. Once the parametric models of the interference components have been estimated, several alternative detection procedures are available. In this paper we present two such methods: the parametric fully-adaptive processing, and the parametric partially-adaptive processing.

2. THE RANDOM FIELD MODEL

In this section we shall briefly describe the 2-D Wold-like decomposition of random fields, [6]. Let $\{y(n, m)\}$, $(n, m) \in \mathbb{Z}^2$, be a complex valued, regular, homogeneous random field. Then, $y(n, m)$ can be uniquely represented by the orthogonal decomposition

$$y(n, m) = w(n, m) + v(n, m) \quad (1)$$

The field $\{v(n, m)\}$ is a deterministic random field. The field $\{w(n, m)\}$ is purely-indeterministic and has a unique

This work supported by the Air Force Office of Scientific Research under Grants F49620-99-1-0067 and F49620-00-1-0083.

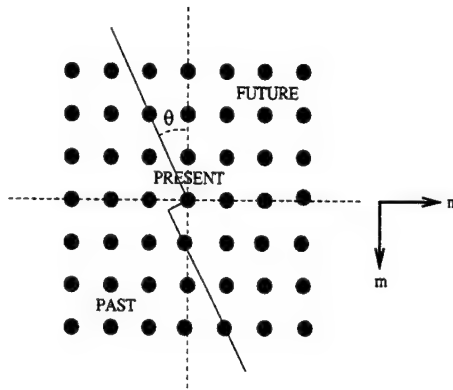


Figure 1: RNSHP support; example with $\alpha = 2$ and $\beta = 1$.

white innovations driven moving average representation, given by

$$w(n, m) = \sum_{(0,0) \preceq (k,\ell)} b(k, \ell) u(n-k, m-\ell) \quad (2)$$

where $\sum_{(0,0) \preceq (k,\ell)} b^2(k, \ell) < \infty$; $b(0,0) = 1$, and $\{u(n, m)\}$ is the innovations field of $\{y(n, m)\}$. The notation \preceq implies that the summation is performed over all the samples that are in the "past" of the (n, m) sample, where the past is defined with respect to any selected choice of NSHP total-ordering on the 2-D lattice. (See, for example, Fig. 1.) It is possible to define, [6], a family of NSHP total-order definitions such that the boundary line of the NSHP has a rational slope. Let α and β be two coprime integers, such that $\alpha \neq 0$. The angle θ of the slope is given by $\tan \theta = \beta/\alpha$. (See, for example, Fig. 1.) A NSHP of this type is called *rational non-symmetrical half-plane* (RNSHP). For the case where $\alpha = 0$ the RNSHP is uniquely defined by setting $\beta = 1$. (For the case where $\beta = 0$ the RNSHP is uniquely defined by setting $\alpha = 1$.) We denote by O the set of all possible RNSHP definitions on the 2-D lattice, (i.e., the set of all NSHP definitions in which the boundary line of the NSHP has a rational slope). The introduction of the family of RNSHP total-ordering definitions results in the following countably infinite orthogonal decomposition of the deterministic component of the random field:

$$v(n, m) = p(n, m) + \sum_{(\alpha,\beta) \in O} e_{(\alpha,\beta)}(n, m). \quad (3)$$

The random field $\{p(n, m)\}$ is called *half-plane deterministic*. The field $\{e_{(\alpha,\beta)}(n, m)\}$ is the *evanescent* component that corresponds to the RNSHP total-ordering definition $(\alpha, \beta) \in O$.

Hence, if $\{y(n, m)\}$ is a 2-D regular and homogeneous random field, then $y(n, m)$ can be uniquely represented by the orthogonal decomposition

$$y(n, m) = w(n, m) + p(n, m) + \sum_{(\alpha,\beta) \in O} e_{(\alpha,\beta)}(n, m). \quad (4)$$

It is further shown in [6] that the spectral measures of the decomposition components in (4) are mutually singular. A model for the evanescent field which corresponds to the RNSHP defined by $(\alpha, \beta) \in O$ is given by

$$\begin{aligned} e_{(\alpha,\beta)}(n, m) &= \sum_{i=1}^{I(\alpha,\beta)} e_i^{(\alpha,\beta)}(n, m) \\ &= \sum_{i=1}^{I(\alpha,\beta)} s_i^{(\alpha,\beta)}(n\alpha - m\beta) \exp(j2\pi \frac{\nu_i^{(\alpha,\beta)}}{\alpha^2 + \beta^2} (n\beta + m\alpha)) \end{aligned} \quad (5)$$

where the 1-D purely-indeterministic, complex valued processes $\{s_i^{(\alpha,\beta)}(n\alpha - m\beta)\}$ and $\{s_j^{(\alpha,\beta)}(n\alpha - m\beta)\}$, are zero-mean and mutually orthogonal for all $i \neq j$. Hence, the "spectral density function" of each evanescent field has the form of a countable sum of 1-D delta functions which are supported on lines of rational slope in the 2-D spectral domain.

One of the half-plane-deterministic field components, which is of prime importance in the STAP problem is the harmonic random field

$$h(n, m) = \sum_{p=1}^P C_p \exp(j2\pi(n\omega_p + m\nu_p)) \quad (6)$$

where the C_p 's are mutually orthogonal random variables, and (ω_p, ν_p) are the spatial frequencies of the p th harmonic.

3. THE STAP MODEL AND THE 2-D WOLD DECOMPOSITION

The random field parametric model that results from the 2-D Wold-like orthogonal decomposition naturally arises as the physical model in the problem of space-time processing of airborne radar data. In the latter problem the target signal is modeled as a random amplitude complex exponential where the exponential is defined by a space-time steering vector that has the target's angle and Doppler. In other words, in the space-time domain the target model is that of a 2-D harmonic component similar to (6). The purely-indeterministic component of the space-time field is the sum of a white noise field due to the internally generated receiver amplifier noise, and a colored noise field due to the sky noise contribution. The presence of a jammer results in a barrage of noise localized in angle and distributed over all Doppler frequencies. Thus, in the angle-Doppler domain each jammer contributes a 1-D delta function located at a specific angle, and therefore parallel to the Doppler axis. In the space-time domain each jammer is modeled as an evanescent component with $(\alpha, \beta) = (1, 0)$ such that its 1-D modulating process is a white noise process. The ground clutter results in an additional evanescent component of the observed 2-D space-time field. The clutter echo from a single ground patch has a Doppler frequency that linearly depends on its aspect with respect to the platform. Hence, clutter from all angles lies in a "clutter ridge", supported on a diagonal line (that generally wraps around in Doppler) in the angle-Doppler domain. A model of the clutter field is then given by (5) with (α, β) such that $\tan \beta/\alpha$ corresponds to the slope of the clutter ridge. Since the rational numbers

are dense in the set of real numbers, an irrational slope of the clutter ridge can be approximated arbitrarily close, by a rational one. Hence any clutter signal can be either exactly modeled, or approximated by an evanescent field.

We therefore conclude that the foregoing derivation opens the way for new *parametric* solutions that can simplify and improve existing methods of STAP.

4. ESTIMATION OF THE COMPONENTS PARAMETERS: PROBLEM DEFINITION

We next state our assumptions and introduce some necessary notations. Let $\{y(n, m)\}$, $(n, m) \in D$ where $D = \{(i, j) | 0 \leq i \leq S-1, 0 \leq j \leq T-1\}$ be the observed random field.

Assumption 1: The purely-indeterministic component $\{w(n, m)\}$ is a zero mean circular complex valued random field.

Assumption 2: The number $I = \sum_{(\alpha, \beta) \in O} I^{(\alpha, \beta)}$ of evanescent components in the field, is *a-priori* known. This assumption can be later relaxed.

Assumption 3: For each evanescent field $\{e_i^{(\alpha, \beta)}\}$, the modulating 1-D purely-indeterministic process $\{s_i^{(\alpha, \beta)}\}$ is a zero-mean circular complex valued process.

Let $\mathbf{y} = [y(0, 0), \dots, y(0, T-1), \dots, y(S-1, T-1)]^T$, and let \mathbf{w} , $\mathbf{e}_i^{(\alpha, \beta)}$ be similarly defined. Let

$$\begin{aligned} \xi_i^{(\alpha, \beta)} = & \\ & [s_i^{(\alpha, \beta)}(0), s_i^{(\alpha, \beta)}(-\beta), \dots, s_i^{(\alpha, \beta)}(-(T-1)\beta), \\ & s_i^{(\alpha, \beta)}(\alpha), s_i^{(\alpha, \beta)}(\alpha - \beta), \dots, s_i^{(\alpha, \beta)}(\alpha - (T-1)\beta), \\ & \dots, s_i^{(\alpha, \beta)}((S-1)\alpha), \dots, s_i^{(\alpha, \beta)}((S-1)\alpha - (T-1)\beta)]^T \end{aligned} \quad (7)$$

be the vector whose elements are the observed samples from the 1-D modulating process $\{s_i^{(\alpha, \beta)}\}$. Define

$$\begin{aligned} \mathbf{v}^{(\alpha, \beta)} = & \\ & [0, \alpha, \dots, (T-1)\alpha, \\ & \beta, \beta + \alpha, \dots, \beta + (T-1)\alpha, \dots, \\ & (S-1)\beta, (S-1)\beta + \alpha, \dots, (S-1)\beta + (T-1)\alpha]^T \end{aligned} \quad (8)$$

Given a scalar function $f(v)$, we will denote the matrix, or column vector, consisting of the values of $f(v)$ evaluated for all the elements of \mathbf{v} , where \mathbf{v} is a matrix, or a column vector, by $f(\mathbf{v})$. Using this notation, we define

$$\mathbf{d}_i^{(\alpha, \beta)} = \exp(j2\pi \frac{\nu_i^{(\alpha, \beta)}}{\alpha^2 + \beta^2} \mathbf{v}^{(\alpha, \beta)}) \quad (9)$$

Thus, using (5), we have that

$$\mathbf{e}_i^{(\alpha, \beta)} = \xi_i^{(\alpha, \beta)} \odot \mathbf{d}_i^{(\alpha, \beta)}, \quad (10)$$

where \odot denotes an element by element product of the vectors.

Note that whenever $n\alpha - m\beta = k\alpha - \ell\beta$ for some integers n, m, k, ℓ such that $0 \leq n, k \leq S-1$ and $0 \leq m, \ell \leq T-1$, the same element of $\xi_i^{(\alpha, \beta)}$ appears more than once in the

vector. It can be shown, [7], that for a rectangular observed field of dimensions $S \times T$ the number of *distinct* samples from the random process $\{s_i^{(\alpha, \beta)}\}$ that are found in the observed field is $N_c = (S-1)|\alpha| + (T-1)|\beta| + 1 - (|\alpha|-1)(|\beta|-1)$. This is because N_c is the number of different "columns" one can define on such a rectangular lattice for a RNSHP defined by (α, β) . We therefore define the *concentrated version*, $\mathbf{s}_i^{(\alpha, \beta)}$ of $\xi_i^{(\alpha, \beta)}$ to be an N_c dimensional column vector of non-repeating samples of the process $\{s_i^{(\alpha, \beta)}\}$. Thus for any (α, β) we have that

$$\xi_i^{(\alpha, \beta)} = \mathbf{A}_i^{(\alpha, \beta)} \mathbf{s}_i^{(\alpha, \beta)} \quad (11)$$

where $\mathbf{A}_i^{(\alpha, \beta)}$ is rectangular matrix of zeros and ones which replicates rows of $\mathbf{s}_i^{(\alpha, \beta)}$.

Note however that due to boundary effects, the vector $\mathbf{s}_i^{(\alpha, \beta)}$ is not composed of consecutive samples from the process $\{s_i^{(\alpha, \beta)}\}$ unless $|\alpha| \leq 1$ or $|\beta| \leq 1$. In other words, for some arbitrary α and β there are missing samples in $\mathbf{s}_i^{(\alpha, \beta)}$. We note that the covariance matrix $\mathbf{R}_i^{(\alpha, \beta)}$ which characterizes the process $\{s_i^{(\alpha, \beta)}\}$ is defined in terms of the concentrated version vector $\mathbf{s}_i^{(\alpha, \beta)}$ i.e., $\mathbf{R}_i^{(\alpha, \beta)} = E[\mathbf{s}_i^{(\alpha, \beta)} (\mathbf{s}_i^{(\alpha, \beta)})^H]$ and not in terms of the covariance matrix of the vector $\xi_i^{(\alpha, \beta)}$, $\tilde{\mathbf{R}}_i^{(\alpha, \beta)} = E[\xi_i^{(\alpha, \beta)} (\xi_i^{(\alpha, \beta)})^H]$. The matrix $\tilde{\mathbf{R}}_i^{(\alpha, \beta)}$ is a singular matrix, given by $\tilde{\mathbf{R}}_i^{(\alpha, \beta)} = \mathbf{A}_i^{(\alpha, \beta)} \mathbf{R}_i^{(\alpha, \beta)} (\mathbf{A}_i^{(\alpha, \beta)})^T$.

Since the evanescent components $\{e_i^{(\alpha, \beta)}\}$, are mutually orthogonal, and since all the evanescent components are orthogonal to the purely-indeterministic component, we conclude that Γ , the covariance matrix of \mathbf{y} , has the form

$$\Gamma = \Gamma_{PI} + \sum_{(\alpha, \beta) \in O} \sum_{i=1}^{I^{(\alpha, \beta)}} \Gamma_i^{(\alpha, \beta)}, \quad (12)$$

where $\Gamma_i^{(\alpha, \beta)}$ is the covariance matrix of $\mathbf{e}_i^{(\alpha, \beta)}$.

Using (10) and (5) we find that

$$\Gamma_i^{(\alpha, \beta)} = \tilde{\mathbf{R}}_i^{(\alpha, \beta)} \odot (\mathbf{d}_i^{(\alpha, \beta)} (\mathbf{d}_i^{(\alpha, \beta)})^H). \quad (13)$$

5. PARAMETRIC ESTIMATION OF THE INTERFERENCE COMPONENTS

In this section we derive a computationally efficient algorithm for estimating both the jamming and clutter fields, based on the above results. The proposed estimation algorithm of the spectral support parameters of the evanescent field, α, β and $\nu_i^{(\alpha, \beta)}$ is based on the observation (see the evanescent field model (5)) that for a fixed $c = n\alpha - m\beta$ (i.e., along a line on the sampling grid), the samples of the evanescent component are the samples of a 1-D constant amplitude harmonic signal, whose frequency is $\nu_i^{(\alpha, \beta)}$. The algorithm is implemented by the following three-step procedure:

In the presence of an evanescent component, the peaks of the observed field periodogram are concentrated along a straight line, such that its slope is defined by the two coprime integers α and β . Hence, several alternative approaches for obtaining an initial estimate of the spectral

support parameters of the evanescent component can be derived by taking the Radon or Hough transforms, [12], of the observed field periodogram. (The current implementation employs the Hough transform for detecting straight lines in 2-D arrays). However, due to noise presence, this estimate may perturbate. Since on a finite dimension observed field only a finite number of possible (α, β) pairs may be defined, the output of the initial stage is a set of possible (α, β) pairs such that the ratio $\frac{\beta}{\alpha}$ is close to the ratio obtained for the (α, β) pair estimated by the Hough transform.

For each possible (α, β) pair we next evaluate the frequency parameter of the evanescent component, $\nu_i^{(\alpha, \beta)}$. Assuming the considered (α, β) pair is the correct one, we know that in the absence of background noise, for a fixed $c = n\alpha - m\beta$ (i.e., along a line on the sampling grid), the samples of the evanescent component are the samples of a 1-D constant amplitude harmonic signal, whose frequency is $\nu_i^{(\alpha, \beta)}$. Hence, by considering the samples along such a line we obtain samples of a 1-D constant amplitude harmonic signal whose frequency $\nu_i^{(\alpha, \beta)}$ can be easily estimated using any standard frequency estimation algorithm (e.g., the 1-D DFT).

The test for detecting the correct (α, β) and $\nu_i^{(\alpha, \beta)}$ is then based on multiplying the observed signal $y(n, m)$ by $\exp(-j2\pi \frac{\nu_i^{(\alpha, \beta)}}{\alpha^2 + \beta^2} (n\hat{\beta} + m\hat{\alpha}))$, for each of the considered α, β and $\nu_i^{(\alpha, \beta)}$ triplets, and evaluating the variance of this signal along a line on the sampling grid such that $c = n\alpha - m\beta$. Clearly, the best estimate of α, β and $\nu_i^{(\alpha, \beta)}$ is the one that results in minimal variance for the 1-D sequence, as in the absence of noise the correct α, β and $\nu_i^{(\alpha, \beta)}$ result in a zero variance.

Having estimated the spectral support parameters of each evanescent component, we take the approach of first estimating a *non-parametric* representation of its 1-D purely-indeterministic modulating process $\{s_i^{(\alpha, \beta)}\}$, and only at a second stage we estimate the parametric models of these processes. Hence, in the first stage we estimate the particular values which the vectors $\xi_i^{(\alpha, \beta)}$ take for the given realization, i.e., we treat these as unknown constants. The estimation procedure is implemented as follows: Multiplying the observed signal $y(n, m)$ by $\exp(-j2\pi \frac{\nu_i^{(\alpha, \beta)}}{\alpha^2 + \beta^2} (n\hat{\beta} + m\hat{\alpha}))$ and evaluating the arithmetic mean of this signal along a line on the sampling grid such that $c = n\alpha - m\beta$, we have

$$\hat{s}_i^{(\alpha, \beta)}(c) = \frac{1}{N_s} \sum_{n\hat{\alpha} - m\hat{\beta} = c} y(n, m) \exp(-j2\pi \frac{\nu_i^{(\alpha, \beta)}}{\alpha^2 + \beta^2} (n\hat{\beta} + m\hat{\alpha})) \quad (14)$$

where N_s denotes the number of the observed field samples that satisfy the relation $n\alpha - m\beta = c$. Once we obtained the sequence of estimated samples from the 1-D modulating process $\{s_i^{(\alpha, \beta)}\}$, the problem of estimating its parametric model becomes entirely a 1-D estimation problem. Assuming the modulating process is an AR process, and applying to the sequence an AR estimation algorithm (see, e.g., [13]) we obtain estimates of the modulating process parameters, as well.

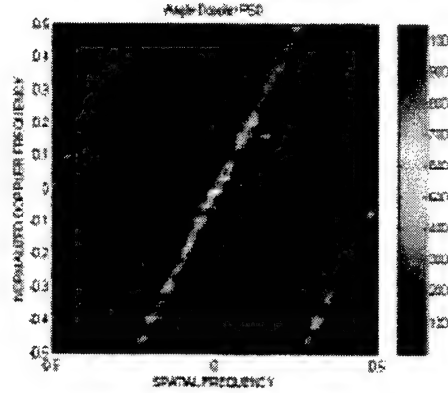


Figure 2: Spectral density of the observed field.

Finally, it is important to note that we solve the difficult problem of evaluating the rank of the low-rank covariance matrix of the interference as a by-product of obtaining the parametric estimates of the interference components: Denote the number of evanescent components (interference sources) of the field by Q . It is then shown in [11] that the rank of the interference covariance matrix is given by $\text{rank}(\Gamma) = S \sum_{k=1}^Q |\alpha_k| + T \sum_{k=1}^Q |\beta_k| - \sum_{k=1}^Q |\alpha_k| \sum_{k=1}^Q |\beta_k|$. In fact the special case where $Q = 1$ and $\alpha = 1$ is the well known Brennan rule, [3], of the rank of the clutter covariance matrix.

6. PARAMETRIC FULLY ADAPTIVE PROCESSING

Having estimated the parametric models of the purely indeterministic and evanescent components of the field, the estimated parameters can be substituted into (12)-(13) to obtain an estimate of the interference-plus-noise covariance matrix Γ .

Let \mathbf{v}_t denote the target steering vector, given by

$$\mathbf{v}_t = \mathbf{b}(\varpi_t) \otimes \mathbf{a}(\vartheta_t) \quad (15)$$

Assuming a linear, uniformly spaced, sensor array and a uniform CPI are employed in our model, the spatial steering vector $\mathbf{a}(\vartheta)$ and the temporal steering vector $\mathbf{b}(\varpi)$ are given by

$$\mathbf{a}(\vartheta) = [1, e^{j2\pi\vartheta}, \dots, e^{j2\pi(S-1)\vartheta}]$$

$$\mathbf{b}(\varpi) = [1, e^{j2\pi\varpi}, \dots, e^{j2\pi(T-1)\varpi}]$$

respectively. It is well known (e.g., [3], p. 57) that the optimum space-time filter is given to within a scale factor by

$$\mathbf{w} = \Gamma^{-1} \mathbf{v}_t \quad (16)$$

The test statistic $z(\varpi, \vartheta)$ is then given by

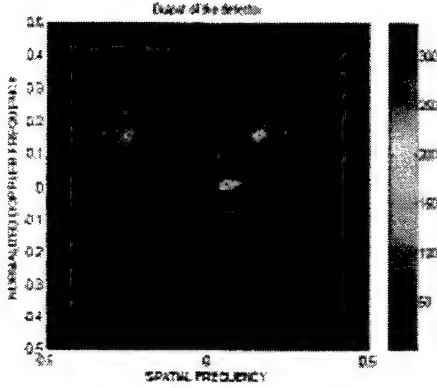


Figure 3: The test statistic $z(\omega, \vartheta)$.

$$z(\omega, \vartheta) = \mathbf{w}^H(\omega, \vartheta) \mathbf{y} = \mathbf{v}_t^H(\omega, \vartheta) (\Gamma^{-1})^H \mathbf{y}. \quad (17)$$

Let $\chi_f = (\Gamma^{-1})^H \mathbf{y}$. We thus have

$$z(\omega, \vartheta) = \mathbf{v}_t^H(\omega, \vartheta) \chi_f = \mathbf{b}^H(\omega) \otimes \mathbf{a}^H(\vartheta) \chi_f. \quad (18)$$

Reorganizing the elements of χ_f into a $T \times S$ matrix Ψ where the elements of the k th row of Ψ are $\chi_f((k-1)S+1) \dots \chi_f(kS)$, we conclude that for a linear, uniformly spaced, sensor array and uniform CPI the test statistic is given by

$$z(\omega, \vartheta) = \sum_{p=1}^T \sum_{q=1}^S e^{-j2\pi(p-1)\omega} e^{-j2\pi(q-1)\vartheta} \Psi(p, q). \quad (19)$$

Thus, $z(\omega, \vartheta)$ and $\Psi(p, q)$ are a 2-D DFT pair, and the test is equivalent to finding the 2-D frequency where the 2-D DFT of $\Psi(p, q)$ is maximal.

To illustrate the operation of the proposed solution we resort to numerical evaluation of some specific examples. Consider a 2-D observed random field consisting of a sum of a purely-indeterministic component (background noise), a single evanescent (interference) component, and three harmonic components (targets). The purely-indeterministic component is a complex valued circular Gaussian white noise field. The evanescent component spectral support parameters are $(\alpha, \beta) = (1, -2)$, $\nu^{(1, -2)} = 0$. The modulating 1-D purely indeterministic process of this evanescent component is a first order Gaussian AR process, such that its driving noise variance $(\sigma^{(1, -2)})^2 = 2$, and $a^{(1, -2)}(1) = -0.5$. There are three targets which are located at $(0.05, 0)$, $(0.15, 0.15)$ and $(-0.25, 0.15)$, respectively. The observed field dimensions are 48×48 .

Let us define the experimental variance of each of the field components as $E_w = \mathbf{w}^H \mathbf{w}$ for the purely indeterministic component; $E_e = (\mathbf{e}^{(\alpha, \beta)})^H \mathbf{e}^{(\alpha, \beta)}$ for the evanescent component; and $E_{h_k} = \mathbf{h}_k^H \mathbf{h}_k$, $k = 1, 2, 3$, for each of the harmonic components, where \mathbf{h}_k is defined in the same way

\mathbf{w} and $\mathbf{e}^{(\alpha, \beta)}$ are defined. In this example we have $\frac{E_e}{E_w} = 6\text{dB}$, while for the three targets we have $\frac{E_{h_1}}{E_w} = -12.8\text{dB}$, $\frac{E_{h_2}}{E_w} = -14.5\text{dB}$, $\frac{E_{h_3}}{E_w} = -15\text{dB}$. Due to the strong interference component, the presence of the three targets is hard to detect in the observed data whose power spectral density is depicted in Fig. 2. However these targets are easily detected by the test statistic $z(\omega, \vartheta)$ depicted in Fig. 3. In Fig. 3, $z(\omega, \vartheta)$ is depicted as a function of the two-dimensional frequencies, i.e., angle and Doppler.

7. PARAMETRIC PARTIALLY ADAPTIVE PROCESSING

Recall that

$$\Gamma_i^{(\alpha, \beta)} = (\mathbf{A}_i^{(\alpha, \beta)} \mathbf{R}_i^{(\alpha, \beta)} (\mathbf{A}_i^{(\alpha, \beta)})^T) \odot (\mathbf{d}_i^{(\alpha, \beta)} (\mathbf{d}_i^{(\alpha, \beta)})^H). \quad (20)$$

Having estimated α, β and $\nu_i^{(\alpha, \beta)}$ using the algorithm in Section 5, the vector $\mathbf{d}_i^{(\alpha, \beta)}$ is known. Hence, demodulating $\mathbf{e}_i^{(\alpha, \beta)}$, we conclude using (10) that the demodulated vector which we denote by $\bar{\mathbf{e}}_i^{(\alpha, \beta)}$ is given by

$$\bar{\mathbf{e}}_i^{(\alpha, \beta)} = \mathbf{e}_i^{(\alpha, \beta)} \odot ((\mathbf{d}_i^{(\alpha, \beta)})^H)^T. \quad (21)$$

From (11) we conclude that the covariance matrix of $\bar{\mathbf{e}}_i^{(\alpha, \beta)}$ is given by

$$\bar{\Gamma}_i^{(\alpha, \beta)} = \mathbf{A}_i^{(\alpha, \beta)} \mathbf{R}_i^{(\alpha, \beta)} (\mathbf{A}_i^{(\alpha, \beta)})^T. \quad (22)$$

In the following it is proved that since α and β are already known, an orthogonal projection matrix onto the low-rank subspace spanned by the evanescent field covariance matrix can be found *without* estimating the parametric model of the evanescent field 1-D modulating process, and hence without estimating $\mathbf{R}_i^{(\alpha, \beta)}$. Moreover this result enables us to avoid the need in both evaluating the field covariance matrix, and in employing a computationally intensive eigenanalysis to the estimated covariance matrix.

More specifically, let us construct the following orthogonal projection matrix

$$\mathbf{T}_i^{(\alpha, \beta)} = \mathbf{A}_i^{(\alpha, \beta)} \left((\mathbf{A}_i^{(\alpha, \beta)})^T \mathbf{A}_i^{(\alpha, \beta)} \right)^{-1} (\mathbf{A}_i^{(\alpha, \beta)})^T. \quad (23)$$

It is easily verified (by substitution) that $\mathbf{T}_i^{(\alpha, \beta)}$ is an orthogonal projection onto the range space of $\bar{\Gamma}_i^{(\alpha, \beta)}$ since for any ST dimensional vector \mathbf{v}

$$\bar{\Gamma}_i^{(\alpha, \beta)} \mathbf{v} = \bar{\Gamma}_i^{(\alpha, \beta)} \mathbf{T}_i^{(\alpha, \beta)} \mathbf{v}. \quad (24)$$

Also, $(\mathbf{T}_i^{(\alpha, \beta)})^2 = \mathbf{T}_i^{(\alpha, \beta)}$, and $(\mathbf{T}_i^{(\alpha, \beta)})^T = \mathbf{T}_i^{(\alpha, \beta)}$.

Note that since $\mathbf{A}_i^{(\alpha, \beta)}$ is a sparse matrix of zeros and ones *only*, the computation of $\mathbf{T}_i^{(\alpha, \beta)}$ is very simple.

The projection matrix onto the subspace orthogonal to the interference space is therefore given by $(\mathbf{T}_i^{(\alpha, \beta)})^\perp = \mathbf{I} - \mathbf{T}_i^{(\alpha, \beta)}$. Hence by projecting the demodulated observed data vector $\bar{\mathbf{y}} = \mathbf{y} \odot ((\mathbf{d}_i^{(\alpha, \beta)})^H)^T$ onto the subspace orthogonal to the interference subspace, a reduced dimension data vector given by $\bar{\mathbf{y}} = ((\mathbf{T}_i^{(\alpha, \beta)})^\perp)^H \bar{\mathbf{y}}$ is obtained, such that

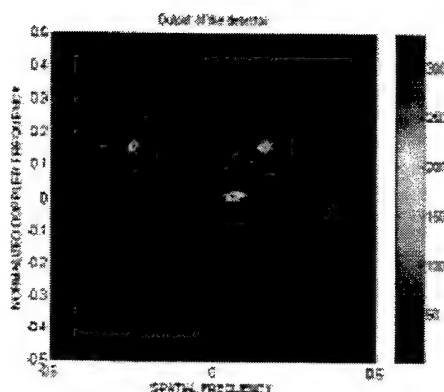


Figure 4: Spectral density of the field after being projected onto the subspace orthogonal to the interference subspace.

the interference contribution to the observed signal is mitigated. Remodulating \tilde{y} by evaluating $\tilde{y} \odot d_i^{(\alpha, \beta)}$, followed by sequentially applying this procedure to mitigate each of the interference sources, the detection problem is reduced to that of detecting a target in the presence of background noise only. Thus, in the special case where the background noise is known to be a white noise field, the statistical test is equivalent to finding the 2-D frequency where the 2-D DFT of the processed data vector (organized back into a 2-D array) is maximal.

As an example consider the same field as in the previous section. Due to the strong interference component, the presence of the three targets is hard to detect in the observed data whose power spectral density is depicted in Fig. 2. However these targets are easily detected in the processed data as illustrated in Fig. 4. This result is obtained without estimating the parametric model of the evanescent field 1-D modulating process, and hence without estimating the interference-plus-noise covariance matrix. Since both the estimation of the interference-plus-noise covariance matrix, as well as its analysis are saved, the proposed parametric partially adaptive processing method is robust and computationally attractive.

8. REFERENCES

- [1] *Proc. 1st IEEE Sensor Array and Multichannel Signal Processing Workshop (SAM 2000)*, Cambridge, MA, March 2000.
- [2] *Proc. 8th Adaptive Sensor Array Processing Workshop (ASAP 2000)*, Lexington, MA, March 2000.
- [3] J. Ward, "Space-time adaptive processing for airborne radar," Technical Report 1015, Lincoln Laboratory, Massachusetts Institute of Technology, Lexington, MA, Dec. 1994.
- [4] R. Klemm, *Space Time Adaptive Processing*, IEE, London, 1998.
- [5] R. Klemm, "Prospectives in STAP Research," *Proc. 8th Adaptive Sensor Array Processing Workshop (ASAP 2000)*, Lexington, MA, March 2000.
- [6] J. M. Francos, A. Z. Meiri and B. Porat, "A Wold-like decomposition of 2-D discrete homogeneous random fields," *Annals Appl. Prob.*, vol. 5, pp. 248-260, 1995.
- [7] J. M. Francos, "Bounds on the accuracy of estimating the parameters of discrete homogeneous random fields with mixed spectral distributions," *IEEE Trans. Info. Theory.*, vol. 43, pp. 908-922, 1997.
- [8] T. K. Sarkar, J. Koh, R. Adve, R. A. Schneible, M. C. Wicks, S. Choi, and M. S. Palma "A pragmatic approach to adaptive antennas," *IEEE Antennas and Propagation Mag.*, vol. 42, pp. 39-55, 2000.
- [9] H. Wang and L. Cai, "On adaptive spatial-temporal processing for airborne surveillance radar systems," *IEEE Trans. Aerospace Electron. Systems*, vol. 30, pp. 660-669, 1994.
- [10] X. Lin and R. S. Blum, "Robust STAP algorithms using prior knowledge for airborne radar applications" *Signal Process.*, vol. 79, pp. 273-287, 1999.
- [11] G. Cohen and J. M. Francos, "Efficient parameter estimation of evanescent random fields," submitted for publication.
- [12] A. K. Jain, *Fundamentals of Digital Image Processing*, Prentice-Hall, 1989.
- [13] B. Porat, *Digital Processing of Random Signals*, Prentice-Hall, 1994.

THE RELATIONSHIP BETWEEN DETECTION ALGORITHMS FOR HYPERSPECTRAL AND RADAR APPLICATIONS

Nirmal Keshava, Stephen M. Kogon, Dimitris Manolakis

MIT Lincoln Laboratory
244 Wood Street Lexington, MA 02420-9185
keshava@ll.mit.edu, (o) (781) 981-3344

ABSTRACT

Hyperspectral data consists of hundreds of contiguous radiometric measurements collected passively from each pixel in a scene. Detection capitalizes on exploiting the difference between target and background spectral signatures. Many detection methods in hyperspectral processing employ signal models commonly used in radar even though it is an active sensor. Starting from a common signal model, we discuss adaptive detection algorithms for hyperspectral data by outlining fundamental similarities and differences with radar. We demonstrate detection using hyperspectral data through experiments with real data and discuss the fundamental applicability of adaptive radar signal models to detection in hyperspectral processing.

1. INTRODUCTION

The potential of hyperspectral sensors to perform target detection has begun to emerge as data from current and projected sensors has shown that passive, spectral measurements can distinguish targets from background. The basis for detection resides in exploiting the differences in reflective properties that occur in the hundreds of contiguous spectral bands that comprise hyperspectral signals. Collectively, these measurements constitute a vector signal that may be used in detection algorithms designed to maximize the separation between target and background signals.

For detection algorithms to be successful in operational scenarios, they must employ accurate statistical descriptions of both the target and background. Many of the algorithms currently in use have been adapted from signal models used for detection in radar systems. Consequently, despite the significant differences in the physical mechanisms, a strong parallelism can be drawn that maps the measured signals from each sensor to a common signal model.

This work was sponsored by the Department of the Defense under Contract F19628-00-C-0002. Opinions, interpretations, conclusions, and recommendations are those of the author and are not necessarily endorsed by the United States Air Force.

2. MODELS FOR HYPERSPECTRAL SENSING AND MTI RADAR

In order to understand the relationship between the signal models for hyperspectral sensing and MTI radar, we first explain the basic concepts behind both sensor models.

2.1. Hyperspectral Imaging

Hyperspectral sensors passively collect measurements of radiation in hundreds of contiguous spectral bands. Collectively, hyperspectral imaging (HSI) provides continuous coverage of the electromagnetic spectrum over a wide range of wavelengths. Incident radiation from the sun follows several pathways as it reaches the sensor where it is measured in terms of *radiance* (Watts/steradian/cm²/μm). Mathematically, the radiance arriving at the sensor, $L_{sensor}(\lambda)$, can be described as

$$L_{sensor}(\lambda) = L_{solar}(\lambda)\rho(\lambda)\tau(\lambda) + L_{path}(\lambda) \quad (1)$$

where $L_{solar}(\lambda)$ is the radiance spectrum entering the atmosphere at a designated time and location as a function of wavelength. $\tau(\lambda)$ is the atmospheric transmittance, and $\rho\lambda$ is the surface reflectance, and $L_{path}(\lambda)$ is the additive path radiance arising from interactions with the atmosphere.

In some cases, processing of the radiance arriving at the sensor can yield useful results. However, in most cases, the surface reflectance, $\rho(\lambda)$, is the quantity that is desired because it is an intrinsic property of the area being imaged and is invariant to differences in atmospheric conditions during observation. Reflectance is defined as the ratio of the intensity arriving at the surface of an object to the intensity reflected ($0 \leq \rho(\lambda) \leq 1$), and the recovery of $\rho(\lambda)$ from $L(\lambda)$ is accomplished through *atmospheric compensation*. In this procedure, the surface reflectance for each pixel is recovered by removing the effects of gaseous and water vapor absorption in the atmosphere. Atmospheric compensation is derived from radiative transfer models and is by no means an exact science. In addition to being computationally demanding, the amount of error in the compensation is

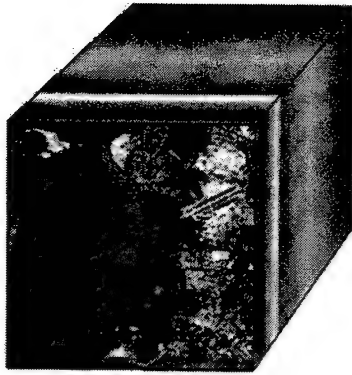


Fig. 1. 3-D datacubes for HSI.

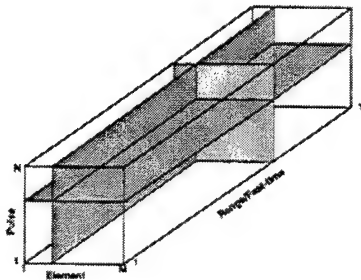


Fig. 2. 3-D CPI datacube for MTI radar.

difficult to quantify. Nevertheless, most hyperspectral processing is performed "in reflectance."

Hyperspectral sensors collect data along two spatial axes derived from the motion of the sensor (along-track and across-track) and another spectral axis. The resulting three-dimensional cube is depicted in Figure 1. The spatial resolution in HSI is a consequence of several factors, but generally can be determined from only two: instantaneous field of view (IFOV) and altitude. IFOV is a parameter describing the optics that conveys the angular expanse of one element on the focal plane array that measures radiance. Multiplying the IFOV by the altitude of the sensor gives the pixel size of the scene.

2.1.1. Linear Mixing Model

Hyperspectral processing attempts to exploit the wavelength-dependent features of the reflectance spectrum measured from a pixel. However, it is quite common for the surface area occupying a pixel to be a combination of distinct materials, or endmembers (e.g., water, trees, vehicle), each possessing their own reflectance functions. The reflectance

function of a mixed pixel is some combination of the distinct reflectance functions of each endmember. In general, accurate physical modelling of the reflective properties of mixtures is not trivial, and is a function of numerous molecular parameters, as well, as the proportions in which the endmembers appear. Several physically-derived models have been proposed to model mixing under different conditions.

A common assumption for describing the mixing process throughout hyperspectral processing that is analytically tractable is that the reflectance spectrum of a mixed pixel is a weighted linear combination of the individual endmember reflectance functions, where the weights are the proportions in which each endmember appears. Thus, the mathematical model describing this recipe for a mixed pixel is

$$\mathbf{x} = \mathbf{S}\mathbf{a} + \mathbf{n} = \sum_{i=1}^P a_i \mathbf{s}_i + \mathbf{n} \quad (2)$$

Here, \mathbf{x} is the reflectance spectrum of a mixed pixel, and \mathbf{S} is a matrix whose P columns are the reflectance spectra of the endmembers, and \mathbf{a} is a $P \times 1$ vector of non-negative fractional abundances. The additive noise vector, \mathbf{n} , represents the inaccuracies in the model. Two important constraints on \mathbf{a} must be imposed. The *non-negativity* constraint demands that $a_i \geq 0, i = 1, \dots, P$, and to ensure the composition of a mixed pixel is completely accounted for, the *additivity* constraint requires $\sum_{i=1}^P a_i = 1$. Collectively, these constraints and the synthesis equation for mixed pixels in (2) are referred to as the Linear Mixing Model (LMM).

2.2. MTI Radar

The objective of MTI radar systems is to detect the presence of moving objects. MTI radars on airborne platforms illuminate a scene with a waveform and sample the return at each element of a multi-element array (We restrict our attention to uniform linear arrays (ULA)). The process is repeated during a coherent processing interval (CPI). After pulse compression, the data is organized into a three-dimensional CPI datacube, as depicted in Figure 2, that is indexed by 1) pulse number, 2) element number, and 3) sample number (range).

At each range value, a two-dimensional function locates the presence of reflecting objects by their cone angle and their corresponding Doppler frequency. For a fixed system, the signal strength returned by a target depends upon its range cross-section (RCS) value and its range. Stationary objects will yield values along a "clutter ridge", whereas moving objects will lie off the ridge by an amount proportional to its velocity relative to the platform. A moving target is most visible when its velocity is high (so as to move it as far away as possible from the clutter ridge), and when it returns a strong signal.

By virtue of linearity, MTI radar observes a signal model similar to the LMM in (2). The vector signal measured by an antenna array is the linear superposition of reflections received from all directions, and when a target is present, the corresponding signal is given by

$$\mathbf{x} = \mathbf{t} + \mathbf{c} + \mathbf{n}. \quad (3)$$

Here, \mathbf{x} is an $M \times 1$ observation vector, where M is the number of elements on the ULA, \mathbf{c} and \mathbf{n} are clutter and noise, respectively, and \mathbf{t} is the target and is expressed as $\mathbf{t} = \alpha \mathbf{v}(\phi, f)$. α is the relative amplitude of the return signal, and \mathbf{v} is the steering vector which is related to the geometry of the ULA as well as signal parameters. The entries of \mathbf{v} are given by:

$$v_{mn} = e^{j2\pi[(m-1)\text{PRF} + (n-1)\frac{d}{\lambda} \cos \phi]} \quad (4)$$

where $m = 1, \dots, M$, is the element number, $n = 1, \dots, N$, is the pulse number, ϕ is the azimuth angle, f is the Doppler frequency, λ is the wavelength, d is the array element spacing, and PRF is the pulse repetition frequency. Resolution in MTI radar systems is driven in the range direction by the signal bandwidth of the interrogating signal and by the aperture length in azimuth.

2.3. Relationships Between HSI and MTI Radar

We can see from (2) and (3) that signal models for HSI and MTI radar are quite similar. Both sensors organize measurements that occupy three axes (See Figures 1 and 2). Despite the fact that HSI is passive and yields non-negative vector measurements, and MTI radar is a form of active sensing producing complex-values, the key to this equivalence is the parallelism between endmembers and steering vectors as well as RCS and fractional abundances.

In (4), \mathbf{v} is a vector whose structure gives rise to the complex-valued signal in \mathbf{x} . When a target is in motion at a specific range, its location in azimuth and Doppler frequency decide the exact value of the steering vector. The one-dimensional subspace defined by the target vector, \mathbf{t} , varies depending on the location and speed of the target. In most instances, the resolution cell size is sufficiently small that only one moving target resides in it. In the case, however, where multiple moving targets reside in a single cell, the response from the cell will be the sum of weighted steering vectors, each having their own Doppler frequency. The target response, \mathbf{t} , can be extended to include P targets, so that $\mathbf{t} = \sum_{i=1}^P \alpha_i \mathbf{v}_i = \mathbf{V} \mathbf{a}$. Compared to (2), the steering vectors that are columns of \mathbf{V} are analogous to the endmembers in \mathbf{S} . Further, in (4), \mathbf{c} and \mathbf{n} are comparable to the background and additive noise in (2), and their statistics are key factors in the detectors for each sensor type.

3. TARGET DETECTION

Based on the comparable signal models for HSI and MTI radar discussed in Section 2, we can consider strategies for detection in each. The LMM has been employed in numerous circumstances to describe the mixing process. For the purpose of target detection, it is capable of conveying the mathematical relationship between the spectra of targets and background. By virtue of the LMM, we assume that all pixels in a scene imaged by a hyperspectral sensor consist of at least one endmember from the columns of \mathbf{S} .

A specific type of target possesses a spectrum, but variability can arise due to many factors, including changes in observation conditions. Depending on its source, variability can be accounted for by adding endmembers (and corresponding abundances) to describe the same target under different conditions, or by shaping the additive noise, \mathbf{n} , in the LMM to reflect statistical variability. \mathbf{S}_t denotes the subset of columns in \mathbf{S} describing targets, and \mathbf{S}_b denotes background endmembers. Because the entries of \mathbf{S} are non-negative, \mathbf{S}_t and \mathbf{S}_b cannot be mutually orthogonal spaces, and the subspaces they span necessarily overlap.

3.1. Types of Hyperspectral Detection

The task of detection can be posed for two separate circumstances that are of interest in hyperspectral processing [1]. The **Known Target** detection problem occurs when the presence of a specific target is to be detected amid background and noise, and \mathbf{S}_t is known. In contrast the **Unknown Target** detection problem has no knowledge of a target subspace, but attempts to detect any pixel that is different from the background. For this reason, detectors designed for this goal are often called *anomaly* detectors.

The class of **Known Target** detection algorithms can be further divided into two categories. The set of **structured background** algorithms assumes that the subspace where the background resides, \mathbf{S}_b , is known so that the LMM in (2) can be re-written as

$$\mathbf{x} = \mathbf{S}_t \mathbf{a}_t + \mathbf{S}_b \mathbf{a}_b + \mathbf{n} \quad (5)$$

$$= \sum_{i=1}^{P_T} a_i \mathbf{s}_i + \sum_{i=P_T+1}^{P_B+P_T} a_i \mathbf{s}_i + \mathbf{n} \quad (6)$$

where $P = P_T + P_B$. Note that the obstacles to perfect detection, background and additive noise, have been modelled as two distinct entities, $\mathbf{S}_b \mathbf{a}_b$ and \mathbf{n} . The resulting binary detection test for structured background is

$$\mathbf{H}_0 : \quad \mathbf{x} = \mathbf{S}_b \mathbf{a}_b + \mathbf{n} \quad (7)$$

$$\mathbf{H}_1 : \quad \mathbf{x} = \mathbf{S}_t \mathbf{a}_t + \mathbf{S}_b \mathbf{a}_b + \mathbf{n} \quad (8)$$

Alternatively, if the background endmembers are unknown, the sources of interference cannot be separated into

separate background and noise terms. The **unstructured background** problem lumps all non-target pixel contributions into a single vector, \mathbf{w} , and the resulting binary detection test is written as:

$$H_0 : \quad \mathbf{x} = \mathbf{w} \quad (9)$$

$$H_1 : \quad \mathbf{x} = \mathbf{S}_t \mathbf{a}_t + \mathbf{w} \quad (10)$$

The different pairs of hypotheses in (7-8) and (9-10) convey varying levels of knowledge about the detection problem and are critical to the formulation of optimal detectors.

When the size of a target is expected to be equal to or greater in size than that of a pixel, i.e., the target is resolved, the background is no longer present in either hypothesis. This is a significant departure from radar detection models which assume an *additive* target appears in addition to clutter. A *replacement* target displaces some amount, or all, of the environmental interference, or background. The fact that the amount of background displaced by a target in a mixed pixel can vary means that the statistics of the interference will also vary. As a consequence, the foremost challenge in the design of optimal, statistical detectors for sub-pixel targets stems from the uncertainty of what fraction of the pixel the target occupies.

3.2. MTI Detection

Like the techniques for hyperspectral detection, algorithms in MTI radar find moving targets by exposing the Doppler effect in signals measured by a ULA. Just as the subspaces defined by target and background endmembers in HSI detection provide the basis for separating target and background pixels, the geometry of the array, along with the signal parameters, are combined by algorithms to maximize the visibility of moving targets.

Algorithms for detecting \mathbf{t} in (3) optimally suppress the presence of \mathbf{c} and \mathbf{n} by means of Space-Time Adaptive Processing (STAP) [2]. Resembling the detection model for a known target in an unstructured background, the binary detection model for a moving target, \mathbf{t} , is given by

$$H_0 : \quad \mathbf{x} = \mathbf{w} \quad (11)$$

$$H_1 : \quad \mathbf{x} = \mathbf{t} + \mathbf{w}, \quad (12)$$

where $\mathbf{w} = \mathbf{c} + \mathbf{n}$ in (3).

Moving targets may be present at any range and azimuth position, and each pixel in the MTI radar datacube is a candidate for a detection test. For a specific range value, the cube of MTI data reduces to a single plane having MN resolution cells. It is well known that the detector which maximizes the SNR whitens the received signal based on a filter derived from the covariance of the interference. A covariance, \mathbf{R}_w , having size $MN \times MN$ introduces significant complications, and, most often, a local covariance of a

smaller size is generated from a local neighborhood around the cell being processed. Confining the covariance to a neighborhood reduces the possibility of introducing non-stationary behavior and results in a more precise estimate.

3.3. Relationship Between HSI and MTI Detection

As noted earlier, reflectance values in hyperspectral processing are non-negative and no greater than one, and unlike the intuition from radar, targets do not necessarily induce signals of greater magnitude than background. Rather, targets are discerned from background reflectance spectra primarily by their shape, and detectors exploit the differences in spectral shapes represented by the endmembers to separate targets from background.

3.4. Detectors

We have shown that the signal models for hyperspectral target detection in (7-8) and (9-10) and the signal model for the detection of moving targets in (11-12) are similar. The key to the parallelism lies in the similar roles played by endmembers and steering vectors and the equivalence of abundances and RCS values and is further driven by the assumption of linearity when combining multiple signals.

By (11-11), detection in MTI radar compares range-angle cells to a threshold to determine whether or not a target is moving. Numerous detectors have been proposed to perform this comparison, each equipped to adaptively optimize some aspect of the decision. Notably, the most desirable features of detectors are: 1) CFAR (Constant False Alarm Rate), 2) maximum SNR, and 3) speed of computation. A detector might be able to assure one of these features, at the expense of maintaining the others, and the trade-off of these qualities is instrumental to an appropriate implementation.

The same set of circumstances also surrounds hyperspectral detection. A taxonomy of hyperspectral detectors for both the known and unknown target case hyperspectral data appears in [1], indicating the hierarchy of common detectors. The Generalized Likelihood Ratio Test (GLRT) [3] is a CFAR detector that utilizes the unstructured background signal model, and for a single known target spectrum, \mathbf{s} , the GLRT for a test pixel spectrum, \mathbf{x} , is given by:

$$\mathcal{T}_{GLRT}(\mathbf{x}) = \frac{(\mathbf{s}^T \mathbf{R}_w^{-1} \mathbf{x})^2}{(\mathbf{s}^T \mathbf{R}_w^{-1} \mathbf{s})(1 + \mathbf{x}^T \mathbf{R}_w^{-1} \mathbf{x})} \underset{H_0}{\overset{H_1}{>}} \eta_0. \quad (13)$$

Other familiar detectors may be derived directly from the GLRT under specific circumstances, such as the Adaptive Matched Filter (AMF) [3] and the Adaptive Coherence Estimator (ACE) [4, 5]. In the improbable case where the interference covariance is the identity matrix, the ACE simplifies to a simple cosine measure between \mathbf{s} and \mathbf{x} , often

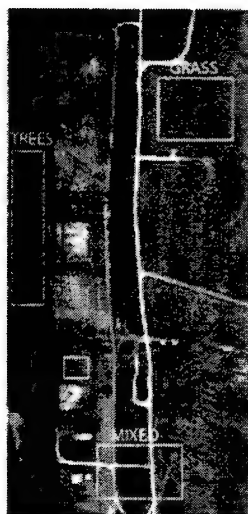


Fig. 3. Forest Radiance I scene.

referred to in the hyperspectral processing literature as the Spectral Angle Mapper (SAM). It is defined as:

$$T_{SAM}(x) = \frac{s^T x}{\sqrt{s^T s} \sqrt{x^T x}} \quad (14)$$

With no incorporation of background statistics, clearly, SAM cannot be CFAR or optimum in any sense.

4. HYPERSPECTRAL DETECTION RESULTS

Figure 3 displays the RGB image of the Forest Radiance I scene imaged by the (Hyperspectral Digital Imagery Collection Experiment) HYDICE sensor. The data collection acquired 210 bands of spectral data in spectral bins 3 – 11 nm wide ranging from 399 – 2501 nm (Visible to Shortwave Infrared). The scene consists of 1280 lines of data, each having 320 samples with approximately 1 m × 1 m spatial resolution. Three regions of distinct background type have been demarcated: trees, grass, and mixed. In addition, a separate region is outlined encompassing several vehicles of the same type, from which pure target pixels are derived. Figure 4(a) illustrates the mean target spectrum obtained from 37 pure target pixels.

We demonstrate detection with hyperspectral data in two different experiments. The goal of the first experiment is to demonstrate how sub-pixel targets are detected when they appear mixed with background. The second experiment considers the extreme case of the sub-pixel target problem when the target is resolved and obscures all background when it is present. For both experiments, the performance of the SAM and GLRT detectors is compared side-by-side.

4.1. Sub-pixel Targets

Sub-pixel target spectra have been created synthetically by adding the pure mean target spectrum from Figure 4(a) in varying proportions to the 8232 pure tree spectra (background) in Figure 3. Although, there is no assurance that spectra mix linearly in real mixed pixels, we have employed this assumption for our investigation until accurate sub-pixel target data and ground truth become available.

We have estimated the background covariance from the homogeneous tree spectra. Both detectors yield values between 0 (background) and 1 (target), and pure background detection statistic values have been generated from the 8232 tree pixels. An equal number of target mixtures resulted by combining the same background pixels with the mean target vehicle spectrum in 25%/75%, 50%/50%, and 75%/25% target/background proportions. The range of detection statistic values for the SAM detector appears in Figure 4(b) and for the GLRT in Figure 4(c).

In Figures 4(b) and 4(c), the regions of dark blue correspond to the range of statistic values induced by the tree pixels. The regions of red correspond to the range of target mixture statistic values. Intervals of light blue, if any, correspond to regions where test statistics from pure background pixels and sub-pixel targets overlap and indicate pixels where false alarms and missed detections could occur. A white strip appears at the value of the mean target/background statistic. Regions of yellow indicate the amount of separation, if any, between target and background. The greater the width of the yellow region, the better the detector is capable of separating sub-pixel targets from pure background.

4.2. Resolved Targets

The 37 target pixels in Figure 3 are fully resolved, and they completely obscure any background. In spite of the fact that there is no background to whiten when the target is present, and using the 37 target pixels and the 8232 background pixels, we assessed the performance of the SAM and GLRT detectors in separating pure target and pure background spectra. In Figure 4(d), both the SAM and GLRT detection results for resolved targets are depicted side-by-side.

4.3. Discussion

In Figure 4(b) the SAM detector is unable to successfully separate every sub-pixel target until 75% of the pixel is occupied by the target. This is not surprising since SAM does nothing to suppress the background. On the other hand, in Figure 4(c), the GLRT has a relatively large pure background and target/background separation even when the target occupies only 25% of the pixel. This is due to the suppression of the background through whitening by the in-

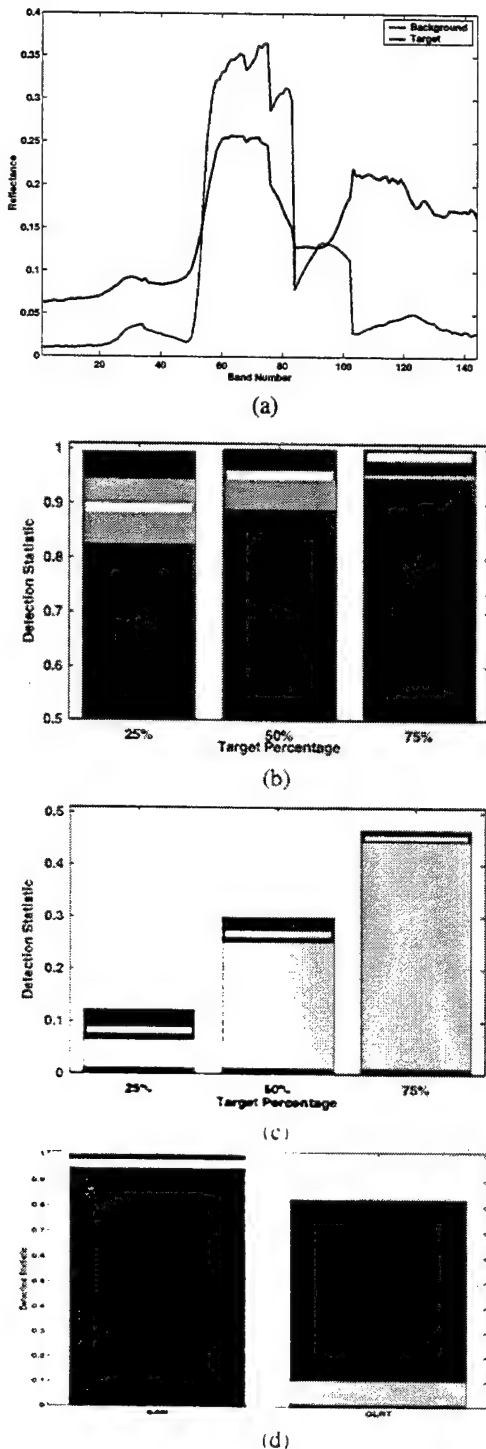


Fig. 4. (a) Mean target spectrum; (b) Sub-pixel detection statistics for SAM; (c) Sub-pixel detection statistics for GLRT; (d) Resolved target detection results for SAM and GLRT.

verse covariance, R_w^{-1} in (13). For resolved targets, Figure 4(d) confirms that the effect of whitening significantly improves the separability of target and background.

In both experiments, the same estimated covariance was used regardless of the percentage of background present. For this target and background, the results in Figure 4 show that, even when the background covariance is mismatched to the amount of background present, the performance still exceeds that of the SAM detector. Proper cancellation of background for hyperspectral detection is a function of the percentage of background present as well as the relationship between the target and background subspaces. Based on the LMM, this relationship will be key for

5. CONCLUSION

We have demonstrated in this paper that, under the assumption of linear mixing, detection in hyperspectral processing bears significant similarities with detection in MTI radar. The key to this parallelism is the analogous relationship between endmembers and steering vectors as well as abundances and RCS values. Our detection results indicate that statistical detectors for radar can be adapted to hyperspectral signals for both the sub-pixel and resolved target problem. even though sub-pixel targets give rise to replacement target models. Moreover, future work will continue to investigate methods for translating the optimalities of radar detection to the hyperspectral domain.

6. REFERENCES

- [1] Dimitris Manolakis, Gary Shaw, and Nirmal Keshava, "Comparative analysis of hyperspectral adaptive matched filter detectors," in *Algorithms for Multispectral, Hyperspectral, and Ultraspectral Imagery VI*, Apr. 2000, vol. 4049 of *Proceedings of the SPIE*, pp. 2–17.
- [2] James Ward, "Spate-time adaptive processing for airborne radar," Tech. Rep. TR-1015, MIT Lincoln Laboratory, 1994.
- [3] E. J. Kelly, "An adaptive detection algorithm," *IEEE Transactions on Aerospace and Electronic Systems*, vol. 22, no. 5, pp. 115–127, Mar. 1986.
- [4] L. L. Scharf and L. T. McWhorter, "Adaptive matched subspace detectors and adaptive coherence," in *Proc. 30th Asilomar Conf. On Signals and Systems*, 1996, pp. 1114–1117.
- [5] C. D. Richmond, "Performance of the adaptive sidelobe blanker detection algorithm in homogeneous environments," *IEEE Transactions on Signal Processing*, vol. 48, no. 5, pp. 1235–1247, May 2000.

LINEAR FEATURE DETECTION IN SAR IMAGES

Ph. Courmontagne

ISEM
Laboratoire L2MP UMR 6137 CNRS

Maison des Technologies
Place Georges Pompidou

83000 TOULON

FRANCE

philippe.courmontagne@isem.tvt.fr

ABSTRACT

The problem treated in this paper is the one of detection and restoration of ship wakes in Synthetic Aperture Radar (SAR) images. This cannot be easily made, because SAR images are corrupted by a granular noise, called speckle and because there is no information about the direction and the level of the wake. For these reasons, most detection algorithms use the Radon transform, which makes square a straight with a point. We propose here a new method, based on the marriage between the Radon transform and a filtering method used to interpolate the image in a rotating reference system, introduced by the Radon transform theory. This filtering technique is the stochastic matched filtering technique, which allows to maximize the signal to noise ratio after processing. Experimental results on SIR-C/X-SAR images are presented and compared to those obtained using the classical approach.

1. INTRODUCTION

Recently, a great deal of research has been dedicated to ship wake detection in Synthetic Aperture Radar (SAR) images. Indeed, it is well known that SAR images are able to show ship wakes as lines darker or sometimes brighter than the surrounding sea. Most of the detection algorithms use the Radon transform [2, 7, 8]. Indeed, when an image contains a straight line or a segment, its Radon transform exhibits a narrow peak if the line is brighter than its surroundings and a trough in the opposite case. Thus, the problem in finding lines is related to detect these peaks and troughs in the transform domain. Other methods use the detection on both ships and ship wakes [5]. Given that SAR images are affected by a granular, multiplicative noise (called speckle), most of these detection algorithms pre-filter the data in order to improve the visibility of the ship wakes.

We know that the application of the Radon transform requires the computation of interpolated image in a rotating reference system. In this paper, we propose a new method based on the marriage between the Radon transform and a filtering method. We use this filtering technique to compute the interpolations of the SAR image, in order to estimate properly the signal of interest (the ship wake) in the rotating reference system. This processing is called the stochastic matched filtering technique [1]. It is based on the signal expansion into series of functions with uncorrelated random

variables for decomposition coefficients. This corresponds to the Karhunen-Loeve expansion in the case of a white noise. Because the chosen basis functions improve the signal to noise ratio after processing, there is no more sinusoidal curves corresponding to the speckle in the Radon domain, and the detection of the peak (or trough) corresponding to the ship wake is improved.

First of all, we recall in section 2 the discrete Radon transform [4], in the case of a two-dimensional signal. Then, we present, in section 3, an interpolation-filtering method for noise corrupted image in a rotating reference system. First, we recall the stochastic matched filtering technique and then we describe how to perform an interpolation based on this method and using the discrete cosine transform. We finish this section with the explanation of the subimage processing. Next, in section 4, we propose an example of application of our processing on a SIR-C/X-SAR image, which shows a moving ship and its dark turbulent wake. We finish this article with a comparison of our results with those obtained by the classical approach, which uses the Radon transform based on the nearest neighbor interpolation.

2. THE DISCRETE RADON TRANSFORM

The Radon transform on Euclidean space was first established by Johann Radon in 1917. Nearly half a century after Radon's work, the Hough transform for detecting straight lines in digital pictures was introduced. But this transform is actually a special case of the Radon transform. We are going to recall in this section the discrete Radon transform of a two-dimensional signal.

Considering an image I , $(M+1) \times (M+1)$ pixels, its discrete Radon transform, \hat{I} is expressed by:

$$\hat{I}(x_\theta, \theta) = \sum_{y_\theta=-M/2}^{M/2} I(x_\theta \cos \theta - y_\theta \sin \theta, x_\theta \sin \theta + y_\theta \cos \theta),$$

where x_θ and y_θ are integers which are bounded by $-\frac{M}{2}$ and $\frac{M}{2}$; θ corresponds to the rotation angle and takes values between 0 and π .

The previous equation shows that the computation of the Radon transform requires, for each parameter θ , the calculation of the new pixel values in reference system \mathcal{R}_θ . Indeed, the new coordinates are not integer values and so are not corresponding to the native mesh of the image.

By nature, the Radon transform accentuates linear features in an image by integrating along all possible lines. The result is that an image which is non zero in a single point (x_0, y_0) has a Radon transform which is non zero along a sinusoidal curve of equation $x_\theta = x_0 \cos \theta + y_0 \sin \theta$. The phase and frequency of this sinusoidal curve depend on the spatial location of the corresponding point in the original image. If the original image contains a straight line or a segment, its Radon transform exhibits a narrow peak, if the line is brighter than its surrounding, and a trough in the opposite case. The coordinates of the peak (or trough) are (x_{θ_0}, θ_0) which correspond to the parameters of the polar equation $x_{\theta_0} = x \cos \theta_0 + y \sin \theta_0$ of the straight line. Thus, the problem of finding lines is reduced to the detection of peaks and troughs in the transform domain. The Radon transform is particularly suited for finding lines in a noise-corrupted image, because the integration process tends to cancel out intensity fluctuations due to the noise. For this reason, we can find in the literature several applications in the domain of wakes detection (see [2, 7, 8] for example).

3. INTERPOLATION-FILTERING OF A ROTATING IMAGE

We have seen that the Radon transform of an image implies, for each value of the θ parameter, the computation of an interpolated image. We want to use the Radon transform in order to detect ship wakes in SAR images. Given that SAR images are corrupted by a granular noise, called speckle, it is of great interest to take into account this noise to compute the interpolation of such an image, in order to give a good estimation of the signal of interest in the rotating reference system. For this reason, we present here an interpolation method, based on the stochastic matched filtering method, which principle is to expand the noise-corrupted signal into series of functions with uncorrelated random variables for decomposition coefficients.

3.1. The stochastic matched filtering method

Consider a two-dimensional noise-corrupted signal, $Z(x, y)$, defined over $D = [-T; T] \times [-T; T]$. This one corresponds to the superposition of a signal of interest $S(x, y)$ with a noise $B(x, y)$:

$$Z(x, y) = S(x, y) + B(x, y) \quad \forall (x, y) \in D,$$

where $S(x, y)$ and $B(x, y)$ are assumed to be independent and stationary.

We want to expand simultaneously the signal of interest and the noise into series of the form:

$$\begin{cases} S(x, y) = \lim_{N \rightarrow \infty} \sum_{n=1}^N s_n \Psi_n(x, y) \\ B(x, y) = \lim_{N \rightarrow \infty} \sum_{n=1}^N b_n \Psi_n(x, y), \end{cases}$$

In these expressions, $\Psi_n(x, y)$ are the deterministic linearly independent basis functions, and s_n and b_n represent zero-mean, random variables expressed by the following relations:

$$\begin{cases} s_n = \iint_D S(x, y) \Phi_n(x, y) dx dy \\ b_n = \iint_D B(x, y) \Phi_n(x, y) dx dy. \end{cases} \quad (1)$$

The determination of these random variables depends on the choice of the set of deterministic functions $\{\Phi_n(x, y)\}$. We will use the set, which provides the uncorrelation of the random variables, i.e.:

$$\begin{cases} E\{s_n s_m\} = E\{s_n^2\} \delta_{n,m} \\ E\{b_n b_m\} = E\{b_n^2\} \delta_{n,m}. \end{cases}$$

Now, we show how to determine these functions $\Phi_n(x, y)$. In order to find them, let us consider the stochastic matched filtering technic [1].

If we consider a deterministic, stationary two-dimensional signal, called $S(x, y)$, which is defined over D , corrupted by an ergodic, stationary noise $B(x, y)$, the matched filtering technic consists in finding a function $\Phi(x, y)$, defined over D , in order to maximize the signal to noise ratio K , expressed by the following relation:

$$K = \frac{|\iint_D S(x, y) \Phi(x, y) dx dy|^2}{E\{|\iint_D B(x, y) \Phi(x, y) dx dy|^2\}}.$$

When the signal is not deterministic, but a random, zero-mean, stationary, two-dimensional signal $S(x, y)$, we can show that K can be explained as follows:

$$K = \frac{E\{|\iint_D S(x, y) \Phi(x, y) dx dy|^2\}}{E\{|\iint_D B(x, y) \Phi(x, y) dx dy|^2\}}.$$

Given that this signal to noise ratio can be rewritten as the ratio of two quadratic forms, it appears to be a Rayleigh quotient, so it will be maximized if $\Phi(x, y)$ is the two-dimensional eigenfunction associated to the maximal eigenvalue of the following integral equation:

$$\begin{aligned} \iint_D \Gamma_{SS}(x - x', y - y') \Phi_n(x', y') dx' dy' = \\ \lambda_n \iint_D \Gamma_{BB}(x - x', y - y') \Phi_n(x', y') dx' dy', \end{aligned} \quad (2)$$

for all $(x, y) \in D$ and where Γ_{SS} and Γ_{BB} represent the covariances of the signal and of the noise, respectively.

Random variables s_n and b_n are uncorrelated, when the $\Phi_n(x, y)$ functions are the eigenfunctions of integral equation (2), with eigenvalues λ_n verifying:

$$\lambda_n = \frac{E\{s_n^2\}}{E\{b_n^2\}}.$$

When eigenfunctions $\Phi_n(x, y)$ are normalized such as the following integral

$$\iint_D \iint_D \Gamma_{BB}(x - x', y - y') \Phi_n(x, y) \Phi_n(x', y') dx dx' dy dy'$$

takes one for value, we can show that functions $\Psi_n(x, y)$ are expressed by:

$$\Psi_n(x, y) = \iint_D \Gamma_{BB}(x - x', y - y') \Phi_n(x', y') dx' dy'. \quad (3)$$

In these conditions and considering the z_n random variables, obtained by projecting functions $\Phi_n(x, y)$ on noise-corrupted signal $Z(x, y)$, we can show that the use of the following expansion

$$Z(x, y) = \lim_{N \rightarrow \infty} \sum_{n=1}^N z_n \Psi_n(x, y)$$

corresponds to a signal to noise ratio of the n^{th} component of $Z(x, y)$ expressed by:

$$\frac{\sigma_S^2}{\sigma_B^2} \lambda_n,$$

where σ_S^2/σ_B^2 is the signal to noise ratio before processing. So all the eigenfunctions $\Phi_n(x, y)$ associated to eigenvalues λ_n greater than one can contribute to an improvement of the signal to noise ratio. For this reason, filtering the observed signal can be made by keeping all the components with a signal to noise ratio greater to a certain level, anyhow greater than 1.

3.2. Interpolation using the stochastic matched filtering method

To compute an interpolation based on the stochastic matched filtering method, the basic idea is to expand the observed signal and then to restore the signal of interest using the $\Psi_n(x, y)$ functions previously interpolated. But this reasoning presents some defaults. Indeed, it implies an heavy CPU budget and some memory problems may appear. For these reasons, we are going in this section to propose a new formulation for the stochastic matched filtering method by using the discrete cosine transform.

3.2.1. Analytical approximation for the solutions of the integral equation

We can find in the literature several works based on the stochastic matched filtering technic in its discrete form (see [6] for example). Unfortunately, when we consider the discrete form of integral equation (2), the eigenvectors solution of this generalized eigenvalue problem are linked to the native increment of the image and could cause problems for image interpolation. So, we do not consider the discrete relation but the continuous one to find the $\Phi_n(x, y)$ functions.

Considering the DCT¹ coefficients $\alpha_{k,l}^{\Gamma_{SS}}$, $\Omega_{k,l,p,q}^{\Gamma_{SS}}$ and $\Omega_{k,l,p,q}^{\Gamma_{BB}}$ of functions $\Phi_n(x, y)$, $\Gamma_{SS}(x-x', y-y')$ and $\Gamma_{BB}(x-x', y-y')$, we can show that solving integral equation (2) becomes equivalent to solving the following linear system:

$$\sum_{k=0}^{Nf} \sum_{l=0}^{Nf} \alpha_{k,l}^{\Gamma_{SS}} \Omega_{k,l,p,q}^{\Gamma_{SS}} = \lambda_n \sum_{k=0}^{Nf} \sum_{l=0}^{Nf} \alpha_{k,l}^{\Gamma_{BB}} \Omega_{k,l,p,q}^{\Gamma_{BB}}, \quad (4)$$

where $(Nf+1)$ corresponds to the number of DCT coefficients taken account and is high enough to ensure the uniform convergence of the series to their respective functions.

Finally, the analytical approximation $\hat{\Phi}_n(x, y)$ of the $\Phi_n(x, y)$ functions solution of the integral equation, is obtained with the following relation, for $(x, y) \in D$:

$$\hat{\Phi}_n(x, y) = \sum_{k=0}^{Nf} \sum_{l=0}^{Nf} \alpha_{k,l}^{\Gamma_{SS}} \cos\left(\frac{\pi k(x-T)}{2T}\right) \cos\left(\frac{\pi l(y-T)}{2T}\right).$$

This new method for finding an analytical approximation for the solutions of the integral equation has been quantified and compared to the classical approach, in the case of the Fredholm integral equation, that is when the noise covariance describes a white noise [3].

¹Discrete Cosine Transform

3.2.2. Interpolation-filtering method

We propose in this subsection a new formulation of the stochastic matched filtering method by using the discrete cosine transform. In these conditions, we are looking for the expression of the coefficients of the filtered signal expanded into cosine series; we shall reconstruct the approximation of the restored signal in the final phase of the processing.

Let $Z(x, y)$ be the observed signal to be expanded and let $\hat{Z}(x, y)$ be the reconstructed filtered signal. We have:

$$\hat{Z}(x, y) = \sum_{n=1}^Q z_n \Psi_n(x, y) \quad \forall (x, y) \in D, \quad (5)$$

where Q is chosen such as λ_Q is greater to a certain threshold, anyhow greater than 1.

In the last relation, z_n are the random variables to be determined from the input data:

$$z_n = \iint_D Z(x, y) \Phi_n(x, y) dx dy. \quad (6)$$

We have seen that these random variables are uncorrelated when functions $\Phi_n(x, y)$ are the eigenfunctions of integral equation (2). The $\Psi_n(x, y)$ basis functions are obtained by projecting functions $\Phi_n(x, y)$ on the noise covariance as described in relation (3).

First, we modify this relation, in order to express the $\beta_{p,q}^n$ coefficients of the $\Psi_n(x, y)$ cosine series. It comes:

$$\beta_{p,q}^n = T^2 \sum_{k=0}^{Nf} \sum_{l=0}^{Nf} \alpha_{k,l}^{\Gamma_{SS}} \Omega_{k,l,p,q}^{\Gamma_{BB}}, \quad (7)$$

for $(p, q) = 0, 1, \dots, Nf$.

In like manner, from expansion (5), we obtain for expression of the $\hat{\vartheta}_{k,l}$ DCT coefficients of restored signal $\hat{Z}(x, y)$:

$$\hat{\vartheta}_{k,l} = \sum_{n=1}^Q z_n \beta_{k,l}^n. \quad (8)$$

To end, we have to explain the z_n coefficients in terms of the coefficients of the observed signal and of the eigenfunctions. We can show that relation (6) is equal to:

$$z_n = T^2 \sum_{p=0}^{Nf} \sum_{q=0}^{Nf} \vartheta_{p,q} \alpha_{p,q}^n, \quad (9)$$

where $\vartheta_{p,q}$ represent the $Z(x, y)$ DCT coefficients.

Considering the θ rotation angle, it is possible to compute the interpolated-filtered signal using the following relation:

$$Z_\theta(x_\theta, y_\theta) = \sum_{k=0}^{Nf} \sum_{l=0}^{Nf} \hat{\vartheta}_{k,l} \cos\left(\frac{\pi k(x_\theta-T)}{2T}\right) \cos\left(\frac{\pi l(y_\theta-T)}{2T}\right),$$

where (x_θ, y_θ) represents the new coordinates of the pixels in rotating reference system \mathcal{R}_θ .

With such a formulation, it is possible to use the stochastic matched filtering method for image interpolation in a very short time, because all the computations can be made by using only the algorithm of fast discrete cosine transform.

3.3. Subimages processing

To apply the stochastic matched filtering method, it is necessary to respect the stationary condition for the signal and the noise. We know that we cannot consider an image as a realization of a stationary process. But after segmentation, we can define several areas representative of a texture. So a particular area of the image (a subimage) can be considered as a stationary process. For this reason, we are going to cover the noise-corrupted image with subimages. The subimage size is chosen such as the subimages are assumed to be a texture. For each angle θ , we apply the proposed processing on subimages, with $M \times M$ pixels. Scanning all the image allows a complete processing.

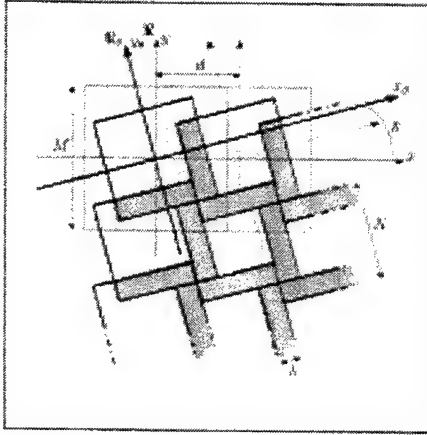


Figure 1: Subimages processing showing the overlapping between adjacent subimages

When we compute the interpolation of a subimage, we find an edge effect. Indeed, in rotating reference system \mathcal{R}_θ , the coordinates of the pixels localized on the edge of the subimage do not depend on the native subimage in reference system \mathcal{R} . This edge effect being maximal for angle θ equal to $\frac{\pi}{4}$, the subimage size after processing is $N \times N$, with N equal to $\frac{M}{\sqrt{2}}$. To limit these edge effects, it is necessary to segment the native image to obtain subimages which overlap, as shown in figure 1. The gray areas correspond to the superposition of subimages. d and h coefficients represent the distance between the center of two adjacent subimages (in line or row) and the width of the overlapping area respectively. We have:

$$d = \frac{N}{\cos \theta + \sin \theta} \text{ and } h = \left| \frac{N \sin \theta}{\sin \theta + \cos \theta} \right|.$$

We now apply the interpolation-filtering method, proposed in the previous section, to each zero-mean subimage. Assuming that the noise is high-frequency compared to the signal, when we apply this processing to the whole noise-corrupted image with the same number Q of basis functions for each subimage, the resulting image may be smoothed or still noise-corrupted. Indeed, the signal to noise ratio is not the same for each area of the image. For this reason, we are going to process each subimage, with different number Q of basis functions. To find this number, let us consider mean square error $\bar{\epsilon}$ between reconstructed signal $\hat{Z}(x, y)$ and signal of

interest $S(x, y)$. We can show:

$$\bar{\epsilon} = \sigma_S^2 + \frac{1}{4} \sum_{n=1}^Q (\sigma_B^2 - \lambda_n \sigma_S^2) \sum_{k=0}^{Nf} \sum_{l=0}^{Nf} (\beta_{k,l}^n)^2.$$

So, for each subimage, we compute $\bar{\epsilon}$ for different values of parameter Q (Q being in the interval $[1; Q_{max}]$, such as $\lambda_{Q_{max}}$ greater than 1). We only keep the Q values, which minimize the mean square error. The noise power, σ_B^2 , will be computed in a homogeneous area of the whole noise-corrupted image and the signal power, σ_S^2 , will be estimated in the subimage to be processed. Considering now the problem posed by the overlapping areas, the corresponding processed pixels will be computed by averaging each pixel having the same position in the overlapping subimage.

4. SHIP WAKES DETECTION

To illustrate our processing, we have chosen to apply it to an image acquired by the Spaceborne Imaging Radar-C/X-band Synthetic Aperture Radar (SIR-C/X-SAR), which shows a moving ship and its dark turbulent wake. This image is presented figure 2.

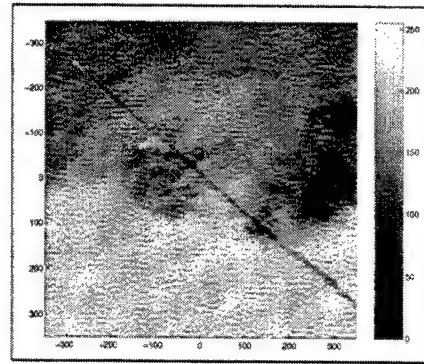


Figure 2: SIR-C/X-SAR image (698 × 698 pixels)

The image size is 698 × 698 pixels. The number of gray levels is 256 (0: black, 255: white). The dark patches in the upper right of this image correspond to smooth areas of low wind. The ship's wake is about 28 kilometers (17 miles) long in this image and investigators believe that may reveal that the ship is discharging oil. Classically, to quantify the perturbation level of a SAR image, we determine its speckle level. This one is obtained by computing the variation coefficient (C in the following), obtained on several homogeneous areas of the image. Let W be the number of homogeneous areas I_n , we have:

$$C = \frac{1}{W} \sum_{n=1}^W \frac{\sigma_n}{E\{I_n\}}.$$

For the studied image, the variation coefficient is equal to 0.277. We have now enough information about the studied image to process it.

4.1. Signal and noise auto-correlation functions

We have seen that the interpolation-filtering method, presented in section 3, requires the *a priori* knowledge of the signal and the

noise auto-correlation functions. In order not to favor any particular wake orientation, we have chosen to represent the signal auto-correlation function by an isotropic model. This one results, for different θ values, from the averaging of several auto-correlation function computations of a two colors straight line placed in a rotating reference system. This model is presented figure 3.a.

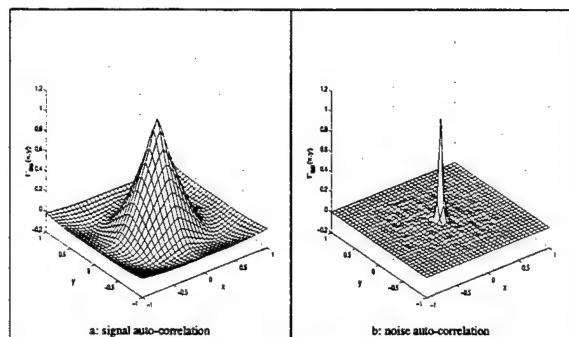


Figure 3: Normalized model for the signal and noise auto-correlation functions ($T = 1$)

The noise auto-correlation function is presented in figure 3.b. This model has been obtained by averaging several realizations of noise auto-correlation functions computed in some homogeneous areas of the native image.

4.2. Radon domain and wakes restoration

After zero-meaning the image presented figure 2, we have processed it with a subimage size equal to 17×17 pixels, to respect the coherence length of the noise.

We present in figure 4 the interpolated-filtered image for angle θ equal to 35° . For this image, number Q of basis functions is included between 1 and 13 depending on the native signal to noise ratio of the subimage to be processed (near 13 basis functions for the restauration of the wake and 1 basis function for the rest of the image).

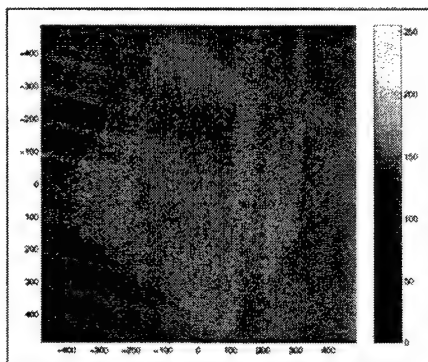


Figure 4: SIR-C/X-SAR image in reference system \mathcal{R}_{35} , (973×973 pixels)

Analyzing this figure, we see that the proposed processing allows

a great reduction of the speckle and a good restitution of the signal of interest (the wake). Indeed, there is no more dark patches and the variation coefficient is now equal to 0.016, so there is an improvement by a factor of 18 of the speckle level.

We present in figure 5 the resulted image in the Radon domain.

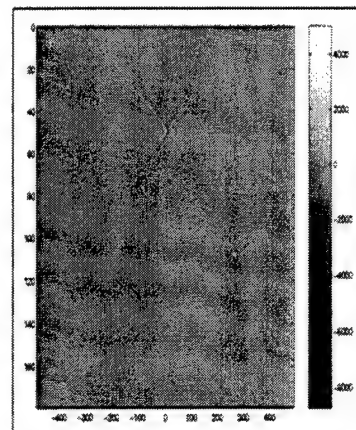


Figure 5: Radon domain obtained using the interpolation-filtering method

In the transform domain, the vertical axis represents the orientation of each integration line, while the horizontal axis represents the distance of each line from the center of the image. The trough corresponding to the wake is clearly evident. Its vertical position is near 51° and corresponds to the orientation of the wake. Furthermore, several sinusoidal curves of poor amplitude regarding to the trough amplitude are visible in the Radon domain and correspond to the Radon transform of the residual perturbations after interpolation-filtering.

From this transform domain, we have used the inverse Radon transform to find the location of the wake in the spatial domain. This inverse transform has been applied to the image, presented in figure 5, before raised to the power of three in order to improve the amplitude of the trough in regards to the rest of the image. The different interpolations have been made using a nearest neighbor interpolation. We present in figure 6 the resulted image.

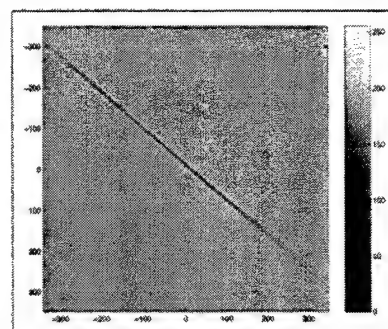


Figure 6: Restored wake from figure 5 (696×696 pixels)

The resulted image shows that our processing allows a great im-

provement of the wake readability. All the disruptive pixels have disappeared. The variation coefficient for this image is equal to 0.002 compared to 0.277 for the original image.

5. COMPARISON WITH CLASSICAL PROCESSING

We present figure 7 the transform domain of the SIR-C/X-SAR image. Each image in the rotating reference system has been computed using a nearest neighbor interpolation.

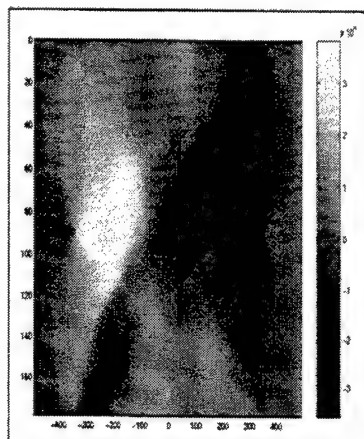


Figure 7: Radon domain obtained using the classical approach

In the transform domain, we can see several overlapping sinusoidal curves. They are due to the presence of the speckle in the native image and they limit the visibility of the trough corresponding to the wake. Furthermore, the dark patches in the original image create in the transform domain a large sinusoidal curve with an amplitude higher than the one of the trough. So, using a threshold to extract the trough will be misleading, because the minima of the transform domain do not correspond to the trough. In this case, the detection cannot be released with this processing.

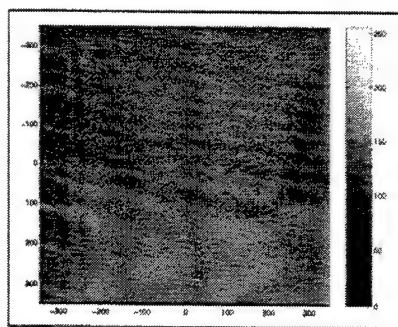


Figure 8: Restored wake from figure 7 (698 x 698 pixels)

To illustrate the previous remarks, we present in figure 8 the result obtained after having applied the inverse Radon transform, with the same process as for the image presented in figure 6. It confirms that this processing is not efficient for such an image. Indeed, we

remark a lot of perturbations, mainly due to the presence of the dark patches. The variation coefficient for this image is equal to 0.145 and the improvement is only a factor of 2.

6. CONCLUSIONS

We have presented in this paper a new processing which allows ship wakes detection in SAR images. This processing is based on the computation of the SAR image Radon transform. The original contribution of this work, compared to the classical approaches in this domain consists in taking into account the noise for the image interpolation in the rotating reference system. This allows the perturbations to have a lower impact in the transform domain, the corresponding sinusoidal curves having an amplitude smaller than the peak or trough characteristic of the wake. We have compared the transform domain and the restored wake obtained by our processing on SAR images, with those obtained with the classical processing. In all cases, our processing presents far better results. With our processing, the probability of false alarm or no detection is lower than with the classical approach, because only the signal of interest is considered.

An important drawback of the Radon transform is that it is global by nature, so this transform cannot tell the difference between long and short straight lines. For this reason, future work in this domain concerns the application of the proposed interpolation method for the computation of the localized Radon transform [2], which allows to localize the beginning of the wake.

7. REFERENCES

- [1] J.-F. Cavassilas, *Stochastic matched filter*, Proceedings of the Institute of Acoustics (International Conference on Sonar Signal Processing), Vol. 13, Part 9, pp. 194-199, 1991.
- [2] A.C. Copeland, G. Ravichandran, M.M. Trivedi, *Localized Radon transform-based detection of ship wakes in SAR images*, IEEE Transactions on Geoscience and Remote Sensing, Vol. 33, N° 1, pp. 33-45, January 1995.
- [3] P. Courmontagne, *A new formulation for the Karhunen-Loeve expansion*, Signal Processing, 79, pp. 235-249, 1999.
- [4] S.R. Deans, *The Radon transform and some of its applications*, A Wiley Interscience Publication, John Wiley & Sons, 1983.
- [5] K. Eldhuset, *An automatic ship and ship wake detection system for spaceborne SAR images in coastal regions*, IEEE Transactions on Geoscience and Remote Sensing, Vol. 34, N° 4, pp. 1010-1019, July 1996.
- [6] M. Grandchamp, J.-F. Cavassilas, *Improved multilook techniques applied to complex SAR images*, Proceedings IEEE International Conference on Acoustics, Speech and Signal Processing (ICASSP'97), Munich, Germany, Vol. 4, pp. 2821-2824, April 1997.
- [7] L.M. Murphy, *Linear feature detection and enhancement in noisy images via the Radon transform*, Pattern recognition letters, Vol. 4, N° 4, pp. 279-284, September 1986.
- [8] M.T. Rey, J.K. Tunaley, J.T. Folinsbee, P.A. Jahans, J.A. Dixon, M.R. Vant, *Application of Radon transform techniques to wake detection in Seasat-A SAR images*, IEEE Transactions on Geoscience and Remote Sensing, Vol. 28, N° 4, pp. 553-560, July 1990.

Space-Time Adaptive Matched-Field Processing (STAMP)

Yung P. Lee

Science Applications International Corporation

1710 SAIC Drive

McLean, VA 22102

tel: (703) 676-6512, fax: (703) 893-8753

yung@osg.saic.com

Abstract:

Space-time adaptive processing (STAP) is two-dimensional adaptive filtering employed for the purpose of clutter cancellation to enable the detection of moving targets. It has been a major focus of research activity in radar applications for which the platform is in motion, e.g., airborne or space-based systems. In this setting, an antenna sensor array provides spatial discrimination, while a series of time returns or pulses form a synthetic array that provide Doppler (velocity) discrimination.

The application of STAP for the mobile towed-array sonar system is non-trivial because of the complex multi-paths in the underwater environment. On the other hand, Matched-field processing (MFP) that uses a propagation code to predict the complex multi-path structure and coherently combines it to provide range/depth discrimination has been studied and demonstrated. MFP with a synthetic array (a series of snapshots) to estimate the source velocity and localize source in range and depth has also been demonstrated⁽¹⁾.

STAMP combines the adjacent-filter beamspace post-Doppler STAP⁽²⁾ and MFP to provide improved performance for the mobile multi-line-towed-array sonar applications. The processing scheme includes: transforming phone time snapshots into frequency domain, at each frequency bin forming horizontal beams in the directions of interest for each towed line, then combining signals from multi-towed-lines and adjacent Doppler bins and beams that cover the multi-path Doppler spread due to motion using adaptive MFP. A study of STAMP performance in the towed-array forward-looking problem will be discussed. In this problem, the own-ship signal and its bottom scattered energy can be treated as stationary interference with a moving target at constant speed within processing interval of a few minutes.

1. Introduction

Element-space pre-Doppler STAP⁽²⁾ is two-dimensional fully adaptive processing that coherently combines the signals from the elements of an array and the multiple snapshots of coherent signals, to obtain large spatial and temporal signal gain, to suppress interference, and to provide target detection in azimuth and velocity. Computational complexity and the need to estimate the

interference from limited snapshots make it impractical. The adjacent-filter beamspace post-Doppler STAP is a reduced-dimension partially adaptive approach. It performs a Doppler filtering with a temporal Fourier transform and a spatial filtering with the conventional beamforming before adaptive processing. The adaptive processing is done in a selected sub-space including a few beams and a few Doppler bins.

In the complex multi-path underwater environment, the signal will spread over many beams (especially when the array is steered away from broadside) and over many Doppler bins if a long estimation time is used. Without combining these bins a processor will encounter severe signal degradation. STAMP is different from the beamspace post-Doppler STAP in that it uses a propagation code to model the signal spread over beam and Doppler bins and coherently combines them. This new approach should provide improvement in signal estimation, while providing range and depth localization.

Single-element pre-Doppler space-time MFP had been reported in ref.(1). In this work, we will study the performance of the beamspace post-Doppler space-time adaptive MFP through a simulation. In section 2, we will describe the STAMP processing and the simulation scenario for the forward-sector processing. The simulation results will be discussed in section 3, and a summary will be given in section 4.

2. STAMP processing and Forward-Sector Processing Simulation Geometry

Figure 1 shows the STAMP processing diagram for a multi-line array. It starts with the Fourier transform of phone time series $x_l(t)$ into frequency domain $X_k(f)$, $X_k(f)=[X_{k1}(f) \dots X_{kn}(f)]$ where k is the line index and l is the phone index. A conventional beamforming response $b_k(f, \theta)$ then is calculated at each frequency bin for each towed line. A long beam-space vector $B(f)$ is formed with beam responses at selected beams and Doppler bins from all towed lines. The covariance matrix R is formed by the outer product of $B(f)$ and ensemble averaged over a wide Doppler band. For MFP, replicas are generated with a propagation code and passed through the same Doppler processing and conventional beamforming, then forming the beam-space replicas. The adaptive weight vectors are calculated with the wide-band covariance matrix R and the beam-space replicas, then applied on each $B(f)$ to get the adaptive narrowband response. It is

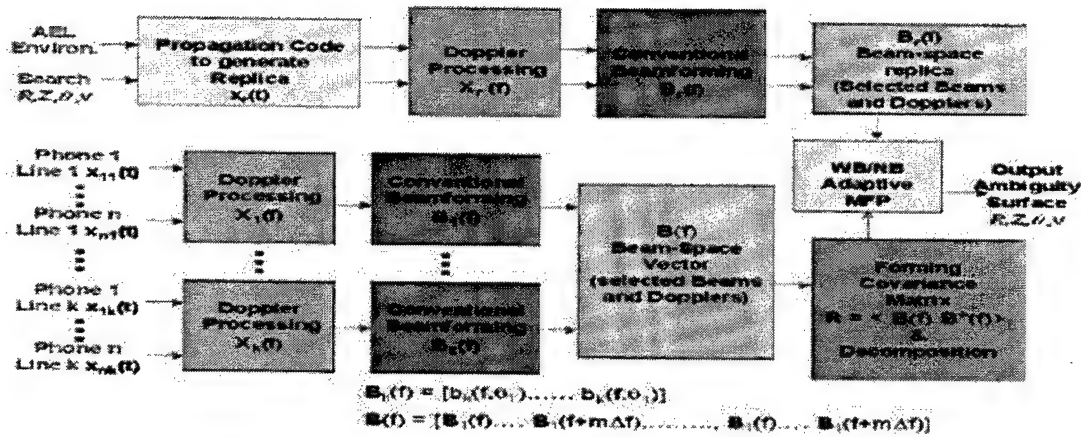


Figure 1: Space-Time Adaptive Matched-field Processing (STAMP)

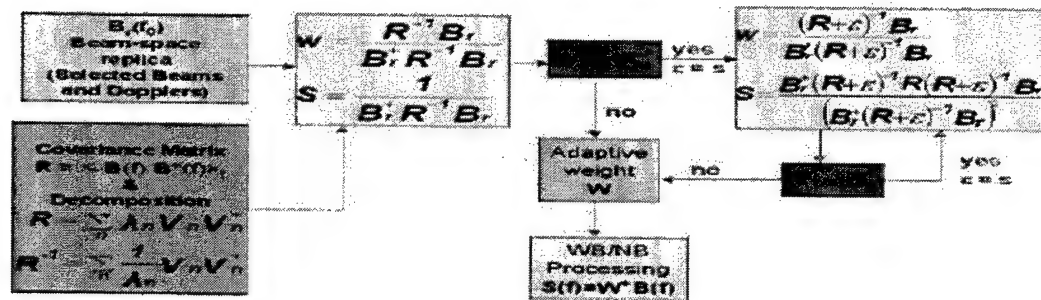


Figure 2: Wideband-Narrowband (WB/NB) Feedback-Loop White-Noise-Constrained (FLWNC) adaptive processing

noted that STAMP will be the same as conventional STAP when one replaces the propagation code with a plane-wave signal model.

Figure 2 shows the processing diagram of wideband-narrowband (WB/NB) Feedback-Loop White-Noise-Constrained (FLWNC) ⁽³⁾ adaptive processing. At each search cell, FLWNC iteratively adjusts the additive white noise until the white noise processing gain $|w|^2$ falls within the constraints δ_1 and δ_2 . The calculated adaptive weight then is used to filter snapshots at each Doppler bin. This is called wideband-narrowband processing because the weight is calculated with the covariance matrix that is ensemble averaged over a broader Doppler band and then it is applied to narrowband snapshots at each Doppler bin.

Figure 3 shows the simulation geometry of forward-sector processing. The own-ship noise and its bottom bounce energy are treated as stationary broadband point-interference. The target at 90 m in depth broadcasts a narrowband signal and moves toward the tow ship with a relative speed of 6 kts. In the simulations, three array configurations were considered: single-Line, 4-Line-Sequential, and 4-Line-vertical. Each single-Line consists of 48 phones with a spacing of 2.25 m. The arrays are at a nominal depth of 90 m. The 4-Line-Sequential configuration connects four single-lines to form a long line. The 4Line-Vertical configuration stacks 4 single-lines vertically with a vertical spacing of 10 m.

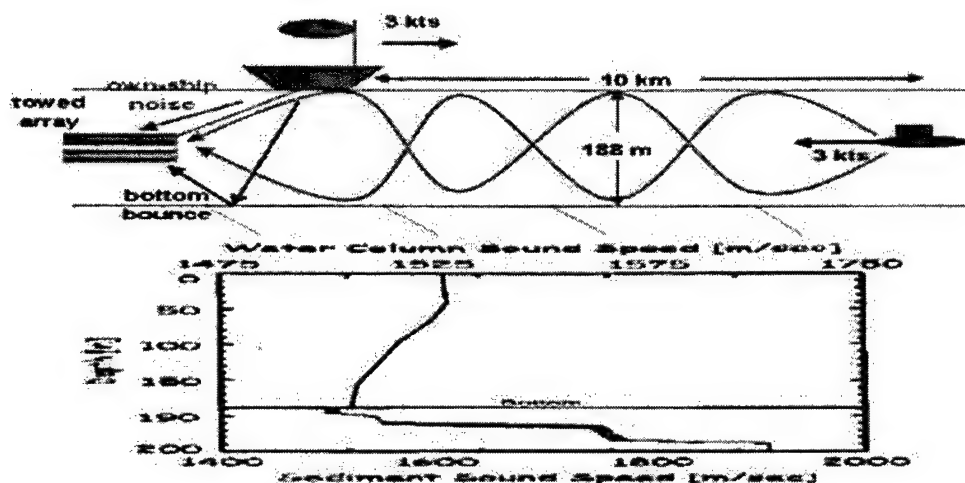


Figure 3: Simulation geometry, $F=200$ Hz, target(NB)=120 dB, own-ship(BB)=120 dB, bottom bounce (BB)=115 dB, white NL=120 dB, 0.1 random phase error, no environmental mismatch.

3. Simulation Results

From the conventional plane-wave beamforming of a single-Line, Figures 4 and 5 show beam/time responses (BTRs) and beam/Doppler responses of each signal component, respectively. The own-ship and the bottom interference arrive at relatively higher angles away from the forward endfire at 0° . The target component will be buried underneath the own-ship interference in the combined BTR, but with 256-sec integration time, it begins to separate from own-ship noise in the beam/Doppler response. The narrowband target signal is spread in Doppler and azimuth due to multi-paths that can be coherently combined with MFP to enhance detection and localization. This is the motivation of the STAMP study.

The top two panels in Figure 6 show the plane-wave beam spectrograms for single-Line steered at 10° off the forward endfire. The high-angle own-ship noise leaks into this shallow angle and causes the high noise background in the conventional beam spectrogram, but is significantly suppressed by the adaptive processing. The bottom left panel shows the STAMP track-cell-gram that tracks the target location and the bottom right panel shows the maximum response over Doppler. The STAMP uses beams of 0° to 30° and 6 Doppler bins for 6-kt search. It is noted that STAMP processing provides 2-3 dB more signal gain than the plane-wave processing for single-Line and provides 89 dB more with 4Line-Vertical array.

Figure 7 shows the range tracking performance of the STAMP. In the simulation the target starts at 10 km and moves toward the towed ship. With single-Line, the conventional MFP does not provide range discrimination of the target. With adaptive MFP, single-Line STAMP starts to show the target track that is closing in range. The 4Line configurations help to suppress the range sidelobes, and the 4Line-Vertical array provides a better performance than the 4Line-Sequential array.

Figure 8 shows depth discrimination of STAMP range tracking with the 4Line-Vertical array. The target track is formed only at the target depth of 90 meters. The target-related cascaded sidelobes are seen at other depths. Similarly, Figure 9 shows speed discrimination of STAMP range tracking with the 4Line-Vertical array. The target track is formed at the target speed of 3 m/s. Away from the target speed, the track becomes defocused and only target-related cascaded sidelobes are seen at search speeds far away from the target speed.

4. Summary

STAMP processing that combines STAP and MFP has been developed. Simulations show that STAMP coherently combines signal multi-path spread in azimuth and Doppler and greatly enhances the target detection as well as providing target range and depth classification and localization. In a future study, we will address how robust STAMP is against array shape error, frequency mismatch, and environmental mismatch as well as how STAMP performs in other tactical scenarios.

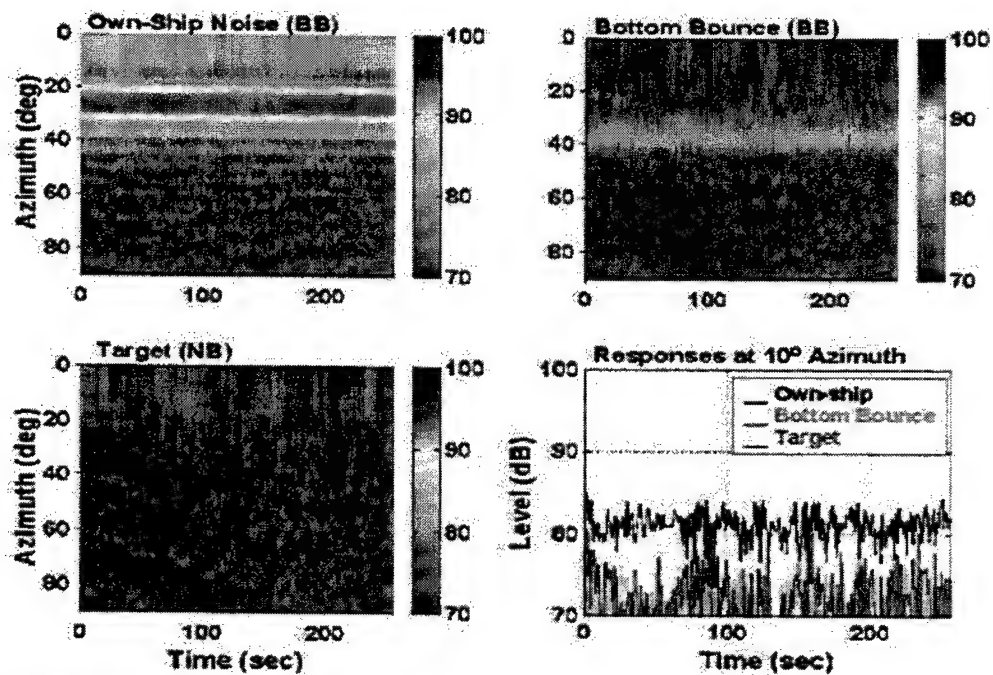


Figure 4 : Single-Line BTRs of each signal component.

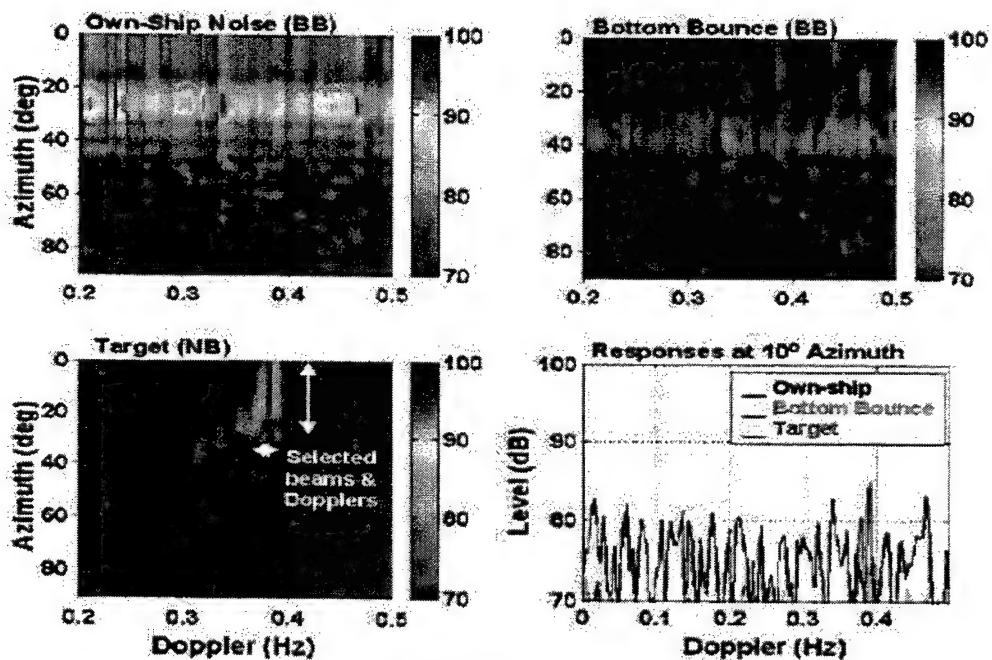


Figure 5: Single-Line Doppler/Azimuth responses of each signal component, 256-sec integration time.

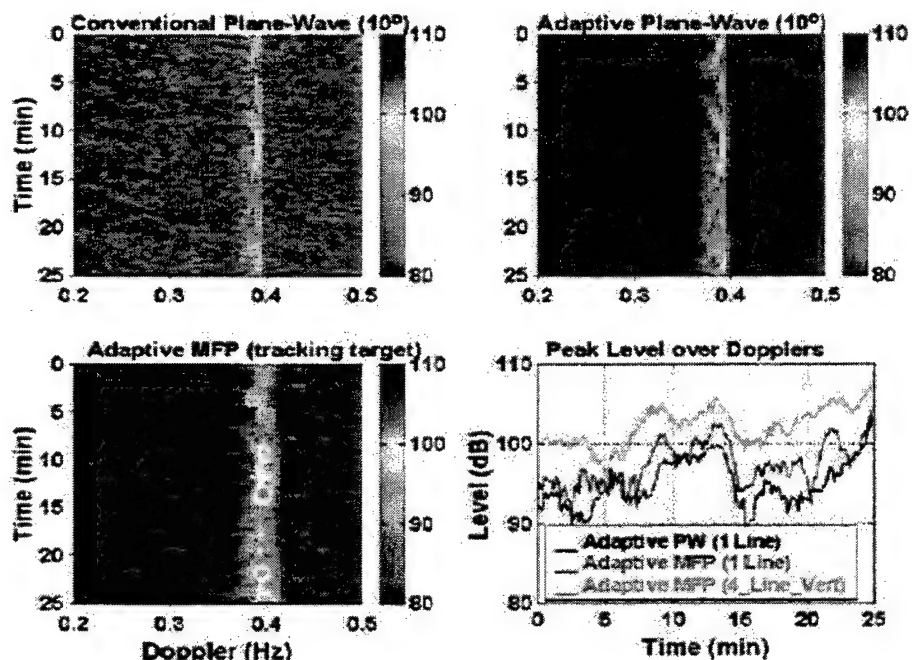


Figure 6: Single-Line beam/cell spectrograms.

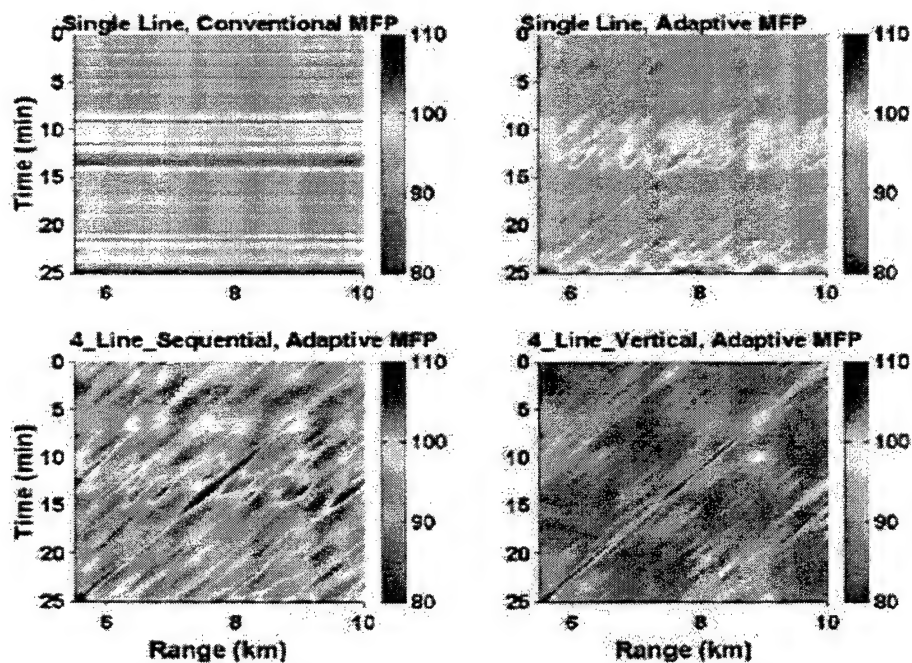


Figure 7: Array-size dependence of MFP range tracking search at target depth and target speed.

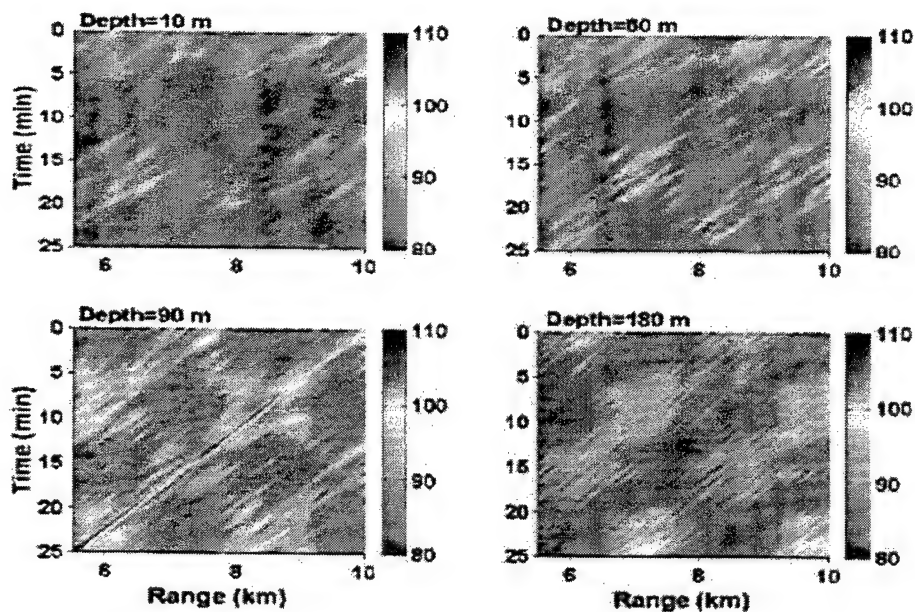


Figure 8: Depth discrimination of adaptive MFP range tracking, 4-Line-Vertical array search at target speed.

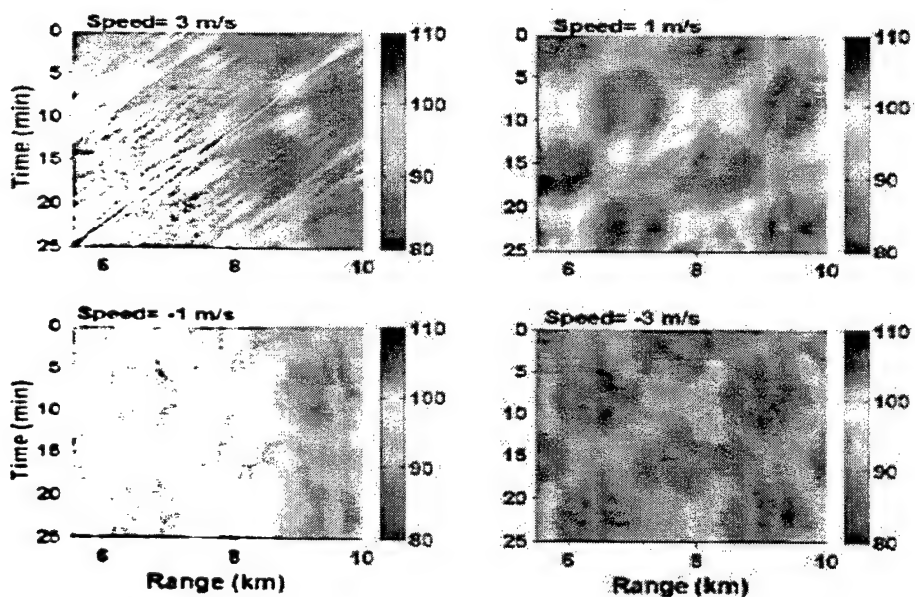


Figure 9: Speed discrimination of adaptive MFP range tracking, 4-Line-Vertical array search at target depth.

Reference:

- (1) "Synthetic aperture matched-field processing," Yung P. Lee, JASA 100, pp2851 (1996).
- (2) "Space-Time Adaptive Processing for Airborne Radar," J. Ward, Lincoln Laboratory Technical Report TR-1015, December 13, 1994.

- (3) "Robust adaptive matched-field processing," Y. Lee, H. Freese, J. Hanna, and P. Mikhalevsky, Proc. IEEE Oceans'93, vol.3, pp 387-392, October, 1993.

MOVING TARGET DEPTH ESTIMATION FOR PASSIVE SONAR, USING SEQUENTIAL RESAMPLING TECHNIQUES

Shawn Kraut and Jeffrey Krolik

Dept. of ECE, Box 90291
Duke University
Durham, NC 27708-0291
kraut@ee.duke.edu, jk@ee.duke.edu

ABSTRACT

We examine the problem of passive localization of a moving target in a littoral environment, based on its depth and range-rate. We compare performance with the conventional matched field processor, which localizes in depth and range. Range-rate localization is more robust with respect to uncertainties in the environment, and with respect to associated uncertainties in the horizontal wave numbers of the channel modes used for the matched field target response. In our approach the complex amplitudes of the modes are treated as nuisance parameters, which comprise a hidden, first-order Markov state process. In lieu of an analytic expression for the evolution of the likelihood function as new snapshots are integrated, we evaluate a method of particle filtering, or sequential resampling.

1. INTRODUCTION

Matched field processing (MFP) techniques localize targets in shallow water environments by computing a replica vector based on channel modes associated with a given set of environmental parameters, including the sound-speed profile [3]. They typically suffer from high sidelobes and ambiguous peaks produced at ambiguous ranges and depths, a problem that is exacerbated by environmental uncertainties. Modifications to the MVDR beamformer have been proposed to make it more robust to these uncertainties, by constraining the weight vector to stabilize its response over an ensemble of environments [1]. An additional problem is target motion, which spreads the target peak, decreasing its visibility. Previous work on target motion has focused on applying a transformations to successive data snapshots that compensate for motion corresponding to a particular hypothesized velocity, resulting in a focused peak in the range-depth ambiguity surface for a target having that velocity [2]. The main idea of this paper is to view target

motion as an asset rather than a liability, and to jointly estimate depth and range-rate in a manner that not only compensates for target motion, but also enhances robustness to environmental uncertainty. We propose to implement this by constructing a state model for the replica vector, using an assumed target velocity to constrain the state evolution, and leaving the initial state, which depends on target range, as a nuisance parameter. Because we do not have a closed-form, analytic solution for the updating of the likelihood function that arises from this state model, we instead examine a non-parametric method of approximating the likelihood, a sequential resampling or "particle filtering" method [4, 5].

2. MATCHED FIELD PROCESSING

Matched field processing obtains a replica vector for a target in shallow water based on the Green's function for the target response. For a shallow water environment, the response at the n^{th} sensor can be expanded in terms of the eigenmodes of the channel as follows [6, 7]:

$$s_k(n) = \sum_{m=1}^M \sqrt{\frac{2\pi}{k_r(m)r}} \psi_m(c_n) \psi_m(d) \exp(-j k_r(m) \cdot r). \quad (1)$$

Here k , m , and n index the time of the snapshot, the mode number, and the array sensor number, respectively. The sum is over the M eigenmodes $\psi_m(z)$ supported by the channel, where z is the depth coordinate. The eigenmodes are sampled at c_n , the depth of the n^{th} sensor, and at d , the depth of the target. The amplitude of the m^{th} mode includes a phase factor proportional to the product of its horizontal wave number $k_r(m)$ and the target range r . Rewriting this expression in terms of the N -dimensional replica vector \underline{s}_k , where N is the number of hydrophone sensors, we have:

$$\underline{s}_k(d, r) = \Psi(\underline{c})[\underline{\phi}(d, r) \odot \underline{x}_k(r)], \quad (2)$$

where \odot denotes the Hadamard, or element-by-element, vector product. Here the n^{th} element of \underline{s}_k is $s_k(n)$, the (n, m)

This work was supported by the Office of Naval Research under Contract No. N00014-01-1-0119.

element of Ψ is $\psi_m(c_n)$, and the m^{th} element of $\phi(d, r)$ is $\sqrt{\frac{2\pi}{k_r(m)r}} \psi_m(d)$. The modal phases have been collected into a vector $\underline{x}_k(r)$, whose m^{th} element is given by $\exp(-j k_r(m) \cdot r)$.

If the target is presumed to be stationary, so that the replica vector is constant across a window of K snapshots, $\underline{s}_k = \underline{s}$, then summing over the matched-filter output of K snapshots yields the conventional matched field processor, or Bartlett estimate [8]:

$$\frac{1}{K} \sum_{k=1}^K \frac{\|\underline{s}^\dagger \underline{y}_k\|^2}{\underline{s}^\dagger \underline{s}} = \frac{\underline{s}^\dagger \hat{\mathbf{R}}_{yy} \underline{s}}{\underline{s}^\dagger \underline{s}}, \quad (3)$$

where $\hat{\mathbf{R}}_{yy} = \frac{1}{K} \sum_k \underline{y}_k \underline{y}_k^\dagger$, is the sample correlation matrix of the data.

This estimator is also justified by the likelihood of the data, as a function of depth d and range r , over the window of snapshots, if the data has the random model $\underline{y}_k = a_k \underline{s} + \underline{n}_k$. Here the signal has a Gaussian distributed complex amplitude $a_k \sim CN[0, \sigma_s^2]$, and there is additive white measurement noise $\underline{n}_k \sim CN[0, \sigma_n^2 \mathbf{I}]$. Then by using Woodbury identities (a brief derivation is reproduced in in Appendix 3.7 of [9]), the likelihood of the k^{th} snapshot can be shown to be

$$f(\underline{y}_k | \underline{s}(d, r)) = \frac{1}{(\pi \sigma^2)^N \left(1 + \frac{\sigma_s^2}{\sigma_n^2} \underline{s}^\dagger \underline{s}\right)} \cdot \exp \left\{ -\frac{\underline{y}_k^\dagger \underline{y}_k}{\sigma_n^2} + \frac{\|\underline{s}^\dagger \underline{y}_k\|^2}{\sigma_n^2 \left(\frac{\sigma_s^2}{\sigma_n^2} + \underline{s}^\dagger \underline{s}\right)} \right\}. \quad (4)$$

Conditioned on \underline{s} , all the data vectors \underline{y}_k are independent and share the same likelihood. In the high SNR limit, $\sigma_s^2 \gg \sigma_n^2$, their joint log-likelihood, as a function of (d, r) , is proportional to the Bartlett estimate of Equation 3.

An alternative approach, the MVDR beamformer or Capon spectrum, has advantages for suppressing interfering sources and sidelobes. However it is more sensitive to target nulling if the presumed target replica vector is mismatched with respect to the true target response. In this work we investigate robustness with respect to errors in environmental parameters, which can produce target mismatch. We evaluate our Moving Target Depth Estimator (MTDE) and the Bartlett estimator, or conventional matched field processor, as a baseline estimator for comparison.

3. TARGET MOTION, ENVIRONMENTAL MISMATCH, AND DEPTH AMBIGUITY

Two phenomenon which degrade the performance of the Bartlett estimator are target motion and environmental mismatch. Here we examine the scenario in which a target is

moving in range at a constant velocity and constant depth. Target motion tends to smear out the peak target power across range, reducing peak height and the effective post-beamformer SNR. An example realization of an ambiguity surface is shown in Figure 1, where the target has moved from 10 to 10.5 km over 50 snapshots spaced two seconds apart, as indicated by the white line segment bounded by stars. Note that there are ambiguous peaks at other ranges at the same depth as the target (20m), but also at a depth of about 83m. (The cause of the ambiguous depth will be discussed below.)

Environmental mismatch produces mismatch of the replica vector \underline{s} . The replica vector is a function of both range and depth, but it is range localization that seems to be more seriously affected by mismatch, as shown in Figure 2. To understand this, consider Equation 2. The depth dependence is contained in the vector $\underline{\phi}$, the mode amplitudes sampled at the source depth. This vector also has a global scaling inversely proportional to range; the average range effectively scales the signal power σ_s^2 . The primary dependence on range is contained the vector of modal phases \underline{x}_k , each phase being proportional to the product of the horizontal wavenumber and the range, $k_r(m) \cdot r$. A small mismatch in the wavenumber $k_r(m)$ can cause a big mismatch in the phase, as it is multiplied by a range r than can be on the order of several kilometers.

Our initial investigation of environmental mismatch is based on the simple Pekeris model, with a uniform sound-speed in the water channel, and in the ocean bottom [6, 7]. Mismatch is implemented by using the Pekeris model to generate synthetic data, then perturbing the vertical wavenumbers k_z assumed in processing the data and forming an ambiguity surface. The wavenumbers are perturbed by a uniform random variable whose extent we express as a fraction of $\frac{v_i}{h}$, the approximate spacing of the vertical wavenumbers, where $h = 100m$ is the depth of the water column. Then the assumed modes $\psi_m(z)$ and horizontal wavenumbers $k_r = \sqrt{k_0^2 - k_z^2}$ are computed accordingly. For example, in Figure 2, they are perturbed by $\pm 4.5 \frac{\pi}{h}$, the total range of the perturbations being $0.9 \frac{\pi}{h}$. Note that while the range information has been lost, there is still significant energy distributed, across several ranges, at the correct depth of 20m and at an ambiguous depth of about 83.5 m

To see the source of the depth ambiguity, refer to Figure 3, in which we plot $\phi(d)$ at $d = 20m$ and $d = 83.5m$, as well as the magnitude of $\phi(d)$. While the amplitudes of the modal phases are different at the two depths, undergoing a relative sign change every other mode, the magnitudes are approximately equal. The sign change can be compensated by a corresponding sign change in the modal phase vector \underline{x}_k , which may occur at another range, as seen in both Figures 1 and 2. For a "perfect" constant-index waveguide, in which the modes are sinusoidal, and the amplitudes go to zero at the bottom, the ambiguity is exact. In this special

case the modes are sinusoidal, given by $\sin(\frac{\pi d}{h}m)$. Now let us try to identify two depths d_1 and d_2 at which the magnitudes of the modes are equal. Equating the magnitudes yields

$$\begin{aligned}\sin^2\left(\frac{\pi d_1}{h}m\right) &= \sin^2\left(\frac{\pi d_2}{h}m\right) \\ \rightarrow \cos\left(\frac{2\pi d_1}{h}m\right) &= \cos\left(\frac{2\pi d_2}{h}m\right).\end{aligned}\quad (5)$$

Using the fact that discrete-time sinusoidal signals of the form $\exp(i\omega m)$ are the same for frequencies ω that are separated by an integer multiple of 2π , we have the following solution:

$$\frac{2\pi d_1}{h} \pm \frac{2\pi d_2}{h} = 2\pi \rightarrow d_1 = d_2 - h. \quad (6)$$

Thus depth values that are symmetric about the middle of the water channel are potentially ambiguous. The ambiguous depth shown in Figure 3, $\sim 83.5m$, is a little bit deeper than the depth predicted by Equation 6, $80m$, since a more realistic "soft" boundary condition is used that causes the eigenmodes to be non-zero in the sediment bottom, and also decreases their vertical wavenumbers, "stretching" them slightly.

4. STATE MODEL FOR TARGET MOTION

We wish to accommodate target motion, and discard the presumption of stationarity of the replica vector used in obtaining the Bartlett processor ($\underline{s}_k = \underline{s}$). We accommodate motion by using a hidden state process, where the state is given by the modal phases \underline{x}_k of Equation 2:

$$\underline{x}_k = \mathbf{A}(\dot{r})(\underline{x}_k \odot \underline{x}_{k-1}). \quad (7)$$

Here the state transition matrix $\mathbf{A}(\dot{r})$ is a diagonal matrix of phase factors, with the m^{th} element being given by $\exp(-j k_r(m) \cdot \dot{r} \Delta t)$, where \dot{r} is range-rate/horizontal-velocity, and Δt is the time between snapshots. The initial phase vector \underline{x}_0 is unknown. So what is assumed known in this model is not the initial range of the target, but only the change in range, or range-rate. The state-noise vector \underline{u}_k consists of small phase perturbations. Its purpose is primarily to relax slightly the constraint imposed on the state sequence by the presumed horizontal wavenumber $k_r(m)$, which may have errors.

Denote the data matrix having the first k data vectors as its columns by \mathbf{Y}_k . Our goal is then to update the cumulative likelihood of the data, given a depth and range-rate pair $f(\mathbf{Y}_k | \dot{r}, d)$, as we acquire new data vectors \underline{y}_k . If the state vectors and the measurement vectors were both Gaussian, with linear transition matrices, then we could apply the expressions of Kalman filtering. The Kalman filter equations

provide expressions for a state prediction, measurement prediction, and state update; these are the conditional means of the densities $f(\underline{x}_k | \mathbf{Y}_{k-1})$, $f(\underline{y}_k | \mathbf{Y}_{k-1})$, and $f(\underline{x}_k | \mathbf{Y}_k)$. The Kalman equations also yield expressions for the error covariances associated with the estimates, which are the covariances of the three densities. The conditional means and covariances are then enough to characterize the densities, since the densities are Gaussian. So rather than viewing the Kalman filter as merely updating state estimates, we can view it as updating these densities, needed in turn to update the likelihood. In standard applications of Kalman filtering, parameters of interest, such as target range and velocity, comprise the state vector, and state estimates will suffice. In the application discussed here, the state consists largely of nuisance parameters; the parameters of interest must be inferred from the cumulative likelihood function $f(\mathbf{Y}_k | \dot{r}, d)$ estimated from approximations to these densities.

5. SEQUENTIAL RESAMPLING FOR STATE ESTIMATION

In lieu of an analytic expression for the updated likelihood, we employ a method of sequential resampling [4, 5]. This represents the densities parametrically, by a collection of samples, known as "particles." Loosely, we can think of the method as evolving histograms of samples, rather than analytic density expressions. The process is as follows [4]: at time-step k , we have some (prediction) samples $\underline{x}_k^{*(i)}$ which are distributed as $f(\underline{x}_k | \mathbf{Y}_{k-1})$. The first step is to scale, or weight, these samples according to the likelihood of the k^{th} data snapshot. The weights are proportional to this likelihood, and normalized to sum to one:

$$w_k^{(i)} = \frac{f(\underline{y}_k | \underline{x}_k^{*(i)})}{\sum_i^N f(\underline{y}_k | \underline{x}_k^{*(i)})}. \quad (8)$$

For our application, the likelihood was obtained by substituting Equation 2 into Equation 4. In the second step, the samples are resampled with a probability given by the likelihood, to yield a new set of (update) samples \underline{x}_k^i , which are distributed as $f(\underline{x}_k | \mathbf{Y}_k)$:

$$\text{Prob}[\underline{x}_k^{(j)} = \underline{x}_k^{*(i)}] = w_k^{(i)}. \quad (9)$$

After this step, one typically has a significant number of samples \underline{x}_k^i that are identical/degenerate, since they correspond to prediction samples $\underline{x}_k^{*(i)}$ that have high weight values. In the third step, the samples are translated according to the state transition equation, and state noise is added. This produces new prediction samples:

$$\underline{x}_{k+1}^{*(i)} = \mathbf{a}(\underline{x}_k^i, \underline{u}_k^{(i)}) \quad (10)$$

(the state noise $\underline{u}_k^{(i)}$ has the side effect of differentiating degenerate samples). One approach is to run separate estimators, or "particle filters," in parallel, one for every hypothesized range-rate and depth (\dot{r}, d) . Then the likelihood for each (\dot{r}, d) pair can be approximated as follows:

$$\begin{aligned} f(\underline{y}_k | \mathbf{Y}_{k-1}; \dot{r}, d) &= \int d\underline{x}_k f(\underline{y}_k | \underline{x}_k; \dot{r}, d) f(\underline{x}_k | \mathbf{Y}_{k-1}; \dot{r}, d) \\ &\simeq \sum_i^N f(\underline{y}_k | \underline{x}_k^{*(i)}; \dot{r}, d). \end{aligned} \quad (11)$$

And the cumulative likelihood is given by

$$f(\mathbf{Y}_k | \dot{r}, d) = \prod_{k=0}^N f(\underline{y}_k | \mathbf{Y}_{k-1}; \dot{r}, d). \quad (12)$$

In practice, running parallel particle filters is likely to be computationally prohibitive. For example, 100 grid points in both depth and range would require 10,000 parallel estimators, each requiring a set of samples to represent the likelihood.

An alternative approach is to include the parameters of interest, in this case (\dot{r}, d) , in the state vector, with a uniform prior. Then an ambiguity surface may be obtained by plotting the marginal histogram of the update samples $\underline{x}_k^{(i)}$, which are distributed as $f(\underline{x}_k | \mathbf{Y}_k)$. The marginal histogram gives an approximation to $f(\dot{r}, d | \mathbf{Y}_k)$, which with a uniform prior on (\dot{r}, d) is proportional to the likelihood $f(\mathbf{Y}_k | \dot{r}, d)$. A difficulty of this approach in practice is that the sequential resampling techniques tend to display the behavior of competitive dynamical systems (see, for example, [10]). That is, even if two sample regions have an equal level fitness with respect to the likelihood, over time one of them will tend to "win", and monopolize the samples. In our investigation we observed that with a target at 20m, some trials would show a peak at 20m, while other trials would show a peak at the depth ambiguity of 83.5m. So the ambiguity surface of a single trial does not reflect the intrinsic ambiguity over the ensemble of trials; it gives an over-optimistic picture of the ambiguity surface, and misleading in this respect.

To alleviate this problem, we chose a hybrid approach, putting velocity in the the state vector, but leaving depth, which we treat as the parameter of primary interest, out of the state vector. This requires a separate particle filter for each hypothesized depth. We chose 100 grid points in depth, leading to 100 corresponding particle filters. The histogram of particles at each depth provides an estimate of $f(\dot{r} | \mathbf{Y}_k, d)$. At each depth, we can use the equivalent of Equation 12 in order to obtain the likelihood:

$$f(\mathbf{Y}_k | d) = \prod_{k=0}^N f(\underline{y}_k | \mathbf{Y}_{k-1}; d). \quad (13)$$

Assuming a uniform prior on d , then normalizing this with respect to d provides an estimate of $f(d | \mathbf{Y}_k)$. We can then compute an ambiguity surface as

$$f(\dot{r}, d | \mathbf{Y}_k) = f(\dot{r} | \mathbf{Y}_k, d) \cdot f(d | \mathbf{Y}_k). \quad (14)$$

Again, with a uniform prior on (\dot{r}, d) , this posterior density is proportional to the likelihood $f(\mathbf{Y}_k | \dot{r}, d)$.

To combat the problem of degeneracy of samples we implemented an approach suggested in [4]. Namely, in the state prediction step, additional state noise was added to differentiate degenerate samples. Since range-rate \dot{r} was included in the state, noise was added to the range-rate values, with a standard deviation of 0.2 m/s. In addition, the 5% of the samples with the largest weights were automatically retained for the next step, to mitigate against losing a sample value on the basis of a single snapshot only.

6. SIMULATION AND RESULTS

Figures 4 and 5 show two ambiguity surfaces obtained in this manner, for a surface and submerged target, respectively. The SNR per sensor element was set at 0 dB. At each hypothesized depth we ran a particle filter with 500 samples or "particles". Depth estimates were obtained by taking the maximum of $f(\mathbf{Y}_k | d)$. Histograms of depth estimates for a surface target, obtained from 100 trials of the Bartlett estimator and the MTDE estimator, are shown in Figure 6. Similar histograms are shown for a submerged target at a depth of 20m in Figure 7. Note the ambiguity at a depth of about 83.5m. Because we run parallel particle filters for all hypothesized depths, the ambiguity surface for a single trial of the MTDE estimator, as in Figure 5, displays this ambiguity.

To investigate the robustness of the estimators with respect to environmental uncertainty, the probability of correct localization (PCL) of the target is plotted versus increasing environmental uncertainty in Figure 8. The region of correct localization includes $\pm 2m$ around the true target depth, and around the depth ambiguity. As discussed in Section 3, the vertical wavenumbers in the estimator were perturbed by a uniform random variable whose range is expressed as a fraction of $\frac{\pi}{h}$. The PCL is plotted as this fraction is increased from 0 to 1.5. This environmental perturbation does not significantly degrade the localization of the surface target, but it does degrade the localization of the submerged target. The degradation is not as severe for the MTDE estimator as it is for the Bartlett estimator.

7. CONCLUSIONS

In this paper we have investigated an approach of joint estimation of range-rate and depth, rather than range and depth. Range-rate provides another dimension with which to discriminate targets against interfering sources (such as moving ships). In addition, discrimination based on range-rate is more robust with respect to environmental uncertainties, as verified by simulations. In lieu of an analytic expression of the updated likelihood, we have investigated a technique of sequential resampling or particle filtering. The limitation of this particular technique seems to be its ability to compensate for low SNR by integrating over many snapshots. It should be emphasized, however, that this is a limitation of the particle-filter implementation investigated here, and not a limitation of the basic state-model approach of localizing with respect to range-rate and depth, rather than range and depth. Our future work will be focused on implementations that more effectively exploit the entire data history.

8. REFERENCES

- [1] J. L. Krolik, "Robust matched-field beamforming with benchmark shallow-water acoustic array data," in *1996 IEEE International Conference on Acoustics, Speech, and Signal Processing*, Atlanta, GA, May 1996.
- [2] L. M. Zurk, N. Lee, J. Ward, and A. Gronosky, "Adaptive matched field processing for a moving target in a noisy shallow water channel," in *Proceedings of the 8th annual workshop on Adaptive Sensor and Array Processing*, Lexington, MA, March 2000, MIT Lincoln Laboratory.
- [3] A. B. Baggeroer, W. A. Kuperman, and P. N. Mikhalevsky, "An overview of matched field methods in ocean acoustics," *IEEE J. of Oceanic Engineering*, vol. 18, no. 4, pp. 401–424, 1993.
- [4] N. J. Gordon, D. J. Salmond, and A. F. M. Smith, "Novel approach to non-linear/non-gaussian bayesian state estimation," *IEE Proceedings-F*, vol. 140, no. 2, pp. 107–113, 1993.
- [5] J. Liu and M. West, "Combined parameter and state estimation in simulation-based filtering," in *Sequential Monte Carlo Methods in Practice*, A. Doucet et al, Ed. Springer-Verlag, 2000.
- [6] F. B. Jensen, W. A. Kuperman, M. B. Porter, and H. Schmidt, *Computational Ocean Acoustics*, American Institute of Physics Press, 1994.
- [7] C. S. Clay and H. Medwin, *Acoustical Oceanography: Principles and Applications*, John Wiley and Sons, 1997.
- [8] P. Stoica and R. Moses, *Introduction to Spectral Analysis*, Prentice Hall, 1997.
- [9] S. Kraut, *Matched and Adaptive Subspace Detectors: Properties and Optimalities, and Statistical Analysis by a Method of Stochastic Representations*, Ph.D. thesis, University of Colorado at Boulder, 1999.
- [10] J. Hofbauer and K. Sigmund, *Evolutionary Games and Population Dynamics*, Cambridge Univ. Press, 1998.

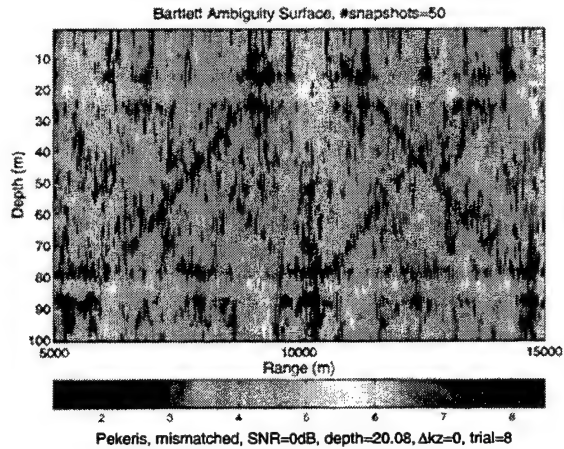


Figure 1: Bartlett estimator on moving target with perfectly known environment.

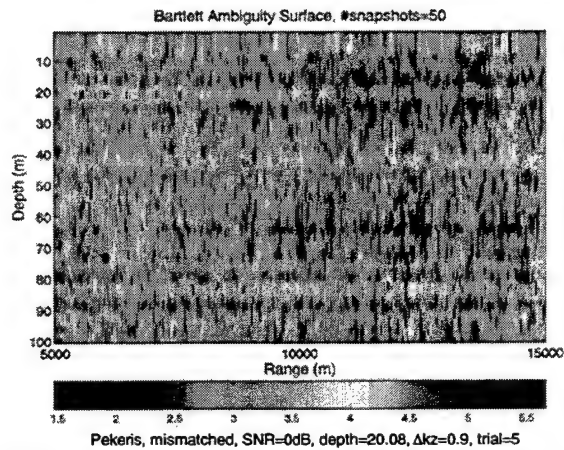


Figure 2: Bartlett estimator on moving target with mismatch in vertical wavenumbers in the range $[0, 0.9 \frac{\pi}{h}]$.

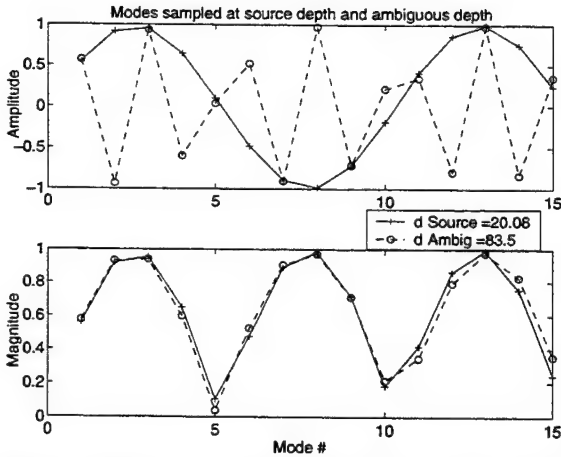


Figure 3: Modes at two ambiguous depths: (a) their amplitudes, and (b) their magnitudes.

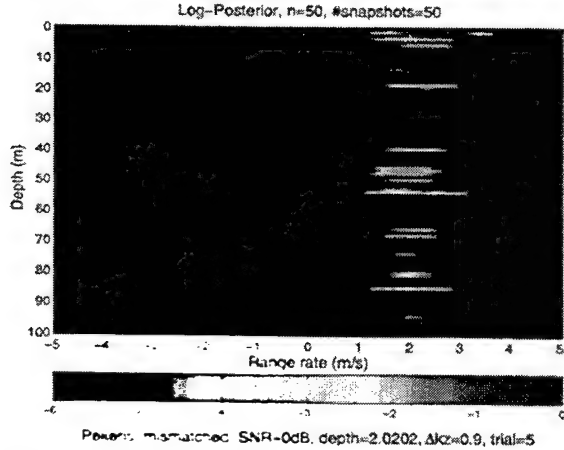


Figure 4: MTDE estimator: depth/range-rate ambiguity surface for a surface target.

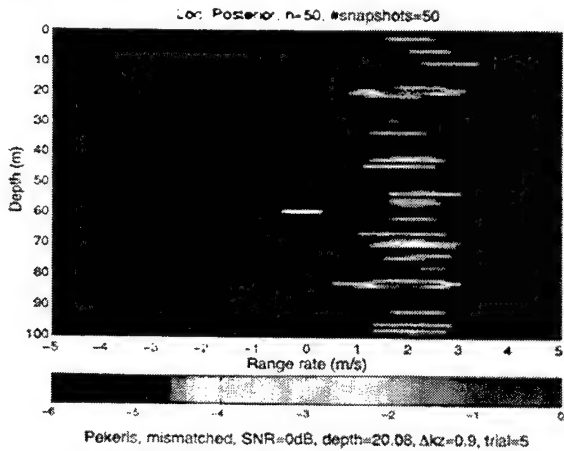


Figure 5: MTDE estimator: depth/range-rate ambiguity surface for a submerged target.

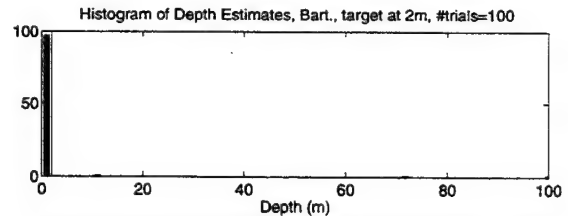
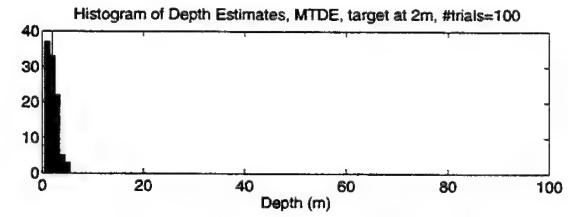


Figure 6: Histograms of depth estimates for a surface target. Pekeris, mismatched, SNR=0dB, #snapshots/trial=80, depth=2m, Δkz=0.9

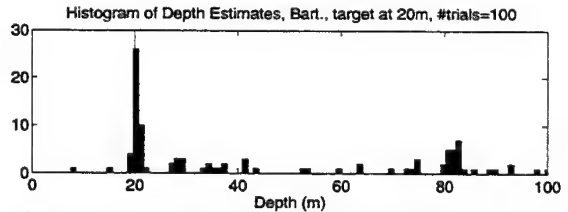
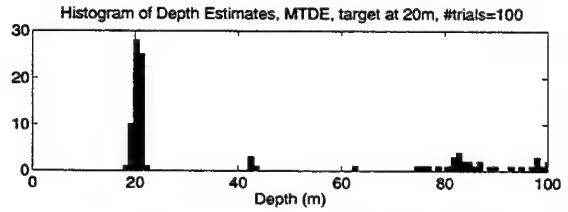


Figure 7: Histograms of depth estimates for a submerged target. Pekeris, mismatched, SNR=0dB, #snapshots/trial=80, depth=20m, Δkz=0.9

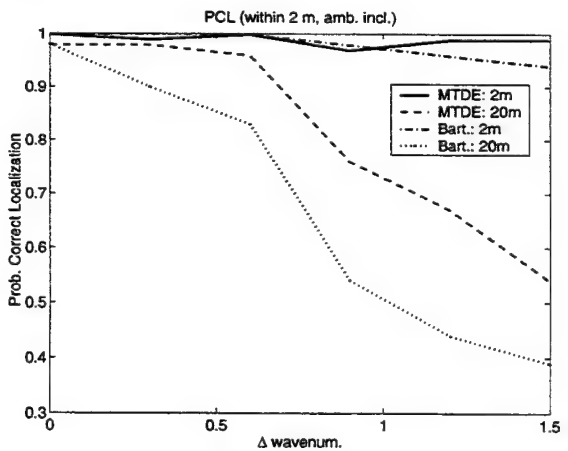


Figure 8: Probability of correct localization for Bartlett and MTDE estimators, on both surface and submerged targets.

Covariance Matrix Filtering for Adaptive Beamforming with Moving Interference

Bruce K. Newhall

Johns Hopkins University
Applied Physics Laboratory
11100 Johns Hopkins Road
Laurel, MD 20723-6099
bruce.newhall@jhuapl.edu

ABSTRACT

An approach is developed for adaptive beamforming for mobile sonars operating in an environment with moving interference from surface shipping. It is assumed that the sound source of each ship is drawn from an ensemble of Gaussian random noise, but each ship moves at constant speed along a deterministic course. An analytic expression for the ensemble mean covariance is obtained. In practice the location, course, speed, mean noise level, and transmission loss of each interferer are not known with sufficient precision to use the modeled ensemble mean as a basis for adaptive beamforming. The problem is thus to accurately estimate the ensemble mean based on data samples. The analytic ensemble mean is not stationary, and thus is not well estimated by the sample mean. The ensemble of covariance samples consists of rapidly varying random terms associated with the emitted noise and more slowly oscillating deterministic terms associated with the source and receiver motion. The non-stationary ensemble covariance mean can be estimated by filtering out the rapidly varying noise while retaining the slow oscillatory terms. Performance of the filters can be visualized and assessed in the "epoch" frequency domain, the Fourier transform of the covariance samples. In this domain, higher bearing rates show up at higher frequencies. The traditional sample mean estimator retains only the zero-frequency bin corresponding to stationary interference. Techniques that can identify and include the appropriate non-zero frequency contributions are better non-stationary estimators than the sample mean. Several such techniques are offered and compared. Simulations are invaluable in evaluating the filter performance, since the ensemble mean can be precisely calculated analytically in the simulation, and compared directly with the sample estimates. Simulations of adaptive beamformers using covariance filtering will be shown to yield improved robustness to shipping motion.

1. INTRODUCTION

At low frequencies, underwater noise is dominated by shipping sources. These sources can be extremely loud, and can dominate the performance of low-frequency passive sonar systems. Since these sources are typically spatially discrete, adaptive techniques ought to apply to eliminate their influence when surveillance is performed in locations in between the loud ships. Unfortunately, the shipping sources are moving, and hence violate the stationary noise assumptions of current adaptive

techniques. Current implementations of adaptive beamformers often do not achieve much gain above conventional, non-adaptive beamformers and hence remain limited by the loud sources of interference. Here we suggest a new class of techniques that may robustly achieve the rejection of loud sources of moving interference.

2. PHYSICAL MODEL OF SHIPPING NOISE

Current adaptive techniques are based on the physical assumption that the sources of interference are stationary in space. This is clearly not valid for the case of moving ocean shipping sources. Hence, we must develop a new physical model for the interference in order to derive the appropriate adaptive processing.

2.1 Pressure Field

Begin by assuming an arbitrary set of ships under deterministic motion in an arbitrary underwater sound channel. We focus on a single frequency, with the assertion that the model can be extended to the broadband case by a straightforward summation across frequencies. In the selected frequency bin, it is reasonable to model the sound source of each ship by a draw from an ensemble of complex Gaussian random noise, and assume that the noises of different ships are fundamentally independent.

These sources are then propagated to each receiver array element. The propagation may be described by a coherent sum over modes [1]. In a range independent environment, these modes arise naturally with the use of a normal mode propagation model. In range-dependent environments, the propagation can be expanded as a sum of local modes in the vicinity of the receiver. This local mode expansion is explicit via the use of coupled or adiabatic mode propagation models, but in principle can be obtained from the field output of any propagation modeling technique. The received acoustic pressure p_n at the n th element in an array is a sum across ships of the sum over the local modes:

$$p_n = \sum_j \sum_m s_j A_{mn}(t) e^{ik_m r_{jn}(t)}$$

where s_j is the source noise sample, A_{mn} is the mode amplitude and k_m is the wavenumber of the m th mode, and r_{jn} is the range from the j th ship to the n th receiver element. Note that the mode amplitudes must incorporate cylindrical spreading and attenuation terms not given explicitly here. The pressure consists of random contributions from the ship noise sources and deterministic time-varying propagation contributions.

2.2 Covariance

Optimal adaptive processing is determined from the mean of the covariance among sensor pressures. This expectation must be taken across the random ensemble of ship sources. The ensemble-mean covariance will be a function of time because of the time varying propagation terms. Therefore the expected covariance cannot be obtained directly from a sample mean across time samples of the covariance. Using the independence of different ships an analytic expression for the ensemble covariance is obtained:

$$\begin{aligned} \langle p_{n_1} p_{n_2}^* \rangle &= \sum_j \sum_{m_1} \sum_{m_2} \langle s_j s_j^* \rangle \\ &\times A_{m_1 n_1} A_{m_2 n_2} e^{i(k_{m_1} r_{j n_1}(t) - k_{m_2} r_{j n_2}(t))} \end{aligned}$$

where the brackets indicate the expectation across the ensemble. The term $\langle s_j s_j^* \rangle$ is the power spectrum of the j th source.

If the ranges, propagation modes, and source level power spectra were all known, this model expression could be calculated at each time and used in a standard minimum variance distortionless response (MVDR) full-rank ABF [2, 3]. This approach might be termed the full knowledge *a priori* model-based MVDR method. Such an ABF would move its nulls in time to optimally reject noise from all the moving ships. Unfortunately, it is unlikely in practice that full knowledge will be available *a priori*. Precisely predicting the propagation structure is quite difficult given the spatial and temporal variability of the ocean. It is also unlikely that the exact source power spectra will be known for every contributing ship. Thus, we usually must attempt to estimate the unknowns in the ensemble mean covariance from data samples.

3. ALGORITHMS

Since the ensemble mean involves deterministic time-varying terms, it cannot be reliably estimated directly from a sample mean taken over time. In particular, the oscillatory nature of the exponential terms will produce a

sample mean that tends to zero over long estimation times, while the ensemble mean is significantly larger. To avoid underestimating the ensemble mean, alternatives to the sample mean are considered.

3.1 Fourier Analysis and Synthesis

An alternative to sample averaging is to apply Fourier analysis to covariance samples. One motivation for this approach is to separate the differing time scales involved. The random source noise varies rapidly from one sample to the next. This rapid variation produces a sample noise that is nearly white. This sample noise will corrupt estimates of the ensemble mean covariance unless it is removed. The deterministic amplitudes and phases from the propagation terms vary more slowly and continuously in time. A low pass filter is expected to separate the rapidly varying sample noise from the slowly varying propagation terms. Since filter behavior is often best analyzed in the frequency domain, this motivates transforming the covariance samples to a corresponding frequency domain. This domain will be referred to as the epoch frequency domain to distinguish it from the acoustic frequency.

A second motivation for considering the Fourier transform of the covariance samples can be obtained by considering the time dependence of the propagation terms. The propagation amplitudes typically evolve very slowly in time, and this variation made be neglected for the moment. The most rapidly changing term is the phase term due to the changing ranges to the interference sources. Expand the ranges in a Taylor series about some reference time:

$$r = r_0 + \dot{r}t + \dots$$

where r_0 is the range at the reference time $t=0$ and \dot{r} is the initial range rate of the source. Again for the moment, higher order terms will be neglected. The ensemble covariance can now be approximated by

$$\begin{aligned} \langle p_{n_1} p_{n_2}^* \rangle &= \sum_j \sum_{m_1} \sum_{m_2} \langle s_j s_j^* \rangle A_{m_1 n_1} A_{m_2 n_2} \\ &\times e^{i(k_{m_1} r_{j n_1 0} - k_{m_2} r_{j n_2 0})} e^{i(k_{m_1} \dot{r}_{j n_1} - k_{m_2} \dot{r}_{j n_2})t} \end{aligned}$$

In this form, the unknowns: source power spectra and propagation amplitudes are coefficients of sinusoidal complex exponentials with epoch frequencies

$\Omega = k_{m_1} \dot{r}_{j n_1} - k_{m_2} \dot{r}_{j n_2}$. This suggests that these unknown coefficients can be estimated by Fourier analysis. Once the coefficients are estimated then the original time series for the ensemble covariance is reconstructed via Fourier synthesis.

The overall approach is summarized as follows. First obtain time samples of the elements of the covariance

matrix, as is currently done in ABF. For each matrix element, transform the time samples of covariance to the epoch frequency domain. Identify the appropriate frequencies associated with the moving ships, and use those frequency coefficients to synthesize the ensemble mean time series. The only portion of the algorithm remaining to specify is the technique of identifying which frequencies in the epoch domain are associated with the shipping noise sources and which are dominated by sample noise. Several methods can be employed.

3.2 Covariance Low-pass Filtering Methods

Since ships generally do not change range significantly within a few time samples, the shipping noise is expected to nearly always occur in the lowest frequency bins of the epoch frequency domain, while sample noise is expected to be nearly white across all bins. Hence, appropriate low pass filters are expected to retain much of the shipping noise energy to be estimated, while rejecting the sample noise. The best selection of pass band is made based on the expected motion of the contributing ships. Current ABF algorithms that employ the sample mean are in fact an example of covariance low pass filtering, since the sample mean is the low pass filter that retains only the spectral power in the zero-frequency bin. The performance of any low pass filter can be improved by matching the filter width to the expected epoch frequency widths associated with typical ship motion. For rapidly moving ships, this can be achieved by retaining more frequency bins in the filter. In order to further improve over current algorithms, advantage must be taken of the specifics of the epoch frequency structure of the shipping noise.

The epoch frequency for each ship given above depends of the difference of the products of a wavenumber times a range rate. Underwater acoustic wavenumbers of the significant modes generally do not exhibit much spread. Furthermore, for operational horizontal line arrays, the interfering ships will almost always occur at ranges significant relative to the horizontal separation between array elements. In these cases the epoch frequency where a ship contributes can be approximated by

$$\Omega \approx k_0 \Delta x \dot{\theta} \sin \theta$$

where k_0 is a reference wavenumber, Δx is the horizontal separation between elements, θ is the bearing to the ship (relative to the line between the elements), and $\dot{\theta}$ is the bearing rate. Note that the epoch frequency increases approximately linearly with separation between elements. This suggests a second filtering approach, in which the low pass filter frequency width is increased linearly proportionally to separation. Elements near the main diagonal of the covariance matrix are less affected by source motion, and hence can be estimated with narrower

low-pass filters. The most separated elements at the farthest corners of the matrix are the most subject to source motion, and require the highest bandwidth low-pass filter. The maximum bandwidth can be selected to match the highest bearing rate typically encountered.

3.2 Covariance Band-pass Filtering Methods

Further improvements in estimation may be potentially obtained by retaining only those epoch frequency bins containing significant shipping noise. One method involves partial knowledge available *a priori*. When the locations and tracks of the significant ships are independently known, for example from radar surveillance, then the bearing rates can be calculated and the epoch frequency bins identified. The energy in the identified bins then represents estimates of the unknown propagation and source level terms. Fourier synthesis using only the identified bins produces the desired covariance time series. The entire process can be described as a set of band pass filters, where each narrow pass band is selected based on the knowledge *a priori* of the bearing rates.

When no knowledge is available *a priori*, the potential exists to take advantage of the linear dependence on separation. Energy from each individual ship will lie along a line in the separation-epoch frequency plane. Line detection methods in this plane have the potential to automatically identify the appropriate bearing rates associated with significant interfering energy. Such methods may include Radon or Hough transforms [4]. Once the appropriate bins have been identified, band pass filters can be constructed to filter the shipping noise from the sample noise.

4. SIMULATION

A simulation was performed to demonstrate the potential utility of these techniques. In the simulation, the exact ensemble mean can be calculated since all quantities are known. Adaptive processing based on this exact mean covariance gives an upper bound to the maximum performance that could be achieved, if, for example, perfect knowledge were available *a priori*. In addition to the ensemble mean, the simulation generated time samples of covariance from four moving ships with Gaussian noise sources. The ships were moving at realistic speeds from between 10 and 20 knots. The tracks of the ships are shown in figure 1. Noise from the ships was propagated with cylindrical spreading in a single mode underwater channel. The noise was received on a line array of 50 elements with a design frequency of 60 Hz. The simulation was performed at this design frequency.

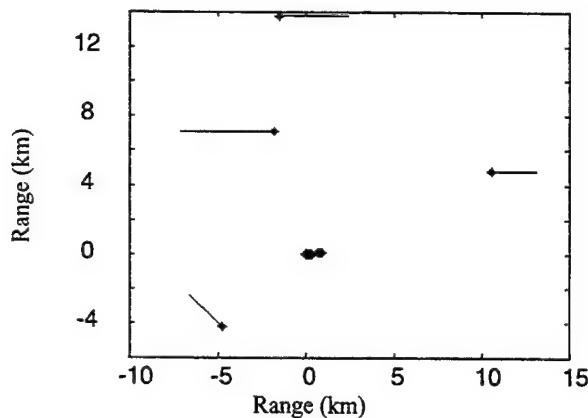


Figure 1. Tracks of the four ships in the simulation relative to array at origin

The simulation calculated the conventional beamformer response and compared with various MVDR beamformer responses for a set of beams spanning all azimuths. The beamformers used various estimates of the ensemble mean covariance. In addition to the exact ensemble mean, the ABF based on the sample mean and the ABF based on an element dependent low-pass filter were simulated. Results of the simulation are summarized by cumulative distributions of noise across all beams shown in figure 2.

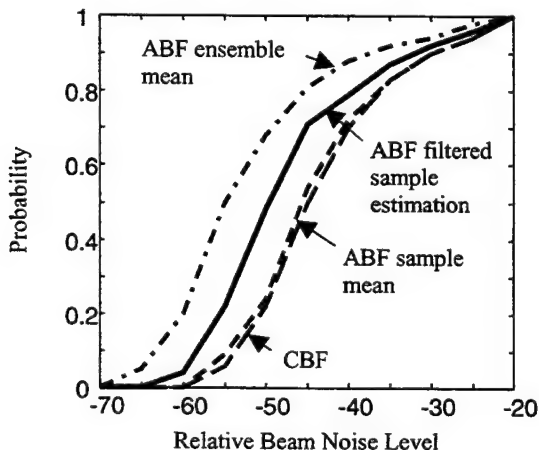


Figure 2. Cumulative distributions of noise for various beamformers

The sample mean ABF performed almost no better than conventional non-adaptive ABF in the simulation. The sample mean was unable to properly capture the motion of the ships, and hence was unable to place nulls in the proper locations to cancel the ship noise. The element dependent ABF filtered sample covariance showed a median improvement of about 5 dB reduction in the noise over the sample mean approach. The perfect ensemble mean displayed 10 dB reduction in noise beyond the sample mean method.

5. CONCLUSIONS

The problem of adapting in the presence of moving sources of interference was considered. Application was particularly addressed to the motion of interfering surface ship noise for passive sonar arrays. The physics of ship motion was modeled, including the received noise field and the noise covariance matrix. An analytic expression of the ensemble mean covariance was obtained. This physical model suggested a new approach of covariance filtering to better estimate the ensemble mean covariance from data samples.

Two paradigms of current adaptive beamforming may need to be abandoned in the presence of interference motion. First, the sample mean may not be the appropriate estimator when the interference sources are in motion. Second, the covariance matrix may not be treated as a single entity, since motion affects different elements of the matrix differently.

The behavior of the covariance under interference motion can be visualized in the epoch frequency domain. This domain is the Fourier transform of the samples of the covariance matrix. It was observed that energy from each moving ship falls along an approximate line in the epoch frequency / element separation plane. Several methods for obtaining improved estimates of the ensemble mean covariance were suggested. Preliminary investigations of relative performance of a few of these methods were obtained via a simulation.

Much remains to be done to develop these methods further. There is great potential for refinement of the algorithms and development of better filtering techniques. The epoch frequency domain has only begun to be explored. Line detection techniques have yet to be attempted. It has been suggested that the covariance matrix may also have a near-toeplitz structure in the epoch frequency domain [5]. If so, then toeplitz averaging, or low-pass filtering along the toeplitz directions may provide additional rejection of sample noise. Finally, applications of this class of techniques to real data are certainly warranted.

6. REFERENCES

- [1] C.A. Boyles, *Acoustic Waveguides Application to Oceanic Science*, Wiley Interscience, New York, 1984, p. 174.
- [2] J.N. Maksym, "A robust formulation of an optimum cross-spectral beamformer for line arrays," *J. Acoustic. Soc. Am.*, vol. 65, no. 4, Apr. 1979, pp. 971-975.
- [3] J. Capon, "High-Resolution Frequency-Wavenumber Spectrum Analysis," *Proceedings of the IEEE*, vol. 57, no. 8, Aug. 1969, pp. 1408-1418.
- [4] J. Illingworth and J. Kittler, "A Survey of the Hough Transform," *Computer Vision, Graphics and Image Processing*, vol. 44, no. 1, 1988, pp. 87-116.
- [5] R. Pitre, personal communication.

Beamspace Adaptive Beamforming for Hydrodynamic Towed Array Self-Noise Cancellation

Vincent E. Premus, Stephen M. Kogon, and James Ward*

MIT Lincoln Laboratory
244 Wood Street, Lexington, MA 02420
vpremus@ll.mit.edu

ABSTRACT

A beamspace adaptive beamformer implementation for the rejection of cable strum self-noise on passive sonar towed arrays is presented. The approach focuses on the implementation of a white noise gain constraint based on the scaled projection technique due to Cox et al. [IEEE Trans. on ASSP, Vol. 35 (10), Oct. 1987]. The objective is to balance the aggressive adaptation necessary for nulling the strong mainlobe interference represented by cable strum against the conservative adaptation required for protection against signal self-nulling associated with steering vector mismatch. Particular attention is paid to the definition of white noise gain as the metric that reflects the level of mainlobe adaptive nulling for an adaptive beamformer. Adaptation control is subsequently performed through the implementation of a constraint on maximum allowable white noise gain at the output of the adaptive processor. The theoretical development underlying the scaled projection based constraint implementation is reviewed. Towed array data results depicting the performance gain of the new ABF algorithm optimized for strum cancellation relative to that of a more conservative baseline ABF algorithm are presented.

1. INTRODUCTION

Hydrodynamic self-noise on passive sonar towed arrays has been a well-known performance-limiting factor for ocean acoustic source detection at low frequency [1]. High wavenumber mechanical vibrations are induced in the array by vortex shedding associated with hydrodynamic flow over the array body and cable scope. These vibrations are known to couple into the hydrophone array as coherent acoustic noise sources and can impair acoustic detection performance, particularly in the forward endfire direction. As a direct consequence of its spatially coherent nature, it has been shown that cable strum noise effects can be mitigated via adaptive

processing [2]. In this work, a new approach to coherent strum noise mitigation, based on a beamspace adaptive beamformer (ABF) architecture with a white noise gain constraint (WNGC) that emphasizes mainlobe interference nulling is introduced. Finally, data results illustrating the performance improvement over an existing beamspace ABF algorithm that emphasizes robustness to mismatch-induced self-nulling are presented.

2. THE PHYSICS OF CABLE STRUM

2.1 Vortex shedding

When an array is subject to hydrodynamic flow with a component normal to its axis, a wake is formed. When the velocity of the transverse flow increases beyond a certain threshold, eddies, or vortices, begin to form and separate from the wake. Eventually these vortices shed from the wake in an asymmetric fashion [3]. This asymmetric shedding imparts an oscillatory lift force locally on the array which, depending on the properties of the array such as tension and density, can excite transverse vibrations which propagate along the array axis. The frequency of vortex shedding in hydrodynamic flow is related to properties of the flow and the array via the empirically determined Strouhal relation [1]:

$$f_s = \frac{Sv}{d},$$

where S is the Strouhal number, equal to 0.21 in the laminar flow regime characteristic of most towed array environments, v is the velocity of flow normal to the array axis, and d is the cable diameter. Note that the normal component of velocity of flow can vary with time in response to platform motion and local inhomogeneities in the turbulent medium

The transfer function to which the Strouhal excitation is applied is governed by the wave equation subject to the boundary conditions of the array under tow. For example,

Sponsored in part by PEO-USW ASTO, under Air Force Contract F19628-00-C-0002. Opinions, interpretations, conclusions, and recommendations are those of the author and are not necessarily endorsed by the U.S. Air Force.

assuming fixed boundary conditions for the array, the preferred frequencies of vibration or modes of the array corresponding to the solution of the wave equation is given by:

$$f_n = \frac{n}{2L} \sqrt{\frac{T}{m_c}},$$

where T is cable tension, m_c is mass per unit length of the cable, and L is the cable length. Figure 1 depicts notionally the interaction of the Strouhal excitation with the structural modes of the array. Cable strum due to vortex shedding is strongly excited when the Strouhal excitation frequency is closely aligned with a resonant mode of the cable transfer function.

2.2 Wavenumber-frequency analysis

The decomposition of an array snapshot into its constituent acoustic and non-acoustic components is accomplished using a wavenumber-frequency, or k - ω , transform. The k - ω transform is a 2-d FFT in space and time. Maximum unambiguous wavenumber resolvable is equal to π/d , where d is the sensor spacing. Resolution in wavenumber is governed by the aperture length, L . For non-dispersive propagation, frequency and wavenumber are linearly related via

$$k(f) = \frac{2\pi f}{c_p},$$

where c_p equals the phase speed of the wavefront.

Figures 2 and 3 depict k - ω plots for two towed arrays under consideration in this work. The first exhibits superior vibration isolation and higher resolution due to its longer aperture. This array experiences only weak sidelobe leakage of vibrational modes into the acoustic cone. As such, under nominal operating conditions, this array does not exhibit a pronounced cable strum interference problem. The second array is characterized by limited vibration isolation. It is subject to significant leakage of vibrational energy into the acoustic cone via mainlobe penetration in forward endfire. Leakage of vibrational energy into acoustic forward endfire is a strong function of own-ship tow speed. For this array, which is the subject array for this paper, cable strum represents a significant mainlobe interference problem.

3. BEAMSPACE ABF FOR CABLE STRUM

The ABF architecture under consideration in this paper consists of a frequency-domain beamspace adaptive beamformer. The adaptive beamspace consists of a 7-

dimensional beam fan with fixed cosine spacing. The beam fan translates with steering direction.

The beamspace ABF derives its cable strum nulling capability from the fact that near endfire the beam fan is partially composed of beams steered to high wavenumber non-acoustic space.

For each time epoch, the element timeseries are transformed to the frequency domain via FFT. A beamspace covariance matrix is formed for each frequency bin independently and a 7-dimensional beamspace MVDR weight vector is subsequently computed. Adaptation control is governed by setting a limit on the maximum allowable white noise gain for the adaptive processor.

3.1 White Noise Gain

White noise gain (WNG) is defined as the gain applied by the adaptive beamformer to a spatially white input noise process, and is represented by

$$\text{WNG} = \bar{\mathbf{w}}^H \bar{\mathbf{w}},$$

where \mathbf{w} represents the MVDR beamformer steering vector given by

$$\bar{\mathbf{w}} = \frac{\mathbf{R}^{-1} \bar{\mathbf{v}}}{\bar{\mathbf{v}}^H \mathbf{R}^{-1} \bar{\mathbf{v}}}.$$

The vector \mathbf{v} represents the CBF weight vector and the matrix \mathbf{R} denotes the sample covariance for the current processing bin. (Actually, the beamformer WNG is a quantity equally applicable to the output of the CBF beamformer, expressed as $\mathbf{v}^H \mathbf{v}$). Beamformer WNG is a measure of the level of mainlobe adaptive nulling effected by the beamformer steering vector. As such, a constraint on maximum allowable WNG can be used to control the level of mainlobe adaptation of the adaptive beamformer relative to that of the ideal conventional beamformer:

$$\bar{\mathbf{w}}^H \bar{\mathbf{w}} \leq \frac{\beta}{N}.$$

Here β is a constant ranging from 1 to infinity, with 1 representing CBF performance (no adaptive nulling capability and best robustness to mismatch) and infinity representing MVDR performance (most adaptive nulling capability and most sensitivity to mismatch). Note that under this convention, the quantity $1/N$ represents the WNG of the conventional CBF beamformer, where N equals the number of elements in the array.

The relative WNG is a particularly important metric to consider when the source of interference lies within the

beamformer mainbeam. Figure 4 depicts the behavior of the WNG of the minimum variance distortionless response (MVDR) ABF relative to that of CBF for a simulation scenario in which an interferer is swept across cosine space and permitted to penetrate the beamformer mainbeam. An elevation in WNG results from the ABF algorithm attempting to drive a mainlobe null concurrent with satisfying the MVDR unity gain constraint in the steering direction. The three inset figures show ABF (shown in red) and CBF (shown in blue) beam patterns in the vicinity of the steering direction for three different interferer cosine positions. The sequence attempts to connect the WNG cosine dependence with the ABF beam pattern shape as the interferer cosine approaches the steering direction. When the interferer is far in the sidelobe of the array beam pattern (inset 3), the ABF and CBF mainlobe beam patterns effectively overlap. In this case, a simple sidelobe null (not pictured) is all that is needed in order to maximize signal-to-interference-plus-noise ratio (SINR). As the interferer penetrates the mainbeam, a squinting or splitting of the adaptive beam pattern occurs coincident with the introduction of a mainlobe null. This squinting is the result of the beamformer's attempt to maximize SINR by trading off interference suppression against excess white noise gain in the vicinity of the steering direction.

3.2 Adaptivity/Robustness Tradeoff

Figure 4 illustrated how an elevation in WNG occurs in response to a mainlobe interferer. We may conclude that WNG is a measure of the mainbeam adaptive nulling being performed by the ABF. It is important to understand that the ABF algorithm is unable to distinguish between most forms of signal model mismatch and a mainlobe interferer. Thus, the ABF will interpret steering vector mismatch as mainlobe interference and attempt to cancel it as well. Some degree of steering vector mismatch is unavoidable in real towed array data applications. Common sources of mismatch include manifold uncertainty, sensor calibration error, and unmodeled multipath propagation. The beamformer signal model is based on an assumption of a perfect plane wave with known sensor gain and known relative sensor location. As the ABF algorithm will attempt to null any data component that deviates from these assumptions, self-nulling due to steering vector mismatch is a major concern. By imposing a constraint on the maximum allowable WNG of the adaptive beamformer, robustness to mismatch induced nulling may be introduced.

Analyses of towed array data have shown that to effect a useful level of strum rejection using the beamspace ABF algorithm, a fairly aggressive adaptation strategy is required. By contrast, signal protection against self-nulling in the cable strum band

requires a very conservative adaptation approach. In this work, it was empirically determined that a WNGC of 6 dB, or a maximum allowable WNG of 4x that of the CBF beamformer, represents the best compromise between mainlobe cable strum nulling and signal preservation in the presence of mismatch.

3.3 Adaptive Weight Power Scaling

The white noise gain constraint (WNGC) employed in the beamspace ABF architecture is based on the scaled projection technique first proposed by Cox *et al.* [4].

The scaled projection WNGC implementation is composed of two essential parts. First, the MVDR weight vector is decomposed into two orthogonal components, non-adaptive and adaptive components respectively, using the following beamspace projection operators:

$$P_{na} = \frac{\bar{v}\bar{v}^H}{\bar{v}^H\bar{v}}, \quad P_a = I - P_{na}$$

Second, upon a WNG threshold exceedance, the adaptive component thus isolated is scaled such that the WNGC at the beamformer output is met exactly.

The orthogonal decomposition prior to adaptive weight scaling is important. This step guarantees that the weight scaling will be applied only to the adaptive, or data-dependent, component of the ABF weight vector. This insures that the scaling process does not modify, scale, or rotate the beamformer response to a signal that is perfectly matched to the steering vector. Consequently, the scaling preserves the constraint of distortionless response in the steering direction. The adaptive component of the MVDR weight vector is given by:

$$\bar{w}_a = P_a \bar{w}.$$

It is straightforward to verify that the non-adaptive and adaptive components derived in this way are indeed orthogonal. The scaled output weight vector is then given by:

$$\bar{w}_o = \bar{w}_{na} + k\bar{w}_a,$$

where the scalar, k , represents the scaling coefficient. We then specify the WNGC at the output of the beamspace ABF processor in terms of a multiplier on the non-adaptive WNG,

$$\bar{w}_o^H T^H T \bar{w}_o \leq \alpha \bar{w}_{na}^H T^H T \bar{w}_{na}.$$

Here, T represents the 7-dimensional transformation from element space to adaptive beamspace. For a 6 dB WNGC the multiplier, α , is equal to 4. Solving the constraint equation results in a quadratic on the scaling coefficient, k [5]. The result is two solutions for k which meet the constraint exactly. We choose the value which minimizes the output power of the ABF. This procedure

is carried out at each processing epoch and for each frequency bin independently. A geometric interpretation of the weight scaling procedure is shown in Figure 5.

4. TOWED ARRAY DATA RESULTS

Figure 6 depicts frequency-azimuth (FRAZ) plots for a typical time epoch for each of four different processors: a) the CBF beamformer, 2) the conservative baseline ABF beamformer, 3) the aggressive 6 dB WNGC ABF optimized for strum rejection, and 4) unconstrained MVDR. The baseline ABF represents the WNGC as implemented in the present towed array processing system. While the details of this WNGC implementation are not presented here, the basic design philosophy of this ABF algorithm is to emphasize robustness to mismatch effects. Upon exceeding the WNG threshold, set in the vicinity of 2 dB, the baseline ABF scales the adaptive weight vector back to the non-adaptive or CBF weight vector. This severely constrains the ability of the baseline ABF to effectively null any strong mainlobe interference such as cable strum.

In Figure 6, the presence of a strong interference source with multiple sidelobes is observed near broadside in the CBF FRAZ display. As expected all of the ABF approaches, conservative and aggressive alike, demonstrate the capacity to null such a strong discrete sidelobe interference source. This result thus serves as a useful consistency check of algorithm implementation.

Next, we direct our attention to the cable strum interference near forward sector, i.e. near cosine equal to 1. In the normalized frequency band $f = 0-0.3$, cable strum is observed to extend over a wide sector of cosine space from forward endfire to near broadside. The important differences between the conservative and aggressive ABF approaches are apparent from the cable strum rejection performance in this frequency band. The conservative ABF algorithm does very little to reduce the amplitude of the strum interference in forward endfire. The bearing extent of the strum is reduced slightly. With its 6 dB WNGC, the bearing extent and amplitude of the cable strum is significantly curtailed relative to that of the conservative baseline ABF algorithm.

Figure 7 shows raw power spectrum density plots to further illustrate the performance improvement realized with increasingly aggressive adaptation. Notice that the cable strum ABF achieves as much as a 15 dB local suppression of the strum-dominated noise floor in the normalized frequency band $f = 0.1-0.3$. The resulting noise floor suppression uncovers the presence of a narrowband feature at $f = 0.2$ that was otherwise

undetectable in the CBF and baseline ABF configurations.

Figure 8 shows the measured WNG plots corresponding to the power spectrum density plots of Figure 7. The measured WNG illustrates the relationship between WNGC and strum rejection. It is clear that at a WNGC of 6 dB most of the strum noise floor suppression performance is realized. Recall that the point here is to allow the ABF algorithm to adapt only as much as necessary to effect useful cable strum noise suppression.

5. CONCLUSIONS

Mechanically induced towed array self-noise limits detection performance in passive sonar systems, particularly at forward endfire. In this work, a beamspace adaptive beamforming architecture for the rejection of strong mainlobe cable strum rejection in forward endfire was presented. The approach focused on the choice of a white noise gain constraint which achieved a suitable balance between aggressive adaptation for effective strum nulling and conservative adaptation for robustness to mismatch-induced self-nulling. A WNGC of 6 dB relative to the WNG for the non-adaptive steering vector was empirically determined to offer the best balance. The WNGC implementation was based on the scaled projection technique first presented by Cox et al. [4]. Significant cable strum suppression performance was shown to be possible, on the order of 15 dB locally within the strum interference band.

6. REFERENCES

- [1] J. W. Bedenbender, R. C. Johnston, and E. B. Neitzel, "Electroacoustic characteristics of marine seismic streamers," *Geophysics*, vol. 35, no. 6, Dec. 1970, pp. 1054-1072.
- [2] V. Premus, "Adaptive Self-Noise Suppression for Passive Sonar Towed Arrays," *Proceedings of the Eighth Annual Workshop on Adaptive Sensor Array Processing, ASAP 2000*, MIT Lincoln Laboratory, March, 2000.
- [3] L. Prandtl, "The generation of vortices in fluids of small viscosity," *J. Royal Aeronautical Society*, Vol. 31, Dec. 1927, pp. 720-741.
- [4] H. Cox, R. Zeskind, and M. Owen, "Robust Adaptive Beamforming," *IEEE Trans. on ASSP*, Vol. 35, No. 10, Oct., 1987.
- [5] Z. Tian, K. Bell, and H. Van Trees, "A Recursive Least Squares Implementation for Adaptive Beamforming Under Quadratic Constraint," *IEEE Trans. on SP*, Feb. 2000.

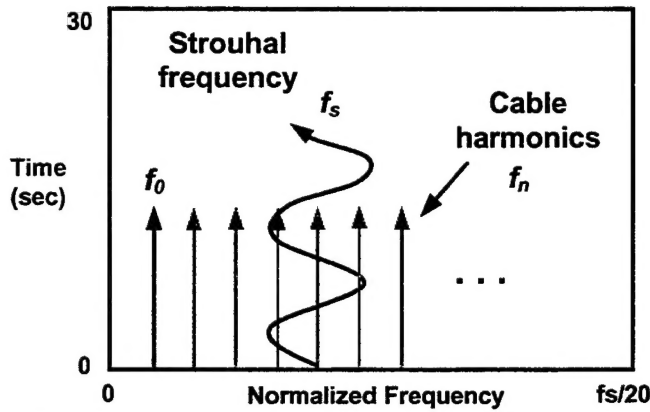


Figure 1: Notional depiction of time varying Strouhal excitation and array vibrational modes.

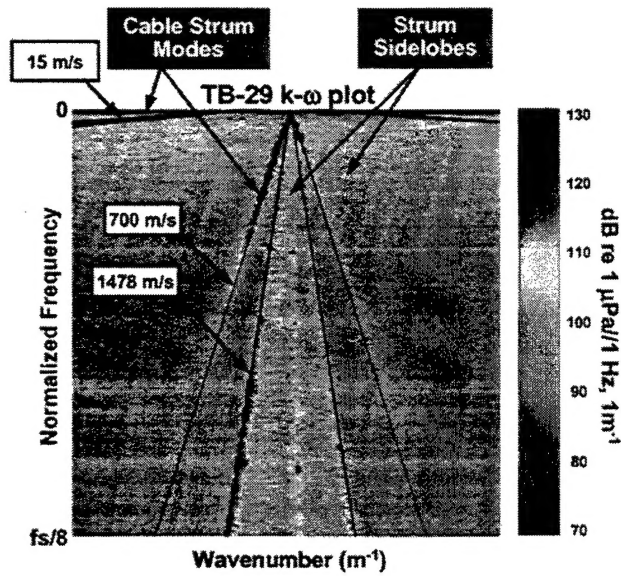


Figure 2: Frequency-wavenumber plot for TB-29 array.

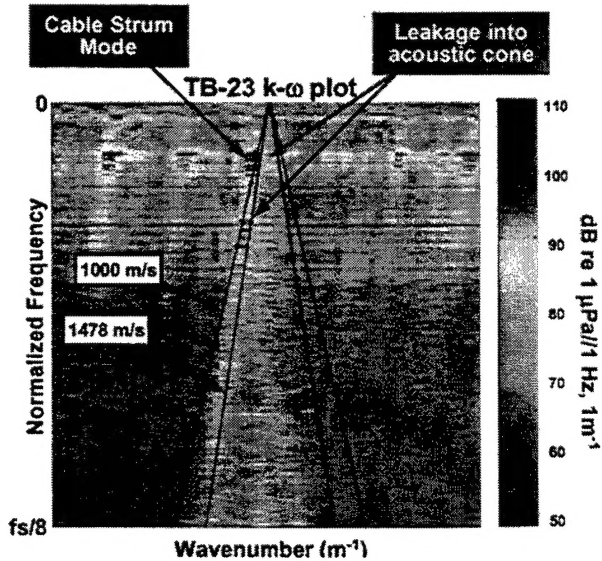


Figure 3: Frequency-wavenumber plot for TB-23 array.

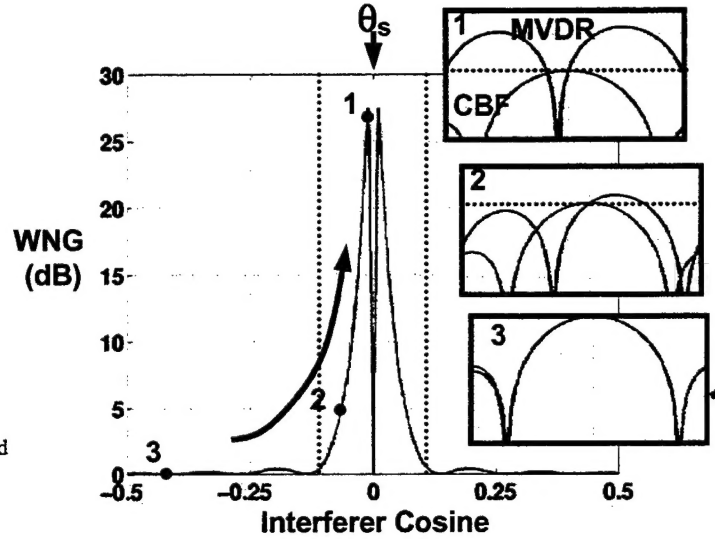


Figure 4: Simulated white noise gain plot and associated CBF and MVDR beampatterns.

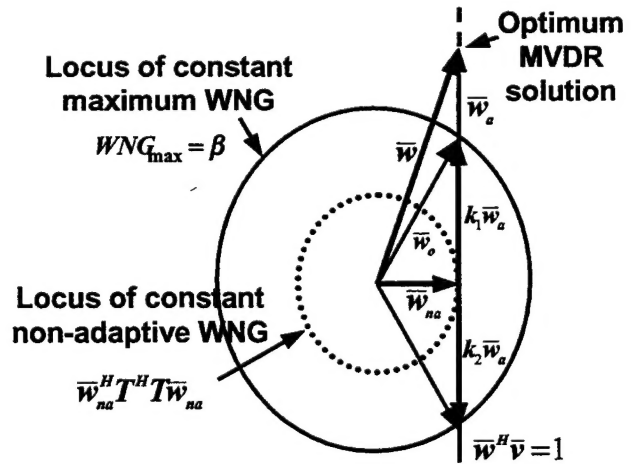


Figure 5: Geometric interpretation of scaled projection weight scaling technique.

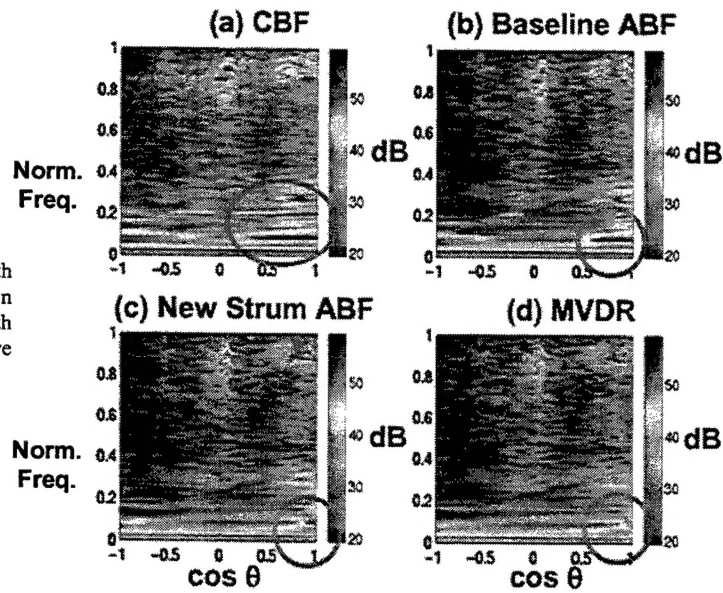


Figure 6: Frequency-Azimuth plots depicting reduction in cable strum cosine extent with increasingly more aggressive adaptation.

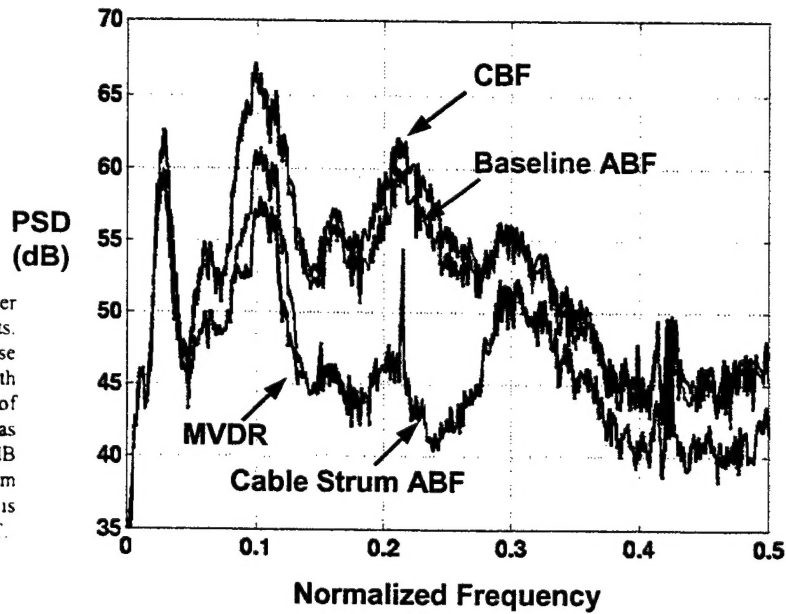


Figure 7: Raw power spectrum density plots illustrating strum noise floor suppression with increasing levels of adaptation. Locally as much as 15 dB improvement in strum noise suppression is realized with 6 dB WNGC.

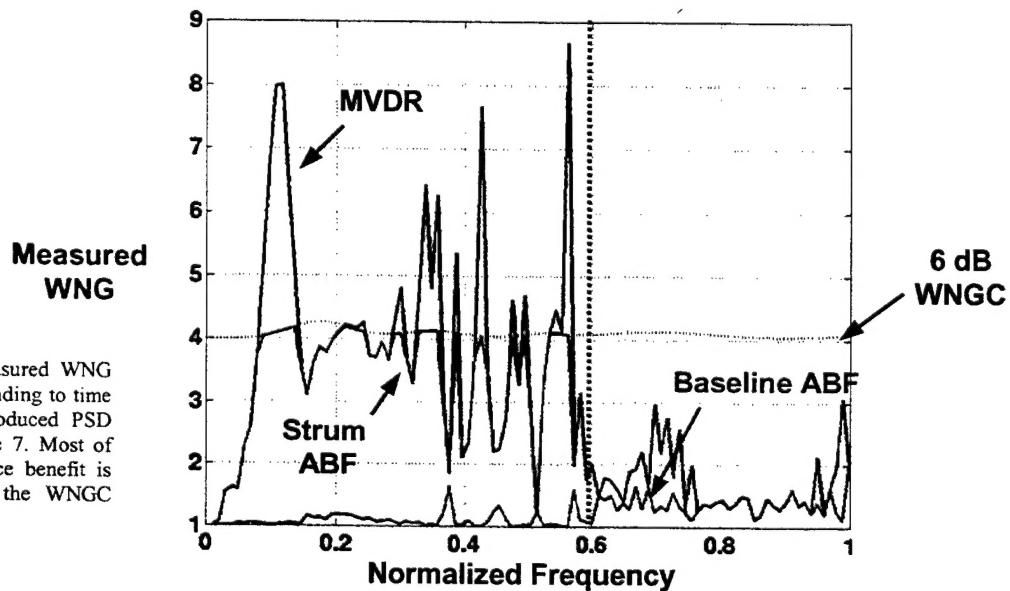


Figure 8: Measured WNG plots corresponding to time epoch that produced PSD plots in Figure 7. Most of the performance benefit is realized with the WNGC equal to 6 dB.

REPORT DOCUMENTATION PAGE			Form Approved OMB No. 0704-0188	
<small>Public reporting burden for this collection of information is estimated to average 1 hour per response, including the time for reviewing instructions, searching existing data sources, gathering and maintaining the data needed, and completing and reviewing the collection of information. Send comments regarding this burden estimate or any other aspect of this collection of information, including suggestions for reducing this burden, to Washington Headquarters Services, Directorate for Information Operations and Reports, 1215 Jefferson Davis Highway, Suite 1204, Arlington, VA 22202-4302, and to the Office of Management and Budget, Paperwork Reduction Project (0704-0188), Washington, DC 20503.</small>				
1. AGENCY USE ONLY (Leave blank)	2. REPORT DATE 20 July 2001	3. REPORT TYPE AND DATES COVERED Project Report		
4. TITLE AND SUBTITLE Proceedings of the Adaptive Sensor Array Processing (ASAP) Workshop, 13-14 March 2001		5. FUNDING NUMBERS C — F19628-00-C-0002		
6. AUTHOR(S) Jane E. Daneu, Editor				
7. PERFORMING ORGANIZATION NAME(S) AND ADDRESS(ES) Lincoln Laboratory, MIT 244 Wood Street Lexington, MA 02420-9108		8. PERFORMING ORGANIZATION REPORT NUMBER ASAP-9, Volume 2		
9. SPONSORING/MONITORING AGENCY NAME(S) AND ADDRESS(ES) DARPA/ISO 3701 N. Fairfax Drive Arlington, VA 22203-1714		10. SPONSORING/MONITORING AGENCY REPORT NUMBER ESC-TR-00-068		
11. SUPPLEMENTARY NOTES None				
12a. DISTRIBUTION/AVAILABILITY STATEMENT Approved for public release; distribution is unlimited.		12b. DISTRIBUTION CODE		
13. ABSTRACT (Maximum 200 words) <p>This year marks the ninth annual Adaptive Sensor Array Processing Workshop, which is sponsored jointly by the DARPA Advanced Technology and Tactical Technology Offices, the Navy AEGIS and E2C Program Offices, the Office of Naval Research, and the NAVSEA Advanced Systems Technology Office.</p> <p>As the ASAP Workshop has evolved over its nine-year history, a common theme has been to highlight the similarity of adaptive sensor array processing techniques for various disciplines. The ASAP forum has provided researchers from academia, government, and industry the opportunity to discuss common problems, developing ideas, and solutions related to how these diverse technologies can be applied to national defense interests. This year will continue to stress the strong coupling between government, industry and academia. A key theme will be the cross-fertilization of ideas to provide new areas of exploration and accelerate technological advances.</p>				
14. SUBJECT TERMS			15. NUMBER OF PAGES 116	
			16. PRICE CODE	
17. SECURITY CLASSIFICATION OF REPORT Unclassified	18. SECURITY CLASSIFICATION OF THIS PAGE Same as Report	19. SECURITY CLASSIFICATION OF ABSTRACT Same as Report	20. LIMITATION OF ABSTRACT Same as Report	